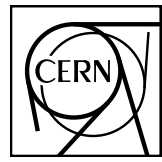


EUROPEAN ORGANIZATION FOR NUCLEAR RESEARCH



ALICE-ANA-2018-xxx
March 26, 2019

ΛK and $\Xi^- K^\pm$ Femtoscopy in Pb-Pb Collisions at $\sqrt{s_{NN}} = 2.76$ TeV from the LHC ALICE Experiment

Jesse T. Buxton¹

1. Department of Physics, The Ohio State University, Columbus, Ohio, USA

Email: jesse.thomas.buxton@cern.ch

Abstract

I present the first femtoscopic analysis of ΛK correlations in Pb-Pb collisions at $\sqrt{s_{NN}} = 2.76$ TeV measured by the ALICE experiment at the Large Hadron Collider (LHC). All pair combinations of Λ and $\bar{\Lambda}$ with K^+ , K^- and K_S^0 are analyzed. The femtoscopic correlations result from strong final-state interactions, and are fit with a parametrization allowing us to both characterize the emission source and measure the scattering parameters for the particle pairs. We observe a large difference in the ΛK^+ and ΛK^- correlations in pairs with low relative momenta ($k^* \lesssim 100$ MeV/c). This might suggest an effect arising from different quark-antiquark interactions within the pairs ($s\bar{s}$ in ΛK^+ and $u\bar{u}$ in ΛK^-), or from different net strangeness for each system. To gain further insight into this hypothesis, we are currently conducting a $\Xi^- K^\pm$ femtoscopic analysis, for which I present preliminary results.

Contents

1	Introduction	7
2	Data Sample and Software	7
2.1	Data Sample	7
2.2	Software	7
3	Data Selection	7
3.1	Event Selection and Mixing	7
3.2	K^\pm Track Selection	8
3.3	V0 Selection	11
3.3.1	General V0 Reconstruction	11
3.3.2	Λ Reconstruction	13
3.3.3	K_S^0 Reconstruction	14
3.3.4	V0 Purity Estimation	16
3.3.5	V0 Purity Background Estimation	16
3.4	Ξ Reconstruction	17
3.5	Pair Selection	19
4	Correlation Functions	23
4.1	Typical Correlation Function Construction	23
4.2	Stavinskiy Correlation Function Construction	26
5	Fitting	29
5.1	Model: ΛK_S^0 , ΛK^\pm , $\Xi^- K_S^0$	29
5.2	Model: $\Xi^- K^\pm$	31
5.3	Momentum Resolution Corrections	32
5.4	Residual Correlations	37
5.5	Non-femtoscopic background	45
5.6	LednickyFitter	49
5.7	Coulomb Fitter	50
6	Systematic Errors	51
6.1	Systematic Errors: ΛK_S^0	52
6.1.1	Particle and Pair Cuts	52

6.1.2	Non-femtoscopic background	52
6.1.3	Fit range	52
6.2	Systematic Errors: ΛK^\pm	53
6.2.1	Particle and Pair Cuts	53
6.2.2	Non-femtoscopic background	53
6.2.3	Fit range	53
6.3	Systematic Errors: ΞK^\pm	53
6.3.1	Particle and Pair Cuts	53
7	Results and Discussion	55
7.1	Results: ΛK_S^0 and ΛK^\pm	55
7.1.1	Correlation functions with fits	58
7.1.2	Discussion of m_T -Scaling	61
7.2	Results: ΞK^\pm	70
A	Results: ΛK_S^0 and ΛK^\pm (Additional Figures)	77
A.1	Fit Method Comparisons	78
A.2	3 Residual Contributors Included in Fit	80
A.3	10 Residual Contributors Included in Fit	87
A.4	No Residual Contributors Included in Fit	92
B	Spherical Harmonics	96
C	Additional Figures	102
C.1	Residuals	102
C.1.1	ΛK^+ Residuals	102
C.1.2	ΛK^- Residuals	108
C.1.3	ΛK_S^0 Residuals	114
D	Useful Gaussian Integrals	120
D.1	Simple univariate Gaussian integral	120
D.2	Product of two univariate Gaussian integrals	120
D.3	Univariate Gaussian with linear term in exponential	122

List of Figures

1	V0 Reconstruction	11
2	K_S^0 contamination in $\Lambda(\bar{\Lambda})$ collection	14
3	$\Lambda(\bar{\Lambda})$ contamination in K_S^0 collection	15
4	V0 ($\Lambda, \bar{\Lambda}, K_S^0$) Purities	17
5	V0 Purity Background Estimation	18
6	Ξ Reconstruction	18
7	$\Xi^-(\bar{\Xi}^+)$ Purity	19
8	Average Separation of $\Lambda(\bar{\Lambda})$ and K_S^0 Daughters	21
9	Average Separation of $\Lambda(\bar{\Lambda})$ Daughter and K^\pm	21
10	Average Separation of Ξ Daughters and K^\pm	22
11	ΛK^+ & $\bar{\Lambda} K^-$ Correlation Functions	24
12	ΛK^- & $\bar{\Lambda} K^+$ Correlation Functions	24
13	ΛK_S^0 & $\bar{\Lambda} K_S^0$ Correlation Functions	25
14	Correlation Functions: ΛK^+ vs ΛK^- for 0-10% Centrality	25
15	ΛK Stavinskiy Correlation Functions (Correct)	27
16	ΛK Stavinskiy Correlation Functions (Correct and Incorrect)	28
17	Momentum Resolution: Sample k_{True}^* vs. k_{Rec}^*	33
18	Particle Contaminations Visible in k_{True}^* vs. k_{Rec}^*	34
19	Momentum Resolution Corrections: Methods Comparison	36
20	Residual Contributions Cartoon	37
21	Sample Transform Matrices for ΛK^+ Analysis	38
22	Sample Transform Matrices for $\bar{\Lambda} K^+$ Analysis	39
23	Reconstruction Efficiencies	40
24	$\Sigma^0 K^+$ Transform	43
25	ΛK^{*0} Transform	44
26	Compare Non-Femtoscopic Backgrounds	45
27	Backgrounds with THERMINATOR, K_S^0 Tweak	46
28	Backgrounds with THERMINATOR 2	47
29	Correlation with background decomposition (THERM)	48
30	Background reduction methods with THERMINATOR	49
31	Extracted scattering parameters	56
32	m_T scaling of radii	57

33	$\Lambda K^+(\bar{\Lambda}K^-)$ data with fits	58
34	$\Lambda K^-(\bar{\Lambda}K^+)$ data with fits	59
35	$\Lambda(\bar{\Lambda})K_S^0$ data with fits	60
36	m_T scaling of radii with individual m_T highlighted	61
37	Numerical integration of Koonin-Pratt equation: ΛK^+	63
38	Numerical integration of Koonin-Pratt equation: ΛK^-	64
39	$\Lambda K^+ C_{00}$ and $\Re C_{11}$ spherical harmonic components (0-10%)	65
40	Extracted radius with pair sources from THERMINATOR 2	66
41	THERMINATOR 2 simulation with artificial Gaussian source	67
42	Varying μ_{Out} with THERMINATOR 2	68
43	Correlation functions: ΛK^+ vs ΛK^- in 0-10% centrality bin	70
44	ΞK^\pm results	71
45	ΞK^\pm data with Coulomb-only bands, 0-10% centrality	72
46	Effect of strong force inclusion on Coulomb-only curve	73
47	ΞK^\pm global Coulomb-only fit (Set 1)	74
48	ΞK^\pm global Coulomb-only fit (Set 2)	75
49	$\Xi^- K^\pm$ Coulomb-only fit: $\Xi^- K^+$ separate from $\Xi^- K^-$	76
A.1	Fit comparison: number of residuals	79
A.2	Fit comparison: free vs fixed λ_{Fit}	80
A.3	Fit comparison: normal CF construction vs. Staninskiy method	81
A.4	Fit comparison: shared vs. separate radii	81
A.5	Fit comparison: experimental vs simulated $\Xi^- K^\pm$	82
A.6	m_T scaling of radii: 3 residuals	82
A.7	Extracted scattering parameters: 3 residuals	83
A.8	$\Lambda K^+(\bar{\Lambda}K^-)$ data with fits: 3 residuals	84
A.9	$\Lambda K^+(\bar{\Lambda}K^-)$ fit contribution from residuals: 3 residuals	84
A.10	$\Lambda K^-(\bar{\Lambda}K^+)$ data with fits: 3 residuals	85
A.11	$\Lambda K^-(\bar{\Lambda}K^+)$ fit contribution from residuals: 3 residuals	85
A.12	$\Lambda(\bar{\Lambda})K_S^0$ data with fits: 3 residuals	86
A.13	$\Lambda K_S^0(\bar{\Lambda}K_S^0)$ fit contribution from residuals: 3 residuals	86
A.14	m_T scaling of radii: 10 residuals	87
A.15	Extracted scattering parameters: 10 residuals	88
A.16	$\Lambda K^+(\bar{\Lambda}K^-)$ data with fits: 10 residuals	89

A.17 $\Lambda K^+(\bar{\Lambda} K^-)$ fit contribution from residuals: 10 residuals	89
A.18 $\Lambda K^-(\bar{\Lambda} K^+)$ data with fits: 10 residuals	90
A.19 $\Lambda K^-(\bar{\Lambda} K^+)$ fit contribution from residuals: 10 residuals	90
A.20 $\Lambda(\bar{\Lambda})K_S^0$ data with fits: 10 residuals	91
A.21 $\Lambda K_S^0(\bar{\Lambda} K_S^0)$ fit contribution from residuals: 10 residuals	91
A.22 m_T scaling of radii: No residuals	92
A.23 Extracted scattering parameters: No residuals	93
A.24 $\Lambda K^+(\bar{\Lambda} K^-)$ data with fits: no residuals	94
A.25 $\Lambda K^-(\bar{\Lambda} K^+)$ data with fits: no residuals	94
A.26 $\Lambda(\bar{\Lambda})K_S^0$ data with fits: no residuals	95
B.1 $\Lambda K^+ C_{00}$ and $\Re C_{11}$ spherical harmonic components	96
B.2 $\Lambda K^- C_{00}$ and $\Re C_{11}$ spherical harmonic components	97
B.3 $\Lambda K_S^0 C_{00}$ and $\Re C_{11}$ spherical harmonic components	98
B.4 ΛK^+ first six components of SH decomposition (0-10%)	99
B.5 ΛK^- first six components of SH decomposition (0-10%)	100
B.6 ΛK_S^0 first six components of SH decomposition (0-10%)	101
C.1 Residuals: $\Sigma^0 K^+$ to ΛK^+ (0-10% Centrality)	102
C.2 Residuals: $\Xi^0 K^+$ to ΛK^+ (0-10% Centrality)	103
C.3 Residuals: $\Xi^- K^+$ to ΛK^+ (0-10% Centrality)	103
C.4 Residuals: $\Sigma^{*+} K^+$ to ΛK^+ (0-10% Centrality)	104
C.5 Residuals: $\Sigma^{*-} K^+$ to ΛK^+ (0-10% Centrality)	104
C.6 Residuals: $\Sigma^{*0} K^+$ to ΛK^+ (0-10% Centrality)	105
C.7 Residuals: ΛK^{*0} to ΛK^+ (0-10% Centrality)	105
C.8 Residuals: $\Sigma^0 K^{*0}$ to ΛK^+ (0-10% Centrality)	106
C.9 Residuals: $\Xi^0 K^{*0}$ to ΛK^+ (0-10% Centrality)	106
C.10 Residuals: $\Xi^- K^{*0}$ to ΛK^+ (0-10% Centrality)	107
C.11 Residuals: $\Sigma^0 K^-$ to ΛK^- (0-10% Centrality)	108
C.12 Residuals: $\Xi^0 K^-$ to ΛK^- (0-10% Centrality)	109
C.13 Residuals: $\Xi^- K^-$ to ΛK^- (0-10% Centrality)	109
C.14 Residuals: $\Sigma^{*+} K^-$ to ΛK^- (0-10% Centrality)	110
C.15 Residuals: $\Sigma^{*-} K^-$ to ΛK^- (0-10% Centrality)	110
C.16 Residuals: $\Sigma^{*0} K^-$ to ΛK^- (0-10% Centrality)	111
C.17 Residuals: $\Lambda \bar{K}^{*0}$ to ΛK^- (0-10% Centrality)	111

C.18 Residuals: $\Sigma^0 \bar{K}^{*0}$ to ΛK^- (0-10% Centrality)	112
C.19 Residuals: $\Xi^0 \bar{K}^{*0}$ to ΛK^- (0-10% Centrality)	112
C.20 Residuals: $\Xi^- \bar{K}^{*0}$ to ΛK^- (0-10% Centrality)	113
C.21 Residuals: $\Sigma^0 K_S^0$ to ΛK_S^0 (0-10% Centrality)	114
C.22 Residuals: $\Xi^0 K_S^0$ to ΛK_S^0 (0-10% Centrality)	115
C.23 Residuals: $\Xi^- K_S^0$ to ΛK_S^0 (0-10% Centrality)	115
C.24 Residuals: $\Sigma^{*+} K_S^0$ to ΛK_S^0 (0-10% Centrality)	116
C.25 Residuals: $\Sigma^{*-} K_S^0$ to ΛK_S^0 (0-10% Centrality)	116
C.26 Residuals: $\Sigma^{*0} K_S^0$ to ΛK_S^0 (0-10% Centrality)	117
C.27 Residuals: ΛK^{*0} to ΛK_S^0 (0-10% Centrality)	117
C.28 Residuals: $\Sigma^0 K^{*0}$ to ΛK_S^0 (0-10% Centrality)	118
C.29 Residuals: $\Xi^0 K^{*0}$ to ΛK_S^0 (0-10% Centrality)	118
C.30 Residuals: $\Xi^- K^{*0}$ to ΛK_S^0 (0-10% Centrality)	119

10 1 Introduction

11 We present results from a femtoscopic analysis of ΛK and $\Xi^- K^\pm$ correlations in Pb-Pb collisions at
 12 $\sqrt{s_{NN}} = 2.76$ TeV by the ALICE experiment at the LHC. All pair combinations of Λ and $\bar{\Lambda}$ with K^+ ,
 13 K^- and K_S^0 are analyzed. The femtoscopic correlations are the result of strong final-state interactions,
 14 and are fit with a parametrization based on a model by R. Lednicky and V. L. Lyuboshitz [1]. This
 15 allows us to both characterize the emission source and measure the scattering parameters for the particle
 16 pairs. We observe a large difference in the $\Lambda K^+(\bar{\Lambda} K^-)$ and $\Lambda K^-(\bar{\Lambda} K^+)$ correlations in pairs with low
 17 relative momenta ($k^* \lesssim 100$ MeV). The results suggest an effect arising from different quark-antiquark
 18 interactions in the pairs, i.e. $s\bar{s}$ in $\Lambda K^+(\bar{\Lambda} K^-)$ and $u\bar{u}$ in $\Lambda K^-(\bar{\Lambda} K^+)$, or from different net strangeness for
 19 each system. To gain further insight into this hypothesis, we currently are conducting a ΞK femtoscopic
 20 analysis.

21 2 Data Sample and Software

22 2.1 Data Sample

23 The analysis used “pass 2” reconstructed Pb-Pb data from LHC11h (AOD145). The runlist was selected
 24 from runs with global quality tag “1” in the ALICE Run Condition Table. Approximately 40 million
 25 combined central, semi-central, and minimum bias events were analyzed. Runs from both positive (++)
 26 and negative (--) magnetic field polarity settings were used.

27 Run list: 170593, 170572, 170388, 170387, 170315, 170313, 170312, 170311, 170309, 170308, 170306,
 28 170270, 170269, 170268, 170230, 170228, 170207, 170204, 170203, 170193, 170163, 170159, 170155,
 29 170091, 170089, 170088, 170085, 170084, 170083, 170081, 170040, 170027, 169965, 169923, 169859,
 30 169858, 169855, 169846, 169838, 169837, 169835, 169591, 169590, 169588, 169587, 169586, 169557,
 31 169555, 169554, 169553, 169550, 169515, 169512, 169506, 169504, 169498, 169475, 169420, 169419,
 32 169418, 169417, 169415, 169411, 169238, 169167, 169160, 169156, 169148, 169145, 169144, 169138,
 33 169099, 169094, 169091, 169045, 169044, 169040, 169035, 168992, 168988, 168826, 168777, 168514,
 34 168512, 168511, 168467, 168464, 168460, 168458, 168362, 168361, 168342, 168341, 168325, 168322,
 35 168311, 168310, 168315, 168108, 168107, 168105, 168076, 168069, 167988, 167987, 167985, 167920,
 36 167915

37 Analysis was also performed on the LHC12a17a_fix (AOD149) Monte Carlo HIJING events for certain
 38 checks. THERMINATOR2 was also used for certain aspects, such as generation of transform matrices
 39 describing feed-down contributions, estimation of λ parameters, and non-femtoscopic background
 40 modeling.

41 2.2 Software

42 The analysis was performed on the PWGCF analysis train using AliRoot v5-09-29-1 and AliPhysics
 43 vAN-20180505-1.

44 The main classes utilized include: AliFemtoVertexMultAnalysis, AliFemtoEventCutEstimators, AliFemto
 45 toESDTrackCutNSigmaFilter, AliFemtoV0TrackCutNSigmaFilter, AliFemtoXiTrackCut, AliFemtoV0PairCut,
 46 AliFemtoV0TrackPairCut, AliFemtoXiTrackPairCut, and AliFemtoAnalysisLambdaKaon. All of these
 47 classes are contained in /AliPhysics/PWGCF/FEMTOSCOPY/AliFemto and .../AliFemtoUser.

48 3 Data Selection

49 3.1 Event Selection and Mixing

50 The events used in this study were selected with the class AliFemtoEventCutEstimators according to the
 51 following criteria:

- 52 – Triggers
- 53 – minimum bias (kMB)
- 54 – central (kCentral)
- 55 – semi-central (kSemiCentral)
- 56 – z-position of reconstructed event vertex must be within 10 cm of the center of the ALICE detector
- 57 – the event must contain at least one particle of each type from the pair of interest

58 The event mixing was handled by the AliFemtoVertexMultAnalysis class, which only mixes events with
 59 like vertex position and centrality. The following criteria were used for event mixing:

- 60 – Number of events to mix = 5
- 61 – Vertex position bin width = 2 cm
- 62 – Centrality bin width = 5

63 The AliFemtoEventReaderAODChain class is used to read the events. Event flattening is not currently
 64 used. FilterBit(7). The centrality is determined by the “V0M” method of AliCentrality, set by calling
 65 AliFemtoEventReaderAOD::SetUseMultiplicity(kCentrality). We utilize the SetPrimaryVertexCorrec-
 66 tionTPCPoints switch, which causes the reader to shift all TPC points to be relative to the event vertex.

67 3.2 K^\pm Track Selection

68 Charged kaons are identified using the AliFemtoESDTrackCutNSigmaFilter class. The single-particle
 69 selection criteria used to select charged kaon candidates are summarized in Tables 1 and 2. K^\pm track
 70 detection utilized both TPC and TOF detectors, and tracks within the range $0.14 < p_T < 1.5 \text{ GeV}/c$ were
 71 accepted. As we are interested in primary particles originating from the primary vertex, to reduce the
 72 number of secondaries (for instance, charged particles produced in the detector material, particles from
 73 weak decays, etc.) in our sample, we established a maximum cut on the distance-of-closest-approach
 74 (DCA) of the track the the primary vertex. This restriction is realized by imposing a DCA cut in both the
 75 transverse and beam directions.

76 PID was performed using both the TPC and TOF detectors via the $N\sigma$ method. Additionally, we include
 77 methods to reduce the contamination in our K^\pm samples from electrons and pions. The specifics for these
 78 cuts are contained in Table 1.

79 The purity of the K^\pm collections was estimated using the HIJING MC data, for which the true identity
 80 of each reconstructed K^\pm particle is known. Therefore, the purity may be estimated as:

$$Purity(K^\pm) = \frac{N_{true}}{N_{reconstructed}} \quad (1)$$

81 $\text{Purity}(K^+) \approx \text{Purity}(K^-) \approx 97\%$

K $^\pm$ selection

Kinematic range	
$ \eta $	< 0.8
p_T	$0.14 < p_T < 1.5 \text{ GeV}/c$
Track quality and selection	
FilterBit	7
Number of clusters in the TPC	> 80
χ^2/N_{DOF} for (ITS, TPC) clusters	< (3.0, 4.0)
DCA to primary vertex (XY, Z)	< (2.4, 3.0) cm
Remove particles with any kink labels	true
$N\sigma$ to primary vertex	< 3.0
K$^\pm$ identification	
PID Probabilities	
K	> 0.2
(π, μ, p)	< (0.1, 0.8, 0.1)
Most probable particle type (fMostProbable =)	Kaon (3)
TPC and TOF N σ Cuts	
$p < 0.4 \text{ GeV}/c$	$N_{\sigma K, \text{TPC}} < 2$
$0.4 < p < 0.45 \text{ GeV}/c$	$N_{\sigma K, \text{TPC}} < 1$
$0.45 < p < 0.80 \text{ GeV}/c$	$N_{\sigma K, \text{TPC}} < 3$ $N_{\sigma K, \text{TOF}} < 2$
$0.80 < p < 1.0 \text{ GeV}/c$	$N_{\sigma K, \text{TPC}} < 3$ $N_{\sigma K, \text{TOF}} < 1.5$
$p > 1.0 \text{ GeV}/c$	$N_{\sigma K, \text{TPC}} < 3$ $N_{\sigma K, \text{TOF}} < 1$

Table 1: K $^\pm$ selection

K\pm selection - Misidentification Cuts			
Electron Rejection: Reject if			$N_{\sigma e^-, \text{TPC}} < 3$
Pion Rejection: Reject if:			
$p < 0.65 \text{ GeV}/c$	TOF and TPC available		$N_{\sigma\pi, \text{TPC}} < 3$ $N_{\sigma\pi, \text{TOF}} < 3$
	Only TPC available	$p < 0.5 \text{ GeV}/c$	$N_{\sigma\pi, \text{TPC}} < 3$
		$0.5 < p < 0.65 \text{ GeV}/c$	$N_{\sigma\pi, \text{TPC}} < 2$
$0.65 < p < 1.5 \text{ GeV}/c$			$N_{\sigma\pi, \text{TPC}} < 5$ $N_{\sigma\pi, \text{TOF}} < 3$
$p > 1.5 \text{ GeV}/c$			$N_{\sigma\pi, \text{TPC}} < 5$ $N_{\sigma\pi, \text{TOF}} < 2$

Table 2: K \pm selection - misidentification cuts

82 **3.3 V0 Selection**

83 **3.3.1 General V0 Reconstruction**

84 $\Lambda(\bar{\Lambda})$ and K_S^0 particles are electrically neutral, and cannot be directly detected, but must instead be re-
 85 constructed through detection of their decay products, or daughters. This process is illustrated in Figure
 86 1, and the main cuts used are shown in Tables 3 and 4. In general, particles which are topologically
 87 reconstructed in this fashion are called V0 particles. The decay channel $\Lambda \rightarrow p\pi^-$ was used for the
 88 identification of Λ hyperons (and, similarly the charge-conjugate decay for the $\bar{\Lambda}$ identification), and K_S^0
 89 $\rightarrow \pi^+\pi^-$ for the identification of K_S^0 mesons. The class AliFemtoV0TrackCutNSigmaFilter (which is an
 90 extension of AliFemtoV0TrackCut) is used to reconstruct the V0s.

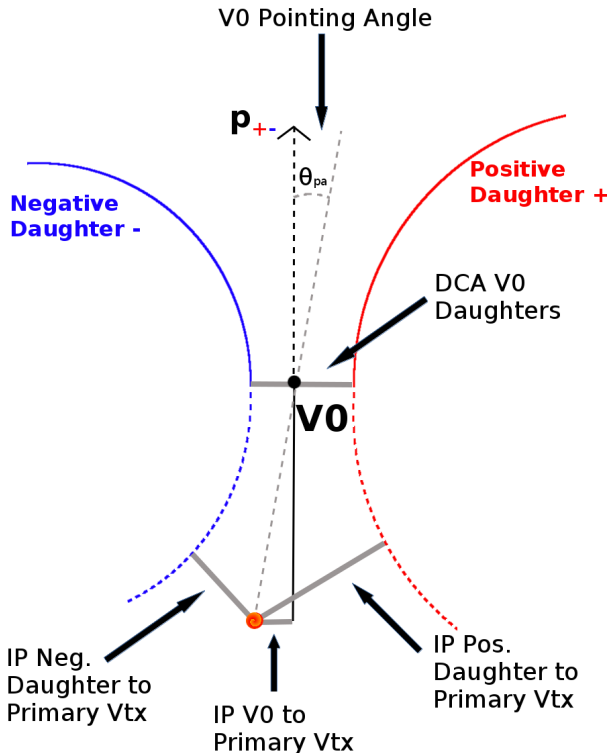


Fig. 1: V0 Reconstruction

91 To construct a V0 particle, the charged daughter tracks must first be found. Aside from typical kinematic
 92 and PID cuts (using TPC and TOF detectors), the daughter tracks are also exposed to a minimum cut
 93 on their impact parameter with respect to the primary vertex. The daughters of a V0 particle should
 94 not originate from the primary vertex, but rather from the decay vertex of the V0, hence the minimum
 95 cut imposition. The decay vertex of the V0 is assumed to be the point of closest approach between the
 96 daughter tracks. To help ensure quality, a maximum value cut is demanded on the distance-of-closest-
 97 approach between the daughters (DCA V0 Daughters). The positive and negative daughter tracks are
 98 combined to form the V0 candidate, the momentum of which is simply the sum of the momenta of the
 99 daughters (calculated at the DCA).

100 A minimum transverse momentum cut on the V0 candidate is introduced to reduce contamination from
 101 fake candidates. Opposite to that of the daughter tracks, the V0 candidate is exposed to a maximum cut
 102 on its impact parameter with respect to the primary vertex. In this case, we do want our V0 candidates
 103 to be primary, hence the maximum cut imposition. To further strengthen our selection of primary V0
 104 candidates, we impose a selection on the pointing angle, θ_{pa} , between the V0 momentum and the vector
 105 pointing from the primary vertex to the secondary V0 decay vertex. We want the V0 candidate's momen-
 106 tum to point back to the primary decay vertex, and therefore a small θ_{pa} ; we achieve this by appointing a

minimum value on $\cos(\theta_{\text{pa}})$ (“Cosine of pointing angle” in Tables 3 and 4).

On occasion, $\Lambda(\bar{\Lambda})$ particles are misidentified as K_S^0 , and vice versa. To attempt to remove these contaminations without throwing away good candidates, we impose a set of misidentification cuts. The intent of these cuts is to judge whether a candidate is more likely a $\Lambda(\bar{\Lambda})$ or a K_S^0 , and are implemented as described below. For a given V0, we calculate the mass assuming different identities (Λ , $\bar{\Lambda}$, K_S^0) of the candidate; the mass assuming K_S^0 hypothesis ($m_{\text{inv}, K_S^0 \text{ hyp.}}$) is calculated assuming $\pi^+\pi^-$ daughters, the mass assuming Λ hypothesis ($m_{\text{inv}, \Lambda \text{ hyp.}}$) is calculated assuming $p\pi^-$ daughters, and the mass assuming $\bar{\Lambda}$ hypothesis ($m_{\text{inv}, \bar{\Lambda} \text{ hyp.}}$) is calculated assuming $\bar{p}\pi^+$ daughters. In addition to the notation just introduced, in the following, m_{PDG, K_S^0} and $m_{\text{PDG}, \Lambda(\bar{\Lambda})}$ denote the particle masses of the K_S^0 and $\Lambda(\bar{\Lambda})$, respectively, as recorded by the Particle Data Group [2].

For $\Lambda(\bar{\Lambda})$ selection, a candidate is assumed to be misidentified and is rejected if all of the following criteria are satisfied:

1. $|m_{\text{inv}, K_S^0 \text{ hyp.}} - m_{\text{PDG}, K_S^0}| < 9.0 \text{ MeV}/c^2$
2. The daughter particles pass daughter cuts intended for K_S^0 reconstruction
 - (a) Λ selection
 - i. p daughter passes π^+ cuts intended for K_S^0 reconstruction
 - ii. π^- daughter passes π^- cuts intended for K_S^0 reconstruction.
 - (b) $\bar{\Lambda}$ selection
 - i. π^+ daughter passes π^+ cuts intended for K_S^0 reconstruction
 - ii. \bar{p} daughter passes π^- cuts intended for K_S^0 reconstruction.
3. $|m_{\text{inv}, K_S^0 \text{ hyp.}} - m_{\text{PDG}, K_S^0}| < |m_{\text{inv}, \Lambda(\bar{\Lambda}) \text{ hyp.}} - m_{\text{PDG}, \Lambda(\bar{\Lambda})}|$

Similarly, for K_S^0 selection, a candidate is rejected if all of the following criteria are satisfied for the Λ case, or for the $\bar{\Lambda}$ case:

1. $|m_{\text{inv}, \Lambda(\bar{\Lambda}) \text{ hyp.}} - m_{\text{PDG}, \Lambda(\bar{\Lambda})}| < 9.0 \text{ MeV}/c^2$
2. The daughter particles pass daughter cuts intended for $\Lambda(\bar{\Lambda})$ reconstruction
 - (a) π^+ daughter passes $p(\pi^+)$ daughter cut intended for $\Lambda(\bar{\Lambda})$ reconstruction
 - (b) π^- daughter passes $\pi^-(\bar{p})$
3. $|m_{\text{inv}, \Lambda(\bar{\Lambda}) \text{ hyp.}} - m_{\text{PDG}, \Lambda(\bar{\Lambda})}| < |m_{\text{inv}, K_S^0 \text{ hyp.}} - m_{\text{PDG}, K_S^0}|$

At this stage, we have a collection of V0 candidates satisfying all of the aforementioned cuts. However, this collection is still polluted by fake V0s, for which the daughter particles happen to pass all of our cuts, but which do not actually originate from a V0. Although the two daughter particles appear to reconstruct a V0 candidate, they are lacking one critical requirement: the system invariant mass does not match that of our desired V0 species (these can be seen outside of the mass peaks in Fig. 4). Therefore, as our final single-particle cut, we require the invariant mass of the V0 candidate to fall within the mass peak of our desired species. Note, however, that some fake V0s still make it past this final cut, as their invariant mass also happens to fall within our acceptance window.

143 Occasionally, we encounter a situation where two V0 candidates share a common daughter. Not both of
 144 these candidates can be real V0s, and including both could introduce an artificial signal into our data.
 145 To avoid any auto-correlation effects, for each event, we impose a single-particle shared daughter cut on
 146 each collection of V0 candidates. This cut iterates through the V0 collection to ensure that no daughter is
 147 claimed by more than one V0 candidate. If a shared daughter is found between two V0 candidates, that
 148 candidate with a smaller DCA to primary vertex is kept while the other is excluded from the analysis.
 149 Note, this single-particle shared daughter cut is unique from the pair shared daughter cut discussed in
 150 Sec. 3.5, the latter of which ensure there is no daughter sharing between the particles in a given pair.
 151 The specific cuts used to reconstruct our $\Lambda(\bar{\Lambda})$ and K_S^0 populations, along with plots showing the effect
 152 of the misidentification cuts, are shown in the following sections.

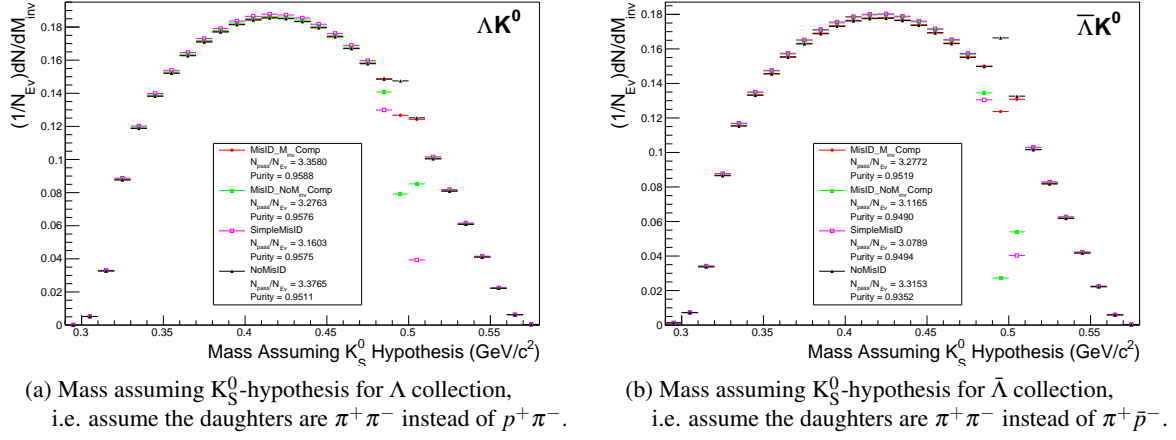
153 3.3.2 Λ Reconstruction

154 The following cuts, in addition to the misidentification and shared daughter cuts presented in Sec. 3.3.1,
 155 were used to select good $\Lambda(\bar{\Lambda})$ candidates:

Λ reconstruction					
$ \eta $	< 0.8				
p_T	> 0.4 GeV/c				
$ m_{\text{inv}} - m_{\text{PDG}} $	< 3.8 MeV				
DCA to prim. vertex	< 0.5 cm				
Cosine of pointing angle	> 0.9993				
OnFlyStatus	false				
Decay Length	< 60 cm				
Shared Daughter Cut	true				
Misidentification Cut	true				
Daughter Cuts (π and p)					
$ \eta $	< 0.8				
Number of clusters in the TPC	> 80				
Daughter status	kTPC χ cut				
DCA πp Daughters	< 0.4 cm				
π-specific cuts					
p_T	> 0.16 GeV/c				
DCA to prim vertex	> 0.3 cm				
TPC and TOF Nσ Cuts					
$p < 0.5 \text{ GeV}/c$	$N\sigma_{\text{TPC}} < 3$				
$p > 0.5 \text{ GeV}/c$	<table border="1"> <tr> <td>if TOF & TPC available</td><td>$N\sigma_{\text{TPC}} < 3 \& N\sigma_{\text{TOF}} < 3$</td></tr> <tr> <td>else</td><td>$N\sigma_{\text{TOF}} < 3$</td></tr> </table>	if TOF & TPC available	$N\sigma_{\text{TPC}} < 3 \& N\sigma_{\text{TOF}} < 3$	else	$N\sigma_{\text{TOF}} < 3$
if TOF & TPC available	$N\sigma_{\text{TPC}} < 3 \& N\sigma_{\text{TOF}} < 3$				
else	$N\sigma_{\text{TOF}} < 3$				
p-specific cuts					
p_T	> $0.5(p) [0.3(\bar{p})] \text{ GeV}/c$				
DCA to prim vertex	> 0.1 cm				
TPC and TOF Nσ Cuts					
$p < 0.8 \text{ GeV}/c$	$N\sigma_{\text{TPC}} < 3$				
$p > 0.8 \text{ GeV}/c$	<table border="1"> <tr> <td>if TOF & TPC available</td><td>$N\sigma_{\text{TPC}} < 3 \& N\sigma_{\text{TOF}} < 3$</td></tr> <tr> <td>else</td><td>$N\sigma_{\text{TOF}} < 3$</td></tr> </table>	if TOF & TPC available	$N\sigma_{\text{TPC}} < 3 \& N\sigma_{\text{TOF}} < 3$	else	$N\sigma_{\text{TOF}} < 3$
if TOF & TPC available	$N\sigma_{\text{TPC}} < 3 \& N\sigma_{\text{TOF}} < 3$				
else	$N\sigma_{\text{TOF}} < 3$				

Table 3: Λ reconstruction

156 Figure 2a shows the mass assuming K_S^0 hypothesis for the Λ collection, i.e. assume the daughters are
 157 $\pi^+ \pi^-$ instead of $p^+ \pi^-$. Figure 2b is a similar plot, but is for the $\bar{\Lambda}$ collection, i.e. assume the daughters
 158 are $\pi^+ \pi^-$ instead of $\pi^+ \bar{p}^-$. The K_S^0 contamination is visible, although not profound, in both, in the slight



(a) Mass assuming K_S^0 -hypothesis for Λ collection,
i.e. assume the daughters are $\pi^+\pi^-$ instead of $p^+\pi^-$.

(b) Mass assuming K_S^0 -hypothesis for $\bar{\Lambda}$ collection,
i.e. assume the daughters are $\pi^+\pi^-$ instead of $\pi^+\bar{p}^-$.

Fig. 2: Mass assuming K_S^0 -hypothesis for V0 candidates passing all Λ (2a) and $\bar{\Lambda}$ (2b) cuts. The “NoMisID” distribution (black triangles) uses the V0 finder without any attempt to remove misidentified K_S^0 . The slight peak in the “NoMisID” distribution around $m_{inv} = 0.5 \text{ GeV}/c^2$ contains misidentified K_S^0 particles in our $\Lambda(\bar{\Lambda})$ collection. “SimpleMisID” (pink squares) simply cuts out the entire peak, which throws away some good Λ and $\bar{\Lambda}$ particles. “MisID_NoM_{inv}Comp” (green squares) uses the misidentification cut outlined in the text, but does not utilize the final invariant mass comparison step. “MisID_M_{inv}Comp” (red circles) utilizes the full misidentification methods, and is currently used for this analysis. “ N_{pass}/N_{ev} ” is the total number of $\Lambda(\bar{\Lambda})$ particles found, normalized by the total number of events. The purity of the collection is also listed.

peaks around $m_{inv} = 0.497 \text{ GeV}/c^2$. If one simply cuts out the entire peak, good Λ particles will be lost. Ideally, the Λ selection and K_S^0 misidentification cuts are selected such that the peak is removed from this plot while leaving the underlying distribution continuous. To attempt to remove these K_S^0 contaminations without throwing away good Λ and $\bar{\Lambda}$ particles, the misidentification cuts introduced in Sec. 3.3.1 were imposed.

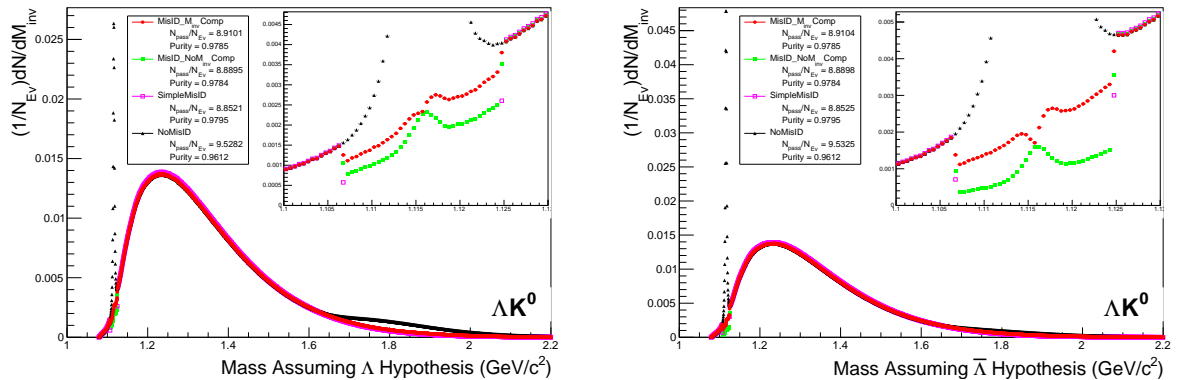
3.3.3 K_S^0 Reconstruction

The following cuts, in addition to the misidentification and shared daughter cuts presented in Sec. 3.3.1, were used to select good K_S^0 candidates:

As can be seen in Figure 3, some misidentified Λ and $\bar{\Lambda}$ particles contaminate our K_S^0 sample. Figure 3a shows the mass assuming Λ -hypothesis for the K_S^0 collection, i.e. assume the daughters are $p^+\pi^-$ instead of $\pi^+\pi^-$. Figure 3b is similar, but shows the mass assuming $\bar{\Lambda}$ -hypothesis for the collection, i.e. assume the daughters are $\pi^+\bar{p}^-$ instead of $\pi^+\pi^-$. The Λ contamination can be seen in 3a, and the $\bar{\Lambda}$ contamination in 3b, in the peaks around $m_{inv} = 1.115 \text{ GeV}/c^2$. Additionally, the $\bar{\Lambda}$ contamination is visible in Figure 3a, and the Λ contamination visible in Figure 3b, in the region of excess around $1.65 < m_{inv} < 2.1 \text{ GeV}/c^2$. This is confirmed as the number of misidentified Λ particles in the sharp peak of Figure 3a (misidentified $\bar{\Lambda}$ particles in the sharp peak of Figure 3b) approximately equals the excess found in the $1.65 < m_{inv} < 2.1 \text{ GeV}/c^2$ region of Figure 3a (Figure 3b).

The peaks around $m_{inv} = 1.115 \text{ GeV}/c^2$ in Figure 3 contain both misidentified $\Lambda(\bar{\Lambda})$ particles and good K_S^0 . If one simply cuts out the entire peak, some good K_S^0 particles will be lost. Ideally, the K_S^0 selection and $\Lambda(\bar{\Lambda})$ misidentification cuts can be selected such that the peak is removed from this plot while leaving the underlying distribution continuous. To attempt to remove these Λ and $\bar{\Lambda}$ contaminations without throwing away good K_S^0 particles, the misidentification cuts introduced in Sec. 3.3.1 were imposed.

K_S^0 reconstruction		
$ \eta $	< 0.8	
p_T	> 0.2 GeV/c	
$m_{PDG} - 13.677 \text{ MeV} < m_{\text{inv}} < m_{PDG} + 2.0323 \text{ MeV}$		
DCA to prim. vertex	< 0.3 cm	
Cosine of pointing angle	> 0.9993	
OnFlyStatus	false	
Decay Length	< 30 cm	
Shared Daughter Cut	true	
Misidentification Cut	true	
π^\pm Daughter Cuts		
$ \eta $	< 0.8	
Number of clusters in TPC	> 80	
Daughter Status	kTPCrefit	
DCA $\pi^+\pi^-$ Daughters	< 0.3 cm	
p_T	> 0.15 GeV/c	
DCA to prim vertex	> 0.3 cm	
TPC and TOF $N\sigma$ Cuts		
$p < 0.5 \text{ GeV}/c$	$N\sigma_{\text{TPC}} < 3$	
$p > 0.5 \text{ GeV}/c$	if TOF & TPC available else	$N\sigma_{\text{TPC}} < 3 \& N\sigma_{\text{TOF}} < 3$ $N\sigma_{\text{TOF}} < 3$

Table 4: K_S^0 reconstruction

 (a) Mass assuming Λ -hypothesis for K_S^0 collection, i.e. assume the daughters are $p^+\pi^-$ instead of $\pi^+\pi^-$.

 (b) Mass assuming $\bar{\Lambda}$ -hypothesis for K_S^0 collection, i.e. assume the daughters are $\pi^+\bar{p}^-$ instead of $\pi^+\pi^-$.

Fig. 3: Mass assuming Λ -hypothesis (3a) and $\bar{\Lambda}$ -hypothesis (3b) for K_S^0 collection. The “NoMisID” distribution (black triangles) uses the V0 finder without any attempt to remove misidentified Λ and $\bar{\Lambda}$. The peak in the “NoMisID” distribution around $m_{\text{inv}} = 1.115 \text{ GeV}/c^2$ contains misidentified Λ (3a) and $\bar{\Lambda}$ (3b) particles in our K_S^0 collection. “SimpleMisID” (pink squares) simply cuts out the entire peak, which throws away some good K_S^0 particles. “MisID_NoM_{inv}Comp” (green squares) uses the misidentification cut outlined in the text, but does not utilize the final invariant mass comparison step. “MisID_M_{inv}Comp” (red circles) utilizes the full misidentification methods, and is currently used for this analysis. “ $N_{\text{pass}}/N_{\text{ev}}$ ” is the total number of K_S^0 particles found, normalized by the total number of events. The purity of the collection is also listed. Also note, the relative excess of the “NoMisID” distribution around $1.65 < m_{\text{inv}} < 2.1 \text{ GeV}/c^2$ shows misidentified $\bar{\Lambda}$ (3a) and Λ (3b) particles in our K_S^0 collection.

3.3.4 V0 Purity Estimation

In order to obtain a true and reliable signal, one must ensure good purity of the V0 collection. The purity of the collection is calculated as:

$$\text{Purity} = \frac{\text{Signal}}{\text{Signal} + \text{Background}} \quad (2)$$

To access both the signal and background, the invariant mass distribution (m_{inv}) of all V0 candidates must be constructed immediately before the final invariant mass cut, as shown in Fig. 4 for Λ , $\bar{\Lambda}$ and K_S^0 candidates in the 0-10% centrality bin. Fig. 4a presents the $p\pi^-$ invariant mass distribution showing the Λ peak, Fig. 4b presents the $\bar{p}\pi^+$ invariant mass distribution showing the $\bar{\Lambda}$ peak, and Fig. 4c presents the $\pi^+\pi^-$ invariant mass distribution showing the K_S^0 peak.

It is vital that this distribution be constructed immediately before the final m_{inv} cut, otherwise it would be impossible to estimate the background. These distributions are used to calculate the collections' purities (defined in Eq. 2). As shown in Figure 4, the background is fit (with a polynomial) outside of the peak region of interest to obtain an estimate for the background within the region. Within the m_{inv} cut limits, the background is assumed to be the region below the fit while the signal is that above the fit. The Λ and $\bar{\Lambda}$ purities were found to be $\approx 95\%$, and the K_S^0 purity was found to be $\approx 98\%$.

3.3.5 V0 Purity Background Estimation

As previously stated, the backgrounds in the m_{inv} distributions are modeled by a polynomial which is fit outside of the final cut region in an attempt to estimate the background within the cut region. As this estimate of the background under the mass peak is vital for our estimate of our V0 purity, it is important for us to ensure that our estimate is accurate. More specifically, it is necessary that we ensure the background is well described by a polynomial fit within the cut region.

To better understand our background, we studied V0 candidates reconstructed with daughters from different events. These mixed-event V0s certainly do not represent real, physical V0s (a single V0 cannot have daughters living in two different events!), but, rather, represent a large portion of the background creeping into our analysis.

The standard AliFemto framework is not equipped to handle this situation, as most are not interested in these fake-V0s. Therefore, we built a new class, `AliFemtoV0PurityBgdEstimator`, to handle our needs. In addition to finding fake-V0s using mixed-event daughters, we also used our new class to find real-V0s using same-event daughters. The purpose here was to compare our new class to the established V0 finder used in standard AliFemto analyses.

Figure 5 shows the results of our study. In the figures, the black points, marked “Data”, correspond to V0s found using the standard V0-finder, and to the V0s used in my analyses. The red and blue points utilize our personal V0-finder (i.e. `AliFemtoV0PurityBgdEstimator`). The red points show real V0s reconstructed using same-event daughters, and the blue points show fake-V0s reconstructed using mixed-event daughters. Both the red and blue points have been scaled by different factors (listed in the legends) to nicely align all three data on a single plot.

Figure 5 shows that our personal V0-finder does a good, but not perfect, job of matching the shape of the m_{inv} plots obtained from the data. The scale factor listed in the legend reveals that we are only finding 1/3 - 1/2 of the V0s found by the standard V0-finder. These two points are not of concern, as our purpose here was to gain a sense of the broad shape of the background. It is revealed in Fig. 5, when studying the red and blue points, that the background distribution within the mass peak region is simply a smooth connection of the backgrounds outside of the cut region, as we assumed. Therefore, our method of fitting the background outside of the cut region, fitting with a smooth polynomial, and extrapolating to the cut

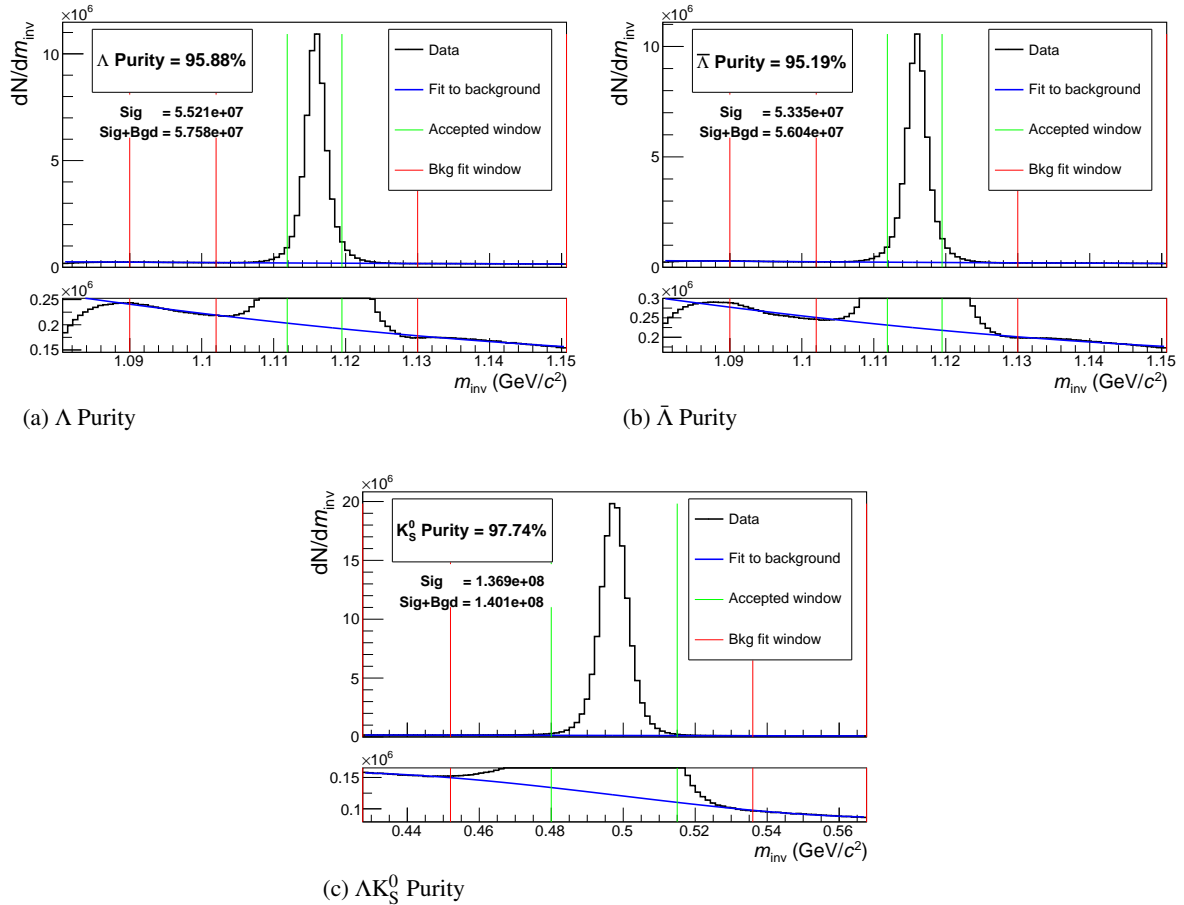


Fig. 4: Invariant mass (m_{inv}) distribution for all Λ (a), $\bar{\Lambda}$ (b), and K_S^0 (c) candidates immediately before the final invariant mass cut. The bottom figures are zoomed to show the background with fit. The vertical green lines represent the m_{inv} cuts used in the analyses, the red vertical lines delineate the regions over which the background was fit, and the blue line shows the background fit. These distributions are used to calculate the collection purities, $\text{Purity}(\Lambda) \approx \text{Purity}(\bar{\Lambda}) \approx 95\%$, and $\text{Purity}(K_S^0) \approx 98\%$.

region is justified.

3.4 Ξ Reconstruction

Our motivation for studying $\Xi^- K^\pm$ systems is to attempt to better understand the striking difference in the ΛK^+ and ΛK^- data at low k^* (Figure 14).

The reconstruction of Ξ particles is one level above V0 reconstruction. V0 particles are topologically reconstructed by searching for the charged daughters' tracks into which they decay. With Ξ particles, we search for the V0 particle and charged daughter into which the Ξ decays. In the case of Ξ^- , we search for the Λ (V0) and π^- (track) daughters. We will refer to this π as the “bachelor π ”.

The following cuts were used to select good Ξ^- ($\bar{\Xi}^+$) candidates:

1. Shared Daughter Cut for Ξ Collection

- Iterate through Ξ collection to ensure that no daughter is used in more than one Ξ candidate
- Remove any candidate in which the bachelor π is also a daughter of the Λ (implemented in AliFemtoXITrackPairCut class)

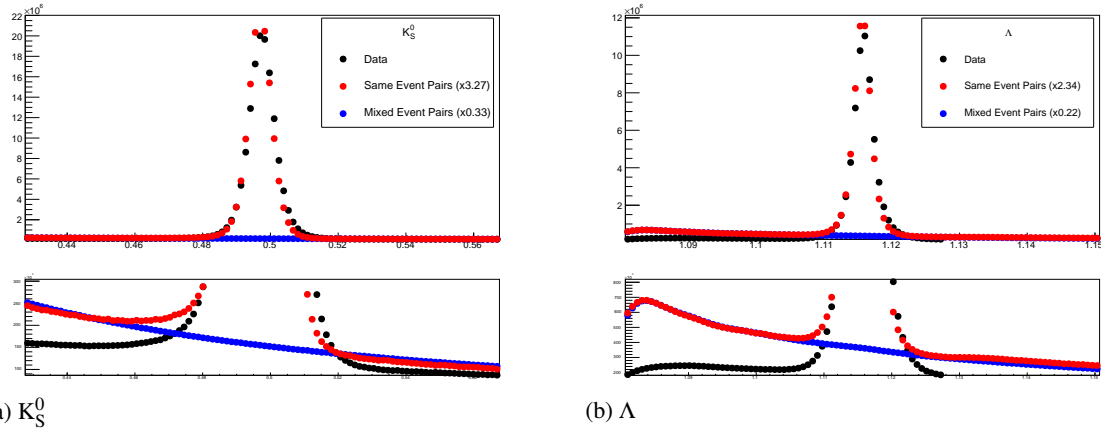


Fig. 5: V0 Purity Background Estimation. The black points, marked “Data”, correspond to real V0s found using the standard V0-finder (i.e. the V0s used in my analyses). The red points, marked “Same Event Pairs”, show real V0s reconstructed with our personal V0-finder in AliFemtoVOPurityBgdEstimator. These data are scaled by a factor (listed in the legend) to match their *Signal + Background* value in the cut region with that of the data. The blue points, marked “Mixed Event Pairs”, show fake-V0s reconstructed with our personal V0-finder using mixed-event daughters. The blue points are scaled by a factor (listed in the legend) to closely match the red points in the side-band region.

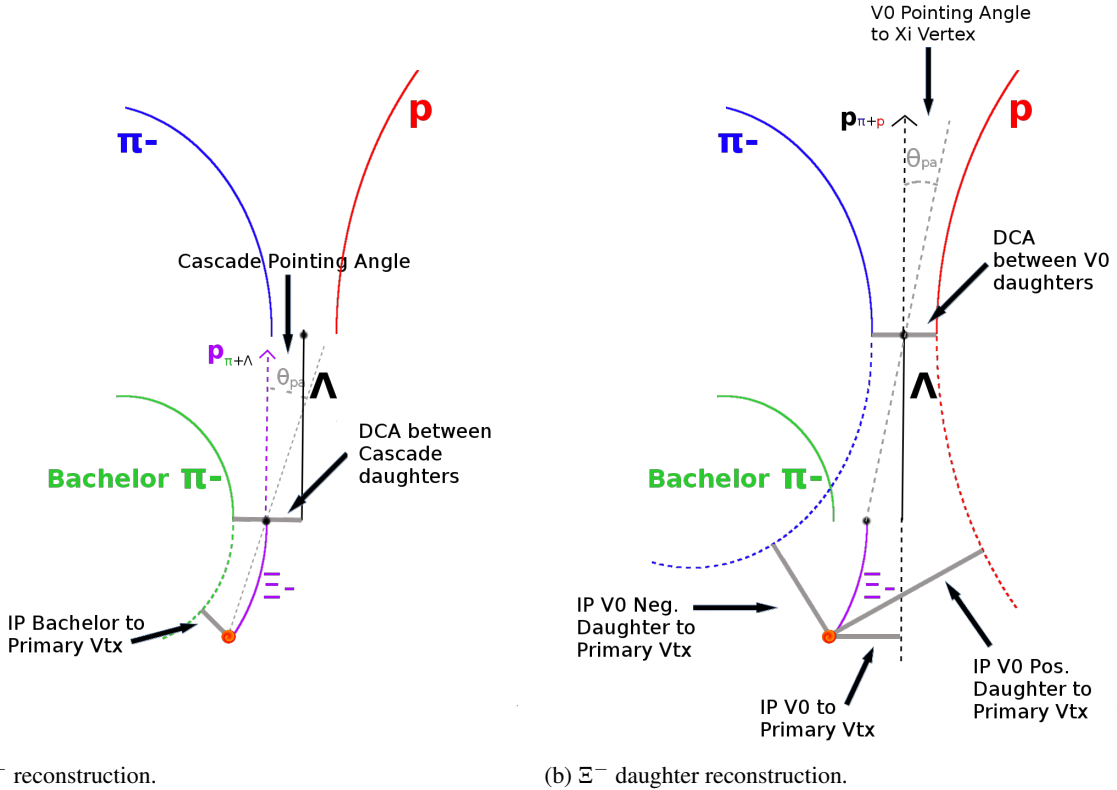


Fig. 6: (Left) Ξ^- reconstruction (DCA to primary vertex for Ξ^- not shown). (Right) Ξ^- daughter reconstruction.

²³⁶ The purity of our Ξ and $\bar{\Xi}$ collections are calculated just as those of our V0 collections 3.3. Figure 7,
²³⁷ which is used to calculate the purity, shows the m_{inv} distribution of our $\Xi(\bar{\Xi})$ candidates just before the
²³⁸ final m_{inv} cut. Currently, we have $\text{Purity}(\Xi^-) \approx 90\%$ and $\text{Purity}(\bar{\Xi}^+) \approx 92\%$.

Ξ reconstruction					
$ \eta $	< 0.8				
p_T	> 0.8 GeV/c				
$ m_{\text{inv}} - m_{\text{PDG}} $	< 3.0 MeV				
DCA to prim. vertex	< 0.3 cm				
Cosine of pointing angle	> 0.9992				
Λ daughter cuts					
DCA to prim. vertex	> 0.2 cm				
Cosine of pointing angle	> 0.0				
Cosine of pointing angle to Ξ decay vertex	> 0.9993				
OnFlyStatus	false				
All other Λ and corresponding (π and p) daughter cuts are same as in primary Λ selection, and can be found in Sec. 3.3.2					
Bachelor π cuts					
$ \eta $	< 0.8				
p_T	> 0.0 GeV/c				
DCA to prim. vertex	> 0.1 cm				
Number of clusters in the TPC	> 70				
Daughter status	kTPC π fit				
TPC and TOF $N\sigma$ Cuts					
$p < 0.5 \text{ GeV}/c$	$N\sigma_{\text{TPC}} < 3$				
$p > 0.5 \text{ GeV}/c$	<table border="1"> <tr> <td>if TOF & TPC available</td> <td>$N\sigma_{\text{TPC}} < 3 \& N\sigma_{\text{TOF}} < 3$</td> </tr> <tr> <td>else</td> <td>$N\sigma_{\text{TOF}} < 3$</td> </tr> </table>	if TOF & TPC available	$N\sigma_{\text{TPC}} < 3 \& N\sigma_{\text{TOF}} < 3$	else	$N\sigma_{\text{TOF}} < 3$
if TOF & TPC available	$N\sigma_{\text{TPC}} < 3 \& N\sigma_{\text{TOF}} < 3$				
else	$N\sigma_{\text{TOF}} < 3$				

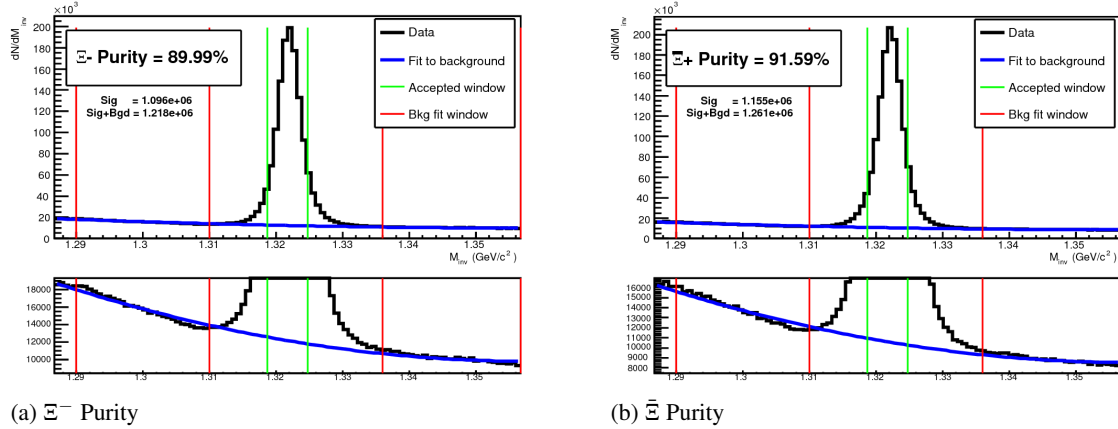
Table 5: Ξ reconstruction

Fig. 7: Invariant mass (m_{inv}) distribution for all Ξ^- (a) and $\bar{\Xi}^+$ (b) candidates immediately before the final invariant mass cut. The bottom figures are zoomed to show the background with fit. The vertical green lines represent the m_{inv} cuts used in the analyses, the red vertical lines delineate the regions over which the background was fit, and the blue line shows the background fit. These distributions are used to calculate the collection purities, $\text{Purity}(\Xi^-) \approx 90\%$ and $\text{Purity}(\bar{\Xi}^+) \approx 92\%$.

239 3.5 Pair Selection

240 The femtoscopic analysis of two-particle correlation functions relies on the proper formation of particle
 241 pairs. As such, it is important to obtain true particle pairs in the analysis. In particular, contamination
 242 from pairs constructed with split or merged tracks, and pairs sharing daughters, can introduce artificial
 243 signals into the correlation function, obscuring the actual physics. In an effort to remove contamination,

244 we impose two main pair cuts: a shared daughter cut, and an average separation cut.

245 The purpose of the shared daughter cut is to ensure the first particle in the pair is unique from the second.
 246 For pairs formed of two V0s (e.g. ΛK_S^0), this cut is implemented by removing all pairs which share
 247 a daughter. For example, in the ΛK_S^0 analysis, if the Λ and K_S^0 in a potential pair claim the same π^-
 248 daughter, the pair is excluded from the analysis. For a pair formed of a single V0 and a charged track
 249 (e.g. ΛK^\pm), the cut removes all pairs in which the charged track is also claimed as a daughter of the V0.
 250 This mistake could only occur if, for instance, either a K^\pm is misidentified as a π or p and used in the V0
 251 reconstruction, or a π or p is misidentified as a K^\pm in the K^\pm selection. In the case of a pair formed from
 252 a charged Ξ and a charged track (e.g. $\Xi^- K^\pm$), the cut removes all pairs in which the charged track is also
 253 claimed as a daughter of the Ξ , be it the bachelor- π daughter directly, or a daughter of the Λ daughter (a
 254 granddaughter of the Ξ). In the $\Xi^- K^\pm$ analysis, as in the ΛK^\pm case, this could only occur if there was
 255 misidentification of a K^\pm as a π or p, or vice versa.

256 The purpose of the average separation cut is to remove splitting and merging effects, and it is employed
 257 in the following way. To calculate the average separation between two tracks, the spatial separation is
 258 determined at several points throughout the TPC (every 20 cm radially from 85 cm to 245 cm), and the
 259 results averaged. For that ΛK_S^0 analysis, which involves two V0 particles, a minimum average separation
 260 cut of 6 cm between the like-charge daughters in the pairs was imposed (for example, between the p
 261 daughter of the Λ and the π^+ daughter of the K_S^0). For the ΛK^\pm analyses, a minimum average separation
 262 cut of 8 cm was enforced between the K^\pm and the Λ daughter sharing the same charge (for example,
 263 in the ΛK^+ analysis, between the p daughter of the Λ and the K^+). Finally, for the $\Xi^- K^\pm$ analysis, a
 264 minimum average separation cut of 8 cm was enforced between any daughter of the Ξ sharing the same
 265 charge as the K^\pm in the pair (for example, in the $\Xi^- K^-$ analysis, between the π^- granddaughter which
 266 decayed from the Λ daughter and the K^- , and between the bachelor- π^- daughter and the K^-).

267 The motivation for the values used in these cuts can be seen in Figures 8, 9, and 10, in which average sep-
 268 aration correlation functions are presented. The average separation correlation functions are formed just
 269 as for our relative-momentum correlation functions, but we instead bin in average separation. Looking at
 270 these average separation correlation functions for like-charge tracks, at lowest average separation we see
 271 an enhancement due to track splitting, followed by (at slightly higher average separation) a suppression
 272 due to track merging. When the average separation correlation function stabilizes to unity, these effects
 273 are no longer abundant, and we choose our cut value. Splitting and merging effects between oppositely
 274 charged tracks was found to be negligible, therefore no cuts on unlike-charge tracks were imposed. To
 275 summarize:

276 Average Separation Cuts ($\overline{\Delta r}$)

277 (a) ΛK_S^0 Analyses

- 278 – $\overline{\Delta r} > 6.0$ cm for like-charge sign daughters
- 279 – No cut for unlike-charge daughters

280 (b) ΛK^\pm Analyses

- 281 – $\overline{\Delta r} > 8.0$ cm for daughter of $\Lambda(\bar{\Lambda})$ sharing charge sign of K^\pm
- 282 – No cut for unlike-charge

283 (c) $\Xi^- K^\pm$ Analyses

- 284 – $\overline{\Delta r} > 8.0$ cm for any daughter of Ξ sharing charge sign of K^\pm
- 285 – No cut for unlike-charge

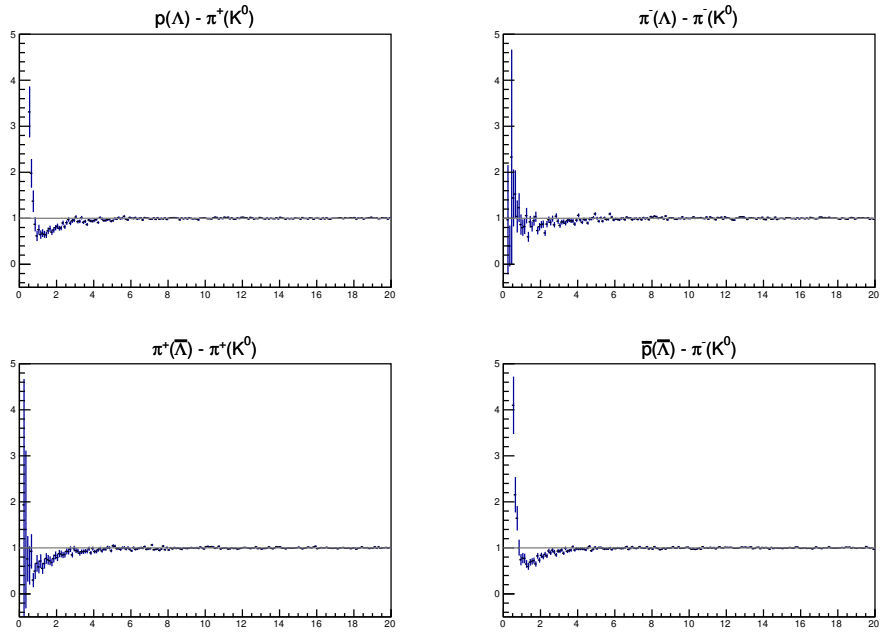


Fig. 8: Average separation (cm) correlation functions of $\Lambda(\bar{\Lambda})$ and K_S^0 Daughters. Only like-sign daughter pairs are shown (the distributions for unlike-signs were found to be flat). The title of each subfigure shows the daughter pair, as well as the mother of each daughter (in “()”), ex. top left is p from Λ with π^+ from K_S^0 .

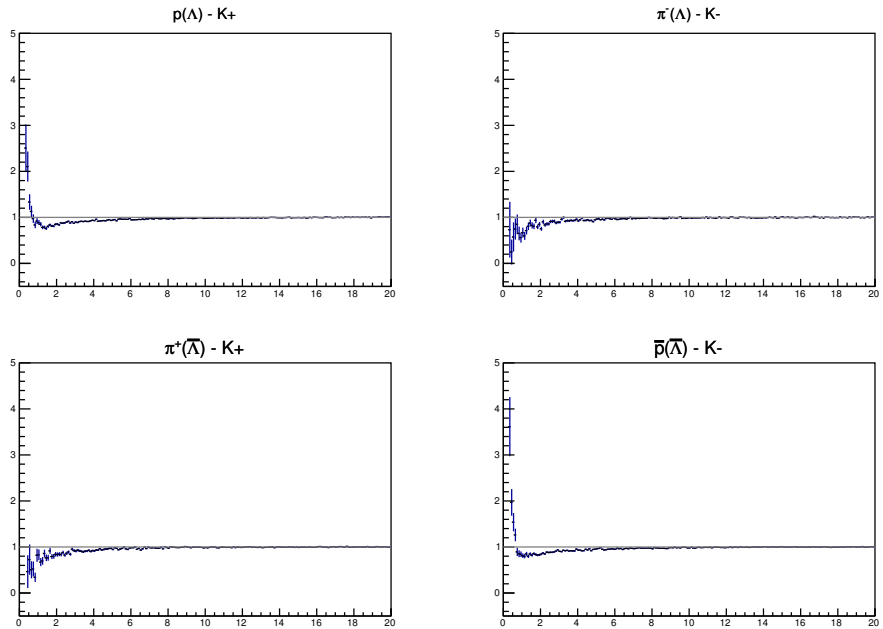


Fig. 9: Average separation (cm) correlation functions of $\Lambda(\bar{\Lambda})$ Daughter and K^\pm . Only like-sign pairs are shown (unlike-signs were flat). In the subfigure titles, the particles in “()” represent the mothers, ex. top left is p from Λ with K^+ .

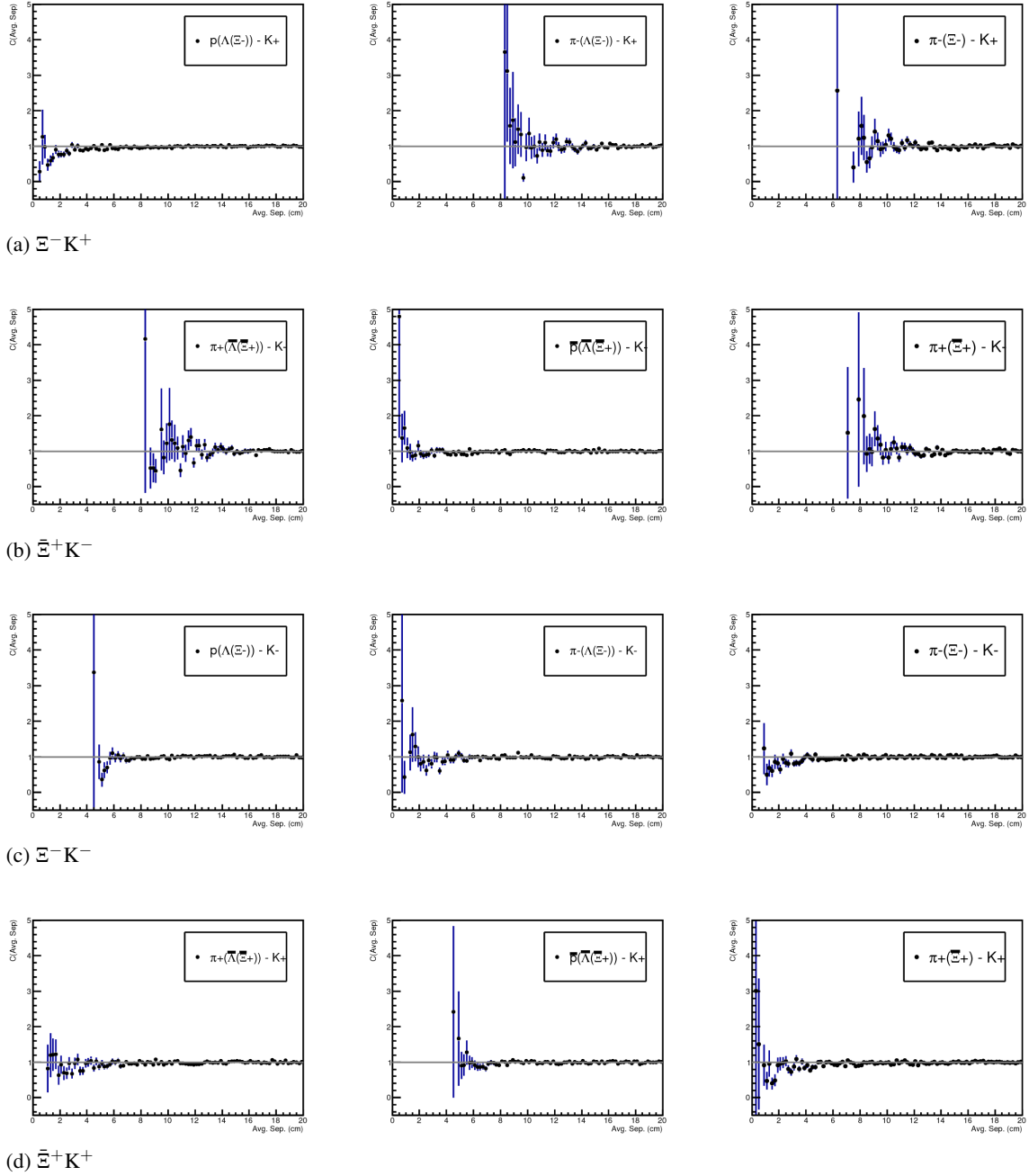


Fig. 10: Average separation (cm) correlation functions of Ξ Daughter and K^\pm . In the subfigure titles, the particles in “()” represent the mothers, ex. top left is p from Λ from Ξ^- with K^+ .

286 **4 Correlation Functions**

287 This analysis studies the momentum correlations of both ΛK and $\Xi^- K^\pm$ pairs using the two-particle
 288 correlation function, defined as $C(k^*) = A(k^*)/B(k^*)$, where $A(k^*)$ is the signal distribution, $B(k^*)$ is the
 289 reference (or background) distribution, and k^* is the momentum of one of the particles in the pair rest
 290 frame. In practice, $A(k^*)$ is constructed by binning in k^* pairs from the same event. Ideally, $B(k^*)$ is
 291 similar to $A(k^*)$ in all respects excluding the presence of femtoscopic correlations [3]; as such, $B(k^*)$
 292 is used to divide out the phase-space effects, leaving only the femtoscopic effects in the correlation
 293 function.

294 This analysis presents correlation functions for three centrality bins (0-10%, 10-30%, and 30-50%), and
 295 is currently pair transverse momentum ($k_T = 0.5|\mathbf{p}_{T,1} + \mathbf{p}_{T,2}|$) integrated (i.e. not binned in k_T). The
 296 correlation functions are constructed separately for the two magnetic field configurations, and, after
 297 assuring consistency, are combined using a weighted average:

$$C_{combined}(k^*) = \frac{\sum_i w_i C_i(k^*)}{\sum_i w_i} \quad (3)$$

298 where the sum runs over the correlation functions to be combined, and the weight, w_i , is the number of
 299 numerator pairs in $C_i(k^*)$. Here, the sum is over the two field configurations (++ and - -).

300 **4.1 Typical Correlation Function Construction**

301 In practice, $B(k^*)$ is typically obtained by forming mixed-event pairs [4], i.e. particles from a given event
 302 are paired with particles from $N_{mix}(= 5)$ other events, and these pairs are then binned in k^* . In forming
 303 the background distribution, it is important to mix only similar events; mixing events with different
 304 phase-spaces can result in an unreliable background distribution, and can introduce artificial signals in
 305 the correlation function. Therefore, in this analysis, we bin our events both in primary vertex location (2
 306 cm bin width) and in centrality (5% bin width), and we only mix events within a given bin; i.e. we only
 307 mix events of like centrality and of like primary vertex location. Also note, a vertex correction is also
 308 applied to each event, which essentially recenters the the primary vertices to $z = 0$.

309 Figures 11, 12, 13 show the correlation functions for all centralities studied for $\Lambda K^+(\bar{\Lambda} K^-)$, $\Lambda K^-(\bar{\Lambda} K^+)$,
 310 and $\Lambda(\bar{\Lambda}) K_S^0$, respectively. All were normalized in the range $0.32 < k^* < 0.4$ GeV/c. It is interesting
 311 to note that the average of the $\Lambda K^+(\bar{\Lambda} K^-)$ and $\Lambda K^-(\bar{\Lambda} K^+)$ correlation functions is consistent with our
 312 $\Lambda K_S^0(\bar{\Lambda} K_S^0)$ measurement.

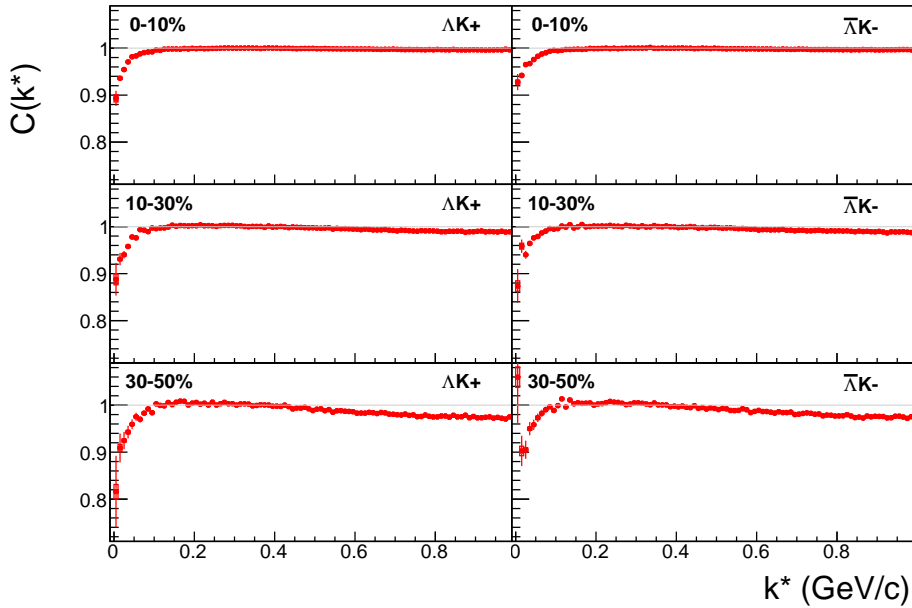


Fig. 11: ΛK^+ (left) and $\bar{\Lambda} K^-$ (right) correlations for 0-10% (top), 10-30% (middle), and 30-50% (bottom) centralities.

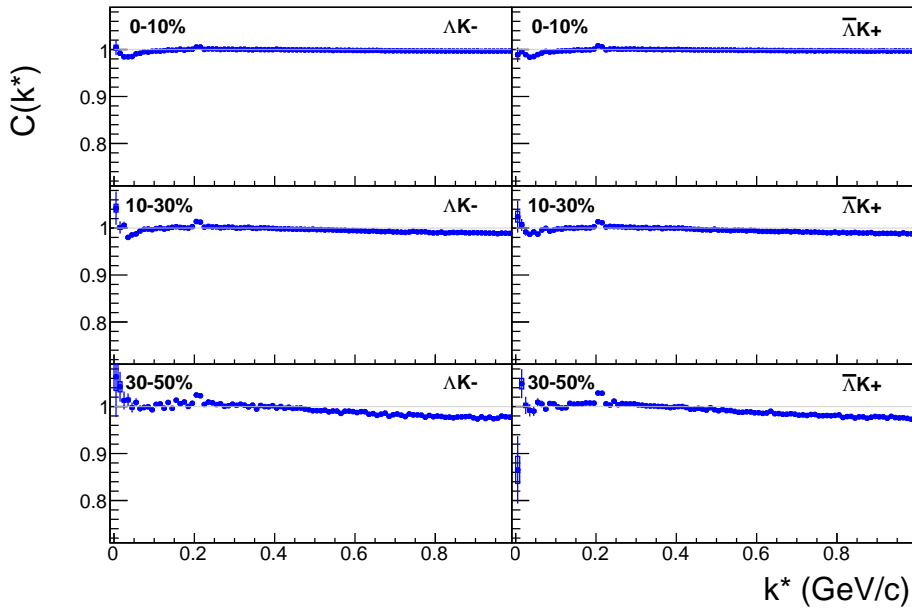


Fig. 12: ΛK^- (left) and $\bar{\Lambda} K^+$ (right) correlations for 0-10% (top), 10-30% (middle), and 30-50% (bottom) centralities. The peak at $k^* \approx 0.2$ GeV/c is due to the Ω^- (and, to a much smaller extent, the $\Xi(1690)$) resonances.

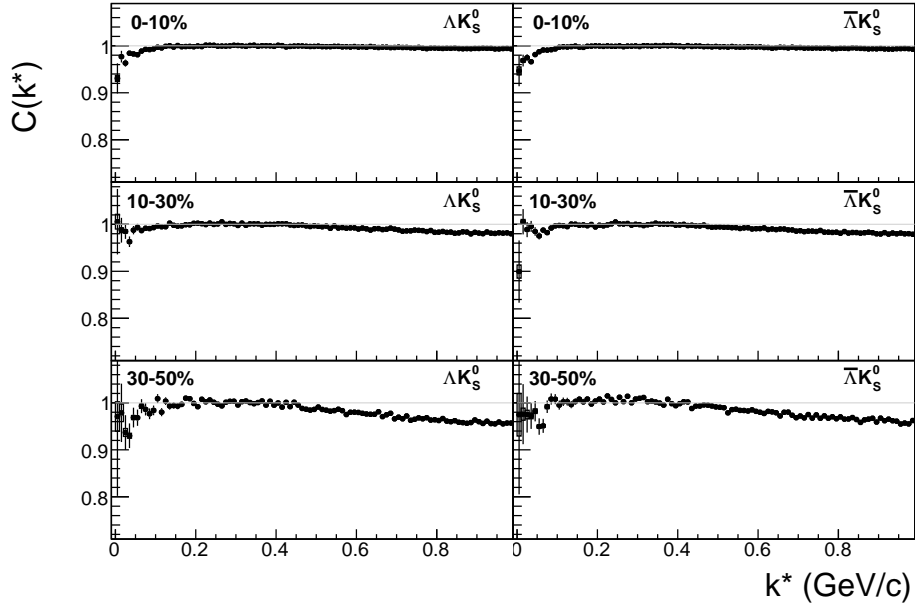


Fig. 13: ΛK_s^0 (left) and $\bar{\Lambda} K_s^0$ (right) correlations for 0-10% (top), 10-30% (middle), and 30-50% (bottom) centralities.

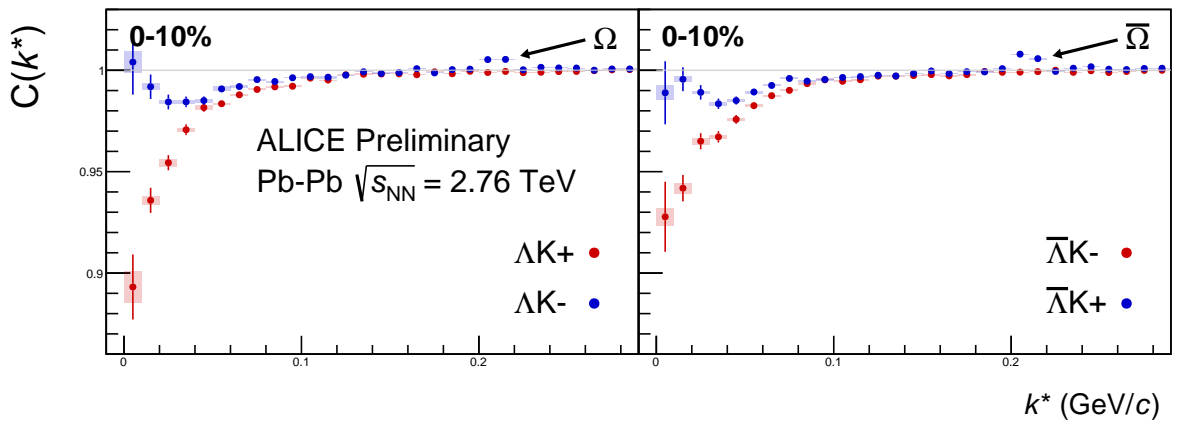


Fig. 14: Correlation Functions: ΛK^+ vs ΛK^- ($\bar{\Lambda} K^+$ vs $\bar{\Lambda} K^-$) for 0-10% centrality. The peak in ΛK^- ($\bar{\Lambda} K^+$) at $k^* \approx 0.2$ GeV/c is due to the Ω^- (and, to a much smaller extent, the $\Xi(1690)$ resonance. The lines represent the statistical errors, while boxes represent systematic errors.

313 4.2 Stavinskiy Correlation Function Construction

314 The purpose of the Stavinskiy method is to rid the correlation functions of the non-femtoscopic back-
315 ground. More specifically, this method is intended to handle background contributions from elliptic
316 flow, and other sources having reflection symmetry in the transverse plane. With the Stavinskiy method,
317 mixed-event pairs are not used for the background ($B(k^*)$); instead, same-event pseudo-pairs, formed
318 by rotating one particle in a real pair by 180° in the transverse plane, are used as a background. This
319 rotation rids the pairs of any femtoscopic correlation, while maintaining correlations due to elliptic flow
320 (and other suitably symmetric contributors).

321 The results of correctly implementing such a procedure are shown in Figure 15. The figure shows the
322 Stavinskiy method does a very good job of ridding the ΛK^\pm correlations of their non-femtoscopic back-
323 grounds. We also see the procedure does not work as well on the ΛK_S^0 system.

324 Now, one must be somewhat careful when applying this Stavinskiy method. We found that, in order to
325 obtain correct results, we had to run our pseudo-pairs through the same pair cuts used in our analyses.
326 In an ideal world, our pair cut would only remove truly bad pairs results from splitting, merging, etc. In
327 the real world, the pair cut always throws out some of the good with the bad. For the pseudo-pairs to
328 form a reliable background, they too must experience the pair cut, and the loss of “good” pseudo-pairs.
329 We found this issue affected mainly our ΛK^+ & $\bar{\Lambda} K^-$ analysis, as can be seen in Figure 16, which shows
330 both a correct implementation of the Stavinskiy method, and an incorrect implementation lacking the
331 additional pair cut on the pseudo-pairs.

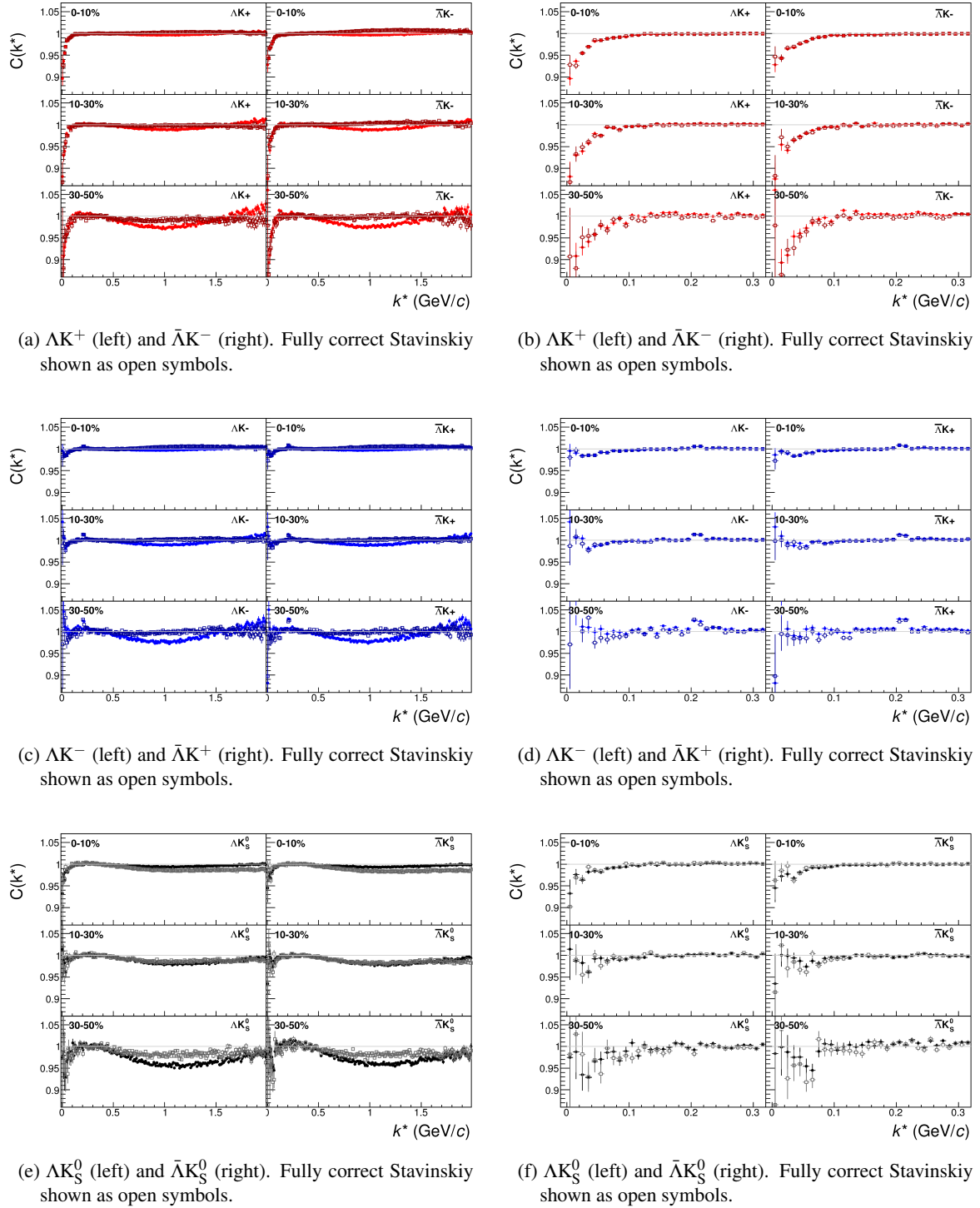


Fig. 15: ΛK and $\bar{\Lambda} \bar{K}$ correlation functions built using the fully correct Stavinskiy method for 0-10%, 10-30%, and 30-50% centralities. In the fully correct method, the pseudo-pairs (same-event pairs with one particle rotated by 180° in the transverse plane) are also run through the pair cuts used in the analysis (an example of an incorrect implementation is shown in Fig. 16. Closed symbols represent correlations built using the normal mixed-event background, while open symbols represent correlations formed using the Stavinskiy same-event pseudo-pairs as a background. Figures in the right column are zoomed-in versions of figures in the left column.

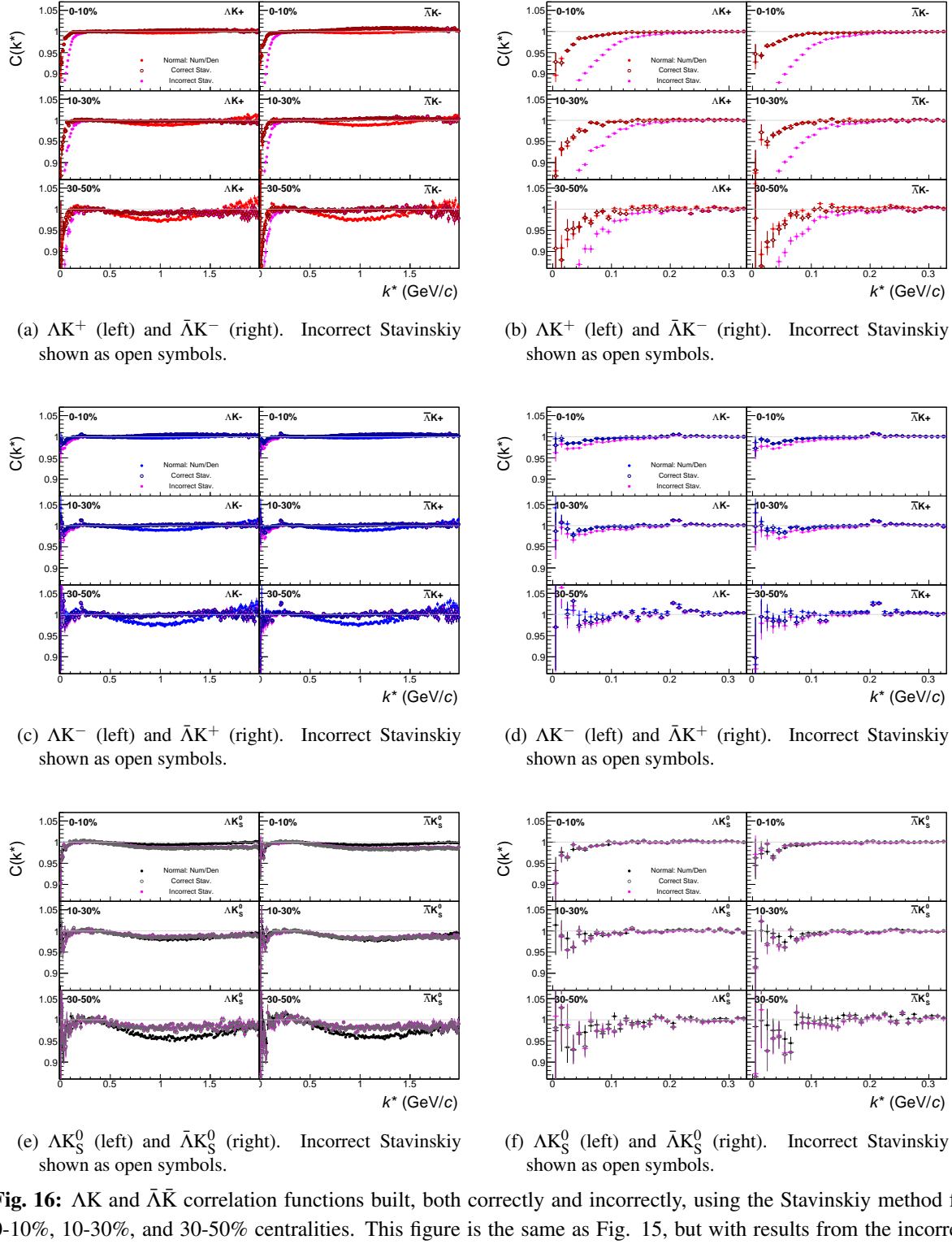


Fig. 16: ΛK and $\bar{\Lambda} \bar{K}$ correlation functions built, both correctly and incorrectly, using the Stavinskiy method for 0-10%, 10-30%, and 30-50% centralities. This figure is the same as Fig. 15, but with results from the incorrect Stavinskiy implementation shown in magenta. The closed, (red, blue, black) symbols represent correlation functions formed using the normal method with mixed-event background pairs. The open, cyan symbols represent correlation functions formed using the correct Stavinskiy method. The closed, magenta symbols represent correlation functions formed using the incorrect Stavinskiy method. In the correct method, the pseudo-pairs (same-event pairs with one particle rotated by 180° in the transverse plane) are also run through the pair cuts used in the analysis; in the incorrect method, they are not. Figures in the right column are zoomed-in versions of figures in the left column.

332 **5 Fitting**

333 **5.1 Model: $\Lambda K_S^0, \Lambda K^\pm, \Xi^- K_S^0$**

334 ***Strong Interaction Only***

335 For the case of interacting particles, the non-symmetrized two-particle wave-function, ψ , may be written
336 as [1]

$$\psi = e^{-iP(x_1+x_2)/2} \left(e^{-ikr} + \phi_{p_1 p_2}(r) \right) \quad (4)$$

337 where $\phi_{p_1 p_2}(r)$ describes the final state interactions (FSI) of the particles. Assuming that the range of the
338 interaction potential is smaller than the distance between the emission points, $\phi_{p_1 p_2}(r)$ may be expressed
339 as

$$\phi_{p_1 p_2}(x) = f(k^*) \Phi_{p_1 p_2}(x) \quad (5)$$

340 where, in the effective range approximation, $f(k^*)$ is of the form

$$f(k^*) = \left(\frac{1}{f_0} + \frac{1}{2} d_0 k^{*2} - ik^* \right)^{-1} \quad (6)$$

341 Furthermore, if we assume the magnitude of the momentum difference is much smaller than the mass of
342 the particles ($k^* \ll m$), and that the particles are emitted at the same time in the pair rest frame, $\Phi_{p_1 p_2}(x)$
343 reduces to

$$\Phi_{p_1 p_2}(x) = \frac{e^{ik^* r^*}}{r^*} \quad (7)$$

344 In other words, $\Phi_{p_1 p_2}(x)$ is a diverging spherical wave. Therefore, we have $\psi_{p_1 p_2} = e^{-ikr} + \phi_{p_1 p_2}(r)$,
345 where $\phi_{p_1 p_2}(r)$ is independent of the directions of the vectors k^* and r [5].

346 Assuming the final state interactions are independent of the spin state, for identical interacting particles,

$$|\Psi|^2 = 1 + g_0 \cos(2kx) + g_i \{ |\phi_{p_1 p_2}(r)|^2 + 2\Re[\phi_{p_1 p_2}(r)] \cos(kx) \} \quad (8)$$

347 where $g_0 = (-1)^{2j}/(2j+1)$ and $g_i = 1 + g_0$.

348 For non-identical interacting particles, where we need not worry about the symmetrization of the wave
349 function, we have:

$$\begin{aligned} |\Psi_{p_1 p_2}|^2 &= 1 + |f(k^*) \Phi_{p_1 p_2}|^2 + e^{ikx} f(k^*) \Phi_{p_1 p_2} + e^{-ikx} \tilde{f}(k^*) \tilde{\Phi}_{p_1 p_2} \\ &= 1 + |f(k^*) \Phi_{p_1 p_2}|^2 + 2\Re[f(k^*) \Phi_{p_1 p_2}] \cos(kx) - 2\Im[f(k^*) \Phi_{p_1 p_2}] \sin(kx) \end{aligned} \quad (9)$$

350 If we allow the interaction, and therefore the two-particle wave function, to depend on the summary spin
351 of the system (but not on the spin projections), things change slightly. Instead of grouping all odd and
352 even summary spins together, as was done in deriving Eqns. 8 and 9, we need to keep track of their
353 individual contributions, as their wave functions will be different. When combining all of the various
354 states with different summary spin S , they must be combined with a weight factor ρ_S , the normalized
355 emission probability for such a state ($\sum_S \rho_S = 1$). In this case, we find

$$\begin{aligned} |\Psi|^2 &= 1 + \left(\sum_{S=\text{even}} \rho_S - \sum_{S=\text{odd}} \rho_S \right) \cos(2kx) + \dots \\ &\quad + 2 \sum_{S=\text{even}} \rho_S \{ |\phi_{p_1 p_2}^S(r)|^2 + 2\Re[\phi_{p_1 p_2}^S(r)] \cos(kx) \} \\ &= 1 + g'_0 \cos(2kx) + 2 \sum_{S=\text{even}} \rho_S \{ |\phi_{p_1 p_2}^S(r)|^2 + 2\Re[\phi_{p_1 p_2}^S(r)] \cos(kx) \} \end{aligned} \quad (10)$$

356 where $g'_0 = \sum_{S=even} \rho_S - \sum_{S=odd} \rho_S$. In the case of unpolarized emission for identical particle pairs,
 357 $\rho_s = (2S+1)/(2j+1)^2$, and we have $g'_0 = g_0 = (-1)^{2j}/(2j+1)$.

358 The case of interacting non-identical particles can be written down immediately from Eq. 9

$$|\Psi_{p_1 p_2}|^2 = \sum_S \rho_s \left\{ 1 + |\phi_{p_1 p_2}^S|^2 + 2\Re[\phi_{p_1 p_2}^S] \cos(kx) - 2\Im[\phi_{p_1 p_2}^S] \sin(kx) \right\} \quad (11)$$

359 where, for the case of unpolarized emission, $\rho_s = (2S+1)/[(2j_1+1)(2j_2+1)]$.

360 Now, up to this point, we have discussed only the wave-functions. Within femtoscopy, this essentially
 361 amounts to assuming point-like sources. In the more realistic scenario, the correlation function should
 362 be averaged over the space-time distribution of particle sources. The two-particle relative momentum
 363 correlation function may be written theoretically by the Koonin-Pratt equation [6, 7]:

$$C(\mathbf{k}^*) = \int S(\mathbf{r}^*) |\Psi_{\mathbf{k}^*}(\mathbf{r}^*)|^2 d^3 \mathbf{r}^* \quad (12)$$

364 where $S(\mathbf{r}^*)$ is the pair source distribution, $\Psi_{\mathbf{k}^*}(\mathbf{r}^*)$ is the two-particle wave-function, and k^* is the
 365 momentum of one particle in the pair rest frame. In the case on one-dimensional analyses, a spherically
 366 symmetric Gaussian pair emission source in the PRF with size R_{inv} is often assumed:

$$S(x) \propto \exp \left[-\frac{r^2}{4R_{inv}^2} \right] \quad (13)$$

367 In the case of identical particles, where the Gaussian offsets are zero and the single particle sources are
 368 obviously described by the same radii, the two-particle source is related by a factor $\sqrt{2}$ to the single
 369 particle sizes.

370 As a side note, a more realistic source would allow for different radii in the out, side and long directions.
 371 Furthermore, for non-identical particle femtoscopy, each single-particle source should be given a unique
 372 offset in the out direction. In such a case, the pair emission source would be

$$\begin{aligned} S_{AB}(\mathbf{r}) &\propto \int \exp \left(-\frac{(r_{a,out} - \mu_{a,out})^2}{2R_{a,out}^2} - \frac{r_{a,side}^2}{2R_{a,side}^2} - \frac{r_{a,long}^2}{2R_{a,long}^2} \right) \times \dots \\ &\quad \times \exp \left(-\frac{(r_{b,out} - \mu_{b,out})^2}{2R_{b,out}^2} - \frac{r_{b,side}^2}{2R_{b,side}^2} - \frac{r_{b,long}^2}{2R_{b,long}^2} \right) \\ &\quad \times \delta(r_{out} - r_{a,out} + r_{b,out}) dr_{a,out} dr_{b,out} \\ &\quad \times \delta(r_{side} - r_{a,side} + r_{b,side}) dr_{a,side} dr_{b,side} \\ &\quad \times \delta(r_{long} - r_{a,long} + r_{b,long}) dr_{a,long} dr_{b,long} \end{aligned} \quad (14)$$

373 Using the results from Appendix D.2, we find

$$\begin{aligned} S_{AB}(\mathbf{r}) &\propto \exp \left(-\frac{[r_{out} - (\mu_{a,out} - \mu_{b,out})]^2}{2(R_{a,out}^2 + R_{b,out}^2)} \right) \times \dots \\ &\quad \times \exp \left(-\frac{r_{side}^2}{2(R_{a,side}^2 + R_{b,side}^2)} \right) \times \dots \\ &\quad \times \exp \left(-\frac{r_{long}^2}{2(R_{a,long}^2 + R_{b,long}^2)} \right) \end{aligned} \quad (15)$$

374 which demonstrates $\mu_{ab,out} = \mu_{a,out} - \mu_{b,out}$, and $R_{ab,i}^2 = R_{a,i}^2 + R_{b,i}^2$ [8].

375 Returning back to our treatment of a one dimensional femtoscopic study with a spherically symmetric
 376 source of width R (Eq. 13). In the absence of Coulomb effects, with the assumptions and approximations
 377 used above (including unpolarized emission), the 1D femtoscopic correlation function can be calculated
 378 analytically as

$$C(k^*) = 1 + C_{QI}(k^*) + C_{FSI}(k^*) \quad (16)$$

379 C_{QI} describes plane-wave quantum interference:

$$C_{QI}(k^*) = \alpha \exp(-4k^{*2}R^2) \quad (17)$$

380 where $\alpha = (-1)^{2j}/(2j+1)$ (i.e. $= g_0$) for identical particles with spin j , and $\alpha = 0$ for non-identical
 381 particles. For all analyses presented in this note, $\alpha = 0$. C_{FSI} describes the s-wave strong final state
 382 interaction between the particles:

$$C_{FSI}(k^*) = \sum_S \rho_S \left[\frac{1}{2} \left| \frac{f^S(k^*)}{R} \right|^2 \left(1 - \frac{d_0^S}{2\sqrt{\pi}R} \right) + \frac{2\Re f^S(k^*)}{\sqrt{\pi}R} F_1(2k^*R) - \frac{\Im f^S(k^*)}{R} F_2(2k^*R) \right] \quad (18)$$

383 where $\rho_s = (2S+1)/[(2j_1+1)(2j_2+1)]$ and

$$F_1(z) = \int_0^z \frac{e^{x^2-z^2}}{z} dx \quad F_2(z) = \frac{1-e^{-z^2}}{z} \quad (19)$$

384 where R is the source size, $f(k^*)$ is the s-wave scattering amplitude, f_0 is the complex scattering length,
 385 and d_0 is the effective range of the interaction.

386 An additional parameter λ is typically included in the femtoscopic fit function to account for the purity
 387 of the pair sample. In the case of no residual correlations (to be discussed in Section 5.4), the fit function
 388 becomes:

$$C(k^*) = 1 + \lambda [C_{QI}(k^*) + C_{FSI}(k^*)] \quad (20)$$

389 **5.2 Model: $\Xi^- K^\pm$**

390 The two-particle correlation function may be written as:

$$C(\mathbf{k}^*) = \sum_S \rho_S \int S(\mathbf{r}^*) |\Psi_{\mathbf{k}^*}^S(\mathbf{r}^*)|^2 d^3 \mathbf{r}^* \quad (21)$$

391 where ρ_S is the normalized emission probability of particles in a state with spin S , $S(\mathbf{r}^*)$ is the pair
 392 emission source distribution (assumed to be Gaussian), and $\Psi_{\mathbf{k}^*}^S(\mathbf{r}^*)$ is the two-particle wave-function
 393 including both strong and Coulomb interactions [9]:

$$\Psi_{\mathbf{k}^*}(\mathbf{r}^*) = e^{i\delta_c} \sqrt{A_c(\eta)} [e^{i\mathbf{k}^* \cdot \mathbf{r}^*} F(-i\eta, 1, i\xi) + f_c(k^*) \frac{\tilde{G}(\rho, \eta)}{r^*}] \quad (22)$$

394 where $\rho = k^* r^*$, $\eta = (k^* a_c)^{-1}$, $\xi = \mathbf{k}^* \cdot \mathbf{r}^* + k^* r^* \equiv \rho(1 + \cos \theta^*)$, and $a_c = (\mu z_1 z_2 e^2)^{-1}$ is the two-
 395 particle Bohr radius (including the sign of the interaction). δ_c is the Coulomb s-wave phase shift, $A_c(\eta)$
 396 is the Coulomb penetration factor, $\tilde{G} = \sqrt{A_c}(G_0 + iF_0)$ is a combination of the regular (F_0) and singular
 397 (G_0) s-wave Coulomb functions. $f_c(k^*)$ is the s-wave scattering amplitude:

$$f_c(k^*) = \left[\frac{1}{f_0} + \frac{1}{2} d_0 k^{*2} - \frac{2}{a_c} h(\eta) - i k^* A_c(\eta) \right]^{-1} \quad (23)$$

398 where, the “h-function”, $h(\eta)$, is expressed through the digamma function, $\psi(z) = \Gamma'(z)/\Gamma(z)$ as:

$$h(\eta) = 0.5[\psi(i\eta) + \psi(-i\eta) - \ln(\eta^2)] \quad (24)$$

399 In this case, the λ parameter may be included as:

$$C(\mathbf{k}^*) = (1 - \lambda) + \lambda \sum_S \rho_S \int S(\mathbf{r}^*) |\Psi_{\mathbf{k}^*}^S(\mathbf{r}^*)|^2 d^3 \mathbf{r}^* \quad (25)$$

400 5.3 Momentum Resolution Corrections

401 Finite track momentum resolution causes the reconstructed momentum of a particle to smear around the
 402 true value. This, of course, also holds true for V0 particles. The effect is propagated up to the pairs
 403 of interest, which causes the reconstructed relative momentum (k_{Rec}^*) to differ from the true momentum
 404 (k_{True}^*). Smearing of the momentum typically will result in a suppression of the signal. More specifically,
 405 the smearing will broaden the signal, which would cause a decrease in the extracted radius of the system.
 406 The effect of finite momentum resolution can be investigated using the HIJING MC data, for which both
 407 the true and reconstructed momenta are available. Figure 17 shows sample k_{True}^* vs. k_{Rec}^* plots for ΛK^\pm
 408 0-10% analyses; Figure 17a was generated using same-event pairs, while Figure 17b was generated using
 409 mixed-event pairs (with $N_{\text{mix}} = 5$).

410 If there are no contaminations in our particle collection, the plots in Figure 17 should be smeared around
 411 $k_{\text{True}}^* = k_{\text{Rec}}^*$; this is mostly true in our analyses. However, there are some interesting features of our results
 412 which demonstrate a small (notice the log-scale on the z-axis) contamination in our particle collection.
 413 The structure around $k_{\text{Rec}}^* = k_{\text{True}}^* - 0.15 \text{ GeV}/c$ is mainly caused by K_s^0 contamination in our $\Lambda(\bar{\Lambda})$ sample.
 414 The remaining structure not distributed about $k_{\text{Rec}}^* = k_{\text{True}}^*$ is due to π and e contamination in our K^\pm
 415 sample. These contaminations are more visible in Figure 18, which show k_{Rec}^* vs. k_{True}^* plots (for a
 416 small sample of the ΛK^\pm 0-10% central analysis), for which the MC truth (i.e. true, known identity of
 417 the particle) was used to eliminate misidentified particles in the $K^+(a)$ and $\Lambda(b)$ collections. (NOTE:
 418 This is an old figure and is for a small sample of the data. A new version will be generated shortly. It,
 419 nonetheless, demonstrates the point well).

420 Information gained from looking at k_{Rec}^* vs k_{true} can be used to apply corrections to account for the
 421 effects of finite momentum resolution on the correlation functions. A typical method (“Ratio” method)
 422 involves using the MC HIJING data to build two correlation functions, $C_{\text{Rec}}(k^*)$ and $C_{\text{True}}(k^*)$, using
 423 the generator-level momentum (k_{True}^*) and the measured detector-level momentum (k_{Rec}^*). The data is
 424 then corrected by multiplying by the ratio, $C_{\text{True}}/C_{\text{Rec}}$, before fitting. This essentially unsmears the data,
 425 which then can be compared directly to theoretical predictions and fits. Although this is conceptually
 426 simple, there are a couple of big disadvantages to this method. First, HIJING does not incorporate final-
 427 state interactions, so weights must be used when building same-event (numerator) distributions. These
 428 weights account for the interactions, and, in the absence of Coulomb interactions, can be calculated using
 429 Eq. 16. Of course, these weights are valid only for a particular set of fit parameters. Therefore, in the
 430 fitting process, during which the fitter explores a large parameter set, the corrections will not remain valid.
 431 As such, applying the momentum resolution correction and fitting becomes a long and drawn out iterative
 432 process. An initial parameter set is obtained (through fitting without momentum resolution corrections,
 433 theoretical models, or a good guess), then the MC data is analyzed to obtain correlation functions needed
 434 to calculate the correction factor, the data is fit using the correction factor, a refined parameter set is
 435 extracted, the MC data is analyzed again to obtain the new correction factor, etc. This process continues

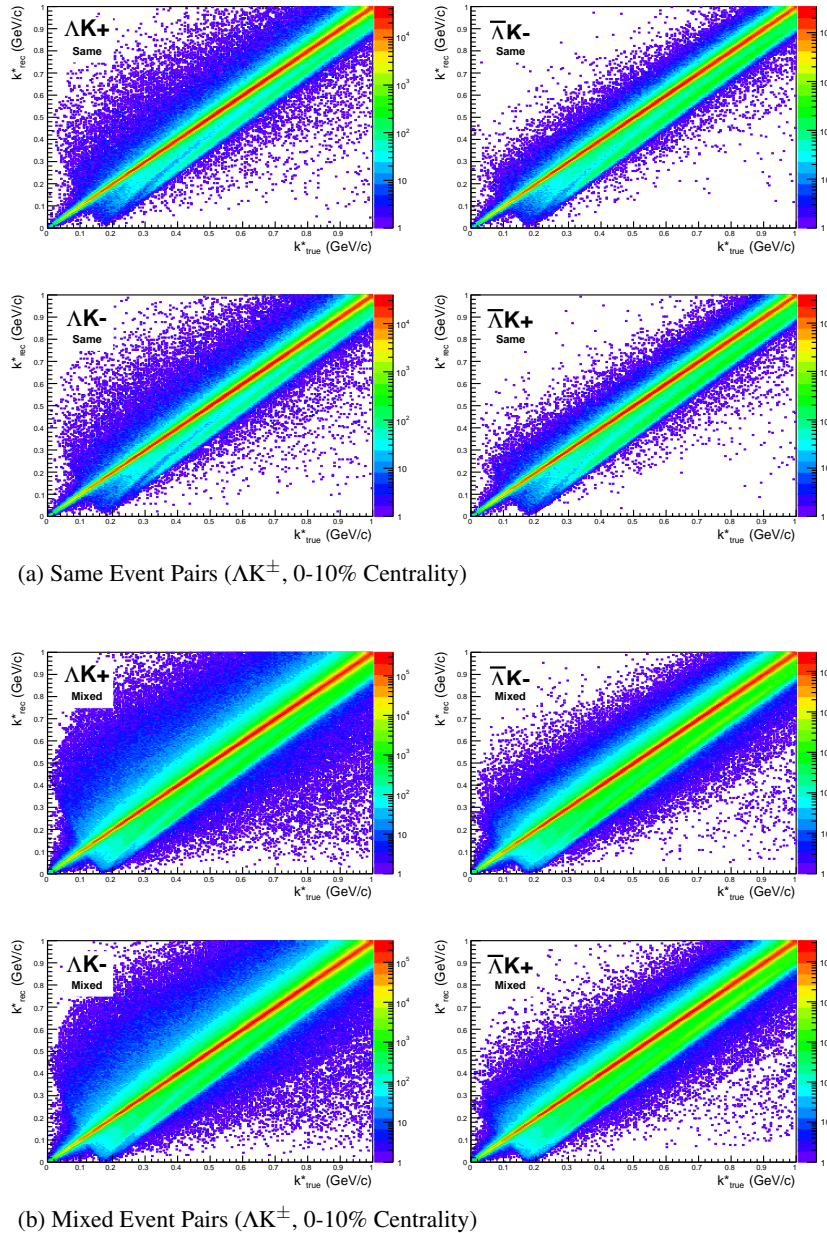
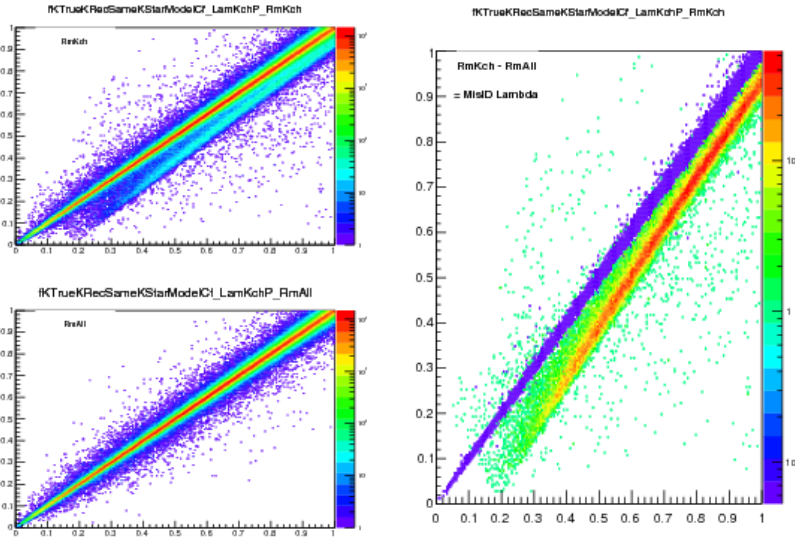


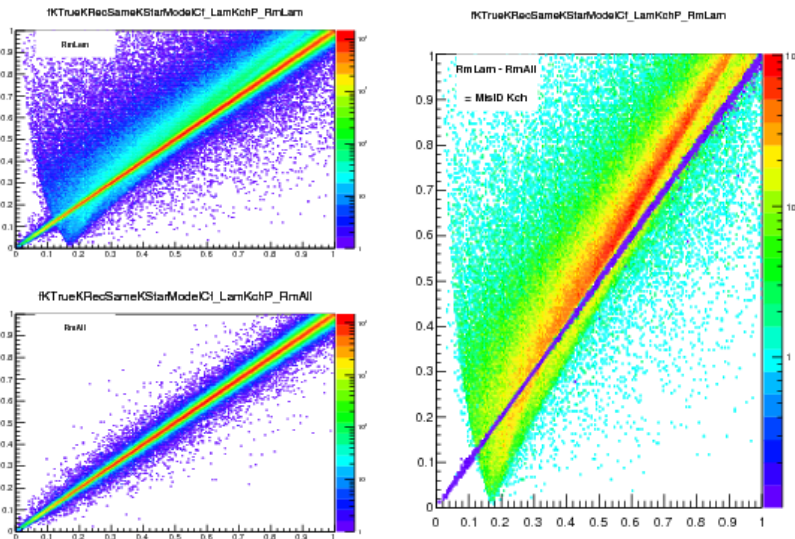
Fig. 17: Sample k_{True}^* vs. k_{Rec}^* plots from MC HIJING events for ΛK^\pm 0-10% analyses. The structure which appears around $k_{\text{Rec}}^* = k_{\text{True}}^* - 0.15 \text{ GeV}/c$ is mainly caused by K_S^0 contamination in our $\Lambda(\bar{\Lambda})$ sample. The remaining structure not distributed about $k_{\text{Rec}}^* = k_{\text{True}}^*$ is due to π and e contamination in our K^\pm sample. These contaminations are more clearly visible in Figure 18

until the parameter set stabilizes. The second issue concerns statistics. With the MC data available on the grid, we were not able to generate the statistics necessary to use the raw $C_{\text{True}}/C_{\text{Rec}}$ ratio. The ratio was not stable, and when applied to the data, obscured the signal. Attempting to fit the ratio to use to generate the corrections also proved problematic. However, as HIJING does not include final-state interactions, the same-event and mixed-event pairs are very similar (with the exception of things like energy and momentum conservation, etc). Therefore, one may build the numerator distribution using mixed-event pairs. This corresponds, more or less, to simply running the weight generator through the detector framework.

A second approach (“Matrix” method) is to use information gained from plots like those in Figure 17,



(a) (Top Left) All misidentified K^+ excluded. (Bottom Left) All misidentified Λ and K^+ excluded. (Right) The difference of (Top Left) - (Bottom Left), which reveals the contamination in our Λ collection. The structure which appears around $k^*_{\text{Rec}} = k^*_{\text{True}} - 0.15 \text{ GeV}/c$ is mainly caused by K_S^0 contamination in our $\Lambda(\bar{\Lambda})$ sample.



(b) (Top Left) All misidentified Λ excluded. (Bottom Left) All misidentified Λ and K^+ excluded. (Right) The difference of (Top Left) - (Bottom Left), which reveals the contamination in our K^+ collection. The structure not distributed about $k^*_{\text{Rec}} = k^*_{\text{True}}$ is due to π and e^- contamination in our K^+ sample.

Fig. 18: In the figure, the y-axis = k^*_{Rec} , and the x-axis = k^*_{True} . (Left) k^*_{Rec} vs. k^*_{True} plots for a small sample of the ΛK^+ 0-10% central analysis, MC truth was used to eliminate misidentified particles in the K^+ (a) and Λ (b) collections. (Right) The difference of the top left and bottom left plots. Contaminations in our particle collections are clearly visible. Figure (a) demonstrates a K_S^0 contamination in our Λ collection; Figure (b) demonstrates a π and e^- contamination in our K^\pm collection.

which can be considered response matrices. The response matrix describes quantitatively how each k^*_{Rec} bin receives contributions from multiple k^*_{True} bins, and can be used to account for the effects of finite momentum resolution. With this approach, the resolution correction is applied on-the-fly during the fitting process by propagating the theoretical correlation function (fit) through the response matrix,

449 according to:

$$C_{\text{Fit}}(k_{\text{Rec}}^*) = \frac{\sum_{k_{\text{True}}^*} M_{k_{\text{Rec}}^*, k_{\text{True}}^*} C_{\text{Fit}}(k_{\text{True}}^*)}{\sum_{k_{\text{True}}^*} M_{k_{\text{Rec}}^*, k_{\text{True}}^*}} \quad (26)$$

450 where $M_{k_{\text{Rec}}^*, k_{\text{True}}^*}$ is the response matrix (Figure 17), $C_{\text{Fit}}(k_{\text{True}}^*)$ is the fit binned in k_{True}^* , and the denominator normalizes the result.

452 Equation 26 describes that, for a given k_{Rec}^* bin, the observed value of $C(k_{\text{Rec}}^*)$ is a weighted average of
 453 all $C(k_{\text{True}}^*)$ values, where the weights are the normalized number of counts in the $[k_{\text{Rec}}^*, k_{\text{True}}^*]$ bin. As
 454 seen in Figure 17, overwhelmingly the main contributions comes from the $k_{\text{Rec}}^* = k_{\text{True}}^*$ bins. Although
 455 the correction is small, it is non-negligible for the low- k^* region of the correlation function.

456 Here, the momentum resolution correction is applied to the fit, not the data. In other words, during
 457 fitting, the theoretical correlation function is smeared just as real data would be, instead of unsmearing
 458 the data. This may not be ideal for the theorist attempting to compare a model to experimental data, but
 459 it leaves the experimental data unadulterated. The current analyses use this second approach to applying
 460 momentum resolution corrections because of two major advantages. First, the MC data must be analyzed
 461 only once, and no assumptions about the fit are needed. Secondly, the momentum resolution correction
 462 is applied on-the-fly by the fitter, delegating the iterative process to a computer instead of the user.

463 The two methods described above, Ratio and Matrix, should reproduce the same results at the parameter
 464 set used to generate the $C_{\text{True}}/C_{\text{Rec}}$ needed for the Ratio method. Figure 19 shows that the two methods
 465 converge as the binning size is decreased.

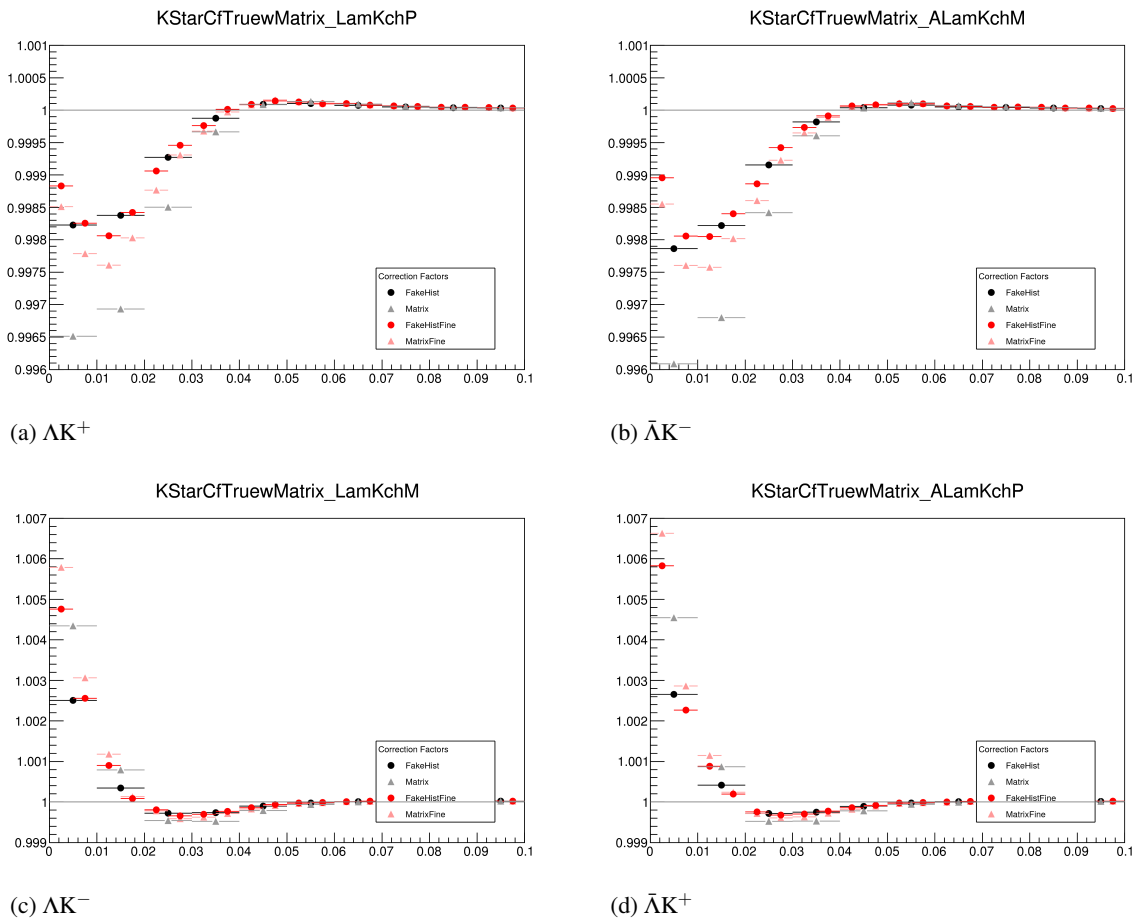


Fig. 19: Comparison of the two methods, Ratio and Matrix, for accounting for momentum resolution effects with HIJING. The Ratio method corresponds to the “FakeHist” histograms (circles), while the Matrix method corresponds to the “Matrix” histograms (triangles). Black shows a course binning, while red shows a finer binning.

466 **5.4 Residual Correlations**

467 The purpose of this analysis is study the interaction and scale of the emitting source of the primary
 468 ΛK pairs. In order to obtain correct results, it is desirable for our particle collections to consist of
 469 primary particles. In practice, this is impossible to achieve; many of our particles are not primary,
 470 but originate as decay products from other resonances. Some of our Λ hyperons decay from Σ^0 , Ξ^0 ,
 471 Ξ^- and $\Sigma^{*(+,-,0)}(1385)$ parents, and some of our K mesons decay from $K^{*(+,-,0)}(892)$ parents. In
 472 these decays, the daughter carries away a momentum very similar to that of its parent. As a result,
 473 the correlations between the particles in the daughter pair will be sensitive to, and dependent upon, the
 474 interaction between the parents. In effect, the correlation between the parents will be visible, although
 475 smeared out, in the daughters' signal. We call this a residual correlation resulting from feed-down. The
 476 contributions from the primary correlation, residual correlations, and fake pairs on the finally measure
 477 data is shown schematically in Figure 20. Residual correlations are important in an analysis when three
 478 criteria are met [10]: i) the parent correlation signal is large, ii) a large fraction of pairs in the sample
 479 originate from the particular parent system, and iii) the decay momenta are comparable to the expected
 480 correlation width in k^* .

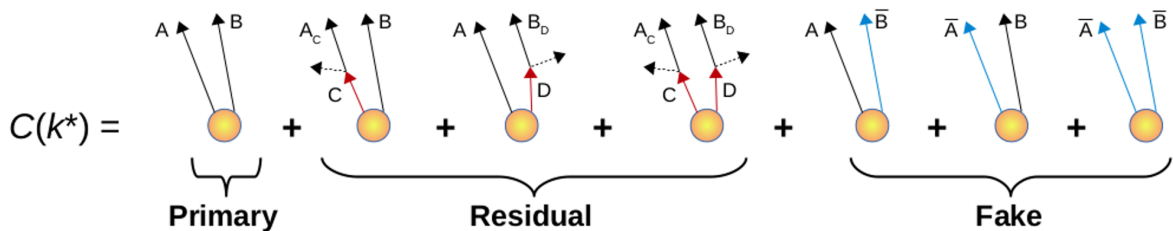


Fig. 20: A schematic representation of the contributions to the finally measured data from the primary correlation, residual correlations, and fake pairs.

481 As it is difficult for us to eliminate these residual correlations in our analyses, we must attempt to account
 482 for them in our fit. The genuine ΛK correlation function may be combined with the contributions from
 483 residual feed-down and misidentified particles to obtain the final, measured correlation function:

$$C_{\text{measured}}(k_{\Lambda K}^*) = 1 + \lambda'_{\Lambda K}[C_{\Lambda K}(k_{\Lambda K}^*) - 1] + \sum_{i,j} \lambda'_{ij}[C_{ij}(k_{\Lambda K}^*) - 1] \quad (27)$$

$$\begin{aligned} \lambda'_{ij} &= \lambda_{\text{Fit}} \lambda_{ij} \\ \sum_{i,j} \lambda'_{ij} &= \lambda_{\text{Fit}} \sum_{i,j} \lambda_{ij} = \lambda_{\text{Fit}} \end{aligned}$$

484 where the ΛK term represents the genuine ΛK correlation, and the i, j terms denote the contributions
 485 from residual feed-down and possible impurities. More specifically, $C_{ij}(k_{\Lambda K}^*)$ is the correlation function
 486 between parents of particle species i and j , expressed in the basis of the relative momentum of the
 487 observed daughter ΛK pairs. The λ parameters serve as weight dictating the strength of the parent
 488 contribution to the daughter pair, and are normalized to unity. The individual λ_{ij} are fixed (and whose
 489 values can be found in Table 6), but the parameter λ_{Fit} is left free. The λ_{Fit} parameter serves as an overall
 490 normalization shared by all contributors.

491 In order to obtain the parent correlation function expressed in the relative momentum of the daughter
 492 pair, one must use a transform matrix. The transform matrix describes the decay kinematics of the parent
 493 system into the daughter, and maps the k^* of the parent pair onto that of the daughter. Using this matrix,
 494 the transformed residual correlation function can be obtained:

$$C_{ij}(k_{\Lambda K}^*) \equiv \frac{\sum_{k_{ij}^*} C_{ij}(k_{ij}^*) T(k_{ij}^*, k_{\Lambda K}^*)}{\sum_{k_{ij}^*} T(k_{ij}^*, k_{\Lambda K}^*)} \quad (28)$$

495 The transform matrix is generated with the THERMINATOR 2 [11] simulation. It is formed for a given
 496 parent pair, ij , by taking all AK pairs originating from ij , calculating the relative momentum of the
 497 parents (k_{ij}^*) and daughters ($k_{\Lambda K}^*$), and filling a two-dimensional histogram with the values. The transform
 498 matrix is essentially an unnormalized probability distribution mapping the k^* of the parent pair to that of
 499 the daughter pair when one or both parents decay. An example of such transform matrices can be found
 500 in Figures 21 and 22.

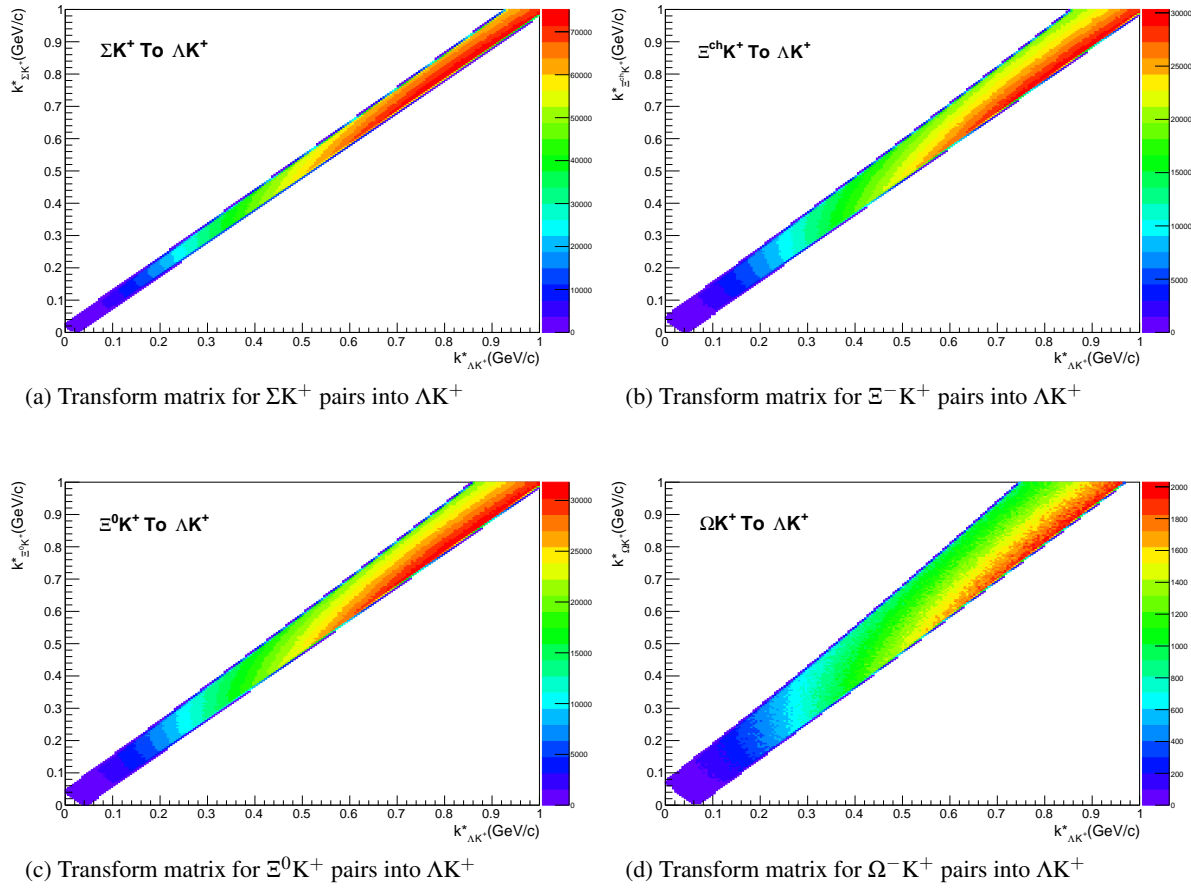


Fig. 21: Sample Transform Matrices generated with THERMINATOR for ΛK^+ Analysis

501 Femtoscopic analyses are sensitive to the pair emission structure at kinetic freeze-out. Therefore, in the
 502 eyes of femtoscopy, any particle born from a resonance decay before last rescattering is seen as primary.
 503 For our study, when including three residual contributors, we consider a particle to be primary if its
 504 parent has a proper decay length of $c\tau < 10$ fm. When including ten residual contributors, we must
 505 reduce this number to $c\tau < 4$ fm for consistency. Moving to ten contributors, we introduce feed-down
 506 from Σ^* and K^* resonances, with proper decay lengths of $c\tau \approx 5$ fm and $c\tau \approx 4$ fm, respectively. As
 507 these are considered non-primary for the case of ten contributors, so must any resonance with $c\tau > 4$ fm.

508 As previously stated, the λ parameters dictate the strength of the parent contribution to the daughter pair.
 509 Therefore, the λ parameter for parent system AB can be estimated as the total number of AK pairs in our

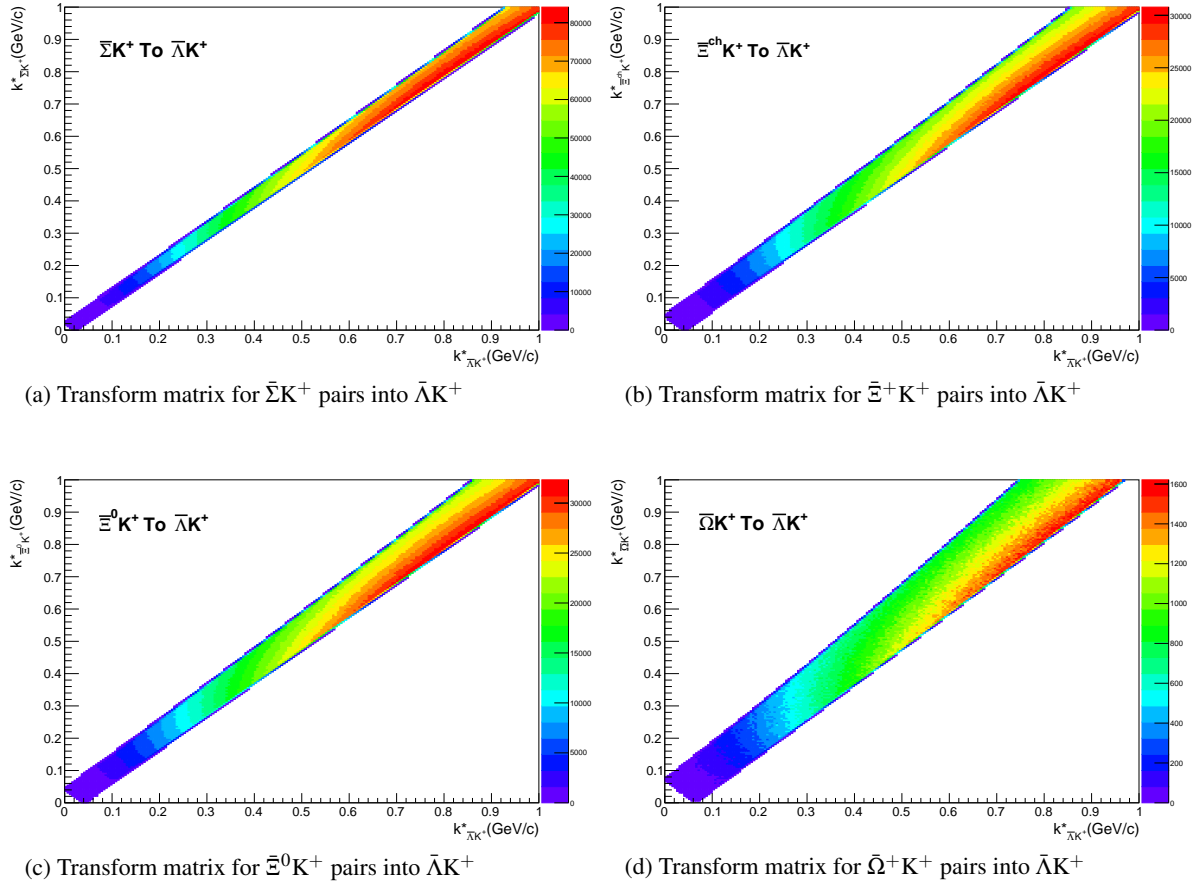


Fig. 22: Sample Transform Matrices generated with THERMINATOR for $\bar{\Lambda}K^+$ Analysis

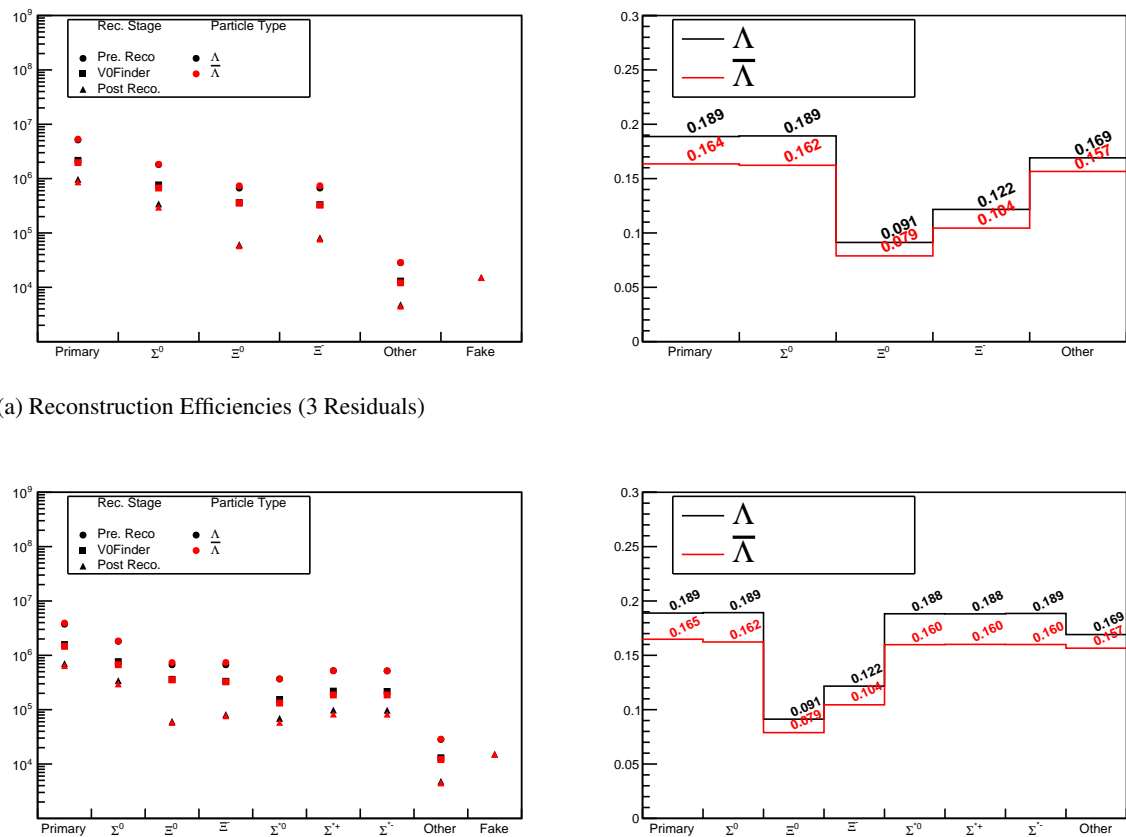
experimental sample originating from AB (N_{AB}) divided by the total number of ΛK pairs (N_{Total}):

$$\lambda_{AB} = \frac{N_{AB}}{N_{Total}} \quad (29)$$

The particle yields can be estimated using THERMINATOR 2 simulation (N_{ij}^{THERM}), while the reconstruction efficiencies (RE_{ij}) are estimated with MC HIJING data, which has been run through GEANT to simulate the detector response (Fig. 23). Thus, the λ parameters are estimated as:

$$\lambda_{AB} = \frac{N_{AB}}{N_{Total}} = \frac{N_{AB}^{THERM} RE_{AB}^{HIJING}}{\sum_{ij} N_{ij}^{THERM} RE_{ij}^{HIJING}} \quad (30)$$

The λ values used can be found in Table 6, for the case of both three and ten residual contributors. In the table, we also list the λ values used for “Other” and “Fakes”. The “Other” category contains pairs which are not primary, and which do not originate from the (3 or 10) residual pairs included in the fit. The “Fakes” category represents pairs that are mistakenly identified as ΛK . To estimate this λ_{Fakes} value, we assumed that the number of fake pairs was equal to the total number of pairs multiplied by the Λ purity (i.e. assuming perfect purity for the kaons); or, more simply, $\lambda_{Fakes} = 1.0 - \text{Purity}(\Lambda)$. For both of these contributors (“Other” and “Fakes”), we assume that these correlations average to unity, and therefore do not contribute to the final correlation function.

**Fig. 23:** Reconstruction Efficiencies

ΛK ⁺ residuals		ΛK ⁻ residuals		ΛK ⁻ residuals		ΛK ⁺ residuals		ΛK _S ⁰ residuals		ΛK _S ⁰ residuals	
Pair System	λ value	Pair System	λ value	Pair System	λ value	Pair System	λ value	Pair System	λ value	Pair System	λ value
3 Residuals (Max Parent $c\tau_{\text{decay}} = 10 \text{ fm}$)											
ΛK ⁺	0.527	ΛK ⁻	0.526	ΛK ⁻	0.526	ΛK ⁺	0.527	ΛK _S ⁰	0.543	ΛK _S ⁰	0.544
Σ ⁰ K ⁺	0.111	Σ ⁰ K ⁻	0.110	Σ ⁰ K ⁻	0.110	Σ ⁰ K ⁺	0.111	Σ ⁰ K _S ⁰	0.120	Σ ⁰ K _S ⁰	0.120
Ξ ⁰ K ⁺	0.039	Ξ ⁰ K ⁻	0.035	Ξ ⁰ K ⁻	0.038	Ξ ⁰ K ⁺	0.036	Ξ ⁰ K _S ⁰	0.042	Ξ ⁰ K _S ⁰	0.039
Ξ ⁻ K ⁺	0.050	Ξ ⁺ K ⁻	0.046	Ξ ⁻ K ⁻	0.050	Ξ ⁺ K ⁺	0.046	Ξ ⁻ K _S ⁰	0.054	Ξ ⁺ K _S ⁰	0.050
Other	0.226	Other	0.235	Other	0.228	Other	0.233	Other	0.194	Other	0.199
Fakes	0.048	Fakes	0.048	Fakes	0.048	Fakes	0.048	Fakes	0.048	Fakes	0.048
10 Residuals (Max Parent $c\tau_{\text{decay}} = 4 \text{ fm}$)											
ΛK ⁺	0.180	ΛK ⁻	0.180	ΛK ⁻	0.179	ΛK ⁺	0.181	ΛK _S ⁰	0.192	ΛK _S ⁰	0.193
Σ ⁰ K ⁺	0.116	Σ ⁰ K ⁻	0.114	Σ ⁰ K ⁻	0.115	Σ ⁰ K ⁺	0.116	Σ ⁰ K _S ⁰	0.125	Σ ⁰ K _S ⁰	0.124
Ξ ⁰ K ⁺	0.040	Ξ ⁰ K ⁻	0.037	Ξ ⁰ K ⁻	0.040	Ξ ⁰ K ⁺	0.037	Ξ ⁰ K _S ⁰	0.043	Ξ ⁰ K _S ⁰	0.040
Ξ ⁻ K ⁺	0.052	Ξ ⁺ K ⁻	0.047	Ξ ⁻ K ⁻	0.052	Ξ ⁺ K ⁺	0.048	Ξ ⁻ K _S ⁰	0.056	Ξ ⁺ K _S ⁰	0.052
Σ ^{*+} K ⁺	0.054	Σ ^{*-} K ⁻	0.051	Σ ^{*+} K ⁻	0.053	Σ ^{*-} K ⁺	0.051	Σ ^{*+} K _S ⁰	0.058	Σ ^{*-} K _S ⁰	0.055
Σ ^{*-} K ⁺	0.048	Σ ^{*+} K ⁻	0.050	Σ ^{*-} K ⁻	0.048	Σ ^{*+} K ⁺	0.050	Σ ^{*-} K _S ⁰	0.052	Σ ^{*+} K _S ⁰	0.054
Σ ^{*0} K ⁺	0.048	Σ ^{*0} K ⁻	0.045	Σ ^{*0} K ⁻	0.048	Σ ^{*0} K ⁺	0.045	Σ ^{*0} K _S ⁰	0.052	Σ ^{*0} K _S ⁰	0.048
ΛK ^{*0}	0.046	ΛK ^{*0}	0.047	ΛK ^{*0}	0.046	ΛK ^{*0}	0.047	ΛK ^{*0}	0.022	ΛK ^{*0}	0.022
Σ ⁰ K ^{*0}	0.041	Σ ⁰ K ^{*0}	0.041	Σ ⁰ K ^{*0}	0.041	Σ ⁰ K ^{*0}	0.041	Σ ⁰ K ^{*0}	0.019	Σ ⁰ K ^{*0}	0.019
Ξ ⁰ K ^{*0}	0.014	Ξ ⁰ K ^{*0}	0.013	Ξ ⁰ K ^{*0}	0.014	Ξ ⁰ K ^{*0}	0.013	Ξ ⁰ K ^{*0}	0.007	Ξ ⁰ K ^{*0}	0.006
Ξ ⁻ K ^{*0}	0.018	Ξ ⁺ K ^{*0}	0.017	Ξ ⁻ K ^{*0}	0.018	Ξ ⁺ K ^{*0}	0.017	Ξ ⁻ K ^{*0}	0.009	Ξ ⁺ K ^{*0}	0.008
Other	0.295	Other	0.310	Other	0.299	Other	0.307	Other	0.318	Other	0.330
Fakes	0.048	Fakes	0.048	Fakes	0.048	Fakes	0.048	Fakes	0.048	Fakes	0.048

Table 6: λ values for the individual components of the ΛK correlation functions for the case of 3 and 10 residual contributions.

522 In practice, we model the correlation function of the parents (ex. $\Sigma^0 K^+$), and run the correlation function
 523 through the appropriate transform matrix to determine the contribution to the daughter correlation func-
 524 tion (ex. ΛK^+). In an ideal world, we would simply look up the parent interaction in some table, and
 525 input this into our model, and form the parent correlation function, C_{ij} , through the Lednicky equation
 526 (for the case of one or more charge neutral particle in the pair), or via the CoulombFitter machinery
 527 described in Sec.5.2. Unfortunately, the world in which we live is not perfect, such a table does not
 528 exist, and little is known about the interaction between the particles in the residual pairs of this study.
 529 Additionally, introducing a unique set of scattering parameters and radii for each residual system would
 530 introduce a large number of additional fit parameters, for which we do not have many constraints, and
 531 would cause our fitter to be too unconstrained and yield untrustworthy results. Therefore, for this analy-
 532 sis, we assume all residual pairs have the same source size as the daughter pair. Furthermore, we assume
 533 Coulomb-neutral residual pairs share the same scattering parameters as the daughter pair. Therefore,
 534 for Coulomb-neutral pairs, such as $\Sigma^0 K$, and $\Xi^0 K$, $C_{ij}(k_{ij}^*)$ is calculated from Eqn. 16, with the help of
 535 Eqn. 18; $C_{ij}(k_{\Lambda K}^*)$ is then obtained by transforming $C_{ij}(k_{ij}^*)$ with Eq. 28, using the appropriate transform
 536 matrix.

537 For residual pairs affected by both the strong and Coulomb interactions, things are a bit more compli-
 538 cated. This is due to the fact that, for the case of both strong and Coulomb interaction, we no longer
 539 have a nice analytical form with which to fit. Generating a correlation function including both is also
 540 time consuming, as described further in Sec.5.2. This increase in formation time is not an issue in gen-
 541 erating single correlation functions, however, it does become a problem when including the method in
 542 the fit process, where thousands of generated correlation functions are needed (the parallelization of the
 543 process across a large number of GPU cores, to drastically decrease run-time, is currently underway).
 544 Therefore, when modeling $\Xi^- K^\pm$ residual correlations, we use the experimental $\Xi^- K^\pm$ data; in this case,
 545 there is no need to make any assumptions about scattering parameters or source sizes. The downside is
 546 that, especially in the 30-50% centrality bin, the statistics are low and error bars large. For the other
 547 cases, we assume the strong interaction is negligible, and generate the parent correlation assuming a
 548 Coulomb-only scenario (see Sec.5.2 for more details). This approximation is well justified here as a
 549 Coulomb-only description of the system describes, reasonably well, the broad features of the $\Xi^{\text{ch}} K^{\text{ch}}$
 550 correlation; the strong interaction is necessary for the fine details. However, as these correlations are
 551 run through a transform matrix, which largely flattens out and fine details, a Coulomb-only description
 552 should be sufficient.

553 In practice, the Coulomb-only scenario is achieved by first building a large number of Coulomb-only
 554 correlations for various radii and λ parameter values, and interpolating from this grid during the fitting
 555 process. This allows us to generate the correlations functions with the speed needed to converge on
 556 fit results within a reasonable amount of time. We find consistent results between using the ΞK data
 557 and the Coulomb-only interpolation method. When quantifying the $\Xi^- K^\pm$ residual contribution, the
 558 experimental $\Xi^- K^\pm$ data is always used. When the number of residual pairs used is increased to 10,
 559 so that contributors such as $\Sigma^{*+} K^-$ enter the picture, the Coulomb-only interpolation method is used.
 560 In other words, the ΞK experimental data is only used to model the ΞK residual contribution, all other
 561 charged pairs are treated with the Coulomb-only interpolation method.

562 Two examples of how very different transform matrices can alter a correlation function are shown in
 563 Figures 24 and 25 below. These figures were taken using parameter values obtained from fits to the data.
 564 In the top left corner of the figures, the input correlation function (closed symbols) is shown together
 565 with the output, transformed, correlation function (open symbols). In the bottom left, the transformed
 566 correlation is shown by itself (with zoomed y-axis). This is especially helpful when the λ parameter is
 567 very small, in which case the contribution in the top left can look flat, but the zoomed in view in the
 568 bottom left shows the structure. The right two plots in each figure show the transform matrix without
 569 (top right) and with (bottom right) a log-scale on the z-axis. Note, more examples of these transforms

570 can be found in Sec. C.

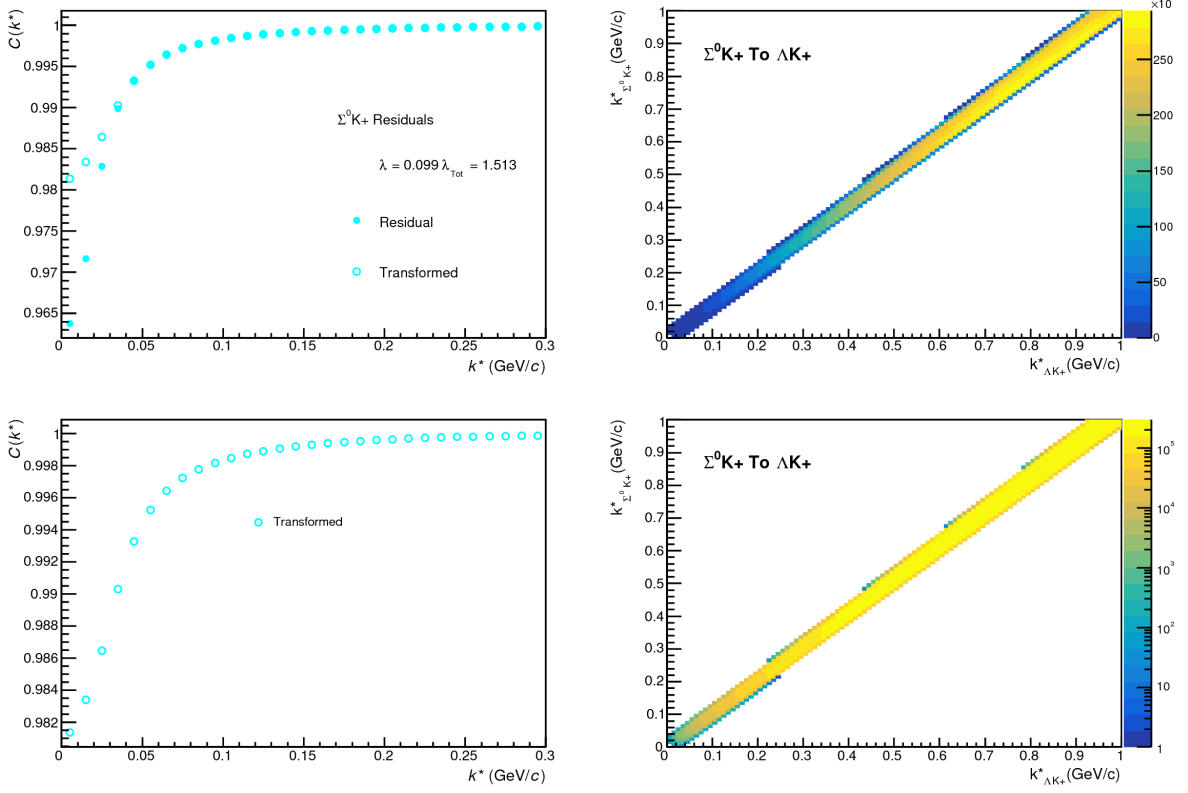


Fig. 24: $\Sigma^0 K^+$ Transform. These figures were taken using parameter values obtained from fits to the data. In the top left corner of the figures, the input correlation function (closed symbols) is shown together with the output, transformed, correlation function (open symbols). In the bottom left, the transformed correlation is shown by itself. The right two plots in each figure show the transform matrix without (top right) and with (bottom right) a log-scale on the z-axis.

571 Concerning the radii of the residual parent pairs, it was suggested that these should be set to smaller
 572 values than those of the daughter pair. In the interest of minimizing the number of parameters in the
 573 fitter, we tested this by introducing an m_T -scaling of the parents' radii. The motivation for this scaling
 574 comes from the approximate m_T -scaling of the radii observed in 32. To achieve this scaling, we assume
 575 the radii follow an inverse-square-root distribution: $R_{AB} = \alpha m_T^{-1/2}$. Then, it follows that we should scale
 576 the parent radii as:

$$R_{AB} = R_{\Lambda K} \left(\frac{m_{T,AB}}{m_{T,\Lambda K}} \right)^{-1/2} \quad (31)$$

577 The values of m_T for each pair system were taken from THERMINATOR. As the fitter dances around
 578 parameter space and selects a new radius for the ΛK system, the radii of the residuals is simply the ΛK
 579 radius scaled by the appropriate factor, given above (Eq.31). In the end, this scaling factor made no
 580 significant difference in our fit results, so this complication is excluded from our final results. Note that
 581 this is not surprising, as the most extreme scaling factor was, in the case of using 10 residual systems,
 582 between ΛK^+ with $m_{T,\Lambda K^+} \approx 1.4 \text{ GeV}/c^2$ and $\Xi^- K^{*0}$ with $m_{T,\Xi^- K^{*0}} \approx 1.8 \text{ GeV}/c^2$, resulting in a scale
 583 factor of ≈ 0.9 .

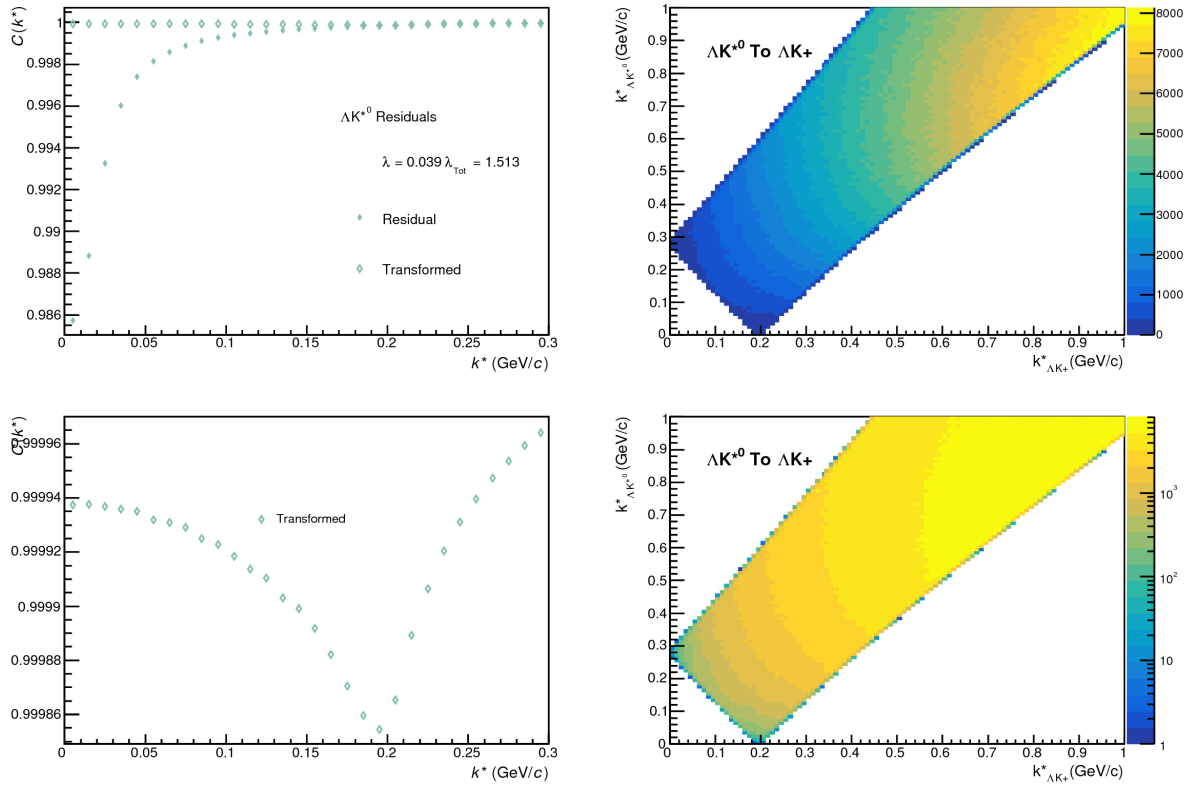


Fig. 25: ΛK^0 Transform. These figures were taken using parameter values obtained from fits to the data. In the top left corner of the figures, the input correlation function (closed symbols) is shown together with the output, transformed, correlation function (open symbols). In the bottom left, the transformed correlation is shown by itself. The right two plots in each figure show the transform matrix without (top right) and with (bottom right) a log-scale on the z-axis.

584 **5.5 Non-femtoscopic background**

585 We observe a significant non-femtoscopic, non-flat, background in all of our correlations at large k^* .
 586 This background increases with decreasing centrality, is the same amongst all ΛK^\pm pairs, and is more
 587 pronounced in the ΛK_S^0 system, as can be seen in Fig. 26. Figure 27a shows that THERMINATOR 2
 588 simulation does a good job of describing the difference in backgrounds between ΛK^\pm and ΛK_S^0 .

589 Before beginning, it is important to note that the difference in ΛK^\pm and ΛK_S^0 backgrounds is due mainly
 590 to the difference in kinematic cuts, not due to any interesting physics. Figure 27b shows that, for THER-
 591 MINATOR simulation, when restrictions are imposed on the p_T of the K_S^0 to more closely match the
 592 K^\pm cuts, the backgrounds align much better. Therefore, we conclude that the difference in background
 593 between ΛK^\pm and ΛK_S^0 observed in our experimental data is simply due to a difference in kinematic cuts
 594 between K^\pm and K_S^0 particles.

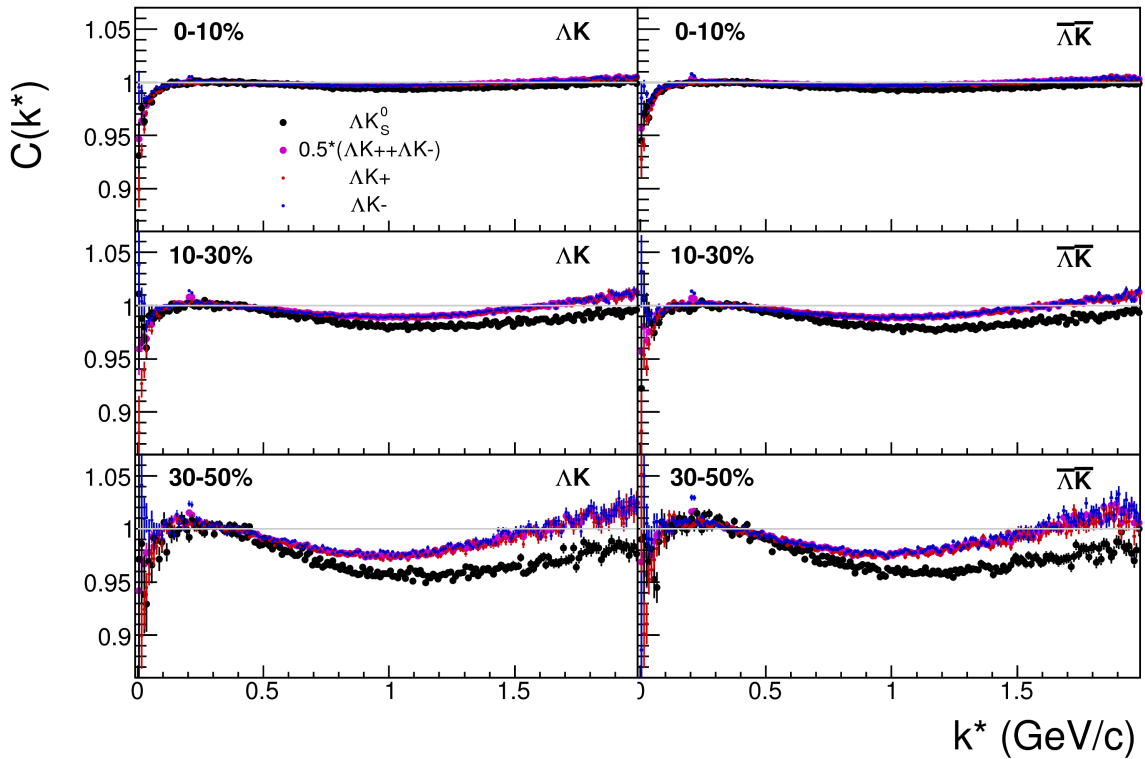


Fig. 26: A comparison on the non-femtoscopic backgrounds observed in our our ΛK experimental data.

595 It is suggested that this background effect is due primarily to particle collimation associated with elliptic
 596 flow [12]. More specifically, these backgrounds result from mixing events with unlike event-plane angles
 597 (Ψ_{EP}). As explained in [12], when elliptic flow is present, all particles are more likely to be emitted in
 598 a specific direction (in-plane), as opposed to a perpendicular direction. Therefore, the difference in
 599 momenta for pairs of particles tends to be smaller, compared to the case of no flow. In the case of mixed-
 600 event pairs, the two events used do not share an event-plane, and therefore there is no collimation effect
 601 in the pairs from flow. As a result, pairs with larger momentum are more likely when mixed-events
 602 are used (in the denominator of the correlation function), causing the correlation function to dip below
 603 unity. In general, the observation of the correlation function below unity, at a given k^* , means it is more
 604 probable to find a pair at that k^* when the daughters are taken from mixed-events, as compared to when
 605 they are taken from the same event. This same reasoning suggests that the background should lead to an
 606 enhancement at low- k^* . The enhancement at high- k^* ($k^* \gtrsim 1.5$ GeV/c) does not result from the collective
 607 flow of the system. We are not certain what causes this enhancement, but typical suspects are jet-like

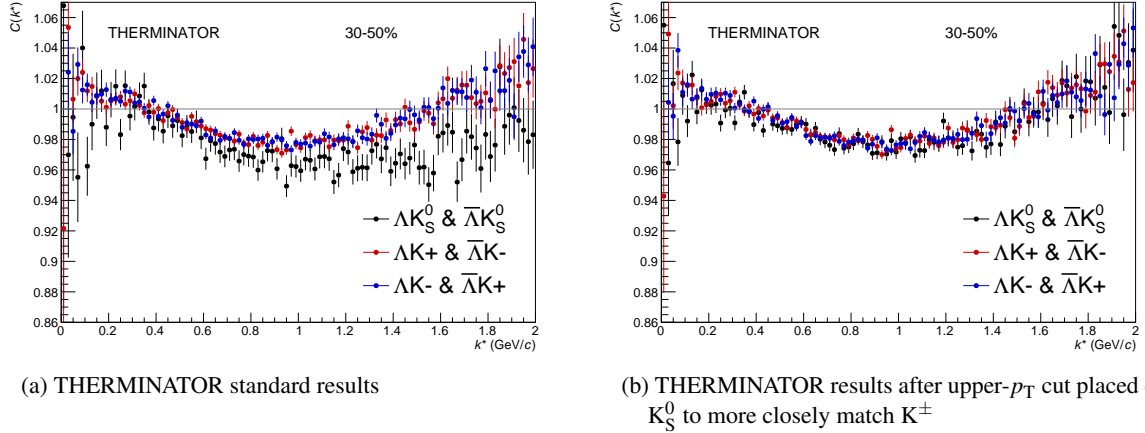


Fig. 27: THERMINATOR 2 simulation for ΛK^+ (red), ΛK^- (blue), and ΛK_S^0 (black). In 27a, we show the standard THERMINATOR 2 results. THERMINATOR 2 does a good job describing qualitatively the different between the ΛK^\pm and ΛK_S^0 backgrounds. In 27b, an upper- p_T cut was placed on the K_S^0 particles to more closely match the K^\pm kinematic cuts. After this tweak, the ΛK^\pm and ΛK_S^0 backgrounds agree much better.

608 correlations and resonance decays.

609 We can split our correlation functions into three main regions. First, the low- k^* region ($k^* \lesssim 0.3$ GeV/c)
610 contains the femtoscopic correlations, as well as a likely enhancement from the background. The
611 intermediate- k^* region ($0.3 \lesssim k^* \lesssim 1.5$ GeV/c) contains a suppression from the background. Finally,
612 the high- k^* region ($k^* \gtrsim 1.5$ GeV/c) contains an enhancement with unknown origin.

613 The issue here is that we need to know the behavior of the non-femtoscopic background in the low-
614 k^* region, but we only cleanly observe it in the region further out where there is no femtoscopic signal.
615 Unfortunately, we cannot simply rotate each event to artificially align their event-planes and rid ourselves
616 of this mixing effect, as our azimuthal angle acceptance is not perfectly uniform, and we have only finite
617 event-plane resolution. With better resolution, one could simply bin events in Ψ_{EP} and only mix events
618 within a given bin. We pursued this direction, and observed a slight decrease in the background; however,
619 going to finer binning, we saw no additional reduction in the background, signaling that we had reached
620 the limits dictated by the resolution. In the end, we are forced to model the background to include it into
621 our fit.

622 THERMINATOR 2 simulation has been shown to reproduce the background features in a πK analysis
623 [12]. After issuing each simulated event a random Ψ_{EP} ¹, we found THERMINATOR 2 did an exceptional
624 job of describing our data. Furthermore, the simulation showed the non-femtoscopic background affects
625 the correlation function as a separable scale factor (Fig 29, discussed below). Figure 28 shows the
626 THERMINATOR 2 simulation (gold) together with experimental data (red, blue, or black). The figure
627 also shows a 6th-order polynomial fit to the simulation (gold), as well as the fit polynomial scaled to
628 match the data (red, blue, black).

629 Figure 29 shows three different correlation function generated using THERMINATOR 2 simulation (“Cf
630 w/o Bgd (A)”, “Cf w. Bgd (B)”, “Bgd(C)”), as well as two histograms describing the relation between
631 the three (“Ratio (B/C)”, “1+Diff(B-C)”). “Cf w/o Bgd (A)” shows a correlation function with a femto-
632 scopic correlation, but without background. When THERMINATOR 2 is run without randomizing event
633 planes, and therefore having all events share a common event plane, no background is observed, as ex-
634 pected. The femtoscopic correlation effect was introduced by assuming a set of scattering parameters for

¹default was for all events to share a common event plane

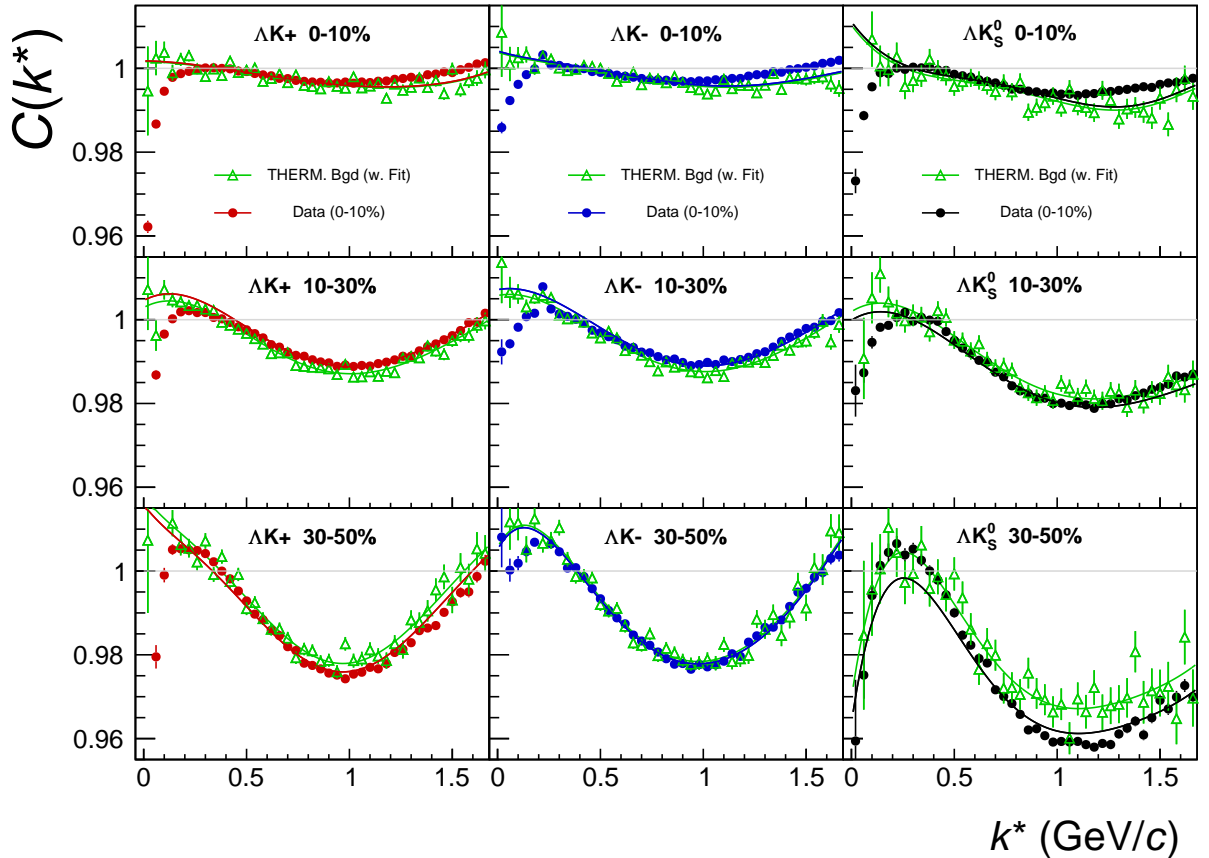


Fig. 28: THERMINATOR 2 simulation (gold) together with experimental data (red, blue, or black). Results are shown for ΔK^+ (left), ΔK^- (middle), and ΔK_s^0 (right). A 6th-order polynomial fit to the simulation is shown as a solid gold line. This polynomial is scaled to match the experimental data. The polynomial fit with scale factor applied is drawn in a color matching the experimental data (red, blue, black).

the system, and weighting the numerators appropriately. The second correlation, "Cf w. Bgd (B)", shows a correlation function with both a femtoscopic correlation and a background (most closely matches our situation in experiment). To generate the background, each event was given a random event-plane angle, as is given to us in experiment. To generate the femtoscopic correlation, the same numerator weighting procedure was used. Finally, "Bgd (C)", shows a correlation function with a non-femtoscopic background, but no femtoscopic correlation, i.e. background only. This is generated just as "Cf w. Bgd (B)", with randomized event planes, but unit weights are used when filling the numerators, so no femtoscopic effects are included.

The main point of Fig. 29 is that the black points match the blue (and purple) points; or, equivalently:

$$C_{fw/oBgd} = \frac{C_{fw.Bgd}}{Bgd} \rightarrow C_{theory} = \frac{C_{exp}}{F_{Bgd}} \rightarrow C_{exp} = C_{theory} \cdot F_{Bgd} \quad (32)$$

i.e. THERMINATOR 2 simulation shows the non-femtoscopic background affects the correlation function as a separable scale factor. We expect this behavior to be roughly the same in the experimental data.

The description by THERMINATOR 2 of the non-femtoscopic backgrounds in the ΔK^\pm systems is remarkable, and can be used in a quantitative fashion to help fit the data. More specifically, the non-femtoscopic backgrounds were modeled by (6th-)order polynomial fits to THERMINATOR 2 simulation for the ΔK^\pm analyses; one polynomial for each centrality class. The form of each polynomial was set

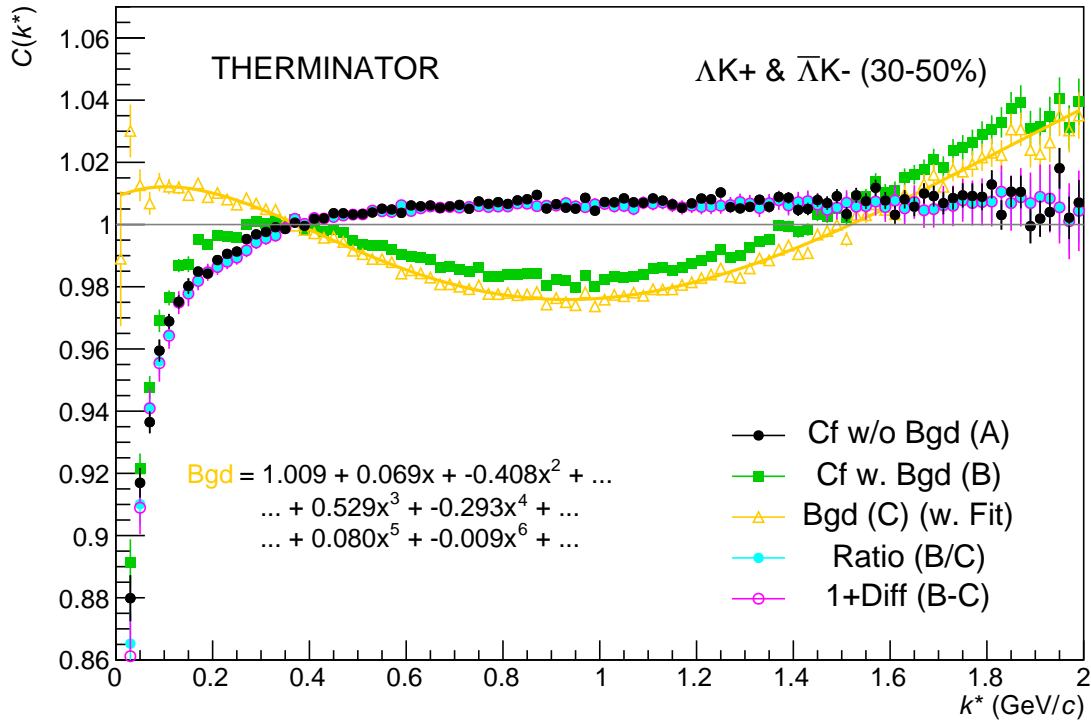


Fig. 29: Correlation with background decomposition with THERMINATOR. "Cf w/o Bgd (A)" shows a correlation function with a femtoscopic correlation, but without background. "Cf w. Bgd (B)", shows a correlation function with both a femtoscopic correlation and a background (most closely matches our situation in experiment). "Bgd (C)", shows a correlation function with a non-femtoscopic background, but no femtoscopic correlation, i.e. background only.

651 before use with the experimental data, by fitting to the THERMINATOR 2 simulation, shown in Fig. 28.
 652 At the time of the fit, the polynomial used to correct each correlation function could only be adjust by a
 653 simple scale factor to best match the data.

654 The description of the ΛK_S^0 is good at a qualitative level, but not quantitatively good enough to be utilized
 655 in our fit. As such, we use a linear form to model the background in the ΛK_S^0 system. The background for
 656 each correlation function was fixed before use in the signal region by fitting a linear form to the region
 657 $0.6 < k^* < 0.9 \text{ GeV}/c$. In all cases, the non-femtoscopic background correction was applied as a scale
 658 factor.

659 An alternative approach to treating the non-femtoscopic background is to instead attempt to eliminate
 660 it. The background may be effectively reduced by forming the reference distribution ($B(k^*)$) with the
 661 "Stavinskiy method". With the Stavinskiy method, mixed-event pairs are not used for the reference
 662 distribution; instead, same-event pseudo-pairs, formed by rotating one particle in a real pair by 180°
 663 in the transverse plane, are used. This rotation rids the pairs of any femtoscopic correlation, while
 664 maintaining correlations due to elliptic flow (and other suitably symmetric contributors). The effect on
 665 our ΛK correlation functions can be seen in the appendix, in Sec. 4.2.

666 Figure 30 demonstrates the use of the Stavinskiy method with THERMINATOR 2. In the figure, unit
 667 weights were used for all numerators, so no femtoscopic signal is included, only background effects.
 668 The black points show an ideal, experimentally unreachable, situation of aligning all of the event-plane
 669 angles. With THERMINATOR 2, when the event-planes are aligned, the background signal is killed.

670 The green points show the case of random event-plane angles, a situation more closely matching that
 671 of experiment. The purple points shown the affect of applying the Stavinskiy method to the case of
 672 random event-planes. The figure shows that this method effectively kills the non-flat background (i.e.
 673 the procedure takes the green points to the purple). Finally, the blue points show the effect of applying
 674 the Stavinskiy method when all of the event-planes are aligned. This shows that the Stavinskiy method
 675 does not introduce any signal to an already flat background.

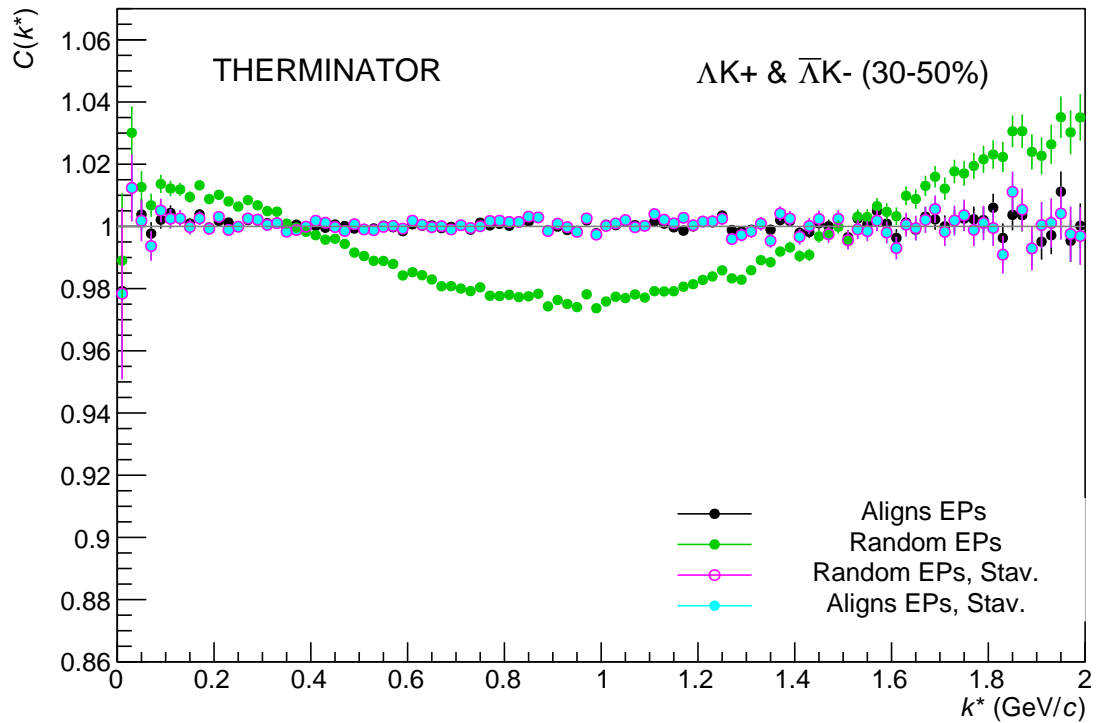


Fig. 30: The use of the Stavinskiy method with THERMINATOR 2. Unit weights were used for all numerators, so no femtoscopic signal is included, only background effects. The black points show an ideal, experimentally unreachable, situation of aligning all of the event-plane angles. The green points show the experimental situation of random event-plane angles. The purple points shown the affect of applying the Stavinskiy method to the case of random event-planes. Finally, the blue points show the effect of applying the Stavinskiy method when all of the event-planes are aligned.

676 5.6 LednickyFitter

677 The code developed to fit the data is called “LednickyFitter”, and utilizes the ROOT TMinuit implemen-
 678 tation of the MINUIT fitting package. In short, given a function with a number of parameters, the fitter
 679 explores the parameter space searching for the minimum of the function. In this implementation, the
 680 function to be minimized should represent the difference between the measured and theoretical corre-
 681 lation functions. However, a simple χ^2 test is inappropriate for fitting correlation functions, as the ratio of
 682 two Poisson distributions does not result in a Poisson distribution. Instead, a log-likelihood fit function
 683 of the following form is used [3]:

$$\chi_{PML}^2 = -2 \left[A \ln \left(\frac{C(A+B)}{A(C+1)} \right) + B \ln \left(\frac{A+B}{B(C+1)} \right) \right] \quad (33)$$

684 where A is the experimental signal distribution (numerator), B is the experimental background distri-

bution (denominator), and C is the theoretical fit correlation function. Therefore, we use Eq. 33 as the statistic quantifying the quality of the fit. The parameters of the fit are: λ , R , f_0 ($\Re f_0$ and $\Im f_0$ separately), d_0 , and normalization N .

With our procedure, we are able to share parameters between different analyses and fit all simultaneously. A given pair and its conjugate (e.g. ΛK^+ and $\bar{\Lambda} K^-$) always share scattering parameters ($\Re f_0$, $\Im f_0$, d_0). However, the three distinct analyses (ΛK^+ , ΛK^- , and ΛK_S^0) are assumed to have scattering parameters unique from each other. We assume the pair emission source for a given centrality class is similar between all analyses; therefore, for each centrality, all ΛK analyses share a common radius parameter. We assume the same is true for the overall normalization λ parameters in Eq. 28. Finally, each correlation function has a unique normalization parameter.

All correlation functions were normalized in the range $0.32 < k^* < 0.40$ GeV/c, and fit in the range $0.0 < k^* < 0.30$ GeV/c. For the ΛK^- analysis, the region $0.19 < k^* < 0.23$ GeV/c was excluded from the fit to exclude the bump caused by the Ω^- resonance. For each pair system, we account for contributions from three residual contributors, as discussed in Sec. 5.4, and whose individual λ values are listed in Table 6 (the cases of zero and ten residual contributors were also investigated, but the case of three contributors was deemed most reasonable). We account for effects of finite track momentum resolution, as outlined in Sec. 5.3. The non-femtoscopic backgrounds are modeled using the THERMINATOR 2 simulation for the ΛK^\pm analyses, and with a linear form for the ΛK_S^0 system, as described in Sec. 5.5. In general, corrections are applied to the fit function, the raw data is never touched.

To summarize, the complete fit function is constructed as follows:

1. The uncorrected, primary, correlation function, $C_{\Lambda K}(k_{\text{True}}^*)$, is constructed using Eqns. 16 and 18
2. The correlation functions describing the parent systems which contribute residually are obtained using:
 - Eqns. 16 and 18 for the case of Coulomb-neutral pairs
 - $\Xi^- K^\pm$ experimental data for $\Xi^- K^\pm$ contributions
 - a Coulomb-only curve, with the help of Sec. 5.7, for other pairs including the Coulomb interaction
3. The residual contributions to the ΛK correlation function is found by running each parent correlation function through the appropriate transform matrix, via Eq. 28
4. The primary and residual correlations are combined, via Eq. 27 with Tab. 6, to form $C'_{\text{Fit}}(k_{\text{True}}^*)$
5. The correlation function is corrected to account for momentum resolution effects using Eq. 26, to obtain $C'_{\text{Fit}}(k_{\text{Rec}}^*)$
6. Finally, the non-flat background correction, $F_{\text{Bgd}}(k_{\text{Rec}}^*)$ is applied, and the final fit function is obtained, $C_{\text{Fit}}(k_{\text{Rec}}^*) = C'_{\text{Fit}}(k_{\text{Rec}}^*) * F_{\text{Bgd}}(k_{\text{Rec}}^*)$

Figures 35, 33, and 34 in Section 7, show experimental data with fits for all studied centralities for $\Lambda K^+(\bar{\Lambda} K^-)$, $\Lambda K^-(\bar{\Lambda} K^+)$, and $\Lambda K_S^0(\bar{\Lambda} K_S^0)$, respectively. For the cases of no and ten residual contributors, see Appendix A.

5.7 Coulomb Fitter

When fitting the $\Xi^-(\bar{\Xi}^+)K^\pm$ results, it is necessary to include both strong and Coulomb effects. In this case, Equation 16 is no longer valid, and, in fact, there is no analytical form with which to fit. We therefore must take a more basic approach, and integrate out Eq. 12 by hand. To achieve this, one has

726 two options. The first option is to numerically integrate Eq.12. The second option is to simulate a large
 727 sample of particle pairs, calculate the wave function describing the interaction, and average to obtain the
 728 integral. Having no experience with either of these options, we elected the latter of simulating pairs. The
 729 code developed to achieve this functionality is called “CoulombFitter”. Currently, in order to generate
 730 the statistics needed for a stable fit, we find that $\sim 10^4$ simulated pairs per 10 MeV bin are necessary. The
 731 nature of this process means that the “CoulombFitter” takes much longer to run than the “LednickyFitter”
 732 of Section 5.1.

733 Unfortunately, with this analysis, we are not sensitive to, and therefore not able to distinguish between,
 734 the iso-spin singlet and triplet states. We proceed with our analysis, but the results must be interpreted
 735 as iso-spin averaged scattering parameters.

736 As stated before, to generate a fit correlation function, we must simulate a large number of pairs, calculate
 737 the wave-function, and average Ψ^2 over all pairs in a given k^* bin. Essentially, we calculate Equation 21
 738 by hand:

$$\begin{aligned} C(\mathbf{k}^*) &= \sum_S \rho_S \int S(\mathbf{r}^*) |\Psi_{\mathbf{k}^*}^S(\mathbf{r}^*)|^2 d^3 \mathbf{r}^* \\ &\longrightarrow C(|\mathbf{k}^*|) \equiv C(k^*) = \sum_S \rho_S \langle |\Psi^S(\mathbf{k}_i^*, \mathbf{r}_i^*)|^2 \rangle_i \\ &\longrightarrow C(k^*) = \lambda \sum_S \rho_S \langle |\Psi^S(\mathbf{k}_i^*, \mathbf{r}_i^*)|^2 \rangle_i + (1 - \lambda) \end{aligned} \quad (34)$$

739 where $\langle \rangle_i$ represents an average over all pairs in a given k^* bin.

740 In summary, for a given k^* bin, we must draw $N_{pairs} \sim 10^4$ pairs, and for each pair:

- 741 1. Draw a random \mathbf{r}^* vector according to our Gaussian source distribution $S(\mathbf{r}^*)$
- 742 2. Draw a random \mathbf{k}^* vector satisfying the $|\mathbf{k}^*|$ restriction of the bin
 - 743 – We draw from real k^* vectors obtained from the data
 - 744 – However, we find that drawing from a distribution flat in k^* gives similar results
- 745 3. Construct the wave-function Ψ

746 After all pairs for a given k^* bin are simulated and wave-functions obtained, the results are averaged to
 747 give the fit result.

748 Construction of the wave-functions, Equation 22, involves a number of complex functions not included
 749 in standard C++ or ROOT libraries (namely, $h(\eta)$, $\tilde{G}(\rho, \eta)$), and $F(-i\eta, 1, i\xi)$. These functions were
 750 even difficult to find and implement from elsewhere. Our solution was to embed a Mathematica kernel
 751 into our C++ code to evaluate these functions. However, having Mathematica work on-the-fly with the
 752 fitter was far too time consuming (fitter would have taken days, maybe weeks to finish). Our solution
 753 was to use Mathematica to create matrices representing these functions for different parameter values.
 754 During fitting, these matrices were then interpolated and the results used to build the wave-functions.
 755 This method decreased the running time dramatically, and we are now able to generate results in under
 756 ~ 1 hour. This process will be explained in more detail in future versions of the note.

757 6 Systematic Errors

758 In order to understand the systematic uncertainties of our data, the analysis code was run many times
 759 using slightly different values for a number of important cuts, and the results were compared. To quantify

the systematic errors on the data, all correlation functions built using all varied cut values were bin-by-bin averaged, and the resulting variance of each bin was taken as the systematic error. The cuts included in the systematic study, as well as the values used in the variations, are shown in Tab. 7 (ΛK_S^0) and Tab. 8 (ΛK^\pm). Note, the central value corresponds to that used in the analysis.

Similarly, the fit parameters extracted from all of these correlation functions were averaged, and the resulting variances were taken as the systematic errors for the fit parameters. As with the systematic errors on the data, this was performed for all varied cut values. Additionally, a systematic analysis was done on our fit method through varying our k^* fit range, as well as varying our modeling of the non-femtoscopic background. Our choice of k^* fit range was varied by $\pm 25\%$. As previously stated, the non-femtoscopic backgrounds are modeled using the THERMINATOR 2 simulation for the ΛK^\pm analyses, and with a linear form for the ΛK_S^0 system. To study the contribution of this choice to our systematic errors, we modeled the backgrounds of all of our systems by fitting to the data with a linear, quadratic, and Gaussian form. Additionally, we modeled the backgrounds of all systems with a polynomial fit to the THERMINATOR simulation, scaled to match the data. The resulting uncertainties in the extracted parameter sets were combined with our uncertainties arising from our particle and pair cuts.

6.1 Systematic Errors: ΛK_S^0

6.1.1 Particle and Pair Cuts

The cuts included in the systematic study, as well as the values used in the variations, are listed below. Note, the central value corresponds to that used in the analysis.

ΛK_S^0 systematics	
DCA to PV $\Lambda(\bar{\Lambda})$	< [4, 5, 6] mm
DCA to PV K_S^0	< [2, 3, 4] mm
DCA $\Lambda(\bar{\Lambda})$ Daughters	< [3, 4, 5] mm
DCA K_S^0 Daughters	< [2, 3, 4] mm
$\cos(\theta_{PA}) \Lambda(\bar{\Lambda})$ to PV	> [0.9992, 0.9993, 0.9994]
$\cos(\theta_{PA}) K_S^0$ to PV	> [0.9992, 0.9993, 0.9994]
DCA to PV of $p(\bar{p})$ Daughter of $\Lambda(\bar{\Lambda})$	> [0.5, 1, 2] mm
DCA to PV of $\pi^-(\pi^+)$ Daughter of $\Lambda(\bar{\Lambda})$	> [2, 3, 4] mm
DCA to PV of π^+ Daughter of K_S^0	> [2, 3, 4] mm
DCA to PV of π^- Daughter of K_S^0	> [2, 3, 4] mm
$\Delta\mathbf{r}$ of Like-Charge Daughters	> [5, 6, 7] cm

Table 7: ΛK_S^0 systematics. In the table, the shorthand used is as follows: PA = pointing angle; PV = primary vertex; DCA = distance of closest approach; $\Delta\mathbf{r}$ = average separation

6.1.2 Non-femtoscopic background

We fit our non-flat background with a linear function. To study the contribution of this choice to our systematic errors, we also fit with a quadratic and Gaussian form. The resulting uncertainties are combined with the uncertainties arising from our particle cuts.

6.1.3 Fit range

Our choice of k^* fit range was varied by $\pm 25\%$. The resulting uncertainties in the extracted parameter sets were combined with our uncertainties arising from our particle and pair cuts.

787 **6.2 Systematic Errors: ΛK^\pm**

788 **6.2.1 Particle and Pair Cuts**

789 The cuts included in the systematic study, as well as the values used in the variations, are listed below.
 790 Note, the central value corresponds to that used in the analysis.

ΛK^\pm systematics	
DCA $\Lambda(\bar{\Lambda})$ to PV	< [4, 5, 6] mm
DCA $\Lambda(\bar{\Lambda})$ Daughters	< [3, 4, 5] mm
$\cos(\theta_{PA}) \Lambda(\bar{\Lambda})$ to PV	> [0.9992, 0.9993, 0.9994]
DCA to PV of $p(\bar{p})$ Daughter of $\Lambda(\bar{\Lambda})$	> [0.5, 1, 2] mm
DCA to PV of $\pi^-(\pi^+)$ Daughter of $\Lambda(\bar{\Lambda})$	> [2, 3, 4] mm
$\overline{\Delta r}$ of $\Lambda(\bar{\Lambda})$ Daughter with Same Charge as K^\pm	> [7, 8, 9] cm
DCA to PV in Transverse Plane of K^\pm	< [1.92, 2.4, 2.88]
DCA to PV in Longitudinal Direction of K^\pm	< [2.4, 3.0, 3.6]

Table 8: ΛK^\pm systematics. In the table, the shorthand used is as follows: PA = pointing angle; PV = primary vertex; DCA = distance of closest approach; $\overline{\Delta r}$ = average separation.

791 **6.2.2 Non-femtoscopic background**

792 We fit our non-flat background with a linear function. To study the contribution of this choice to our sys-
 793 tematic errors, we also fit with a quadratic and Gaussian form. The resulting uncertainties are combined
 794 with the uncertainties arising from our particle cuts.

795 **6.2.3 Fit range**

796 Our choice of k^* fit range was varied by $\pm 25\%$. The resulting uncertainties in the extracted parameter
 797 sets were combined with our uncertainties arising from our particle and pair cuts.

798 **6.3 Systematic Errors: ΞK^\pm**

799 **6.3.1 Particle and Pair Cuts**

800 The cuts included in the systematic study, as well as the values used in the variations, are listed below.
 801 Note, the central value corresponds to that used in the analysis.

$\Xi^- K^\pm$ systematics

$\Xi^- K^\pm$ systematics	
DCA to PV $\Xi(\bar{\Xi})$	< [2, 3, 4] mm
DCA $\Xi(\bar{\Xi})$ Daughters	< [2, 3, 4] mm
$\cos(\theta_{PA}) \Xi(\bar{\Xi})$ to PV	> [0.9991, 0.9992, 0.9993]
$\cos(\theta_{PA}) \Lambda(\bar{\Lambda})$ to $\Xi(\bar{\Xi})$ DV	> [0.9992, 0.9993, 0.9994]
DCA to PV bachelor π	> [0.5, 1, 2] mm
DCA to PV $\Lambda(\bar{\Lambda})$	> [1, 2, 3] mm
DCA $\Lambda(\bar{\Lambda})$ Daughters	< [3, 4, 5] mm
DCA to PV of $p(\bar{p})$ Daughter of $\Lambda(\bar{\Lambda})$	> [0.5, 1, 2] mm
DCA to PV of $\pi^-(\pi^+)$ Daughter of $\Lambda(\bar{\Lambda})$	> [2, 3, 4] mm
$\Delta\mathbf{r}$ of $\Lambda(\bar{\Lambda})$ Daughter and K^\pm with like charge	> [7, 8, 9] cm
$\Delta\mathbf{r}$ of Bachelor π and K^\pm with like charge	> [7, 8, 9] cm
DCA to PV in Transverse Plane of K^\pm	< [1.92, 2.4, 2.88]
DCA to PV in Longitudinal Direction of K^\pm	< [2.4, 3.0, 3.6]

Table 9: $\Xi^- K^\pm$ systematics. In the table, the shorthand used is as follows: PA = pointing angle; PV = primary vertex; DV = decay vertex; DCA = distance of closest approach; $\Delta\mathbf{r}$ = average separation.

802 **7 Results and Discussion**

803 **7.1 Results: ΛK_S^0 and ΛK^\pm**

804 In the following sections, we present our final results, for which three residual contributors are assumed.
 805 Results for the cases of ten residual contributors and no residual correlations may be found in Appendices
 806 A.3 and A.4, respectively. Furthermore, comparisons of results obtained using different variations of the
 807 fit method can be found in Appendix A.1.

808 For the results shown, unless otherwise noted, the following hold true: All correlation functions were
 809 normalized in the range $0.32 < k^* < 0.40$ GeV/c, and fit in the range $0.0 < k^* < 0.30$ GeV/c. For the
 810 ΛK^- and $\bar{\Lambda} K^+$ analyses, the region $0.19 < k^* < 0.23$ GeV/c was excluded from the fit to exclude the
 811 bump caused by the Ω^- resonance. The non-femtoscopic backgrounds for the ΛK^+ and ΛK^- systems
 812 were modeled by a (6th-)order polynomial fit to THERMINATOR simulation, while those for the ΛK_S^0
 813 were fit with a simple linear form. All analyses were fit simultaneously across all centralities, with a
 814 single radius and normalization λ parameter for each centrality bin. Scattering parameters ($\Re f_0$, $\Im f_0$,
 815 d_0) were shared between pair-conjugate systems, but assumed unique between the different ΛK charge
 816 combinations (i.e. a parameter set describing the $\Lambda K^+ & \bar{\Lambda} K^-$ system, a second set describing the
 817 $\Lambda K^- & \bar{\Lambda} K^+$ system, and a third for the $\Lambda K_S^0 & \bar{\Lambda} K_S^0$ system). Each correlation function received a
 818 unique normalization parameter. The fits were corrected for finite momentum resolution effects, non-
 819 femtoscopic backgrounds, and residual correlations resulting from the feed-down from resonances.

820 Lines and boxes on the experimental data represent statistical and systematic errors, respectively. In the
 821 figures showing experimental correlation functions with fits, the black solid curve represents the primary
 822 (ΛK) correlation's contribution to the fit. The green line shows the fit to the non-flat background. The
 823 purple points show the fit after all residual contributions have been included, and momentum resolution
 824 and non-flat background corrections have been applied. The extracted fit values with uncertainties are
 825 printed as (fit value) \pm (statistical uncertainty) \pm (systematic uncertainty).

826 Figure 31 nicely collects and summarizes all of our extracted fit parameters. In the summary plot, we
 827 show the extracted scattering parameters in the form of a $\Im f_0$ vs $\Re f_0$ plot, which includes the d_0 values
 828 to the right side. We also show the λ vs. radius parameters for all three of our studied centrality bins.
 829 The extracted fit parameters are also collected in Table 10. Figure 32 presents our extracted fit radii,
 830 along with those of other systems previously analyzed by ALICE [13], as a function of pair transverse
 831 mass (m_T).

Centrality	λ	R
0-10%	1.40 ± 0.63 (stat.) ± 0.17 (sys.)	6.24 ± 0.92 (stat.) ± 0.66 (sys.)
10-30%	0.90 ± 0.34 (stat.) ± 0.17 (sys.)	4.41 ± 0.50 (stat.) ± 0.39 (sys.)
30-50%	1.00 ± 0.34 (stat.) ± 0.22 (sys.)	3.51 ± 0.44 (stat.) ± 0.28 (sys.)

System	$\Re f_0$	$\Im f_0$	d_0
$\Lambda K^+ & \bar{\Lambda} K^-$	-0.49 ± 0.19 (stat.) ± 0.12 (sys.)	0.42 ± 0.22 (stat.) ± 0.12 (sys.)	-0.55 ± 2.22 (stat.) ± 1.76 (sys.)
$\Lambda K^- & \bar{\Lambda} K^+$	0.19 ± 0.15 (stat.) ± 0.08 (sys.)	0.29 ± 0.17 (stat.) ± 0.08 (sys.)	-7.80 ± 6.15 (stat.) ± 6.10 (sys.)
$\Lambda K_S^0 & \bar{\Lambda} K_S^0$	0.09 ± 0.15 (stat.) ± 0.06 (sys.)	0.53 ± 0.28 (stat.) ± 0.13 (sys.)	-2.59 ± 1.47 (stat.) ± 3.59 (sys.)

Table 10: Fit Results ΛK , with 3 residual correlations included. The fit procedure is as described in the text. The fit is done on the data with only statistical error bars. The errors marked as “stat.” are those returned by MINUIT. The errors marked as “sys.” are those which result from my systematic analysis (as outlined in Section 6).

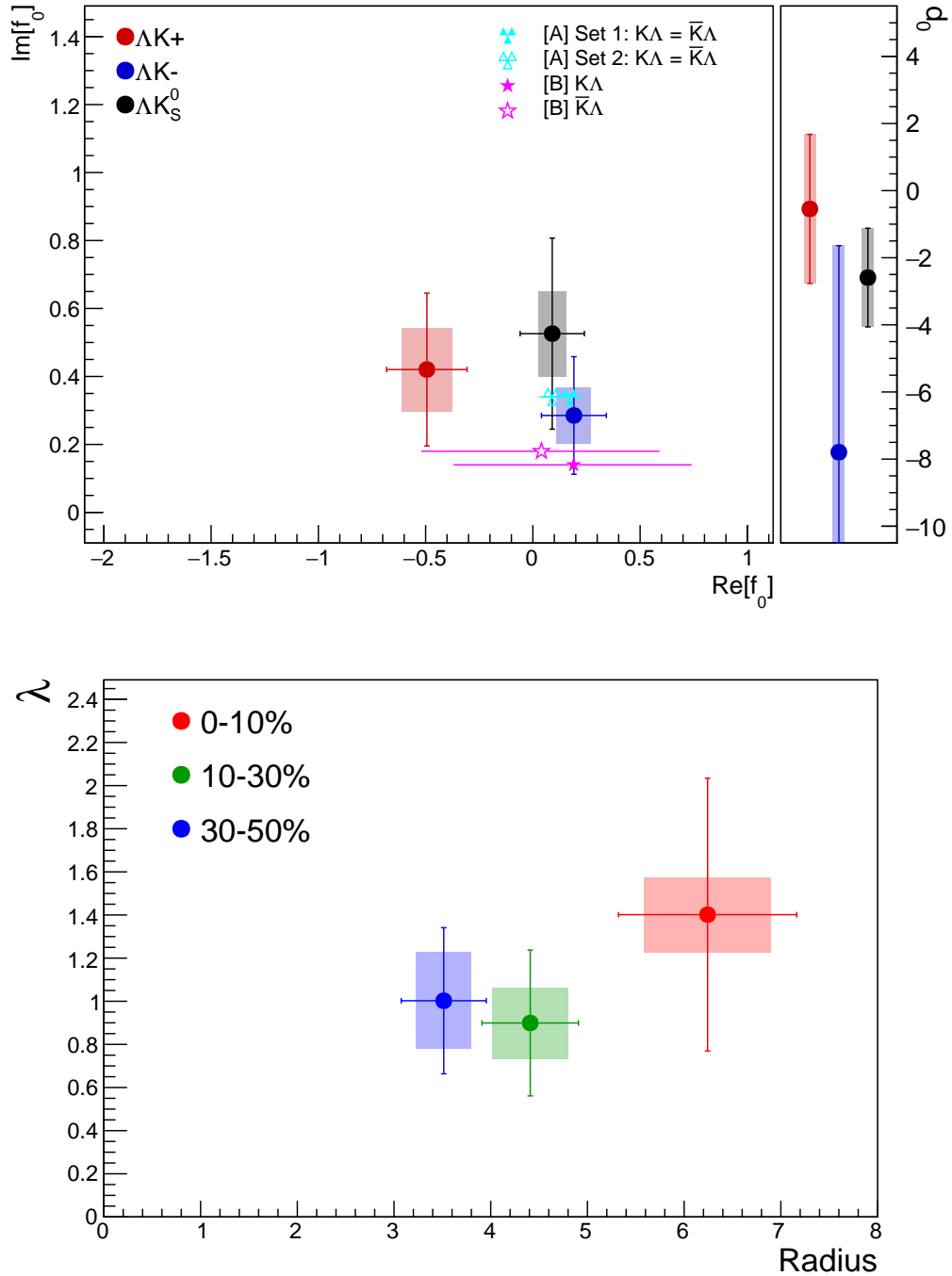


Fig. 31: Extracted fit parameters for the case of 3 residual contributors for all of our AK systems. [Top]: $\Im f_0$ vs. $\Re f_0$, together with d_0 to the right. [Bottom]: λ vs. Radius for the 0-10% (blue), 10-30% (green), and 30-50% (red) centrality bins. In the fit, all AK systems share common radii. The color scheme used in the panel are to be consistent with those in Fig. 32. The cyan ([A] = Ref. [14]) and magenta ([B] = Ref. [15]) points show theoretical predictions made using chiral perturbation theory.

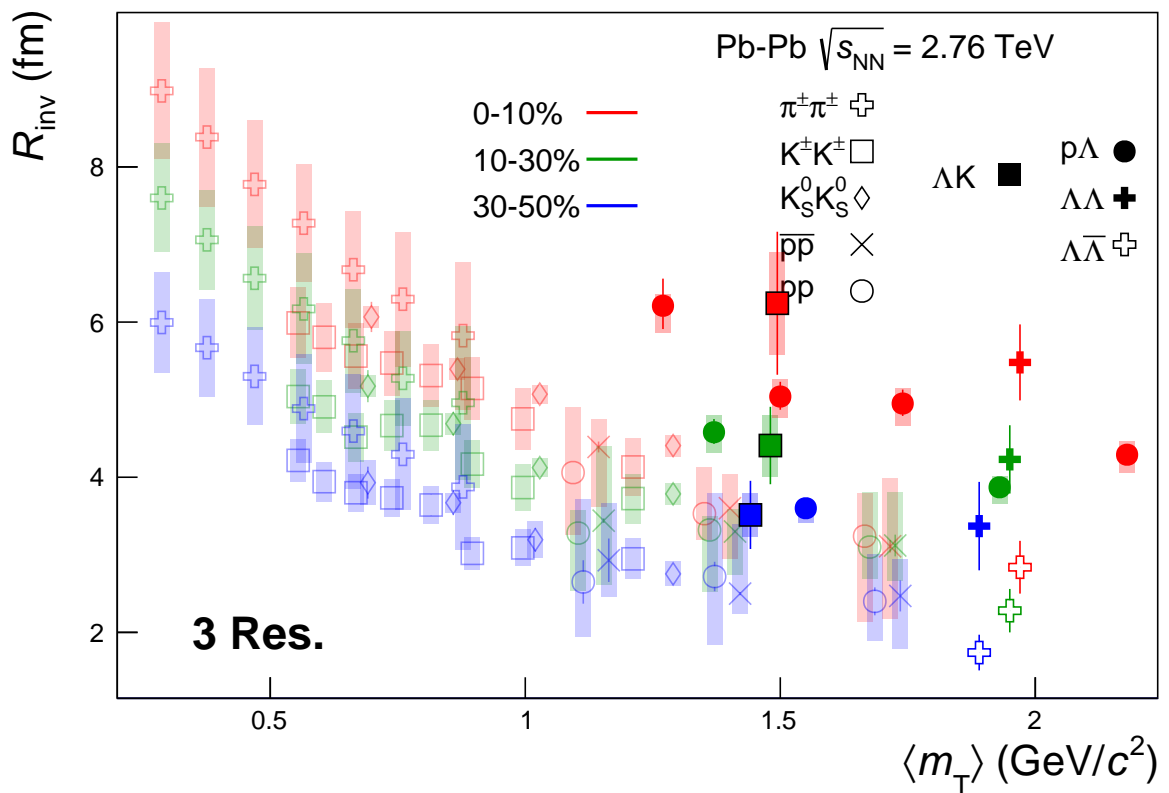


Fig. 32: 3 residual correlations in ΛK fits. Extracted fit R_{inv} parameters as a function of pair transverse mass (m_T) for various pair systems over several centralities. The ALICE published data [13] are shown with transparent, open symbols. The new ΛK results are shown with opaque, filled symbols. The m_T value for the ΛK system is an average of those for the ΛK^+ , $\bar{\Lambda} K^-$, and ΛK_S^0 systems.

832 **7.1.1 Correlation functions with fits**

833 Figures 33, 34, and 35 show the experimental correlation functions with fits, assuming 3 residual contributors,
 834 for all ΛK systems (ΛK^+ , $\bar{\Lambda} K^-$, and ΛK_S^0 , respectively) in all studied centralities. The parameter
 835 sets extracted from the fits can be found in Table 10. Figures with a wider range in k^* , showing bet-
 836 ter the non-femtosopic background, may be found in Appendix A. Also contained in Appendix A are
 837 plots demonstrating the contributions from the residuals, as well as results assuming 10 and no residual
 838 contributors.

839 In Figures 33 - 35, the pair system (e.g. ΛK^+) data is shown in the left column, and the conjugate pair
 840 system (e.g. $\bar{\Lambda} K^-$) in the right. The rows differentiate the different centrality bins (0-10% in the top,
 841 10-30% in the middle, and 30-50% in the bottom). The lines on the data represent the statistical errors,
 842 while the boxes represent the systematic errors. The fit procedure is as described in the text; in short,
 843 all systems are fit simultaneously with shared radii, while each [ΛK^+ , $\bar{\Lambda} K^-$, ΛK_S^0] maintains a unique
 844 set of scattering parameters. The black solid line represents the primary ΛK component of the fit. The
 845 green line shows the fit to the non-flat background. The purple points show the fit after all residuals'
 846 contributions have been included, and momentum resolution and non-flat background corrections have
 847 been applied. The extracted fit values with uncertainties are printed in the top left panel of each figure.

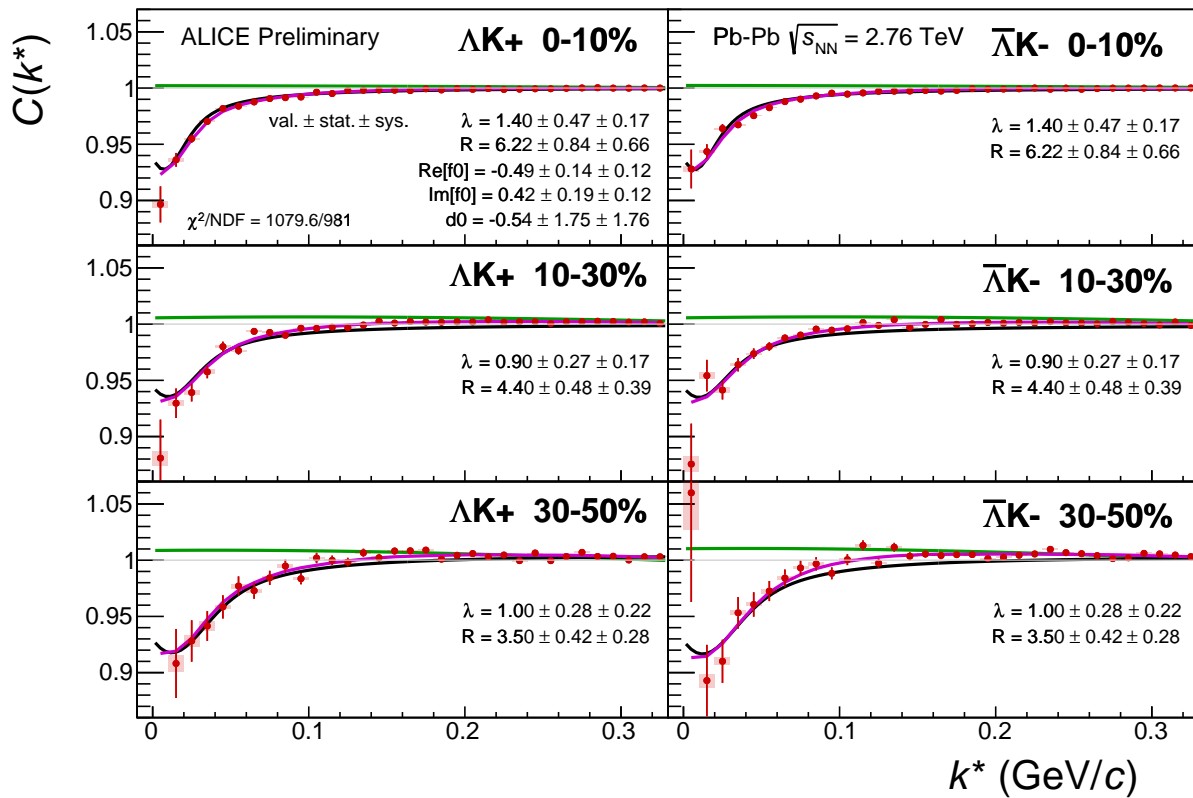


Fig. 33: Fit results, with 3 residual correlations included, for the ΛK^+ and $\bar{\Lambda} K^-$ data. The ΛK^+ data is shown in the left column, the $\bar{\Lambda} K^-$ in the right, and the rows differentiate the different centrality bins (0-10% in the top, 10-30% in the middle, and 30-50% in the bottom). See text for further details.

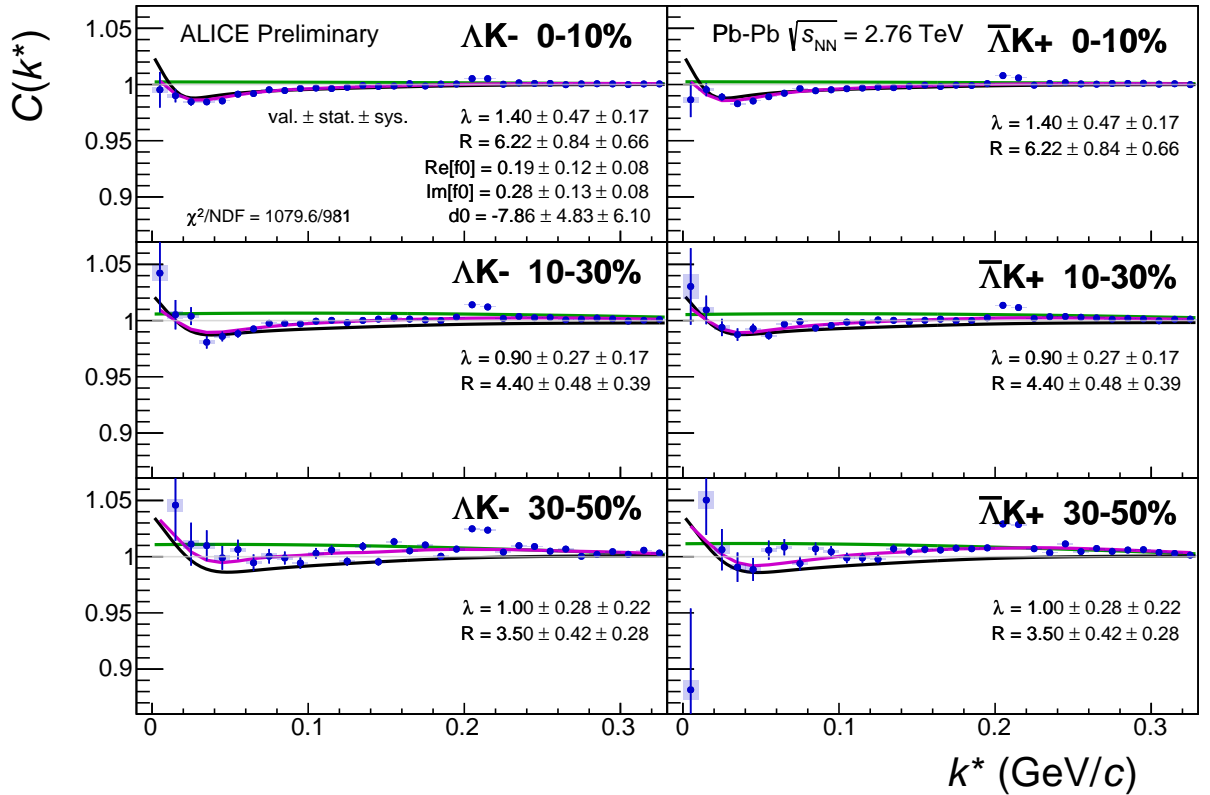


Fig. 34: Fit results, with 3 residual correlations included, for the ΛK^- and $\bar{\Lambda} K^+$ data. The ΛK^- data is shown in the left column, the $\bar{\Lambda} K^+$ in the right, and the rows differentiate the different centrality bins (0-10% in the top, 10-30% in the middle, and 30-50% in the bottom). See text for further details.

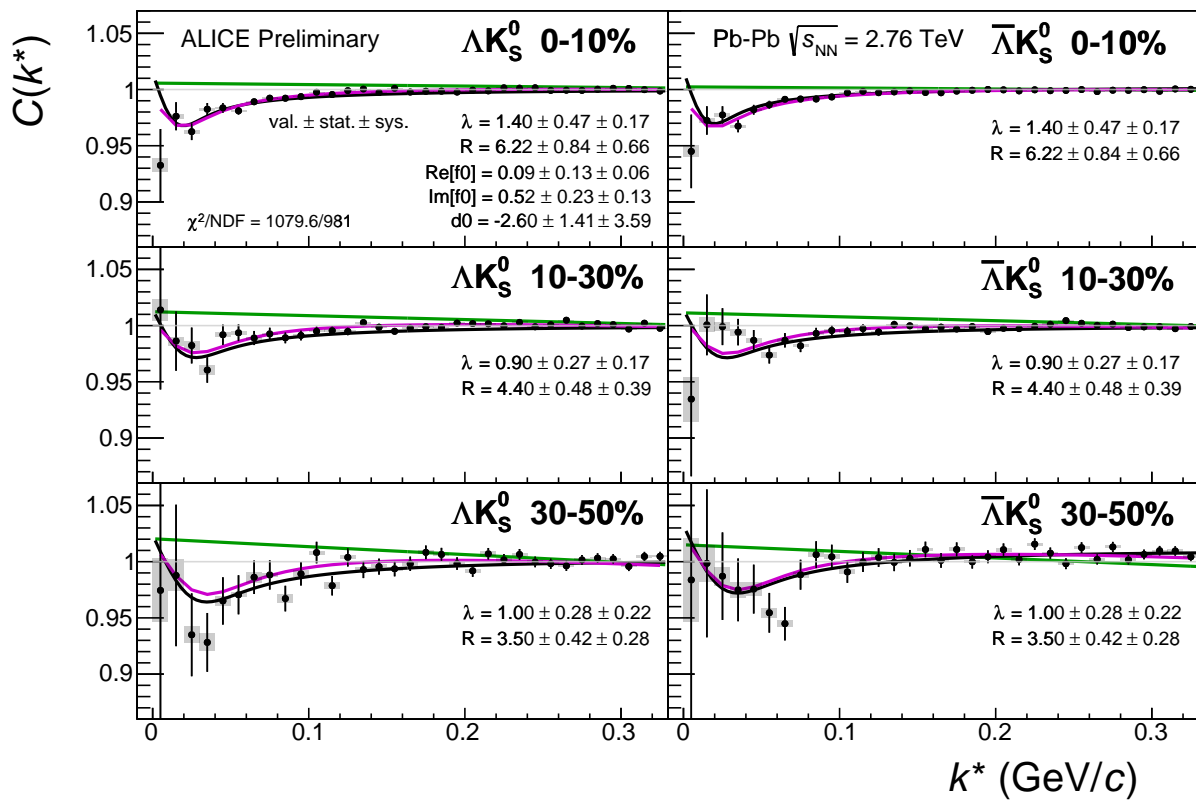


Fig. 35: Fit results, with 3 residual correlations included, for the ΛK_s^0 and $\bar{\Lambda} K_s^0$ data. The ΛK_s^0 data is shown in the left column, the $\bar{\Lambda} K_s^0$ in the right, and the rows differentiate the different centrality bins (0-10% in the top, 10-30% in the middle, and 30-50% in the bottom). See text for further details.

848 **7.1.2 Discussion of m_T -Scaling**

849 It is clear from the results presented in the previous sections, that the ΛK systems do not conform to the
 850 approximate m_T -scaling of the pair source sizes. At first thought, this may appear to be a troubling result;
 851 the approximate scaling is an observed consequence of the collective behavior of the soft (low- p_T) sector
 852 of the produced system. The Λ and K particles certainly participate in the collective expansion of the
 853 QGP medium, so why do their extracted femtoscopic radii not behave as expected? To get straight to
 854 the point: the ΛK systems are comprised on non-identical particles, each with its own and unique single
 855 particle source. Each source is, in general, unique in both its overall size, and in its space-time position
 856 within the produced medium. The hydrodynamic nature of the medium produces the approximate m_T -
 857 scaling with respect to these single-particle sources, not the pair sources. The combination of these
 858 effects, when probing correlations between non-identical particle pairs, leads to extracted radii falling
 859 outside of the (identical particle femtoscopy) m_T -scaling trend. Figure 36 (which contains the same data
 860 as Fig.32), shows again the R_{inv} vs m_T plot, but also highlights (with arrows) the approximate individual
 861 $\langle m_T \rangle$ values of the single particle distributions.

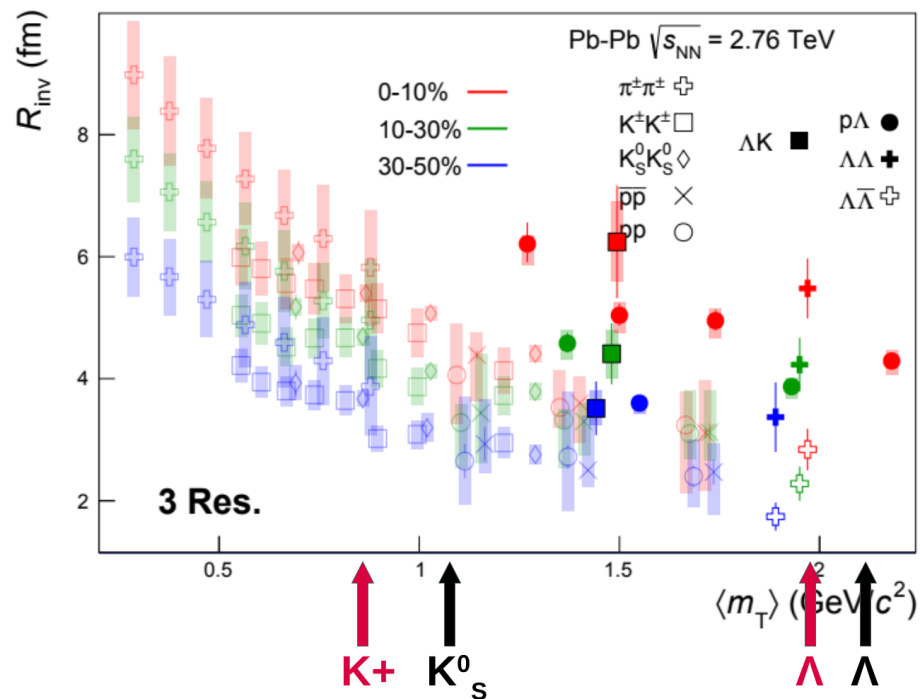


Fig. 36: Same as Fig. 32, but with the individual m_T values for the single particle distributions identified. The grey circles show how the single particle sizes are expected to change with m_T .

862 Taking a close look at Fig. 36, one can see that the previously published data (transparent points) are
 863 for identical particle analyses only. For these cases, the pair source, probed through femtoscopy, is
 864 comprised of two identical sources laying on top of each other. The extracted femtoscopic radii are
 865 related to the single particle source sizes by a factor of $\sqrt{2}$, and of course follow the m_T -scaling trend.
 866 The other (unpublished) non-identical particle femtoscopy study ($p\Lambda$) included in the figure, also shows
 867 radii deviating from the m_T -scaling band. Drawing a comparison with the $\Lambda\bar{\Lambda}$ study shown in Fig. 36
 868 is a bit more complicated; the $\Lambda\bar{\Lambda}$ system, although containing non-identical particles, does contain a
 869 particle with its antiparticle, for which annihilation could conceivably alter the pair source distribution.
 870 In any case, the pair source m_T -scaling visible in the identical particle femtoscopy studies presented in
 871 Fig. 36 is really just a manifestation of the scaling of the single particle sources. For the case presented
 872 here, sampling single particle distributions with significantly different m_T values translates to sampling
 873 distributions differing in size which are separated in space-time. Therefore, our results deviating from
 874 the m_T -scaling curve of the identical particle studies is not surprising.

We can use Fig. 36 to estimate the values of our ΛK radii in the absence of any μ_{out} offset. As previously stated, for identical particle studies, the single particle radii can be obtained from the extracted femtoscopic radii simply by dividing by $\sqrt{2}$. Using the trends shown in Fig. 36, for the m_T values appropriate for our studies, we expect the single particle source sizes in the 0-10% centrality bin to be $R_K \sim 5/\sqrt{2}$ fm and $R_\Lambda \sim 3/\sqrt{2}$ fm. In Eq. 15 from Sec. 5.1, we found the pair source radius was the sum of the single source radii added in quadrature, $R_{ab,i}^2 = R_{a,i}^2 + R_{b,i}^2$. Therefore, we would expect $R_{\Lambda K} \sim 4$ fm, which is clearly below the value we measure. We argue that our larger extracted radii result from a non-zero μ_{out} in the pair source distribution, due to the fact that the single particle Λ and K sources are separated in space-time. In the following sections, we use simulation (a numerical integration method of the Koonin-Pratt equation, and THERMINATOR 2) to demonstrate the effect on one-dimensional source sizes from non-zero offsets in the “out” direction. Furthermore, we use a spherical harmonic decomposition of our experimental correlation functions to demonstrate that the data are consistent with a non-zero μ_{out} .

We emphasize that we do not suggest our extracted source sizes indicate any sort of contradiction to the hydrodynamic picture of the system dictating the substructure of the femtoscopic radii. In fact, our results rather support such a picture. The hydrodynamic response of the system not only confines higher- m_T particles to smaller homogeneity regions, it also pushes their average emissions points further in the “out” direction [16]. As introduced above, these effects can lead to larger extracted radii when studying non-identical particle pairs under the assumption of a spherically symmetric Gaussian source with no offset in the “out” direction. This point is further supported with our numerical integration method of the Koonin-Pratt equation (presented below), as well as with our study varying μ_{out} within the THERMINATOR 2 simulation (presented as the end of this section).

In summary, due to the hydrodynamic response of the system created in heavy-ion collisions, we expect higher- m_T particles to originate from smaller regions of homogeneity located further in the “out” direction. This difference in single particle source sizes, in addition to their separation in space-time, can lead to a deviation of non-identical particle studies from the m_T -scaling trend observed for identical particle pairs. This is not in contradiction to the hydrodynamic response of the system, but rather in support of it. For non-identical particle studies, the individual particle m_T values dictate the single particle source sizes and positions, which in turn dictate the observed femtoscopic signal. Therefore, when reporting results from non-identical studies, it is vital to report the individual particle m_T values, otherwise, comparisons to other measurements will be impossible.

Numerical integration of the Koonin-Pratt equation We investigated the effect of a non-zero offset in the outward direction, μ_{out} , by numerically integrating the Koonin-Pratt equation (Eq. 12), a demonstration of which is shown in Figures 37 and 38. Before going into the details, we find that increasing μ_{out} leads to a correlation function which is more tightly confined to low- k^* values, i.e. the increase in μ_{out} makes the source appear larger. The nice analytic form for generating fit correlation functions derived by Lednický relies on a spherically symmetric source distribution centered at the origin. Using instead the method of numerical integration allows us to alter the source as we wish, which, in this case, amounts to simply adding an outward shift, μ_{out} , to the spherically symmetric Gaussian profile. The cost of this flexibility is a significant decrease in the speed of generating fit curves, and this numerical integration is currently too slow to be used within our fit framework. Nonetheless, the numerical integration method does offer a simple test ground for us to study the effect of a non-zero μ_{out} .

For the curves presented in Figs. 37 and 38, a spherically symmetric Gaussian source ($R_o = R_s = R_i$) was assumed, and the offset in the “out” direction (μ_{out}) was varied. In our numerical integration, we used the appropriate forms of the wave-function and scattering parameters (Eqns. 4-7), which were presented in Sec. 5.1. In the figure, the closed black circles show the curve generated by our numerical integrator for a radius $R_i = 6.24$ fm (where $i = o, s, l$), $\mu_{\text{out}} = 0$ fm, and the parameter sets listed in the figures ($[\Re f_0, \Im f_0, d_0] = [-0.49, 0.42, -0.55]$ for ΛK^+ in Fig. 37, and $[\Re f_0, \Im f_0, d_0] = [0.19, 0.29, -7.80]$ for ΛK^- in Fig. 38). Note, the radius of 6.24 fm and the parameter sets were chosen to qualitatively

match the ΛK^+ and ΛK^- experimental data. The open magenta circles were generated using the analytic Lednický equation (Eqns. 16-19 from Sec. 5.1). The figure shows that our numerical integration method is consistent with the Lednický equation. All of the triangle points assume a radius of 5 fm, again with the parameter sets listed in the legends of the figure, and the different colors correspond to different μ_{out} values.

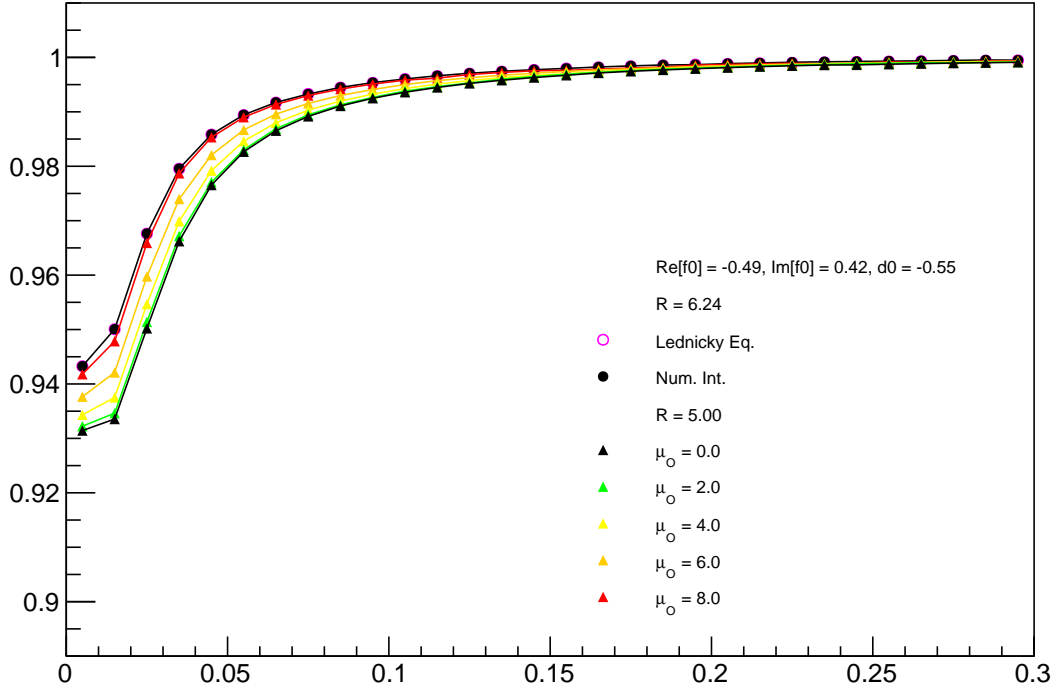


Fig. 37: Numerical integration of the Koonin-Pratt equation, allowing us to study the effect of a non-zero offset in the out direction, μ_{out} . We chose a parameter set to qualitatively match our ΛK^+ data. The assumed scattering parameter set is printed in the top of the legend. All points assume $\mu_{\text{side}} = \mu_{\text{long}} = 0$ fm. The closed black circles and open magenta symbols assume $R_i = 6.24$ fm (where $i = o,s,l$) and $\mu_{\text{out}} = 0$ fm, while the triangle markers assume $R_i = 5$ fm with varying values of μ_{out} . The open magenta circles were obtained with the Lednický equation, all others were obtained with the numerical integration method. See text for more details.

Figures 37 and 38 nicely demonstrate the effect of increasing the magnitude of the offset. Specifically, the figure shows that increasing μ_{out} makes the correlation function more concentrated towards the low- k^* region, which corresponds to larger radii. Furthermore, for a one-dimensional analysis, we see that the case of a spherically symmetric source with $R_i = 6.24$ fm (where $i = o,s,l$) is nearly indistinguishable from a source with $R_i = 5$ fm and $\mu_{\text{out}} = 8$ fm. Therefore, even with a fast numerical integrator, it would be difficult to disentangle the effects of a larger source radius from a shift in the “out” direction. In order to pursue this direction, outside input constraining these parameters would be necessary. This could be accomplished, for instance, by fixing the single particle source sizes, and therefore the pair source size, using identical KK and $\Lambda\Lambda$ results.

Spherical harmonics and varying μ_{out} with THERMINATOR 2 Identical particle femtosopic studies are able to probe only the size of the emitting region, or, more precisely, the second moments of the emission function. In addition to this, non-identical particle studies are able to measure the relative emission shifts, the first moments of the emission function. One method to extract information about the emission asymmetries in the system is via a spherical decomposition of the correlation function. With

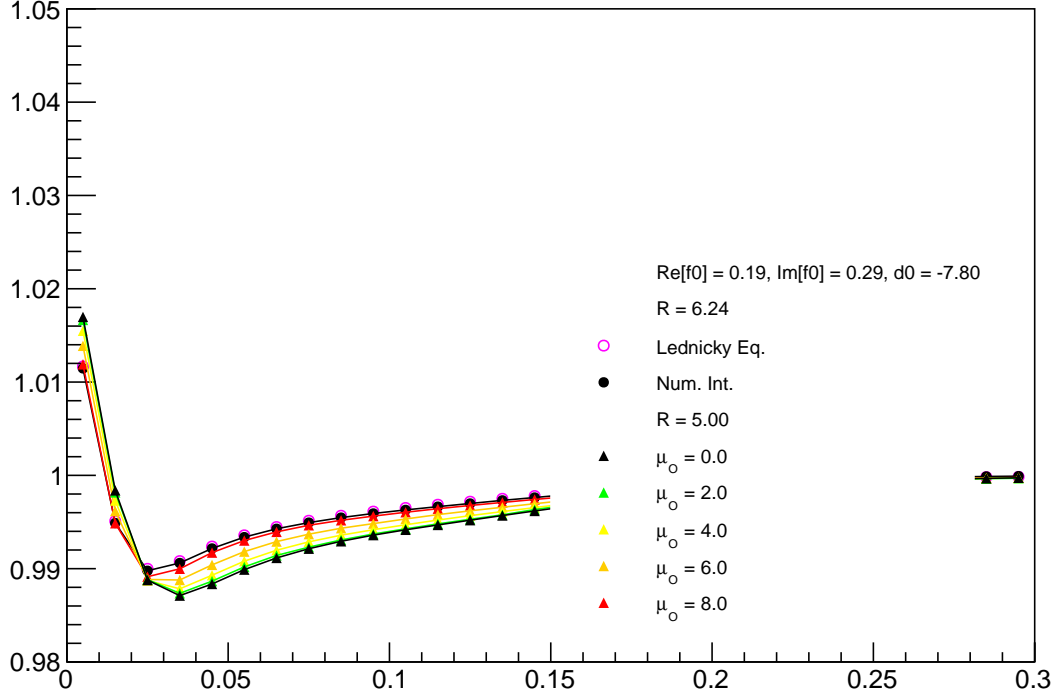


Fig. 38: Numerical integration of the Koonin-Pratt equation, allowing us to study the effect of a non-zero offset in the out direction, μ_{out} . We chose a parameter set to qualitatively match our ΛK^- data. The assumed scattering parameter set is printed in the top of the legend. All points assume $\mu_{\text{side}} = \mu_{\text{long}} = 0$ fm. The closed black circles and open magenta symbols assume $R_i = 6.24$ fm (where $i = \text{o,s,l}$) and $\mu_{\text{out}} = 0$ fm, while the triangle markers assume $R_i = 5$ fm with varying values of μ_{out} . The open magenta circles were obtained with the Lednický equation, all others were obtained with the numerical integration method. See text for more details.

942 this method, one can draw a wealth of information from just a few components of the decomposition.
 943 More specifically, the C_{00} component is similar to the 1D correlation functions typically studied, and
 944 probes the overall size of the source. The $\Re C_{11}$ component probes the asymmetry in the system; a
 945 non-zero value reveals the asymmetry.

946 In Fig. 39 we show results for the C_{00} and $\Re C_{11}$ components from the spherical decomposition of our
 947 ΛK^+ system in the 0-10% centrality bin (red circles). Results from a number of other components within
 948 the decomposition, as well as for our ΛK_S^0 and ΛK^- systems, are contained in App. B. Along with the
 949 experimental data in Fig. 39, we have also included results from THERMINATOR simulation for an
 950 impact parameter of $b = 2$ fm (gold stars). As THERMINATOR does not include any final state effects,
 951 we assumed scattering parameters $(\Re f_0, \Im f_0, d_0) = (-1.16, 0.51, 1.08)$ and weighted the numerator pairs
 952 with $|\Psi|^2$, as discussed previously in Sec. 5.5 (with regard to Fig. 29). Note, for the ΛK^+ system,
 953 THERMINATOR 2 predicts $\mu_{\text{out}} \approx 4$ fm, as shown in Fig. 40. As seen in the figures, the C_{00} signal is
 954 similar to that observed in our one-dimensional study. The $\Re C_{11}$ component shows a clear deviation from
 955 zero, and the negative value signifies that the Λ particles are, on average, emitted further out and/or earlier
 956 than the K mesons (in defining our pairs, we take the heavier Λ as our first particle, which is opposite
 957 the normal convention). Therefore, as expected, our single particle Λ and K sources are separated in
 958 space-time.

959 Fig. 40 shows a closer look at the THERMINATOR simulation, whose spherical harmonic decomposi-
 960 tion was shown along with the data in Fig. 39. The top left of Fig. 40a shows a fit to the one-dimensional

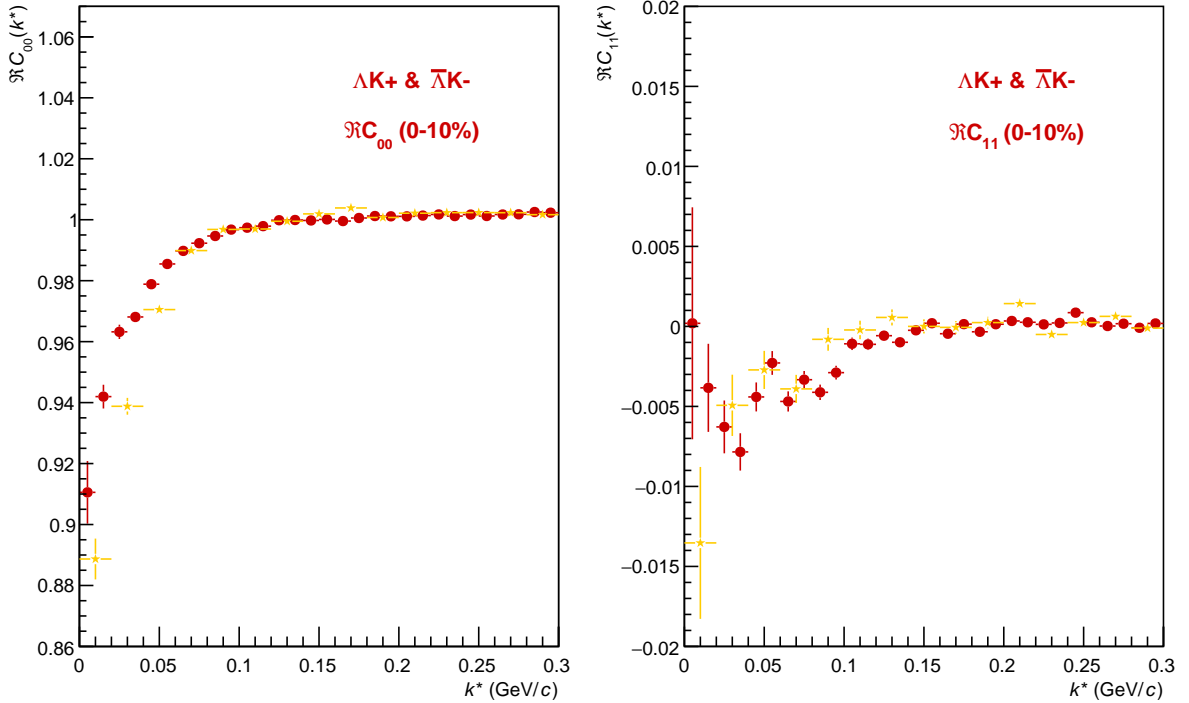
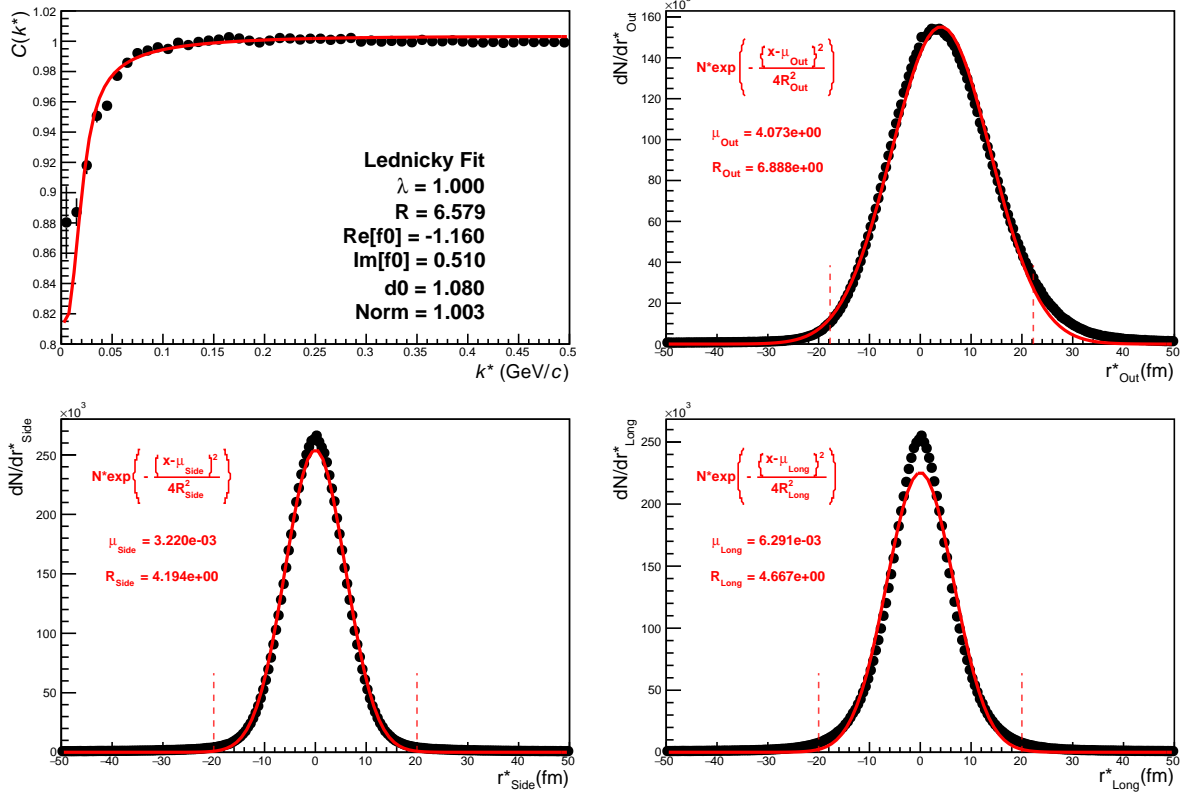


Fig. 39: C_{00} (left) and $\Re C_{11}$ (right) components of a spherical harmonic decomposition of the ΛK^+ correlation function for the 0-10% centrality bin. The C_{00} component is similar to the 1D correlation functions typically studied, and probes the overall size of the source. The $\Re C_{11}$ component probes the asymmetry in the system; a non-zero value reveals the asymmetry

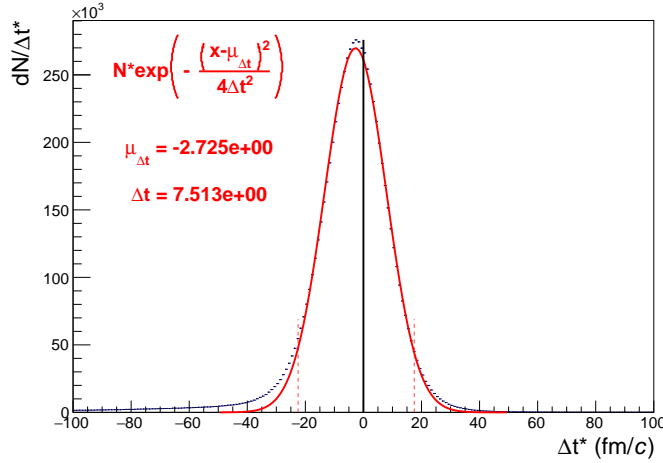
correlation function from THERMINATOR. The scattering parameters are known precisely here, as they served as the weights used in the simulation, and are kept constant in the fit. We are interested at looking at the extracted one-dimensional source size here, so the λ parameter is also fixed at unity. The other three plots in Fig. 40a show the source distribution in the out (top right), side (bottom left), and long (bottom right) directions (all in the PRF). The source distributions have all been fitted with a Gaussian form, the result of which is printed within the respective plots. One immediately sees a significant shift in the out direction, $\mu_{\text{out}} \approx 4$ fm, and negligible shift in the other two directions, $\mu_{\text{side}} \approx \mu_{\text{long}} \approx 0$ fm. The figure demonstrates that, within the THERMINATOR model, the Λ is, on average, emitted further out than its K partner. Finally, Fig. 40b shows the distribution of the relative time of emittance, again in the PRF. The figure shows that the Λ is, on average, emitted earlier than its K partner. These two results from THERMINATOR 2 are as expected.

We end this section with a brief look at how a spatial separation of the single particle sources affects the radii extracted from a femtoscopic analysis. To achieve this, we use THERMINATOR in a similar fashion as described above, but with one important difference. Instead of taking the source information from THERMINATOR, we draw the source from pre-determined Gaussian distributions. In all cases, we take $R_{\text{out}} = R_{\text{side}} = R_{\text{long}} = 5$ fm, and $\mu_{\text{side}} = \mu_{\text{long}} = 0$ fm. Figure 41 shows an example of results obtained from THERMINATOR following this procedure, where $\mu_{\text{out}} = 3$ fm.

In Figure 42, we show results for the case of $\mu_{\text{out}} = 1$ fm, $\mu_{\text{out}} = 3$ fm, and $\mu_{\text{out}} = 6$ fm. In this figure, we do not show the side and long distributions, as they appear identical to those shown in Fig. 41. The figure demonstrates that as the separation μ_{out} increases, so do the extracted femtoscopic radii. This is exactly as expected, and in agreement with our qualitative assessment of the curves generated by our numerical



(a) (Top Left) Simple fit on simulation from THERMINATOR 2. Generated source in the (Top Right) out, (Bottom Left) side, and (Bottom Right) long directions.



(b) Temporal characteristics of the source.

Fig. 40: Extracted radius when performing a simple fit on simulation from THERMINATOR 2, along with the spatio-temporal characteristics generated by the simulation.

982 Koonin-Pratt integrator described above.

983 **Comparing non-identical to identical particle result** Non-identical femtoscopy analyses are not so
 984 simply compared to identical particle studies. However, a method was presented in which the single
 985 particle source sizes can be extracted using three related femtoscopy measurements, which can then be
 986 related to the results from identical particle studies [8]. Extracting the single particle source size from
 987 an identical study simply amounts to dividing the extracted radii by $\sqrt{2}$. For non-identical studies, the

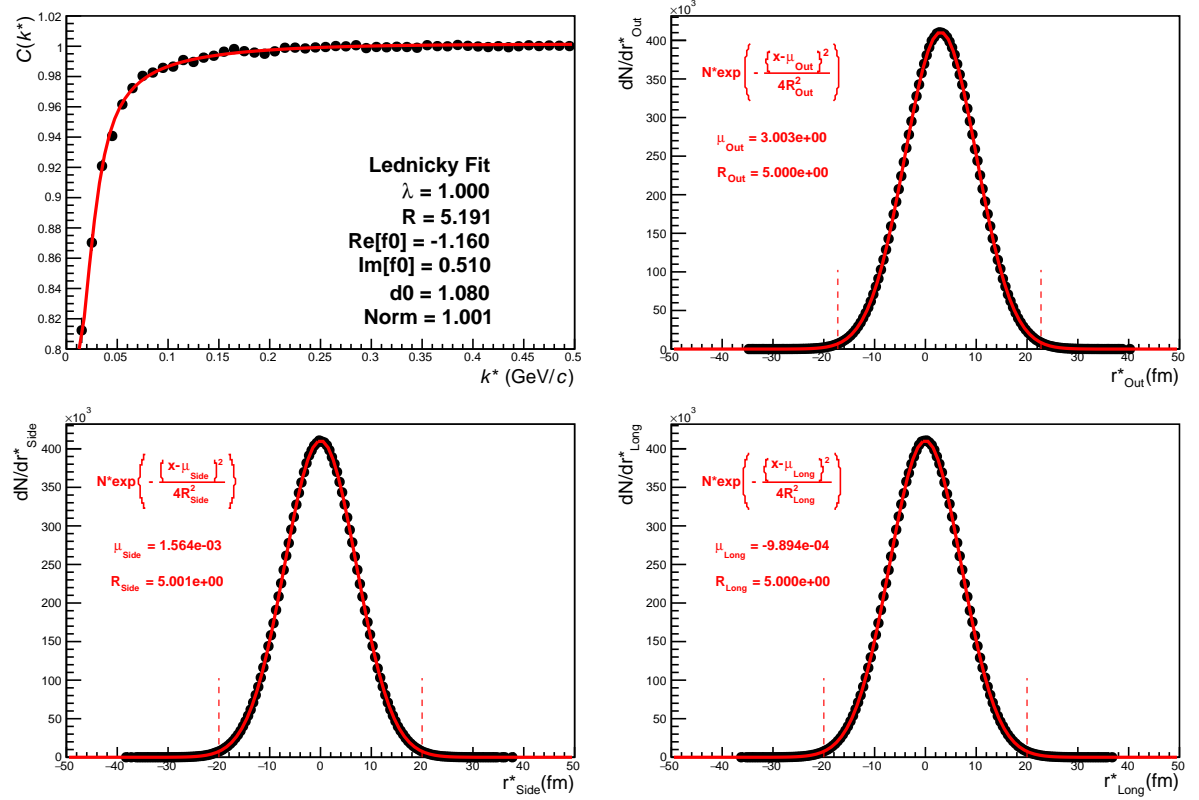


Fig. 41: THERMINATOR 2 simulation with artificial Gaussian source. The figure shows the extracted radius when performing a simple fit on simulation from THERMINATOR 2 (similar to Fig. 40a), except the space-time information provided by the simulation is ignored. Instead, the components of the spatial separation for each pair were drawn from Gaussian distributions, with $\sigma_{o,s,l}^2 = 5 \text{ fm}$, $\mu_{s,l} = 0 \text{ fm}$, and $\mu_o = 3 \text{ fm}$. The separation of emission in time was taken to be zero. (Top Left) Simple fit on simulation from THERMINATOR 2. Source in the (Top Right) out, (Bottom Left) side, and (Bottom Right) long directions.

988 procedure is not so simple. As introduced in Sec. 5.1, assuming the single particle sources are three
 989 dimensional Gaussians with offsets in the “out” direction, the pair source distribution is also a Gaussian
 990 with offset in the “out” direction. The form of the Gaussian is given in Eq. 15, and reproduced here for
 991 convenience.

$$S_{AB}(\mathbf{r}) \propto \exp\left(-\frac{[r_{out} - (\mu_{a,out} - \mu_{b,out})]^2}{2(R_{a,out}^2 + R_{b,out}^2)}\right) \times \dots \\ \times \exp\left(-\frac{r_{side}^2}{2(R_{a,side}^2 + R_{b,side}^2)}\right) \times \dots \\ \times \exp\left(-\frac{r_{long}^2}{2(R_{a,long}^2 + R_{b,long}^2)}\right) \quad (35)$$

992 which demonstrates $\mu_{ab,out} = \mu_{a,out} - \mu_{b,out}$, and $R_{ab,i}^2 = R_{a,i}^2 + R_{b,i}^2$. Unfortunately, with a single femto-
 993 scopic measurement, the two single particle source sizes cannot be extracted. However, in Ref. [8], the
 994 author demonstrated that using three related femtoscopic measurements, the single particle sizes can be
 995 extracted. However, this method does rely on including μ_{out} in the fit.

996 Performing measurements of the systems πK , πp and Kp permits one to extract the single particle π ,
 997 K , and p source sizes. In Ref. [8], the author assumed $R_{out} = R_{side} = \sigma_f$, $R_{long} = 1.3\sigma_f$ and $\mu_{side} =$
 998 $\mu_{long} = 0$. Furthermore, having reliable estimates of the scattering parameters for the systems, only two

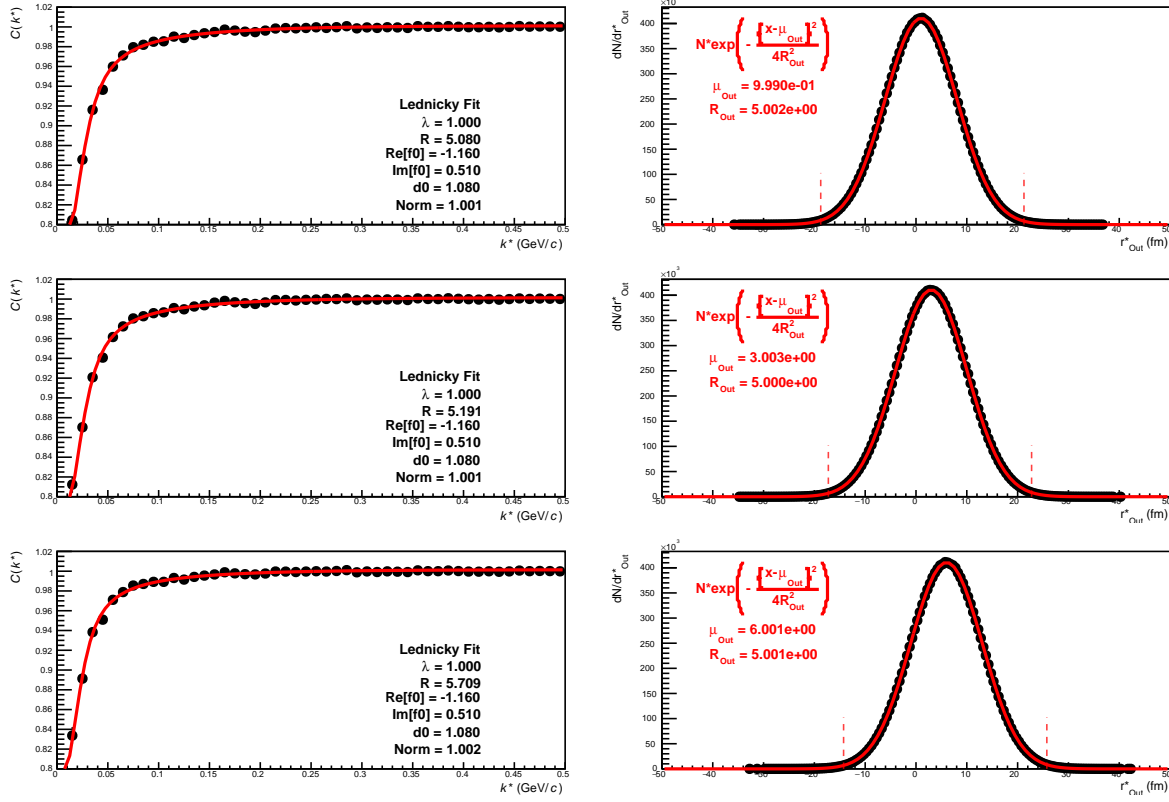


Fig. 42: Probing the effect of varying the source shift in the outward direction, μ_{Out} , within the THERMINATOR 2 framework. To achieve this, we formed particle pairs from the simulation, but altered their spatial characteristics by drawing the out, side, and long components from pre-determined Gaussian distributions. The plots on the left show fits resulting from the sources (in the out direction) shown on the right. The sources in the side and long directions are not shown, and are both Gaussians of width 5 fm centered at the origin for all cases. Moving from top to bottom, μ_{Out} increase from 0 to 6 fm, the effect of which clearly increases the effective radius extracted in the fit.

999 fit parameters, R_{out} and μ_{out} were left, and easily extracted. Given the fact that $R_{ab,i}^2 = R_{a,i}^2 + R_{b,i}^2$, for the
1000 three systems we therefore have

$$\begin{aligned}\sigma_f^{\pi K} &= \sqrt{\sigma_f^{\pi 2} + \sigma_f^{K 2}} \\ \sigma_f^{\pi p} &= \sqrt{\sigma_f^{\pi 2} + \sigma_f^{p 2}} \\ \sigma_f^{K p} &= \sqrt{\sigma_f^K 2 + \sigma_f^p 2}\end{aligned}\quad (36)$$

1001 These three equations can then be solved for the single particle source sizes

$$\begin{aligned}\sigma_f^\pi &= \sqrt{\left(\sigma_f^{\pi K 2} + \sigma_f^{\pi p 2} - \sigma_f^{K p 2}\right)/2} \\ \sigma_f^K &= \sqrt{\left(\sigma_f^{\pi K 2} - \sigma_f^{\pi p 2} + \sigma_f^{K p 2}\right)/2} \\ \sigma_f^p &= \sqrt{\left(-\sigma_f^{\pi K 2} + \sigma_f^{\pi p 2} + \sigma_f^{K p 2}\right)/2}\end{aligned}\quad (37)$$

1002 These extracted single particle source sizes can then be compared to those obtained using identical parti-
1003 cle femtoscopy to check for consistency. Unfortunately, with our analysis, we are unable to include μ_{out}

¹⁰⁰⁴ in our fit, and therefore are unable to utilize a similar type of solution.

1005 7.2 Results: ΞK^\pm

1006 The motivation for studying the $\Xi^- K^\pm$ system was to investigate the striking difference in the ΛK^+
 1007 and ΛK^- correlation functions, as shown explicitly in Fig. 43 (originally presented in Sec. 4.1, and
 1008 reproduced here for convenience). The underlying cause responsible for this interesting effect is still not
 1009 completely understood. Within the femtoscopy framework presented in Section ??, it is clear that there
 1010 are two important components affecting the femtoscopic signal: the pair emission source distribution,
 1011 and the interaction between the particles in the pairs of interest. We expect the pair source distribution
 1012 for ΛK^+ pairs to be similar to that of ΛK^- pairs, therefore, the difference in the femtoscopic signals must
 1013 be due to a difference in their interactions.

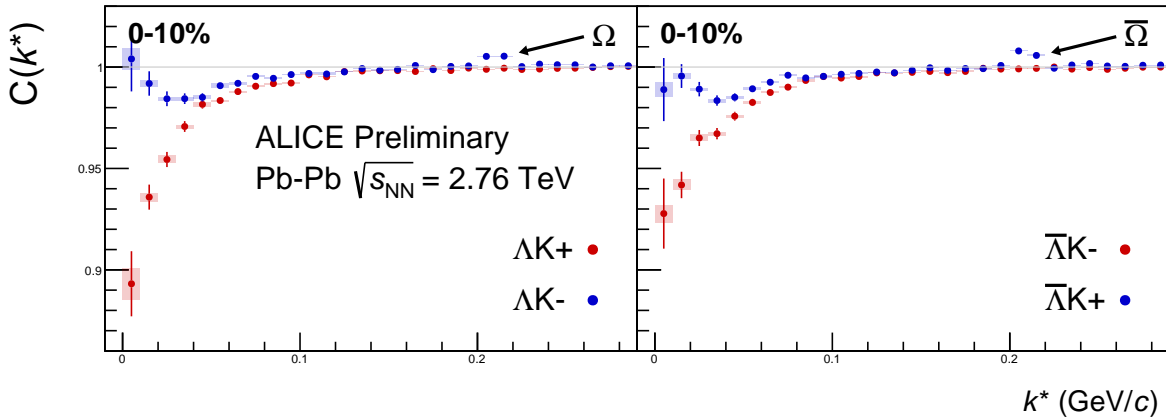


Fig. 43: Correlation Functions: ΛK^+ vs ΛK^- ($\bar{\Lambda} K^+$ vs $\bar{\Lambda} K^-$) for 0-10% centrality. The peak in ΛK^- ($\bar{\Lambda} K^+$) at $k^* \approx 0.2$ GeV/c is due to the Ω^- (and likely the $\Xi(1690)$ resonance, although to a much smaller extent). The lines represent the statistical errors, while boxes represent systematic errors.

1014 Obviously, we do understand that the observed difference in the femtoscopic signals is due to a difference
 1015 in the strong interaction in ΛK^+ pairs compared to that in ΛK^- pairs; our extracted scattering parameters
 1016 demonstrate that. The interesting question to ask is, why does the strong interaction differ so significantly
 1017 between the two? The result could suggest an effect arising from different quark-antiquark interactions
 1018 between the pairs, i.e. $s\bar{s}$ for ΛK^+ and $u\bar{u}$ in ΛK^- . This effect could also result from the difference in
 1019 net strangeness for each system, $S=0$ for ΛK^+ and $S=-2$ for ΛK^- . It is possible that a system with less
 1020 strangeness has more available channels into which it can decay, causing a scarcity of pairs, i.e. a greater
 1021 suppression, of the correlation function at low k^* . However, such an effect should manifest itself in the
 1022 imaginary component of the scattering length, $\Im f_0$, not the real component, $\Re f_0$.

1023 In any case, to help find an explanation for this result, it would be useful to study another system where
 1024 we might anticipate similar effects to be exhibited. The $\Xi^0 K^\pm$ system is an ideal candidate, as the quark
 1025 content of the Ξ^0 is uss . Therefore, studying $\Xi^0 K^\pm$ correlations would allow for the investigation of the
 1026 $s\bar{s}$ vs. $u\bar{u}$ quark-antiquark picture. However, the Ξ^0 unfortunately decays as $\Xi^0 \rightarrow \Lambda \pi^0$, and neutral pions
 1027 are difficult to detect. The next best option is the $\Xi^- K^\pm$ system, as the Ξ^- has quark content dss . In this
 1028 case, we are not able to explore the $s\bar{s}$ vs. $u\bar{u}$ picture, but we are able to investigate $s\bar{s}$ vs. the absence
 1029 of any $q\bar{q}$ interaction. Furthermore, although the net strangeness in the systems here are different than
 1030 those in the ΛK^\pm systems ($S=-1, -3$ instead of $S=0$), studying $\Xi^- K^\pm$ does allow us to explore the effect
 1031 of different net strangeness in similar systems. So, in comparing the $\Xi^- K^\pm$ and ΛK^\pm systems, $\Xi^- K^+$
 1032 ($S=-1$, $s\bar{s}$ picture) is analogous to ΛK^+ ($S=0$, $s\bar{s}$ picture), and $\Xi^- K^+$ ($S=-3$, absence of $q\bar{q}$ picture) is
 1033 analogous to ΛK^- ($S=-2$, $u\bar{u}$ picture).

1034 Figure 44 presents experimental data from our femtosopic analysis of $\Xi^- K^\pm$ pairs, along with the
 1035 conjugate systems. Even without any fits to the data, the fact that the $\Xi^- K^+$ data dips below unity (Fig.
 1036 44) is exciting, as this cannot occur purely from a Coulomb interaction. We hope that this dip signifies

1037 that we are able to peer through the overwhelming contribution from the Coulomb interaction to see the
 1038 effects arising from the strong interaction.

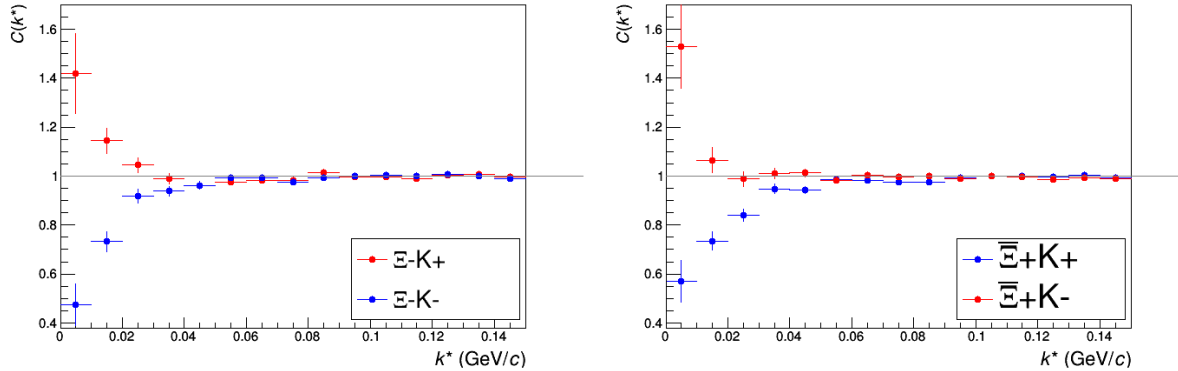


Fig. 44: ΞK^\pm Results for 0-10% Centrality. (Left) $\Xi^- K^+$ and $\Xi^- K^-$ (Right) $\Xi^+ K^+$ and $\Xi^+ K^-$

1039 Figure 45 demonstrates that the $\Xi^- K^+$ results cannot be described by solely the Coulomb interaction. In
 1040 this figure, we present the data along with a Coulomb-only band. The Coulomb-only band is spanned
 1041 by two Coulomb-only curves, whose parameters are given in the figure. The Coulomb-only curves were
 1042 generated using a technique identical to the generation of the fit function, described in Sec. 5.2, except,
 1043 of course, with the nuclear scattering parameters all set to zero. The Coulomb-only curves change
 1044 monotonically with varying λ or varying radius parameters, therefore, any curves built with parameter
 1045 sets intermediate to those use in the Coulomb-only band will be contained in the band.

1046 Including the strong interaction into the simulation can change, sometimes dramatically, the resulting
 1047 correlation function, as shown in Figure 46. In the figure, the solid line represents a Coulomb-only
 1048 curve, i.e. a simulated correlation function with the strong interaction turned off. The dashed lines
 1049 represent a full simulation, including both the strong and Coulomb interactions. The two dashed lines
 1050 differ only in the real part of the assumed scattering length: positive in Set 1, and negative in Set 2. In
 1051 the top figure, for the $\Xi^- K^+$ simulation, we see that parameter set 2, with a negative real part of the
 1052 scattering length, causes the simulated curve to dip below unity, as is seen in the data. This is significant
 1053 not only because a negative $\Re f_0$ matches the data better, but also because we extracted a negative value
 1054 of $\Re f_0$ in our ΛK^+ analysis. As state previously, if there is a parallel to be drawn between this analysis
 1055 and the ΛK^\pm analysis, we expect to see similar effects in the ΛK^+ system and the $\Xi^- K^+$ systems. So,
 1056 this simulation at least moves in the correct direction.

1057 We were asked to perform a global Coulomb-only fit to the data, to ensure that the system truly could not
 1058 be described simply by the Coulomb interaction. In other words, in the fit, the strong force was turned
 1059 off, and the $\Xi^- K^+$, $\Xi^+ K^-$, $\Xi^- K^-$, $\Xi^+ K^+$ systems all share one single radius parameter, while the pair
 1060 and conjugate pair systems share a λ parameter. The results of this fit are shown in Figures 47 and 48. In
 1061 Fig. 47, there was a lower limit of 0.1 fm placed on the radius parameter, and the radius parameter was
 1062 initialized to 3 fm. As is shown in the results, the radius parameter reached this unrealistic lower bound
 1063 of 0.1 fm. In Fig. 48, the parameters were all unbound, and the radius parameter was initialized to 10
 1064 fm. In this case, the radius parameters remains high, and ends at an unrealistic value of 10.84 fm. In both
 1065 cases, the λ parameters are too low. From these figures, we conclude that a global Coulomb-only fit is
 1066 not suitable for the data.

1067 Although the global Coulomb-only fit failed, it is possible that a Coulomb-only fit performed on $\Xi^- K^+$
 1068 and $\Xi^+ K^-$ separately from $\Xi^- K^-$ and $\Xi^+ K^+$ could be suitable. The result of such fits are shown in
 1069 Figure 49. Figure 49a, shows that the fit is not able to describe the dip in the $\Xi^- K^+$ data below unity.
 1070 Of course, this is obviously true for an attractive Coulomb-only fit. The radius parameter of 8.43 fm

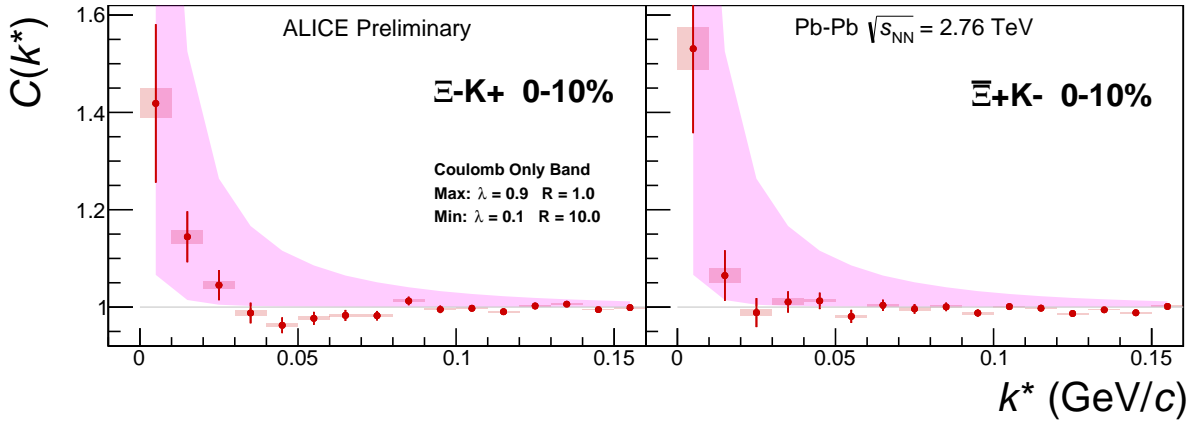
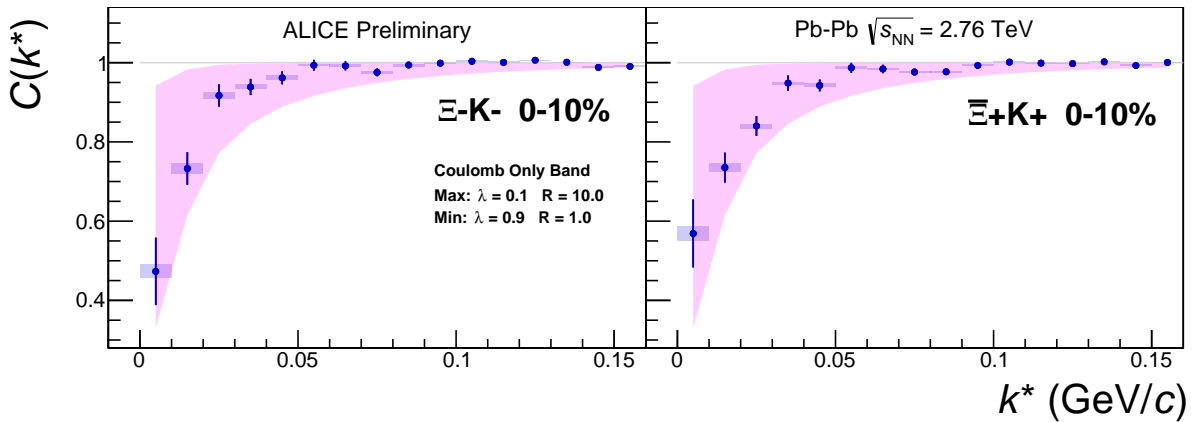
(a) (Left) ΞK^+ and (Right) ΞK^- (b) (Left) ΞK^- and (Right) ΞK^+

Fig. 45: ΞK^\pm data with Coulomb-only bands for the 0-10% centrality bin. The Coulomb-only bands span two sets of Coulomb-only curves: (1) $\lambda = 0.9$, R = 1.0 fm and (2) $\lambda = 0.1$, R = 10.0 fm.

1071 extracted from this fit is probably too large to describe reality. In Figure 49b shows the Coulomb-only fit
 1072 can described the $\Xi\text{-K}^-$ data reasonable well. When considering Fig. 43, this is not terribly surprising,
 1073 as the strong effect in the ΛK^- (analogous to $\Xi\text{-K}^-$) is much weaker than that in the ΛK^+ system
 1074 (analogous to $\Xi\text{-K}^+$). In any case, we would expect for the $\Xi\text{-K}^+$ and $\Xi\text{-K}^-$ systems to be consistent
 1075 with each other in their radii.

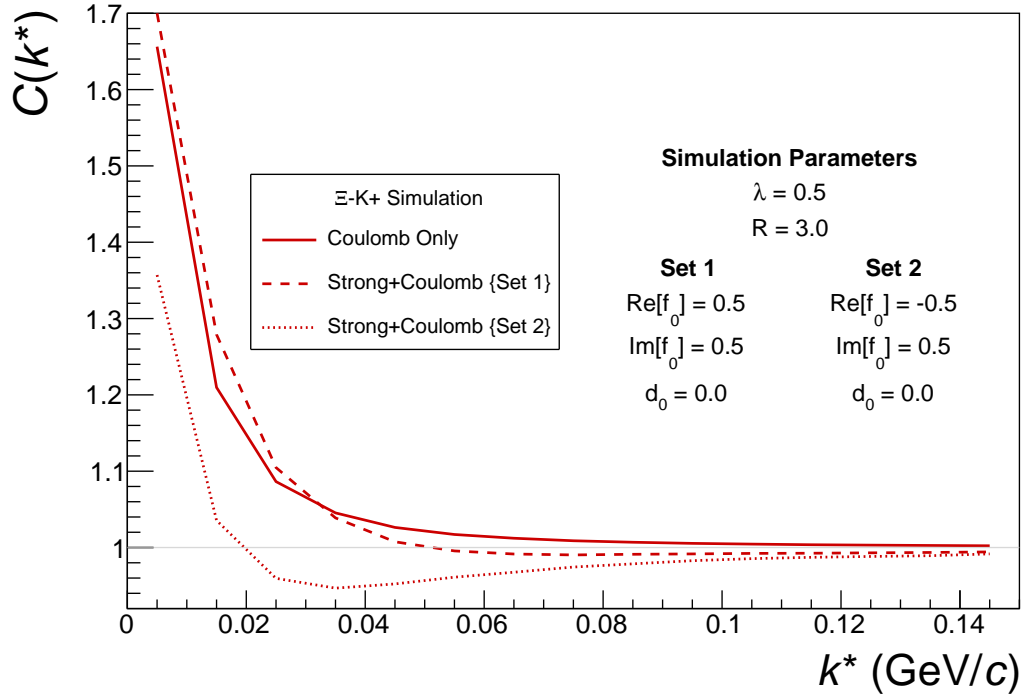
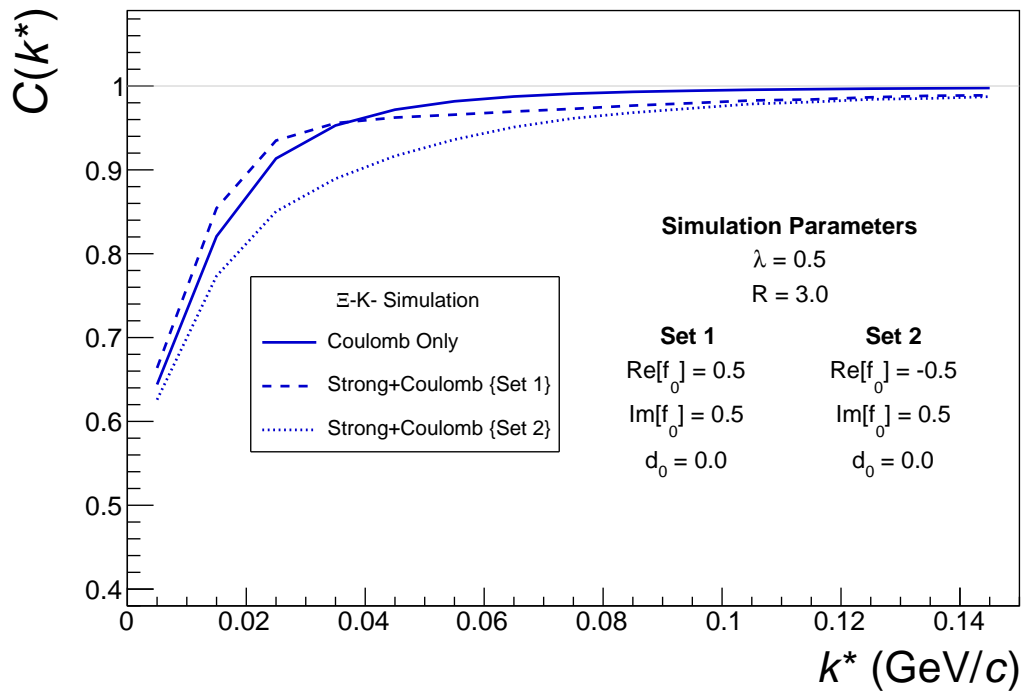
(a) ΞK^+ and $\bar{\Xi} K^-$ simulation(b) ΞK^- and $\bar{\Xi} K^+$ simulation

Fig. 46: Effect on the Coulomb-only curve of including the strong interaction for ΞK^\pm systems. The solid line represents a Coulomb-only curve. The dashed lines represent a full simulation, including both the strong and Coulomb interactions. The two dashed lines differ only in the real part of the assumed scattering length: positive in Set 1, and negative in Set 2.

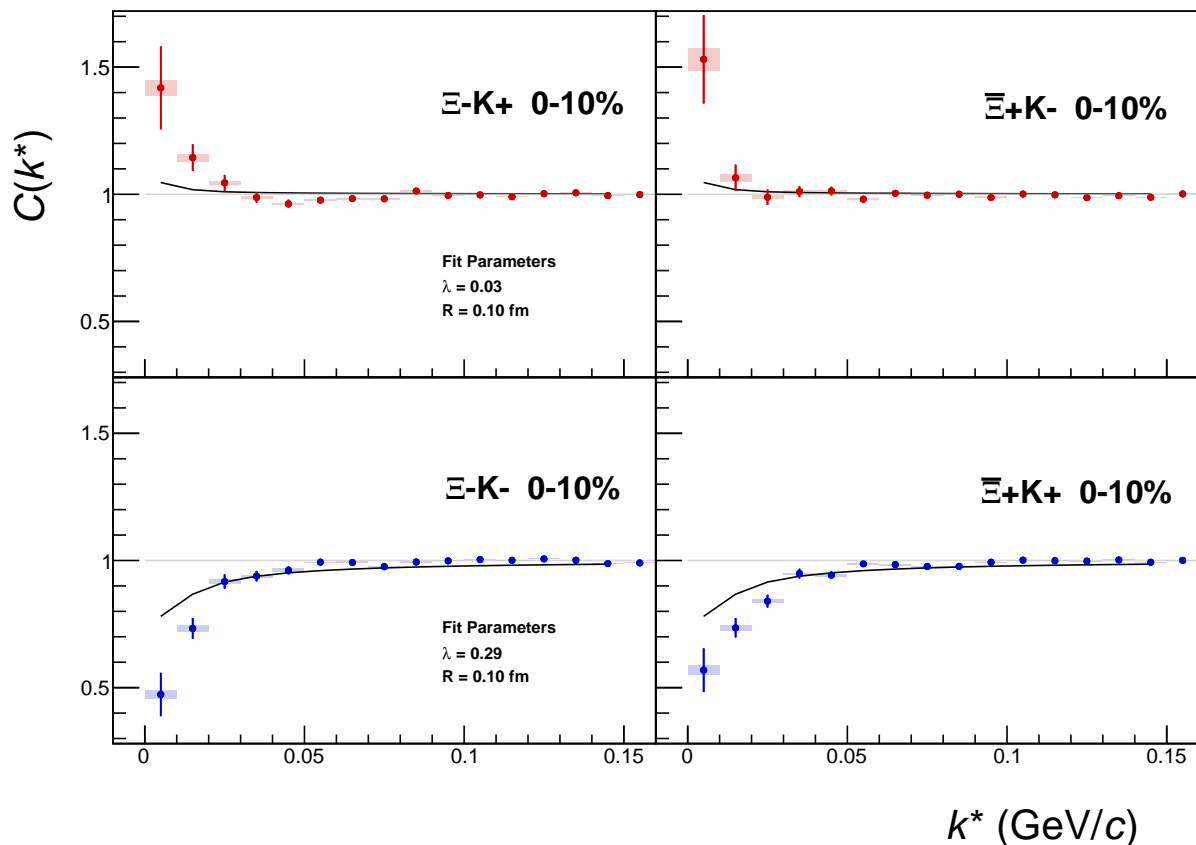


Fig. 47: ΞK^\pm Global Coulomb-only fit (Set 1) for 0-10% centrality. In this fit, there was a lower limit of 0.1 fm placed on the radius parameter, and the radius parameter was initialized to 3 fm.

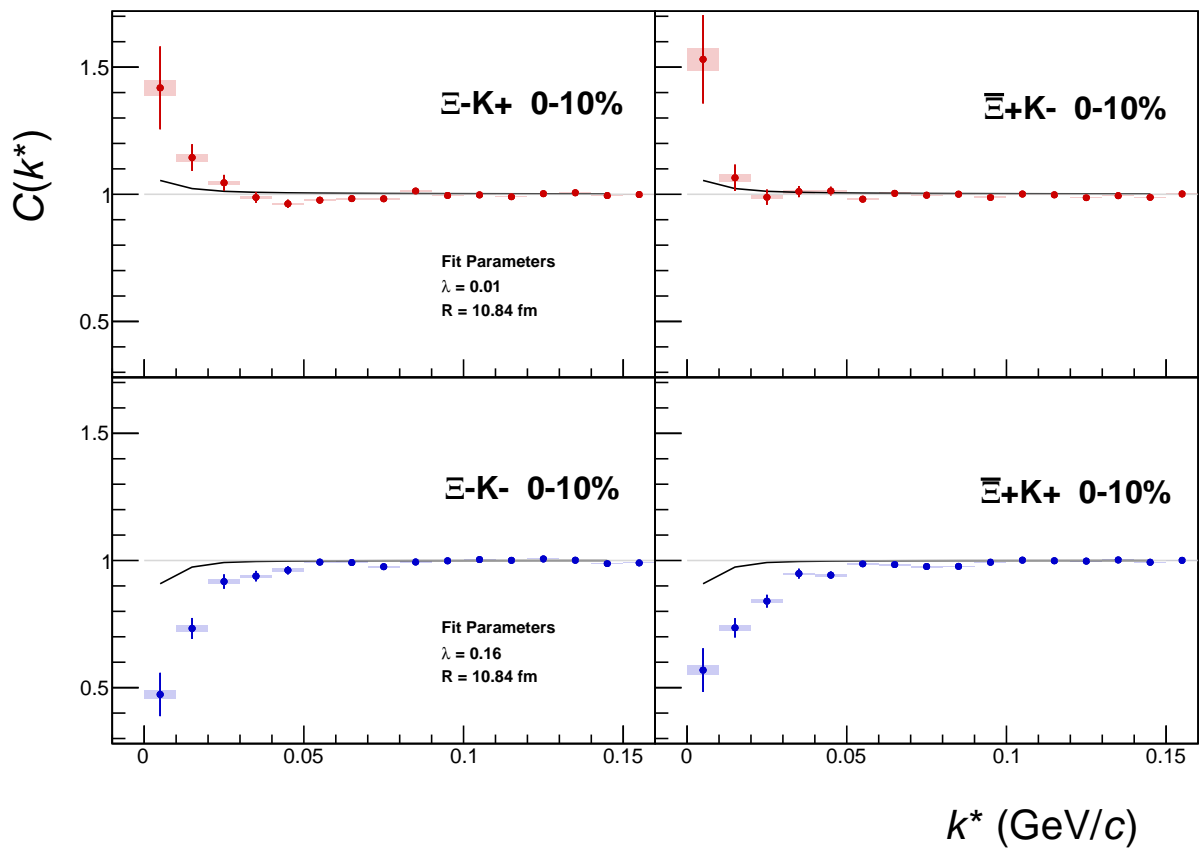
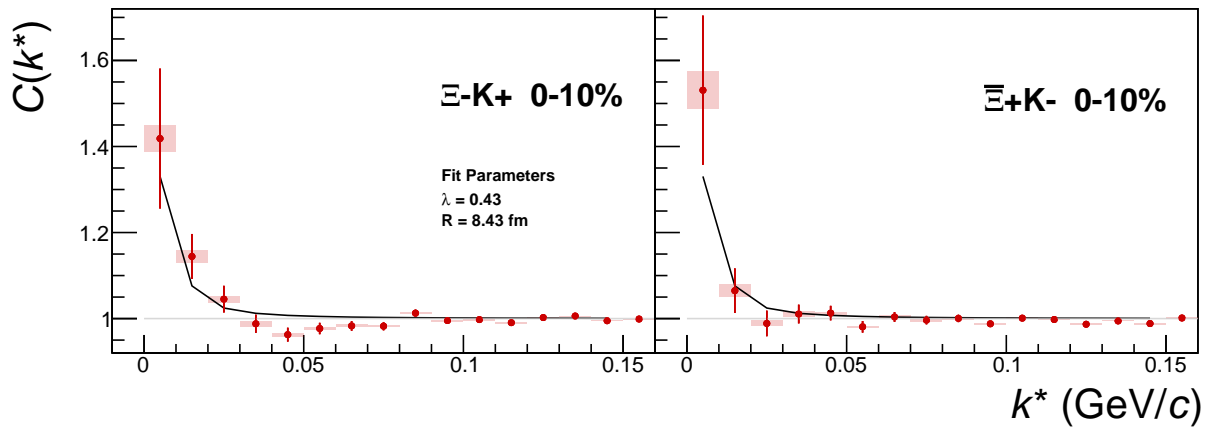
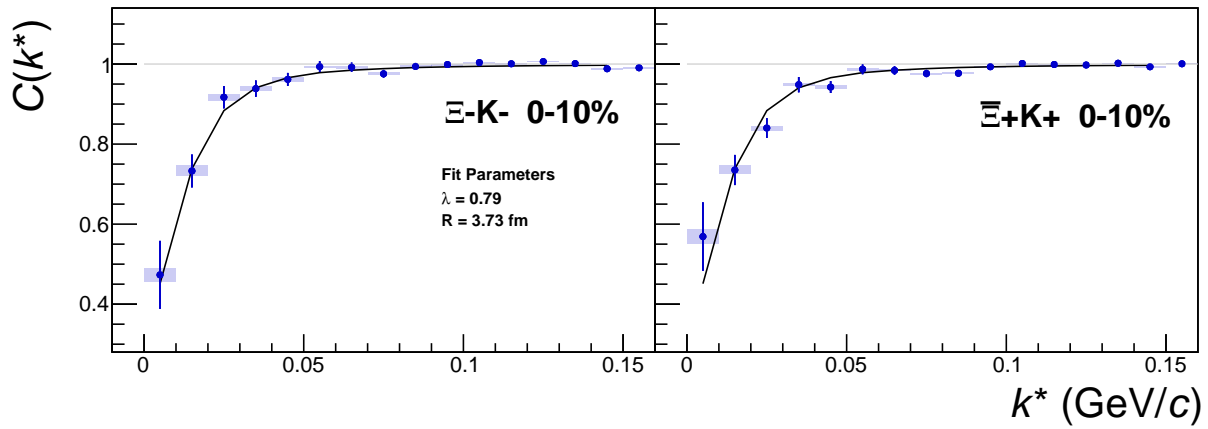


Fig. 48: ΞK^\pm Global Coulomb-only fit (Set 2) for 0-10% centrality. In this fit, the parameters were all unbounded, and the radius parameter was initialized to 10 fm.

(a) $\Xi^- \text{K}^+$ Coulomb-only fit for 0-10% centrality(b) $\Xi^- \text{K}^-$ Coulomb-only fit for 0-10% centrality**Fig. 49:** $\Xi^- \text{K}^\pm$ Coulomb-only fit, with $\Xi^- \text{K}^+$ fit separately from $\Xi^- \text{K}^-$

1076 **A Results: ΛK_S^0 and ΛK^\pm (Additional Figures)**

1077 This appendix presents fit results obtained using different methods and variations of our fit procedure.
 1078 The purpose here is to offer a more in depth and transparent look at how the various assumptions made
 1079 for our final fit procedure affect our results. For all cases, the interesting result remains of the ΛK^+
 1080 system exhibiting a negative $\Re f_0$, the ΛK^- positive, and the ΛK_S^0 system somewhere between.

1081 For our final results, we have chosen to include three residual contributors, as this best matches the
 1082 experimental situation. These three contributors include: $(\Sigma^0 K, \Xi^0 K, \Xi^- K) \rightarrow \Lambda K$. Moving to ten con-
 1083 tributors, we additionally include feed-down from $(\Sigma^{*(+,-,0)} K^{*0}, \Lambda K^{*0}, \Sigma^0 K^{*0}, \Xi^0 K^{*0}, \Xi^- K^{*0}) \rightarrow \Lambda K$.
 1084 As stated in Sec. 5.4, femtoscopic analyses are sensitive to the pair emission structure at kinetic freeze-
 1085 out, therefore any particle born from a resonance decaying before last rescattering is seen as primary.
 1086 The Σ^* and K^* resonances have proper decay lengths $c\tau \approx 5$ fm and 4 fm, respectively. Although some
 1087 of these will decay after, we expect that most will decay before kinetic freeze-out. Therefore, it is best
 1088 to treat Λ and K particles originating from these resonances as primary, and therefore include only three
 1089 residual contributors in our fit procedure. However, it is still interesting to observe how these additional
 1090 sources of residuals would affect our fit results, as the actual situation lies somewhere between the two
 1091 cases (although, weighted much more towards the three residuals case). For a more precise treatment
 1092 (not warranted here, when considering all of the approximations in the measurement), one should esti-
 1093 mate the number of Σ^* and K^* resonances decaying after kinetic freeze-out, and use this information to
 1094 adjust the λ parameters.

1095 In Appendix A.1 we present summary plots demonstrating the effect on the extracted fit parameter sets
 1096 of utilizing the different fit techniques. The comparisons include the effect of using different numbers of
 1097 residual contributors, fixing the overall λ_{Fit} parameter compared to allowing it to be free, fitting a cor-
 1098 relation function built with the Stavinskiy method compared to the normal construction method, sharing
 1099 radii among all ΛK systems compared to sharing radii between only the ΛK^\pm systems, and using the
 1100 experimental $\Xi^- K^\pm$ data compared to modeling it with a Coulomb-only curve for use in the residuals
 1101 treatment.

1102 The final three subsections include a more thorough look into utilizing three (App. A.2), ten (App. A.3),
 1103 and no (App. A.4) residual contributors in the fit routine. These subsections match closely the structure
 1104 of Sec. 7.1, where we presented the final results for our ΛK study. Each begins with a summary plot
 1105 compactly showing the extracted fit parameters, and each contains figures showing the fit plotted on top
 1106 of the experimental data. Different from Sec. 7.1, the correlations are shown out to ~ 1 GeV/c (instead
 1107 of ~ 0.3 GeV/c), to show both the signal region and the non-femtoscopic background. Furthermore,
 1108 Appendices A.2 and A.3 contain figures showing the final fit with the components describing the different
 1109 residual contributions, on top of the experimental data.

1110 As with the results presented in Sec. 7.1, unless otherwise noted, the following hold true: All correlation
 1111 functions were normalized in the range $0.32 < k^* < 0.40$ GeV/c, and fit in the range $0.0 < k^* < 0.30$
 1112 GeV/c. For the ΛK^- and $\bar{\Lambda} K^+$ analyses, the region $0.19 < k^* < 0.23$ GeV/c was excluded from the fit to
 1113 exclude the bump caused by the Ω^- resonance. The non-femtoscopic backgrounds for the ΛK^+ and ΛK^-
 1114 systems were modeled by a (6th-order polynomial fit to THERMINATOR simulation, while those for the
 1115 ΛK_S^0 were fit with a simple linear form. All analyses were fit simultaneously across all centralities, with
 1116 a single radius and normalization λ_{Fit} parameter for each centrality bin. Scattering parameters ($\Re f_0$,
 1117 $\Im f_0$, d_0) were shared between pair-conjugate systems, but assumed unique between the different ΛK
 1118 charge combinations (i.e. a parameter set describing the ΛK^+ & $\bar{\Lambda} K^-$ system, a second set describing
 1119 the ΛK^- & $\bar{\Lambda} K^+$ system, and a third for the ΛK_S^0 & $\bar{\Lambda} K_S^0$ system). Each correlation function received
 1120 a unique normalization parameter. The fits were corrected for finite momentum resolution effects, non-
 1121 femtoscopic backgrounds, and residual correlations resulting from the feed-down from resonances. Lines
 1122 and boxes on the experimental data represent statistical and systematic errors, respectively.

In the figures showing experimental correlation functions with fits, the black solid curve represents the primary (ΛK) correlation's contribution to the fit. The green line shows the fit to the non-flat background. The purple points show the fit after all residual contributions have been included, and momentum resolution and non-flat background corrections have been applied. The extracted fit values with uncertainties are printed as (fit value) \pm (statistical uncertainty) \pm (systematic uncertainty).

A.1 Fit Method Comparisons

The figures in this appendix show comparisons of extracted fit parameters obtained using different fit techniques. Fig. A.1 shows a comparison of results obtained using three, ten, and no residual contributors. In Fig. A.2, we demonstrate the effect of fixing the overall λ_{Fit} parameter compared to allowing it to be free (see Eq. 28 in Sec. 5.4). Fig. A.3 compares our normal fit results to those obtained when the correlation functions are built using the Stavinskiy method (see Sec. 4.2). Fig. A.4 shows the difference between sharing radii among all ΛK systems versus only sharing radii between the ΛK^\pm systems. Finally, Fig. A.5 shows the effect of using the experimental $\Xi^- K^\pm$ data compared to modeling it with a Coulomb-only curve for use in the residuals treatment (see Sec. 5.4).

All of the figures follow the same four-panel structure: [Top Left]: $\Im f_0$ vs. $\Re f_0$, together with d_0 to the right. [Top Right (Bottom Left, Bottom Right)]: λ vs. Radius for the 0-10% (10-30%, 30-50%) bin. The ΛK^+ system is always presented with red markers, the ΛK^- with blue, and the ΛK_S^0 with black. In the case of all ΛK analyses sharing radii, the markers are gold. In the case of only the ΛK^\pm analyses sharing radii, the markers are magenta. The square symbols in the first column of the legends are to signify the color scheme. The black symbols in the second column of the legend describe the fit procedure used.

To better explain the description in the legends, take Fig. A.1 as an example. The square symbols in the first column of the top left figure indicate that the ΛK^+ scattering parameters are shown in red, the ΛK^- in blue, and the ΛK_S^0 in black. The symbols in the second column of the top left figure indicate that the case of three residual contributors is shown with closed circles, ten residual contributors with open crosses, and no residuals with open triangles. For the λ vs. radii plots, the square symbol describing the color scheme in the first column of the top right figure shows that all ΛK analyses share common radii and are shown with gold markers.

Fig. A.4 is a bit more involved example, in terms of the markers, so it is worthwhile to explain as a second example. The square symbols in the first column of the top left figure indicate that the ΛK^+ scattering parameters are shown in red, the ΛK^- in blue, and the ΛK_S^0 in black. The symbols in the second column of the top left figure indicate that the case where all ΛK analyses share common radii is shown with closed circles, the case of only ΛK^\pm analyses sharing radii is shown with open crosses, and the ΛK_S^0 system being fit alone is shown with open triangles. For the λ vs. radii plots, the square symbols describing the color scheme in the first column of the top right figure show that the case where all ΛK analyses share common radii is drawn with gold (in addition to being closed circles, as just described) markers, only ΛK^\pm analyses sharing radii is shown with magenta (in addition to open crosses, as just described) markers, and the ΛK_S^0 system being fit alone is shown with black (in addition to open triangles, as just described) markers.

Fig. A.1 shows a comparison of results obtained using three, ten, and no residual contributors. A more detailed look of the fit with the experimental data can be found in Appendices A.2 - A.4. As shown, the scattering parameters vary significantly between the different cases. For the case of no residual contributors, we would expect the λ_{Fit} parameters to be closer to $\lambda_{\text{Fit}} \sim 0.5$, when considering the value extracted for primary pairs using simulation in Table 6. For the case of 10 residual contributors, the figure shows the magnitude of the scattering parameters tends to increase, as do the λ_{Fit} parameters. The improper treatment of the residuals places less emphasis on the primary interaction, as conveyed through the relative strength of the λ_{Fit} parameters between the three and ten residuals case, presented in Tab. 6. More emphasis is placed on the residual contributors, whose signal is effectively flattened after being run

through the appropriate transform matrices (as shown in Figs. 24 and 25 of Sec. 5.4). This leads to a lot of mostly flat contributions, as shown e.g. in Fig. A.17 in App. A.3. These two effects could account for the (mostly) larger in magnitude scattering parameters and λ_{Fit} parameters extracted when assuming 10 residual contributors.

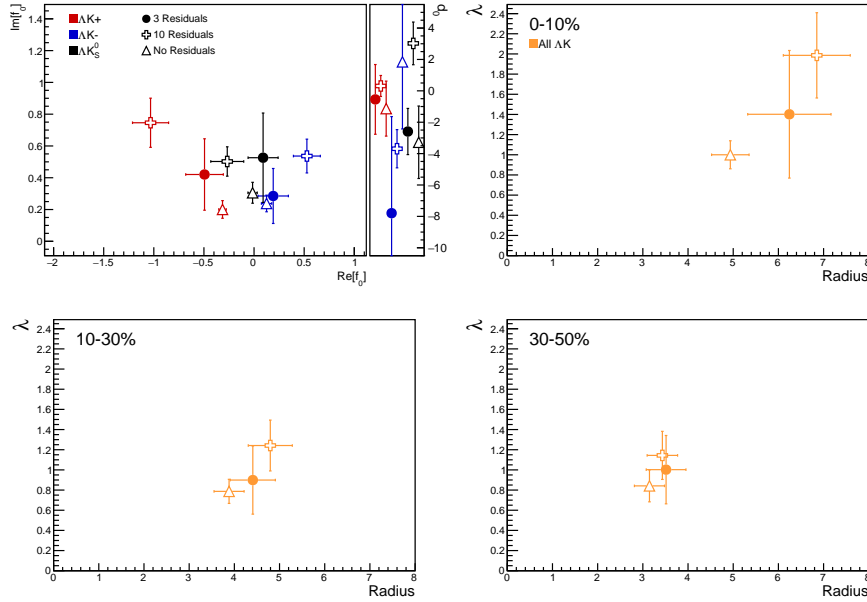


Fig. A.1: Results shown for the case of 3 (closer, circles), 10 (open, crosses), and no (open, triangles) residual contributors included in the fit. See text at beginning of section for color scheme information.

In Fig. A.2 we demonstrate the effect of fixing the overall λ_{Fit} parameter compared to allowing it to be free (see Eq. 28 in Sec. 5.4). As shown, the extracted scattering parameters are mostly unaffected by this choice. The radii behave as expected, when considering the λ_{Fit} and R parameters are strongly correlated. For instance, forcing λ_{Fit} to decrease, as in the 0-10% centrality bin shown in the top right of the figure, causes the fit radius to also decrease.

Fig. A.3 compares our normal fit results to those obtained when the correlation functions are built using the Stavinskiy method (see Sec. 4.2). As shown in the figure, with the exception of the d_0 parameters (which are difficult for us to resolve experimentally), the results from the two methods are within errors of each other. As implemented in this analysis, the Stavinskiy method does a good job of reducing the non-femtoscopic background, but does not completely eliminate it. Nonetheless, it is a simple and elegant method, and should be investigated further in the future.

Fig. A.4 shows the different between sharing radii among all ΛK systems versus only sharing radii between the ΛK^\pm systems. As shown in the figure, the ΛK^\pm systems give consistent results whether or not the ΛK_S^0 system is included in the fit. The ΛK_S^0 system, however, gives significantly different results when fit by itself. The ΛK_S^0 system suffers the most from low statistics, and is the most difficult to fit (for instance, when fit by itself, the λ_{Fit} parameter has to be limited between [0.6, 1.1] to give realistic results). As shown, when fit alone, the ΛK_S^0 fit settles on much smaller radii compared to the ΛK^\pm systems. As we expect the ΛK_S^0 system to share similar radii with the ΛK^\pm systems, we chose to join the three together to combat the low statistics available to the ΛK_S^0 . The purpose of this figure is mainly to demonstrate how the inclusion of the ΛK_S^0 affects the ΛK^\pm results, not the other way around.

Finally, Fig. A.5 shows the effect of using the experimental $\Xi^- K^\pm$ data compared to modeling it with a Coulomb-only curve for use in the residuals treatment (see Sec. 5.4). As shown, the results are consistent. The use of a the experimental data is preferable in that no assumption need to be made about the parent

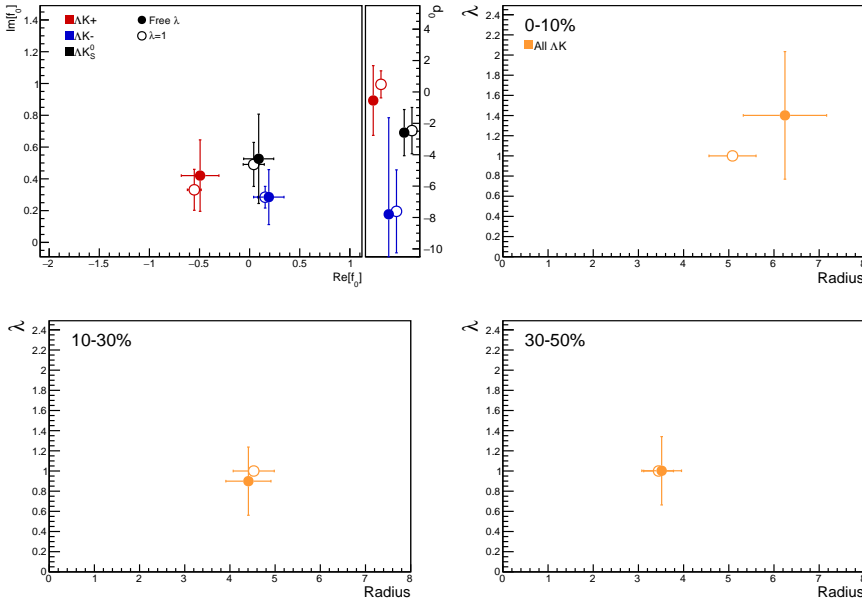


Fig. A.2: Results shown for λ_{Fit} parameters left free (closed, circles) and fixed to 1 (open, circles). See text at beginning of section for color scheme information and Eq. 28 in Sec. 5.4 for more information on the λ_{Fit} parameter.

system's correlation function. However, the low statistics of the parent $\Xi^- K^\pm$ data (especially in the 30-50% centrality bin) could be reason to instead use the Coulomb-only curve. In our description, we choose to use the experimental data, although, as shown in the figure, the choice does not matter much.

1200 A.2 3 Residual Contributors Included in Fit

This section presents our final results, for which three residual contributors were assumed. These three contributors include: $(\Sigma^0 K, \Xi^0 K, \Xi^- K) \rightarrow \Lambda K$. The figures presented do contain supplemental information to that presented in Sec. 7.1, but are here largely for convenience in comparing to the cases of including 10 (App. A.3) and no (App. A.4) residual contributors.

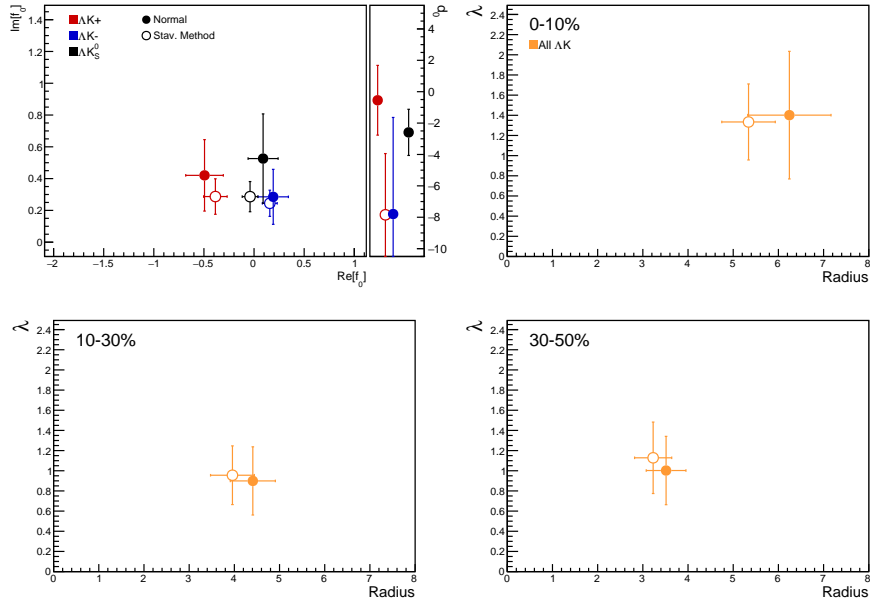


Fig. A.3: Results shown for normal correlation function construction (closed, circles) and when built using the Stavinskiy method (open, circles). See text at beginning of section for color scheme information and Sec. 4.2 for more information on the Stavinskiy method.

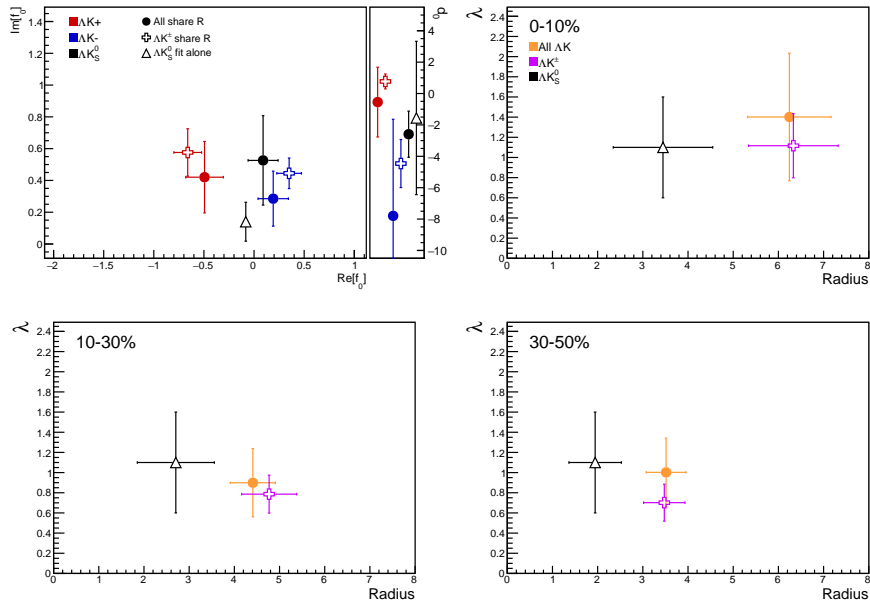


Fig. A.4: Results shown for the case of all ΛK analyses sharing radii (closed, circles) and only the ΛK^\pm analyses sharing radii (open, crossed), with the ΛK_S^0 system fit separately (open, triangles). See text at beginning of section for color scheme information.

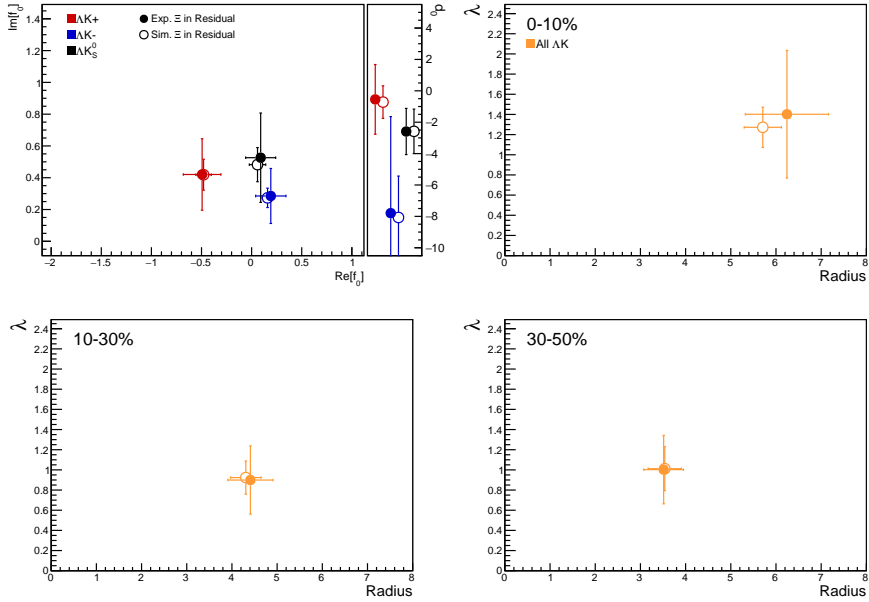


Fig. A.5: Results shown when using experimental Ξ^-K^\pm data (closed, circles) and when simulating the Ξ^-K^\pm correlation function with a Coulomb-only curve (open, circles) for use in the treatment of the residual. See text at beginning of section for color scheme information, and Sec. 5.4 for more information on the Ξ^-K^\pm simulation.

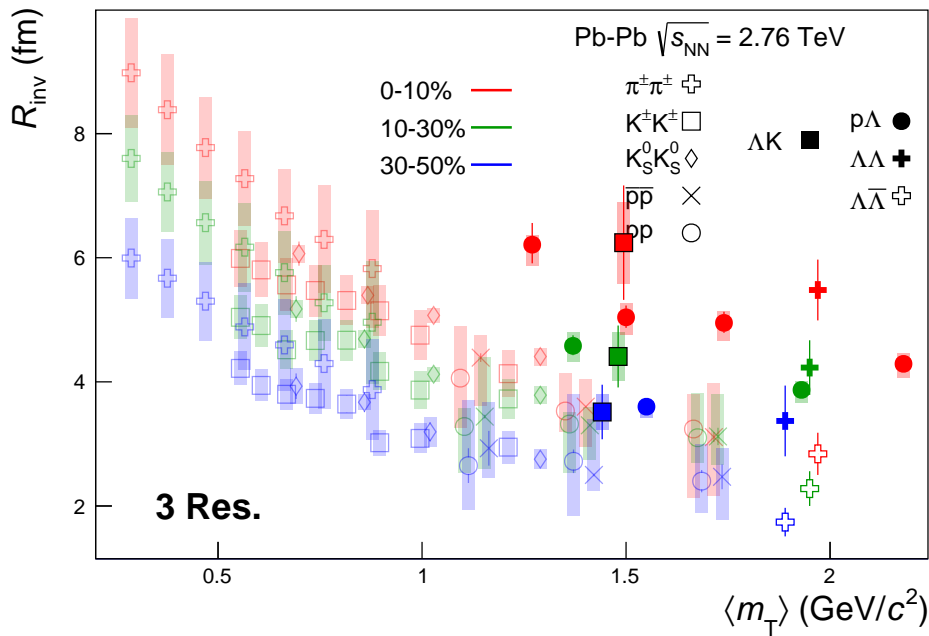


Fig. A.6: 3 residual correlations in ΛK fits. Extracted fit R_{inv} parameters as a function of pair transverse mass (m_T) for various pair systems over several centralities. The ALICE published data [13] are shown with transparent, open symbols. The new ΛK results are shown with opaque, filled symbols. The m_T value for the ΛK system is an average of those for the ΛK^+ , $\bar{\Lambda} K^-$, and ΛK_0^0 systems.

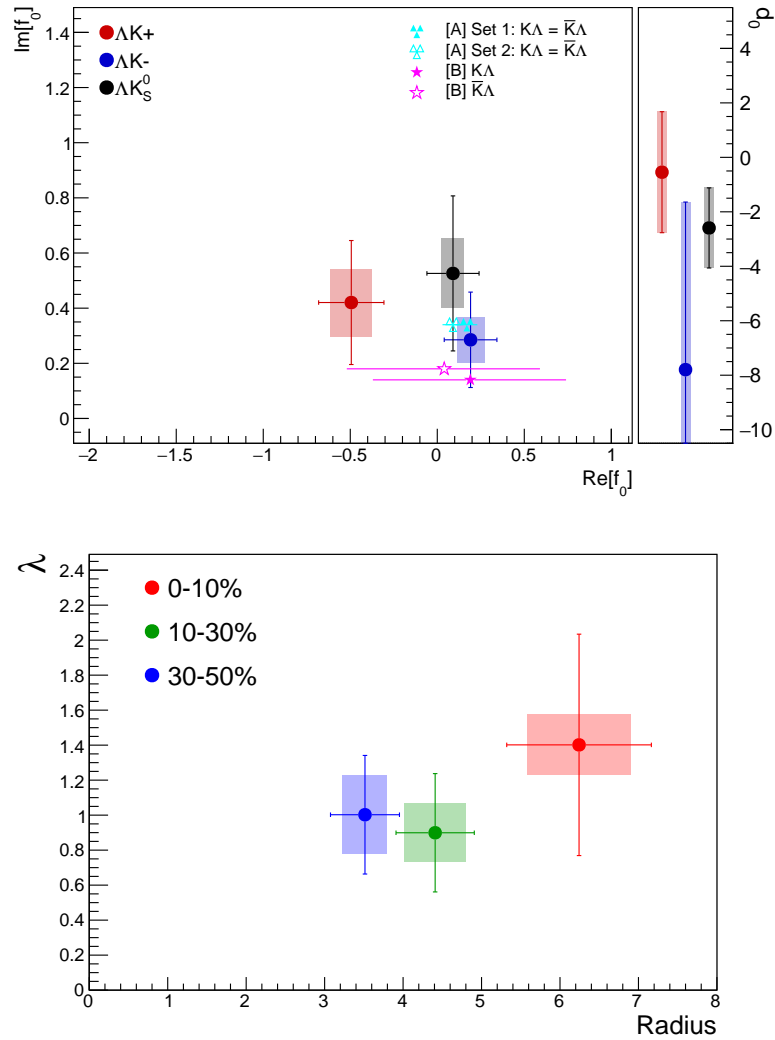


Fig. A.7: Extracted fit parameters for the case of 3 residual contributors for all of our ΛK systems. [Top]: $\Im f_0$ vs. $\Re f_0$, together with d_0 to the right. [Bottom]: λ vs. Radius for the 0-10% (blue), 10-30% (green), and 30-50% (red) centrality bins. In the fit, all ΛK systems share common radii. The color scheme used in the panel are to be consistent with those in Fig. A.6. The cyan ([A] = Ref. [14]) and magenta ([B] = Ref. [15]) points show theoretical predictions made using chiral perturbation theory.

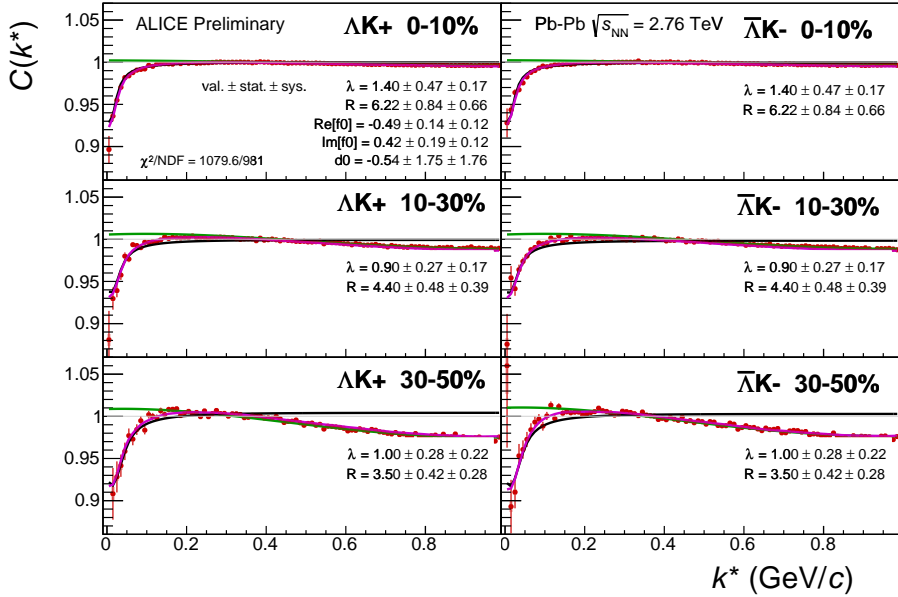


Fig. A.8: Fit results, with 3 residual correlations included, for the ΛK^+ and $\bar{\Lambda} K^-$ data. The ΛK^+ data is shown in the left column, the $\bar{\Lambda} K^-$ in the right, and the rows differentiate the different centrality bins (0-10% in the top, 10-30% in the middle, and 30-50% in the bottom).

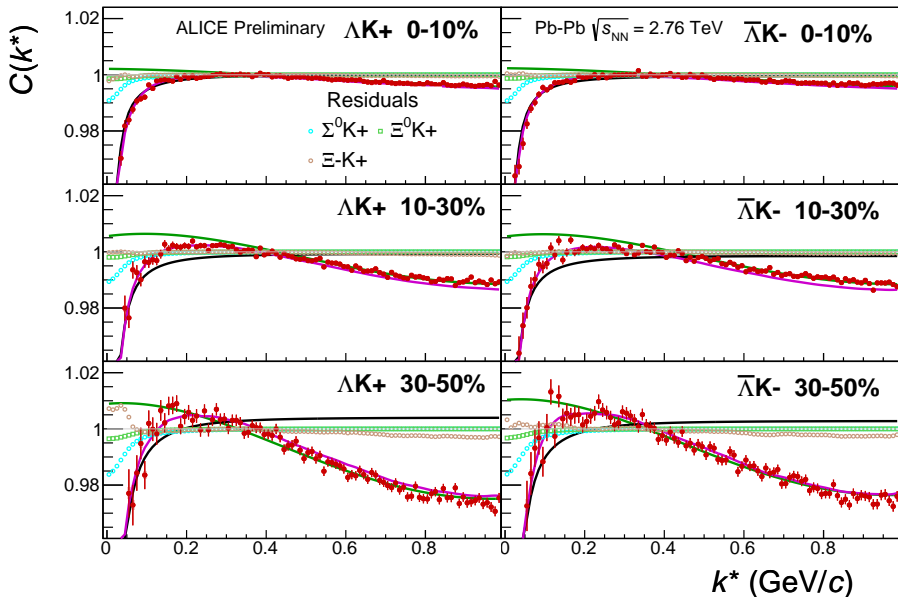


Fig. A.9: Fit results with the 3 residual contributions shown, for the ΛK^+ and $\bar{\Lambda} K^-$ data. The ΛK^+ data is shown in the left column, the $\bar{\Lambda} K^-$ in the right, and the rows differentiate the different centrality bins (0-10% in the top, 10-30% in the middle, and 30-50% in the bottom).

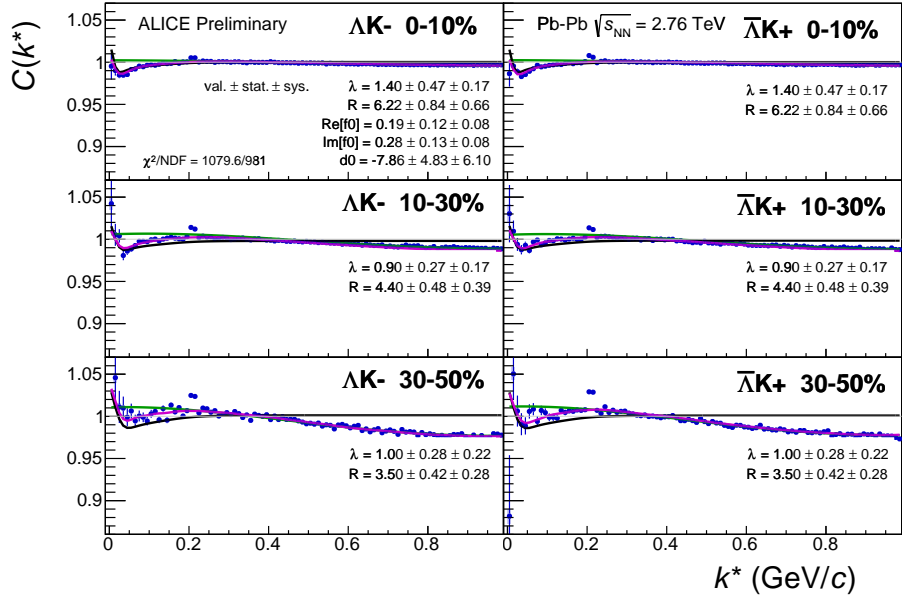


Fig. A.10: Fit results, with 3 residual correlations included, for the ΔK^- and $\bar{\Delta} K^+$ data. The ΔK^- data is shown in the left column, the $\bar{\Delta} K^+$ in the right, and the rows differentiate the different centrality bins (0-10% in the top, 10-30% in the middle, and 30-50% in the bottom).

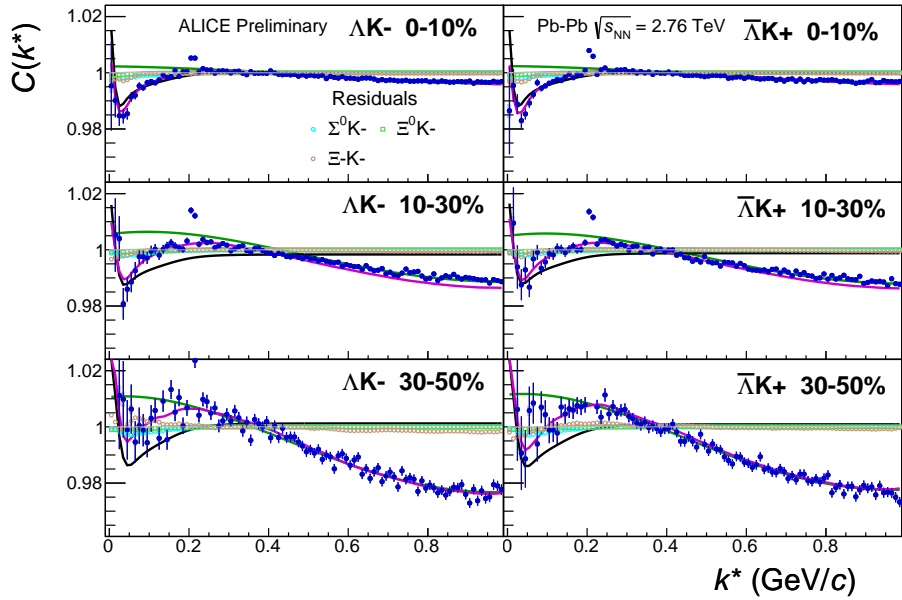


Fig. A.11: Fit results with the 3 residual contributions shown, for the ΔK^- and $\bar{\Delta} K^+$ data. The ΔK^- data is shown in the left column, the $\bar{\Delta} K^+$ in the right, and the rows differentiate the different centrality bins (0-10% in the top, 10-30% in the middle, and 30-50% in the bottom).

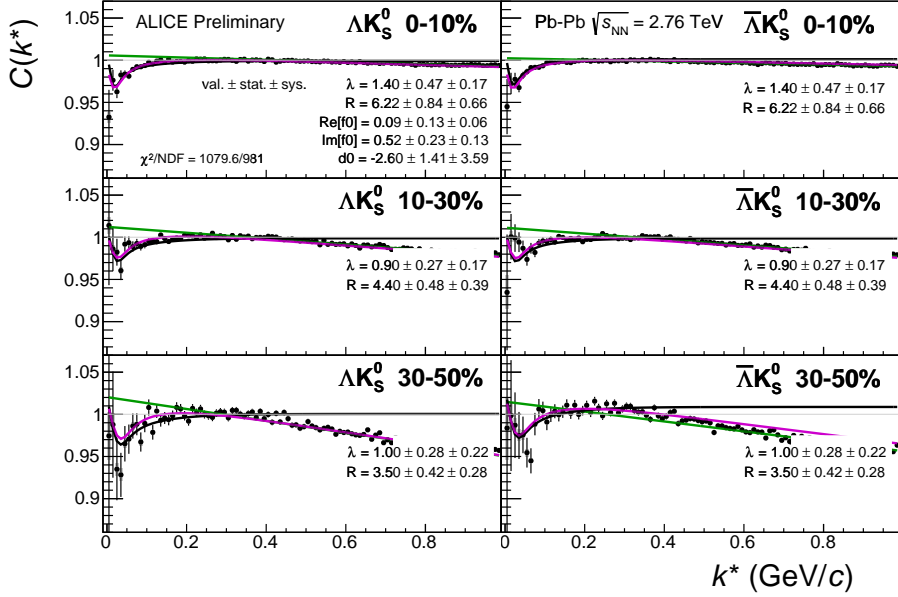


Fig. A.12: Fit results, with 3 residual correlations included, for the ΛK_S^0 and $\bar{\Lambda} K_S^0$ data. The ΛK_S^0 data is shown in the left column, the $\bar{\Lambda} K_S^0$ in the right, and the rows differentiate the different centrality bins (0-10% in the top, 10-30% in the middle, and 30-50% in the bottom).

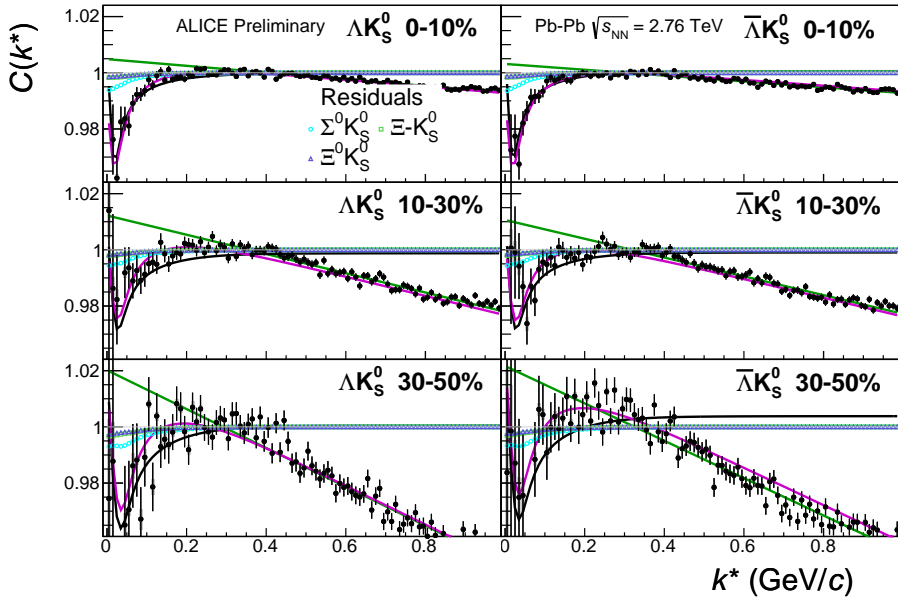


Fig. A.13: Fit results with the 3 residual contributions shown, for the ΛK_S^0 and $\bar{\Lambda} K_S^0$ data. The ΛK_S^0 data is shown in the left column, the $\bar{\Lambda} K_S^0$ in the right, and the rows differentiate the different centrality bins (0-10% in the top, 10-30% in the middle, and 30-50% in the bottom).

1205 **A.3 10 Residual Contributors Included in Fit**

1206 This section presents fit results for which 10 residual contributors were assumed. These contributors
 1207 include those shared by the three contributor case (App. A.2), $(\Sigma^0 K, \Xi^0 K, \Xi^- K) \rightarrow \Lambda K$, and additionally
 1208 the contributors $(\Sigma^{*(+,-,0)} K^{*0}, \Lambda K^{*0}, \Sigma^0 K^{*0}, \Xi^0 K^{*0}, \Xi^- K^{*0}) \rightarrow \Lambda K$. As stated at the beginning of App.
 1209 A, most of the Σ^* and K^* resonances will have decayed before kinetic freeze-out, and therefore it is best
 1210 to treat Λ and K particles originating from these resonances as primary, i.e. only using three residual con-
 1211 tributors. However, it is still interesting to examine how these additional shorter lived sources affect our
 1212 fit result, as presented below. For a comparison of these results to the case of three residual contributors,
 1213 see Fig. A.1 in App. A.1

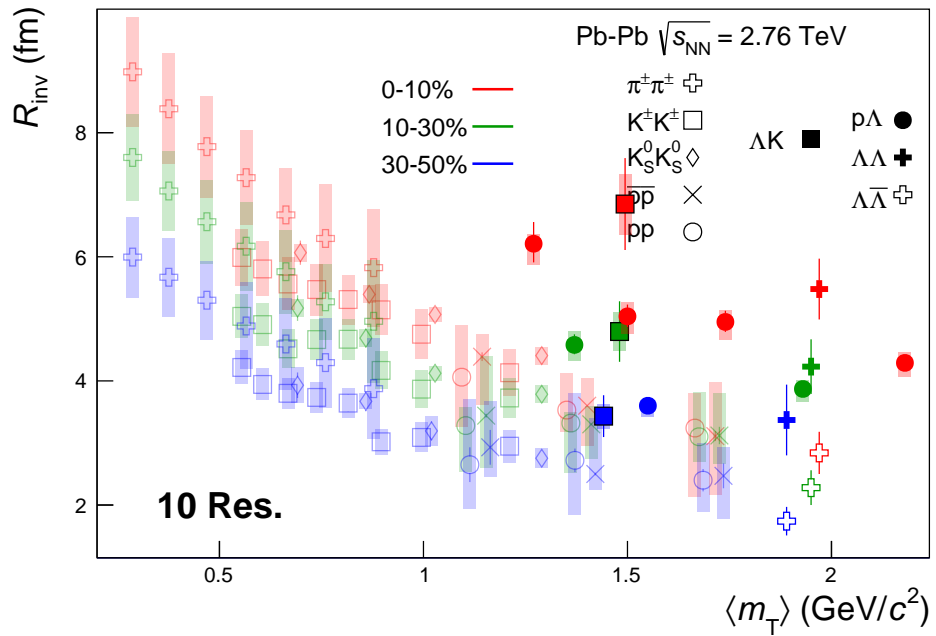


Fig. A.14: 10 residual correlations in ΛK fits. Extracted fit R_{inv} parameters as a function of pair transverse mass (m_T) for various pair systems over several centralities. The ALICE published data [13] are shown with transparent, open symbols. The new ΛK results are shown with opaque, filled symbols. The m_T value for the ΛK system is an average of those for the ΛK^+ , $\bar{\Lambda} K^-$, and ΛK_S^0 systems.

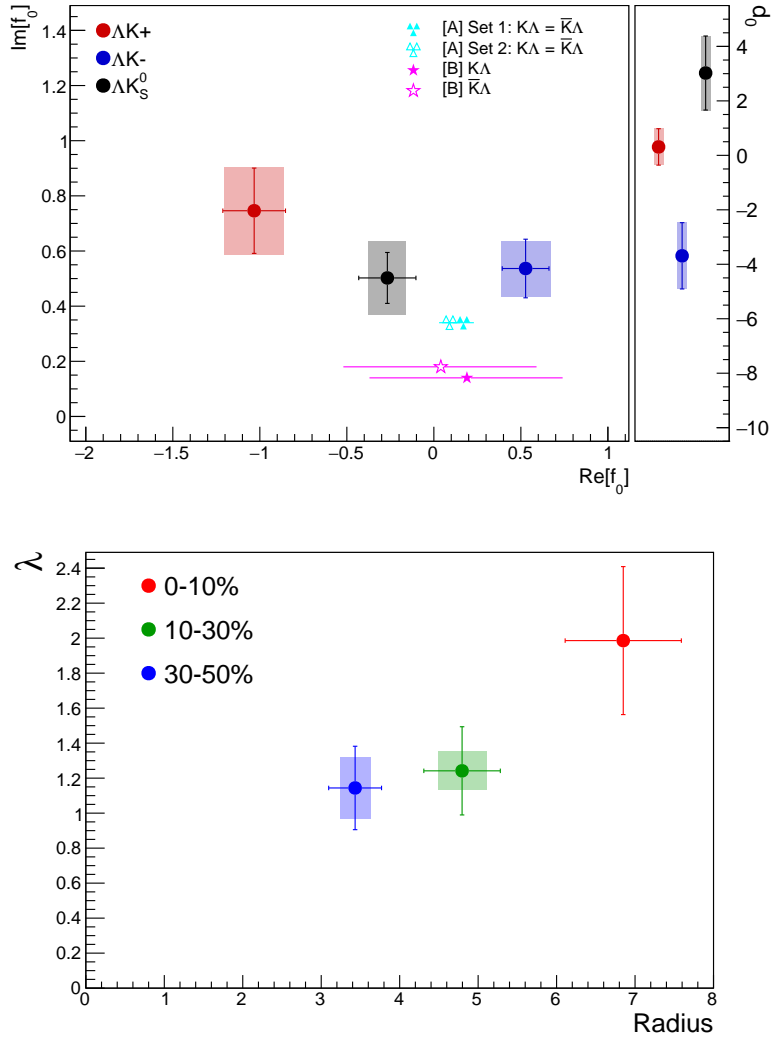


Fig. A.15: Extracted fit parameters for the case of 10 residual contributors for all of our ΛK systems. [Top]: $\Im f_0$ vs. $\Re f_0$, together with d_0 to the right. [Bottom]: λ vs. Radius for the 0-10% (blue), 10-30% (green), and 30-50% (red) centrality bins. In the fit, all ΛK systems share common radii. The color scheme used in the panel are to be consistent with those in Fig. A.14. The cyan ([A] = Ref. [14]) and magenta ([B] = Ref. [15]) points show theoretical predictions made using chiral perturbation theory.

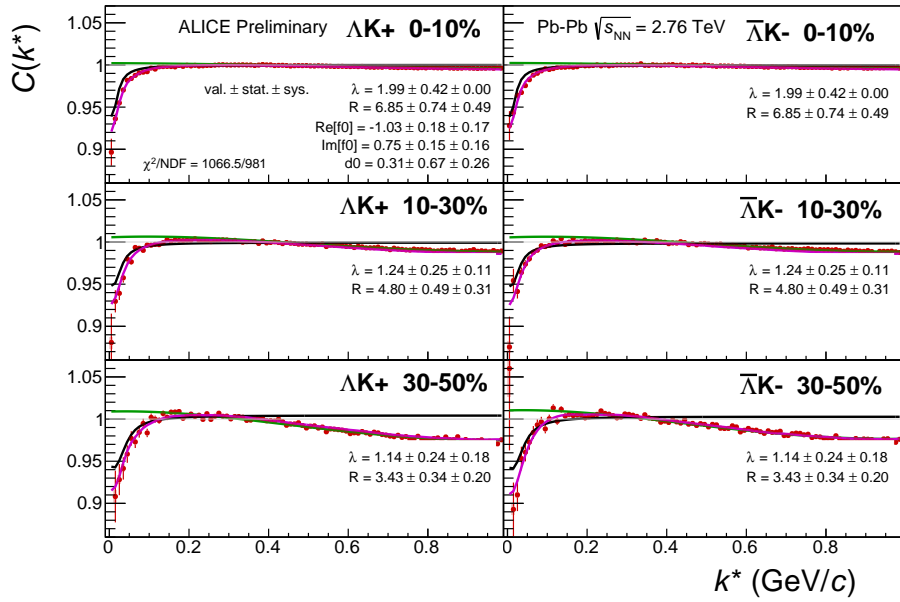


Fig. A.16: Fit results, with 10 residual correlations included, for the ΛK^+ and $\bar{\Lambda} K^-$ data. The ΛK^+ data is shown in the left column, the $\bar{\Lambda} K^-$ in the right, and the rows differentiate the different centrality bins (0-10% in the top, 10-30% in the middle, and 30-50% in the bottom).

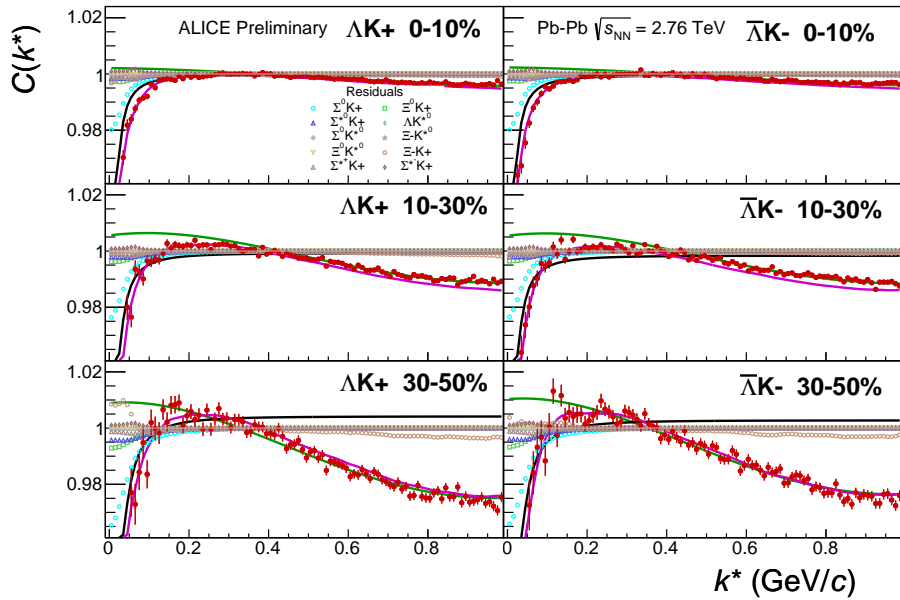


Fig. A.17: Fit results with the 10 residual contributions shown, for the ΛK^+ and $\bar{\Lambda} K^-$ data. The ΛK^+ data is shown in the left column, the $\bar{\Lambda} K^-$ in the right, and the rows differentiate the different centrality bins (0-10% in the top, 10-30% in the middle, and 30-50% in the bottom).

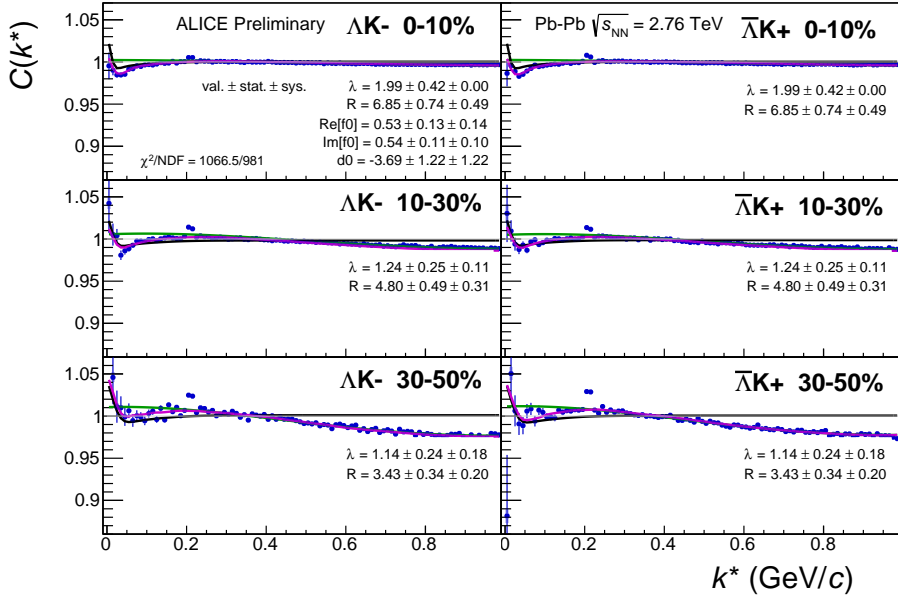


Fig. A.18: Fit results, with 10 residual correlations included, for the ΛK^- and $\bar{\Lambda}K^+$ data. The ΛK^- data is shown in the left column, the $\bar{\Lambda}K^+$ in the right, and the rows differentiate the different centrality bins (0-10% in the top, 10-30% in the middle, and 30-50% in the bottom).

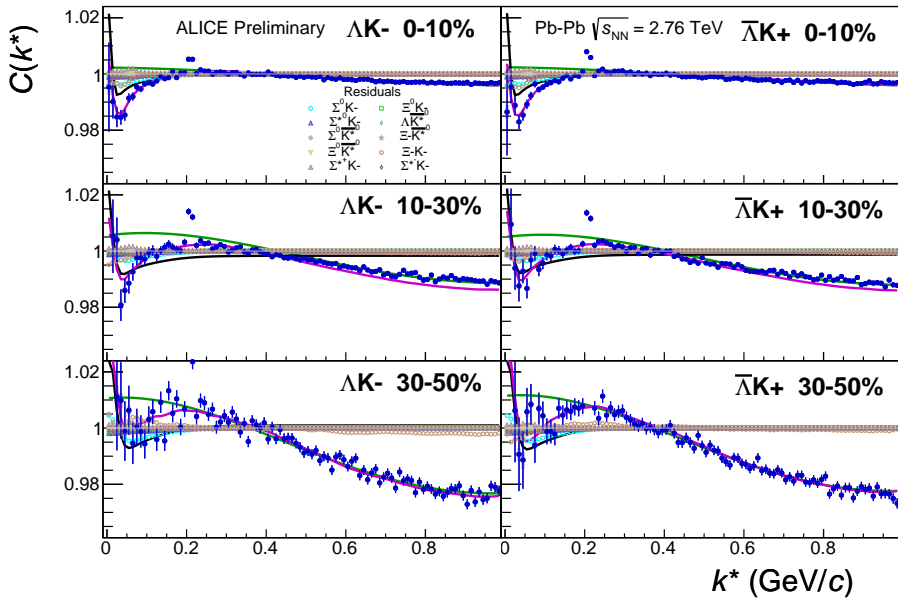


Fig. A.19: Fit results with the 10 residual contributions shown, for the ΛK^- and $\bar{\Lambda}K^+$ data. The ΛK^- data is shown in the left column, the $\bar{\Lambda}K^+$ in the right, and the rows differentiate the different centrality bins (0-10% in the top, 10-30% in the middle, and 30-50% in the bottom).

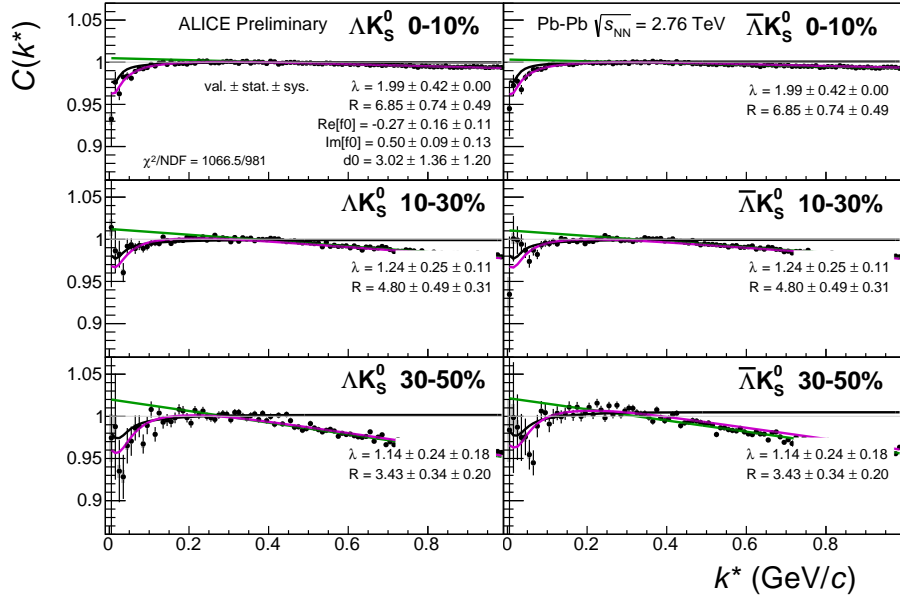


Fig. A.20: Fit results, with 10 residual correlations included, for the ΛK_S^0 and $\bar{\Lambda} K_S^0$ data. The ΛK_S^0 data is shown in the left column, the $\bar{\Lambda} K_S^0$ in the right, and the rows differentiate the different centrality bins (0-10% in the top, 10-30% in the middle, and 30-50% in the bottom).

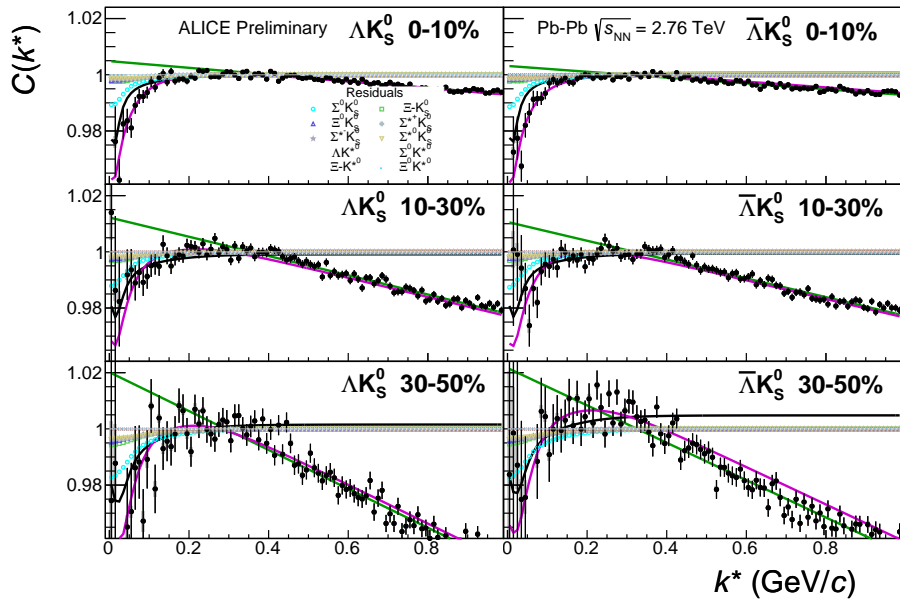


Fig. A.21: Fit results with the 10 residual contributions shown, for the ΛK_S^0 and $\bar{\Lambda} K_S^0$ data. The ΛK_S^0 data is shown in the left column, the $\bar{\Lambda} K_S^0$ in the right, and the rows differentiate the different centrality bins (0-10% in the top, 10-30% in the middle, and 30-50% in the bottom).

1214 **A.4 No Residual Contributors Included in Fit**

1215 This section presents fit results for which no residual contributors were assumed. This is a typical starting
 1216 point for femtoscopic analyses such as ours, and the effects of residual contributions are sometimes
 1217 ignored. Therefore, it is interesting to observe the effects of neglecting residual feed-down from our fit
 1218 description. For a comparison of these results to the case of three residual contributors, see Fig. A.1 in
 1219 App. A.1

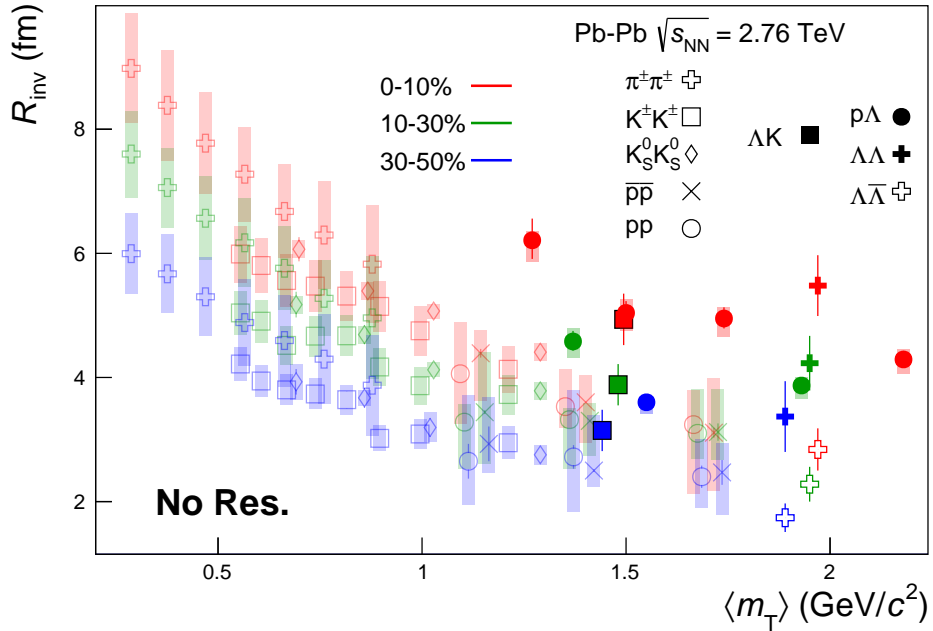


Fig. A.22: No residual correlations in ΛK fits. Extracted fit R_{inv} parameters as a function of pair transverse mass (m_T) for various pair systems over several centralities. The ALICE published data [13] are shown with transparent, open symbols. The new ΛK results are shown with opaque, filled symbols. The m_T value for the ΛK system is an average of those for the ΛK^+ , $\bar{\Lambda} K^-$, and ΛK_S^0 systems.

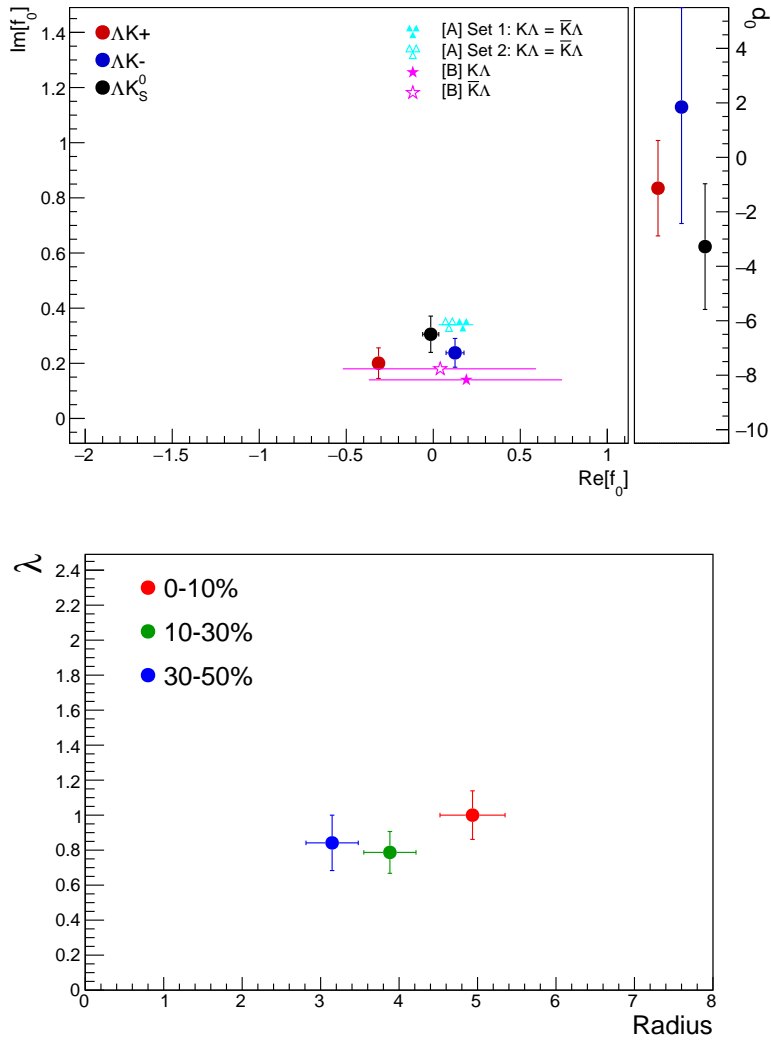


Fig. A.23: Extracted fit parameters for the case of no residual contributors for all of our ΛK systems. [Top]: $\Im f_0$ vs. $\Re f_0$, together with d_0 to the right. [Bottom]: λ vs. Radius for the 0-10% (blue), 10-30% (green), and 30-50% (red) centrality bins. In the fit, all ΛK systems share common radii. The color scheme used in the panel are to be consistent with those in Fig. A.22. The cyan ([A] = Ref. [14]) and magenta ([B] = Ref. [15]) points show theoretical predictions made using chiral perturbation theory.

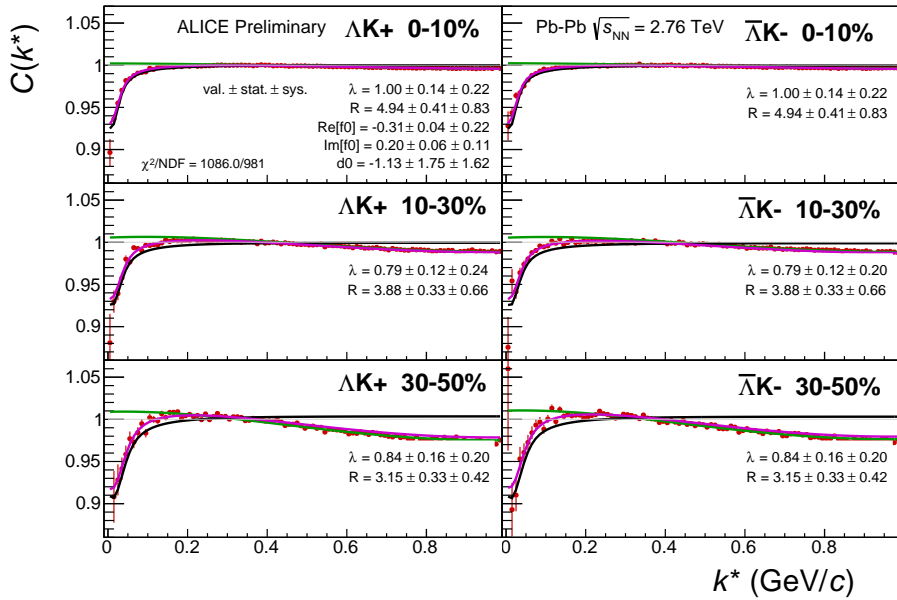


Fig. A.24: Fit results, with no residual correlations included, for the ΛK^+ and $\bar{\Lambda} K^-$ data. The ΛK^+ data is shown in the left column, the $\bar{\Lambda} K^-$ in the right, and the rows differentiate the different centrality bins (0-10% in the top, 10-30% in the middle, and 30-50% in the bottom).

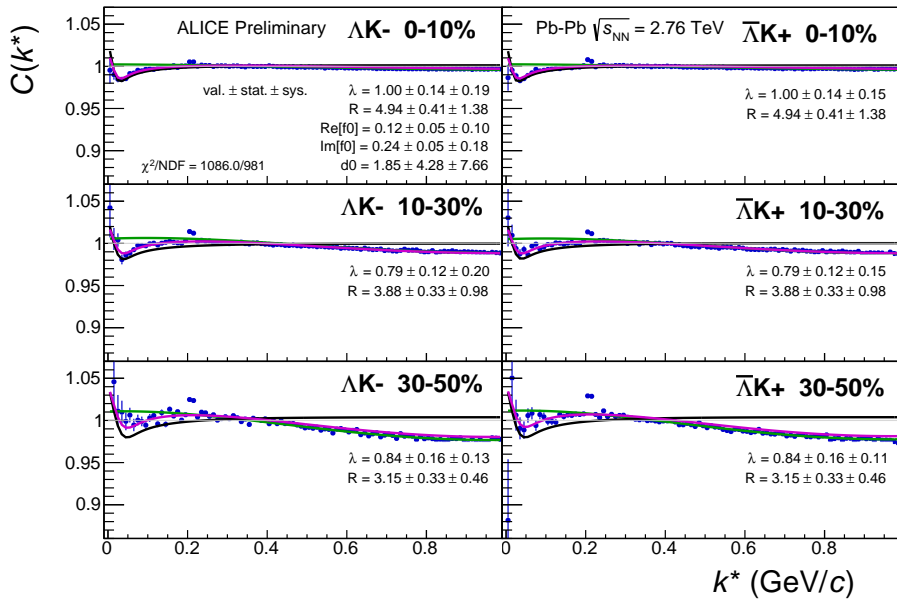


Fig. A.25: Fit results, with no residual correlations included, for the ΛK^- and $\bar{\Lambda} K^+$ data. The ΛK^- data is shown in the left column, the $\bar{\Lambda} K^+$ in the right, and the rows differentiate the different centrality bins (0-10% in the top, 10-30% in the middle, and 30-50% in the bottom).

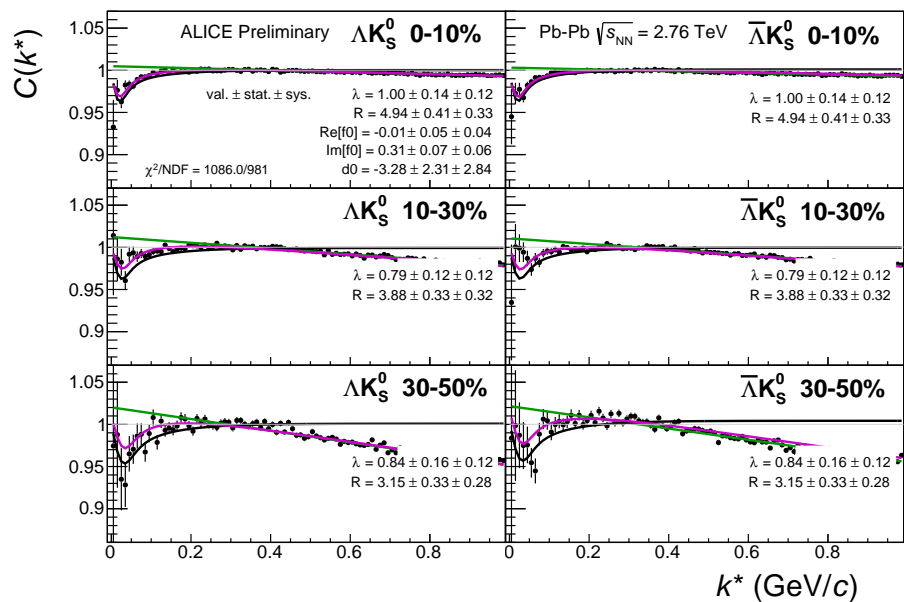


Fig. A.26: Fit results, with no residual correlations included, for the ΛK_S^0 and $\bar{\Lambda} K_S^0$ data. The ΛK_S^0 data is shown in the left column, the $\bar{\Lambda} K_S^0$ in the right, and the rows differentiate the different centrality bins (0-10% in the top, 10-30% in the middle, and 30-50% in the bottom).

1220 **B Spherical Harmonics**

1221 This appendix shows a spherical harmonic decomposition of our ΛK_S^0 correlation functions. For our
 1222 purposes, the most interesting components are C_{00} and $\Re C_{11}$, which are presented in Figures B.1 - B.3.
 1223 In each of the figures, the left column shows C_{00} , the right column $\Re C_{11}$, and the rows separate the
 1224 centrality bins. For the the 0-10% bin, results are also included from a THERMINATOR 2 simulation
 1225 for an impact parameter $b = 2$ fm (gold stars) and assumed scattering parameters $(\Re f_0, \Im f_0, d_0) = (-1.16,$
 1226 $0.51, 1.08), (0.41, 0.47, -4.89)$, and $(-0.41, 0.20, 2.08)$ for the ΛK^+ , ΛK^- , and ΛK_S^0 systems, respectively.
 1227 The coefficient C_{00} quantifies the overall angle-integrated strength of the correlation function, similar to
 1228 that studied in our 1D analysis. The $\Re C_{11}$ term is sensitive to the asymmetry in the outward direction, a
 1229 component interesting for non-identical particle studies. In our analysis, we have taken the Λ to be the
 1230 first particle in our pairs, and a negative value of $\Re C_{11}$ signifies the Λ particles are emitted, on average,
 1231 further out and/or earlier than the K mesons. For completeness, the first six components of the spherical
 1232 harmonic decompositions are shown in Figures B.4 - B.6

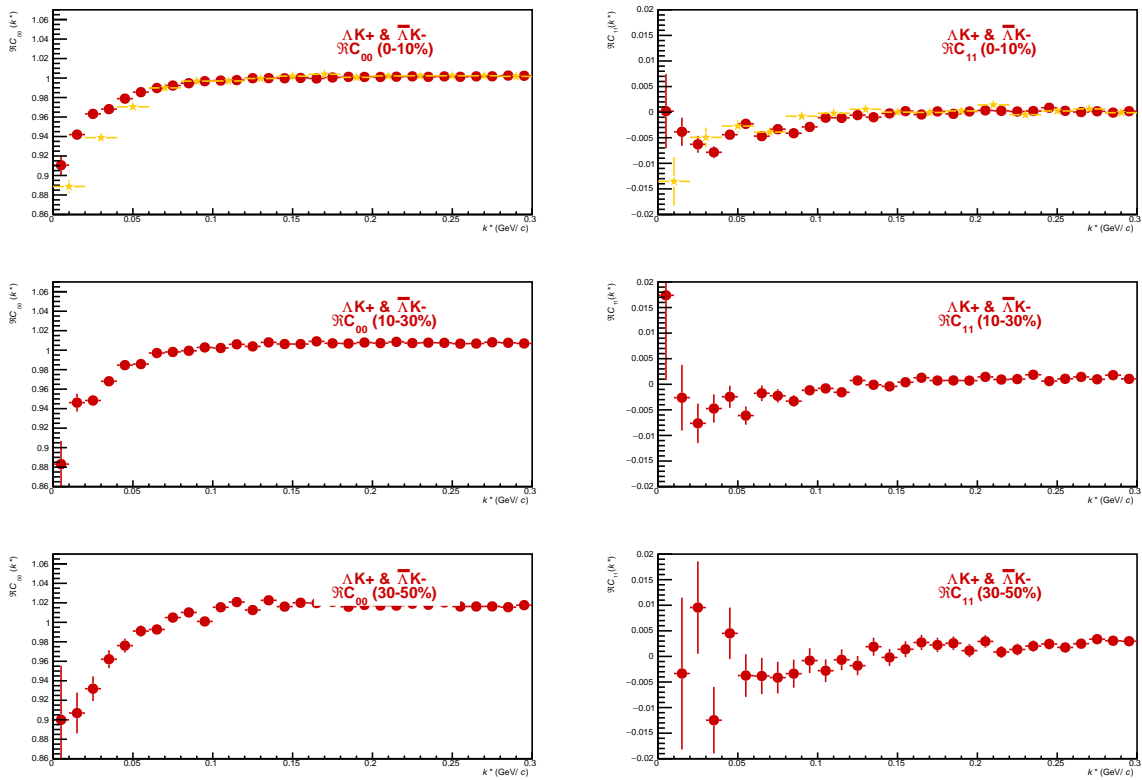


Fig. B.1: C_{00} (left) and $\Re C_{11}$ (right) components of a spherical harmonic decomposition of the ΛK^+ correlation function for the 0-10% (top), 10-30% (middle), and 30-50% (bottom) centrality bins. For the the 0-10% bin, results are also included from a THERMINATOR 2 simulation for an impact parameter $b = 2$ fm (gold stars) and assumed scattering parameters $(\Re f_0, \Im f_0, d_0) = (-1.16, 0.51, 1.08)$.

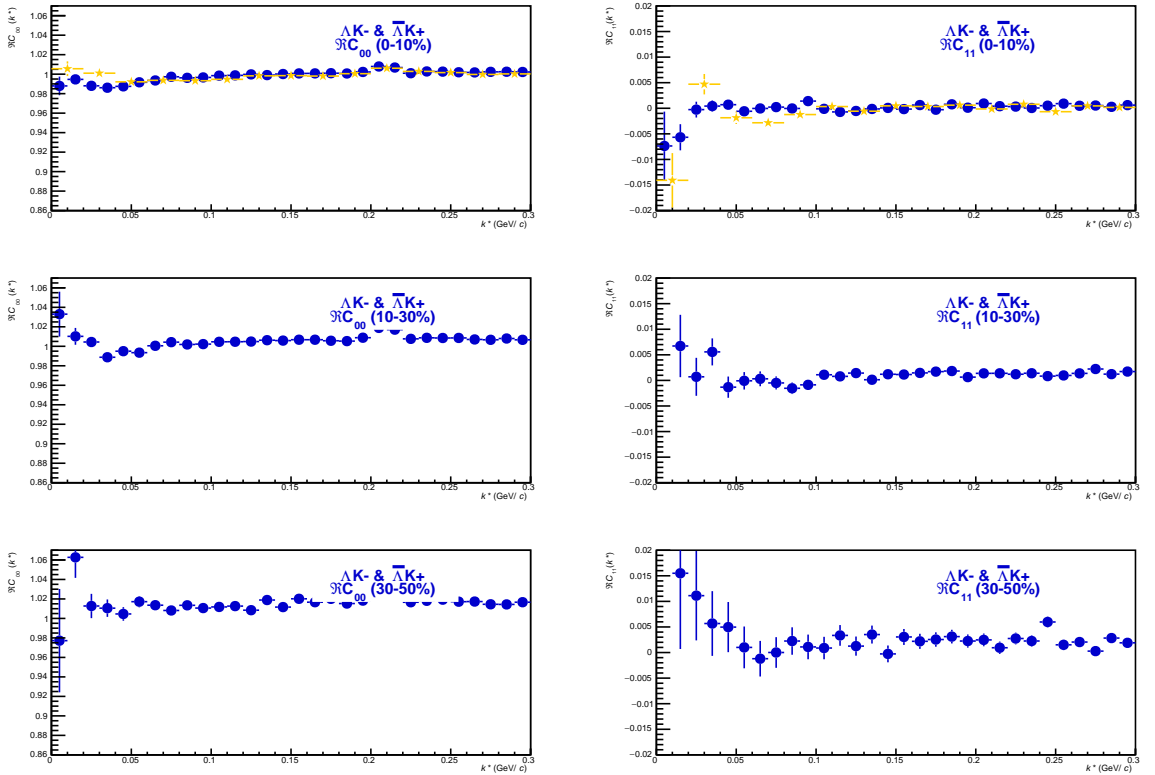


Fig. B.2: C_{00} (left) and $\Re C_{11}$ (right) components of a spherical harmonic decomposition of the ΛK^- correlation function for the 0-10% (top), 10-30% (middle), and 30-50% (bottom) centrality bins. For the the 0-10% bin, results are also included from a THERMINATOR 2 simulation for an impact parameter $b = 2 \text{ fm}$ (gold stars) and assumed scattering parameters $(\Re f_0, \Im f_0, d_0) = (0.41, 0.47, -4.89)$.

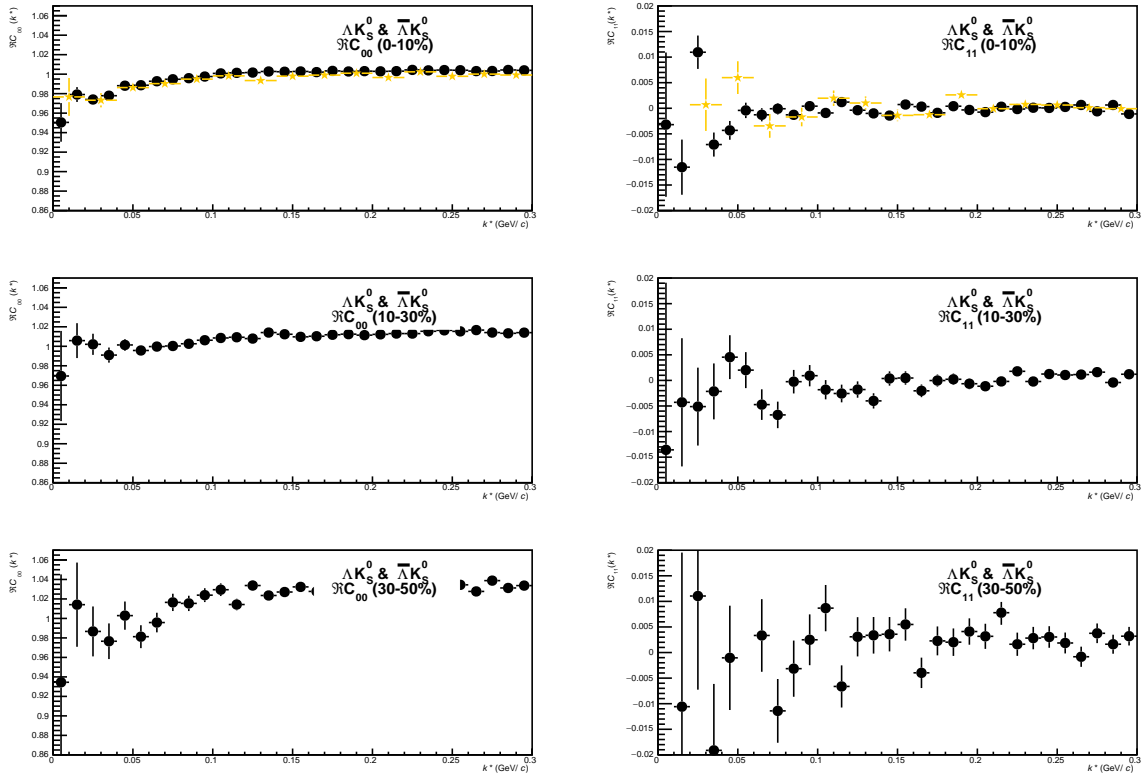


Fig. B.3: C_{00} (left) and $\Re C_{11}$ (right) components of a spherical harmonic decomposition of the ΛK_s^0 correlation function for the 0-10% (top), 10-30% (middle), and 30-50% (bottom) centrality bins. For the the 0-10% bin, results are also included from a THERMINATOR 2 simulation for an impact parameter $b = 2$ fm (gold stars) and assumed scattering parameters $(\Re f_0, \Im f_0, d_0) = (-0.41, 0.20, 2.08)$.

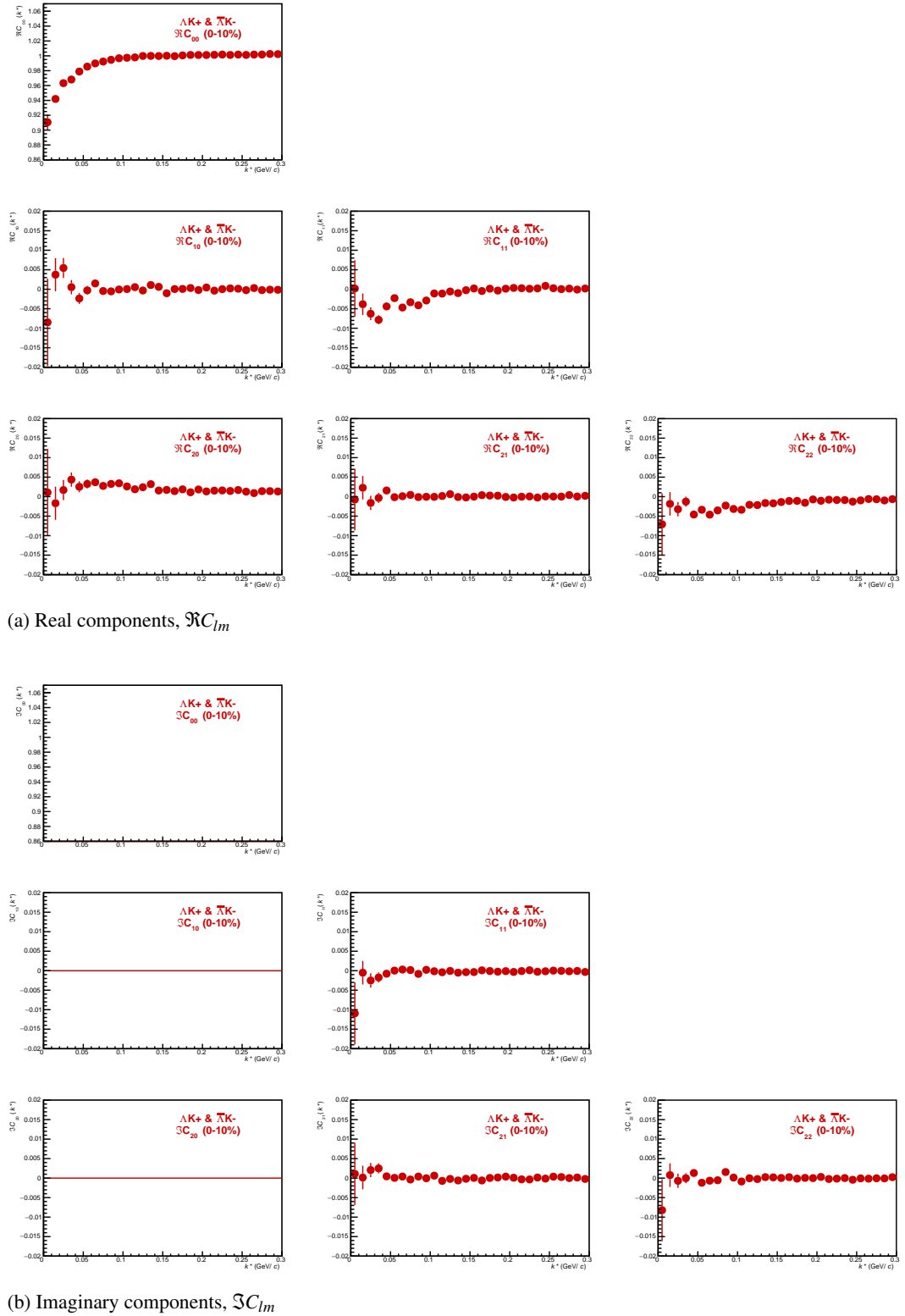


Fig. B.4: First six components ($C_{00}, C_{10}, C_{11}, C_{20}, C_{21}, C_{22}$) of the spherical harmonic decomposition of the ΛK^+ correlation function for the 0-10% centrality bin. Note, $\Im C_{00}$, $\Im C_{10}$, and $\Im C_{20}$ are zero by definition.

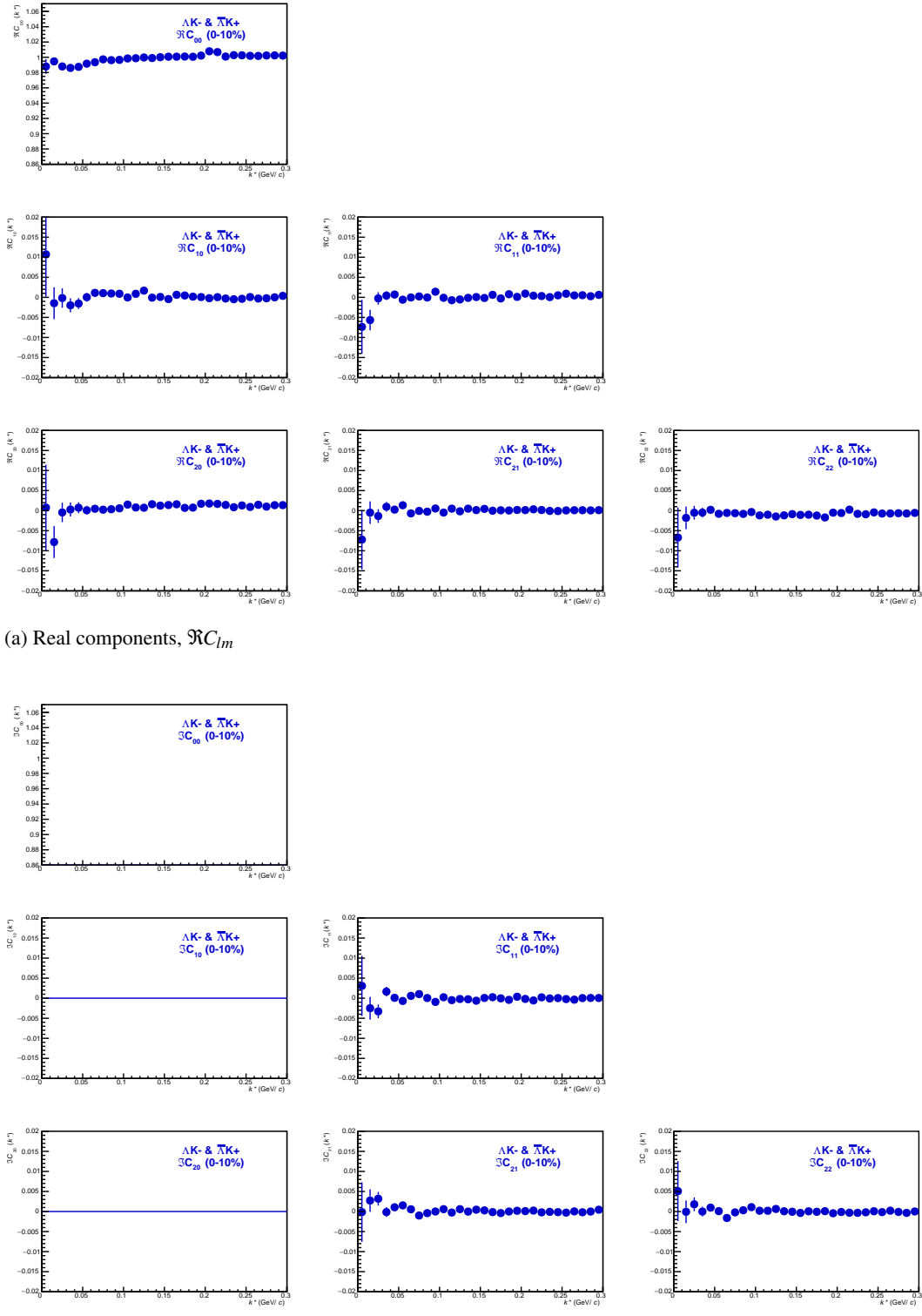


Fig. B.5: First six components ($C_{00}, C_{10}, C_{11}, C_{20}, C_{21}, C_{22}$) of the spherical harmonic decomposition of the ΛK^- correlation function for the 0-10% centrality bin. Note, $\Im C_{00}$, $\Im C_{10}$, and $\Im C_{20}$ are zero by definition.

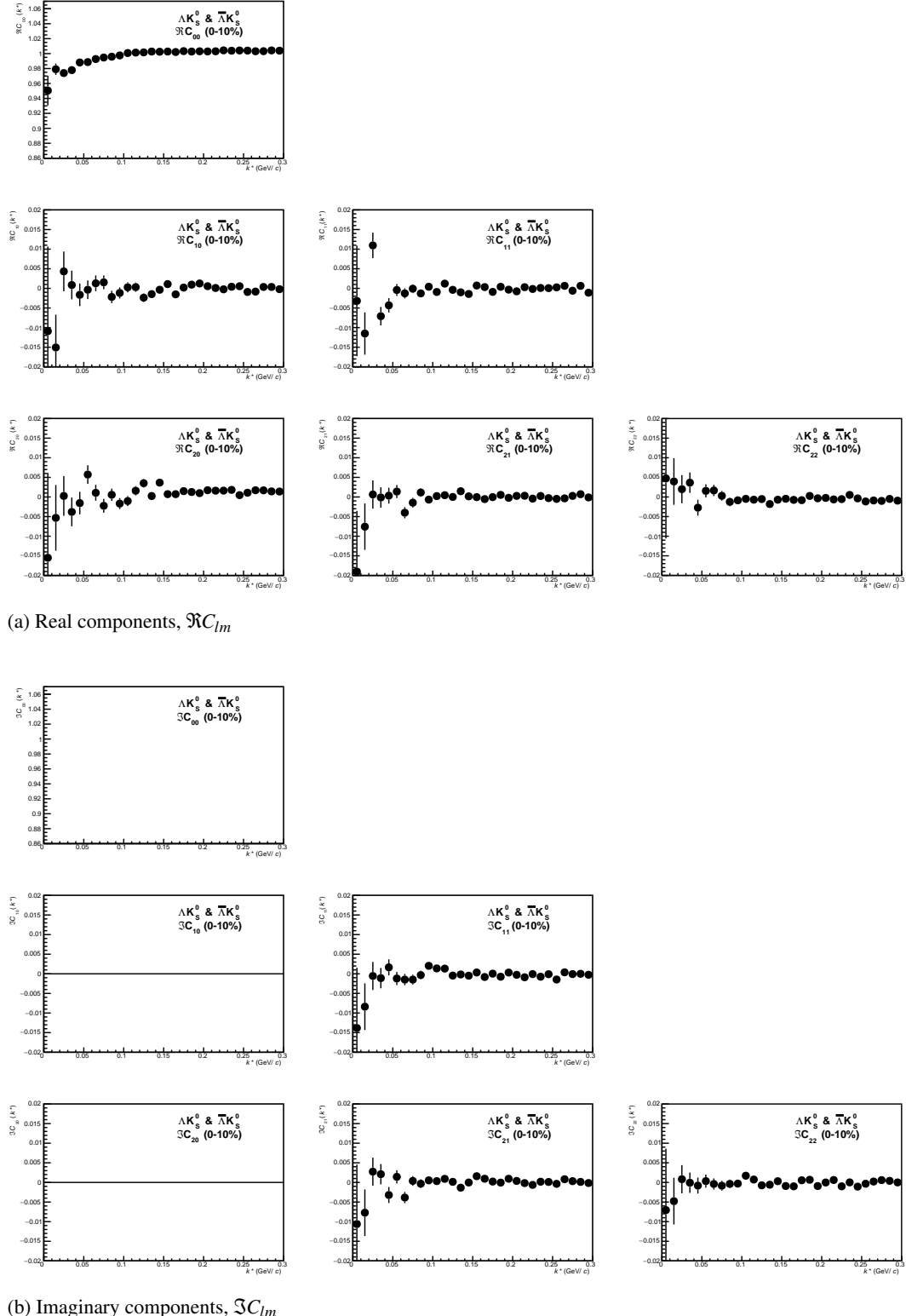


Fig. B.6: First six components ($C_{00}, C_{10}, C_{11}, C_{20}, C_{21}, C_{22}$) of the spherical harmonic decomposition of the ΛK_s^0 correlation function for the 0-10% centrality bin. Note, $\Im C_{00}$, $\Im C_{10}$, and $\Im C_{20}$ are zero by definition.

1233 **C Additional Figures**

1234 **C.1 Residuals**

1235 **C.1.1 ΛK^+ Residuals**

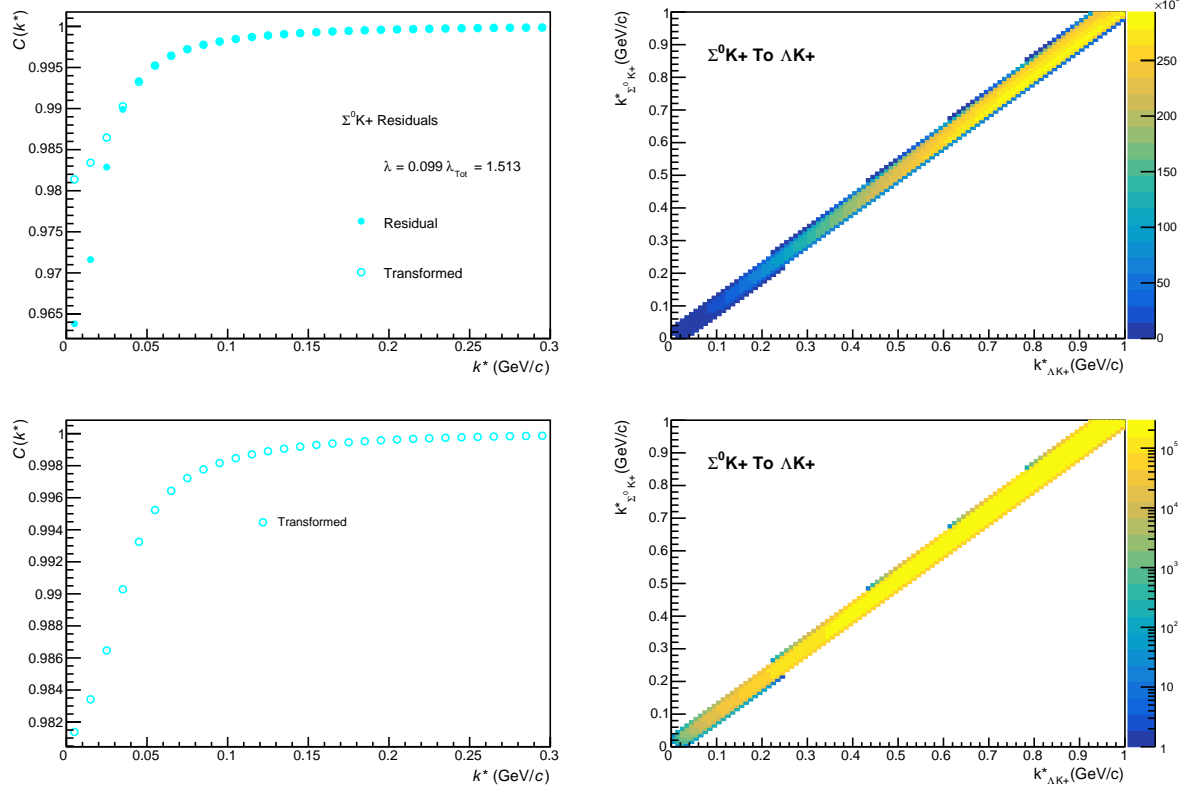


Fig. C.1: Residuals: $\Sigma^0 K^+$ to ΛK^+ (0-10% Centrality)

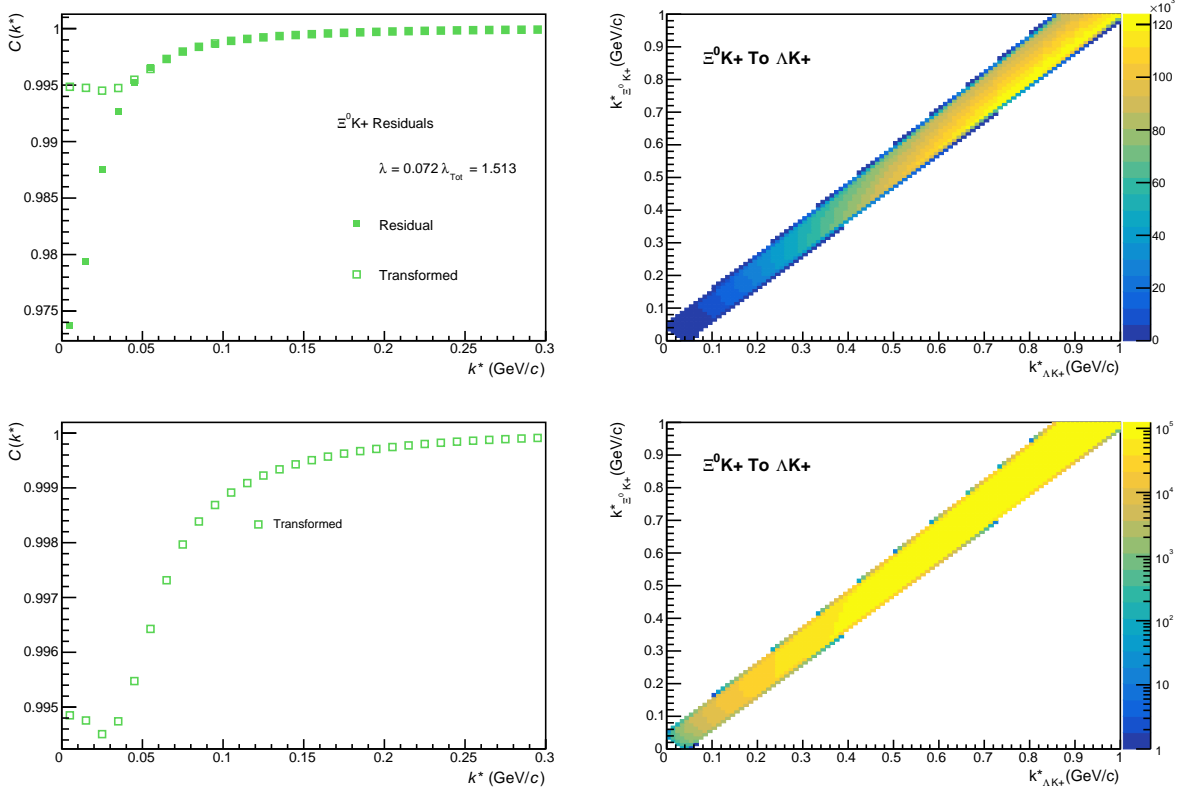


Fig. C.2: Residuals: $\Xi^0 K^+$ to ΛK^+ (0-10% Centrality)

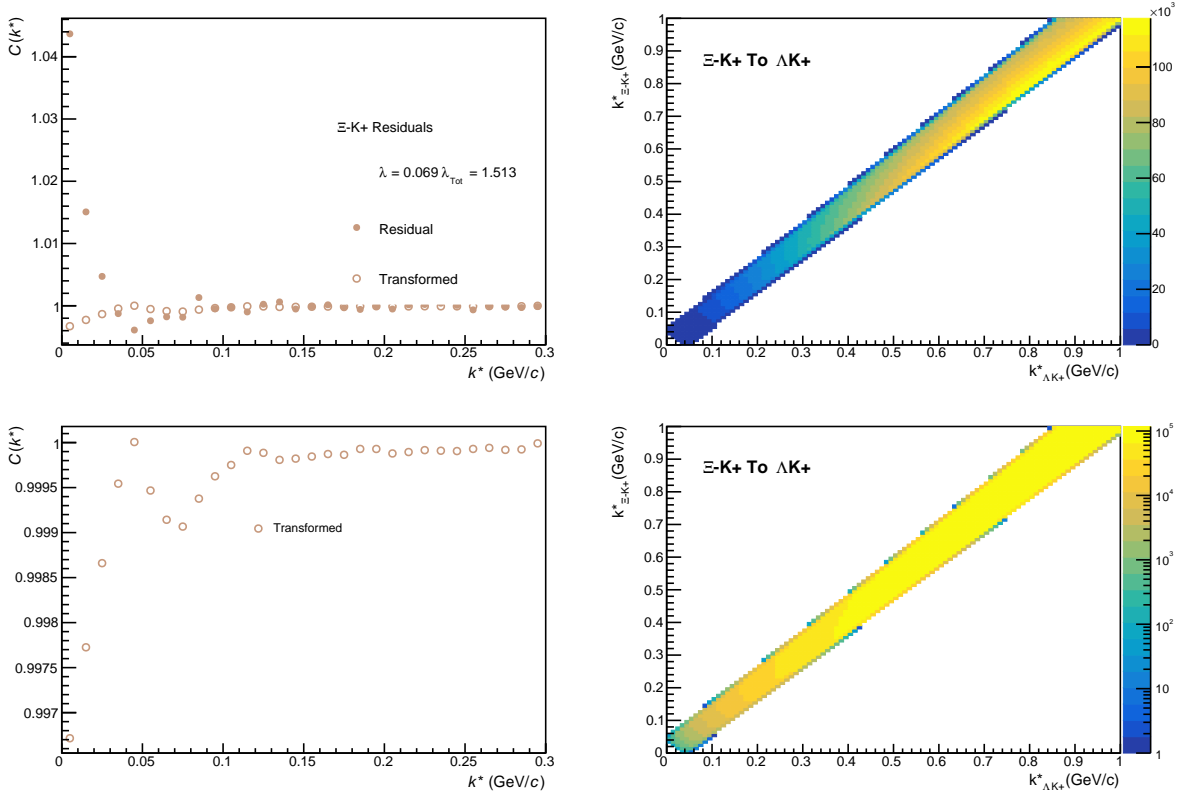


Fig. C.3: Residuals: $\Xi^- K^+$ to ΛK^+ (0-10% Centrality)

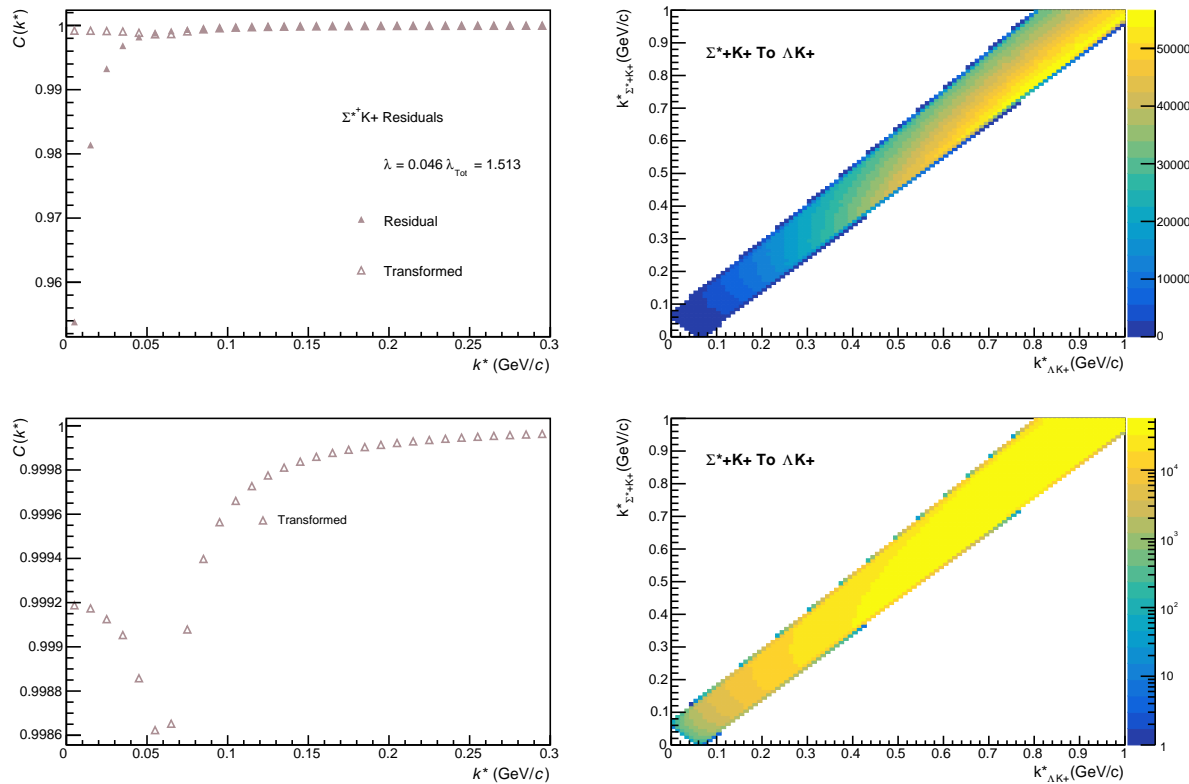


Fig. C.4: Residuals: Σ^+K^+ to ΛK^+ (0-10% Centrality)

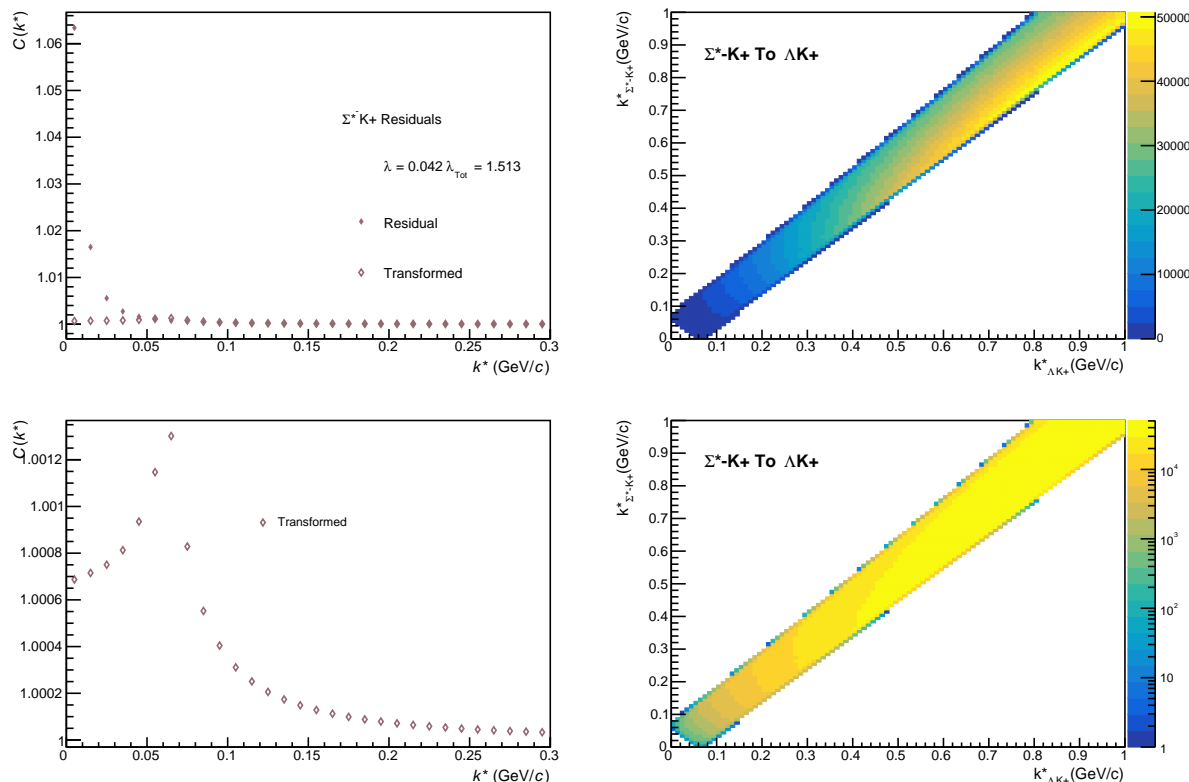


Fig. C.5: Residuals: Σ^-K^+ to ΛK^+ (0-10% Centrality)

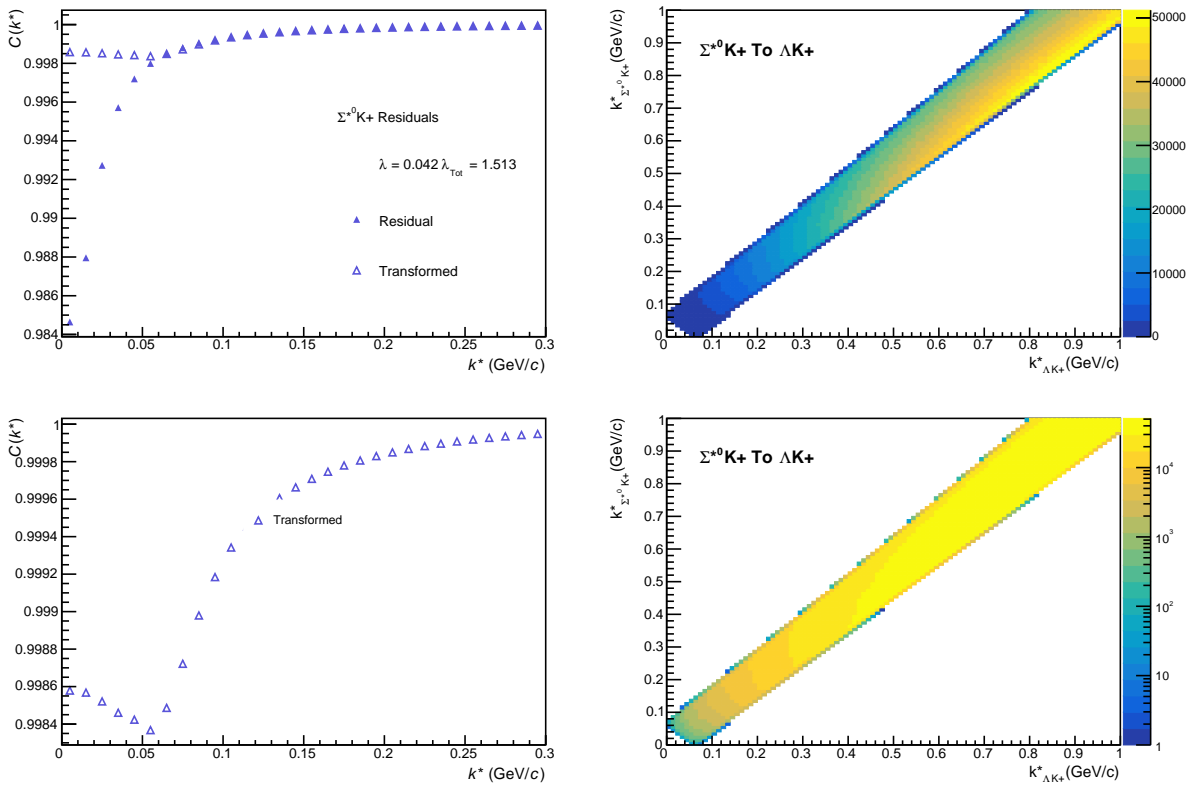


Fig. C.6: Residuals: $\Sigma^{*0} K^+$ to ΛK^+ (0-10% Centrality)

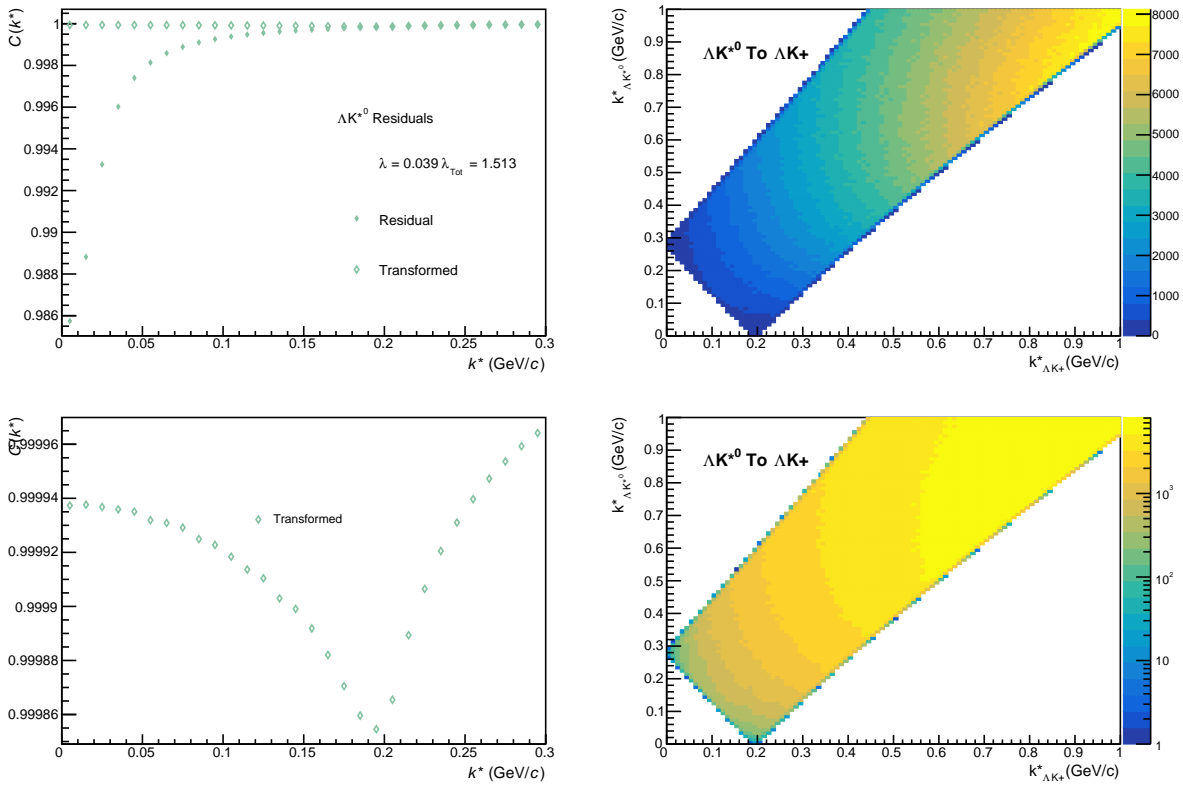


Fig. C.7: Residuals: ΛK^{*0} to ΛK^+ (0-10% Centrality)

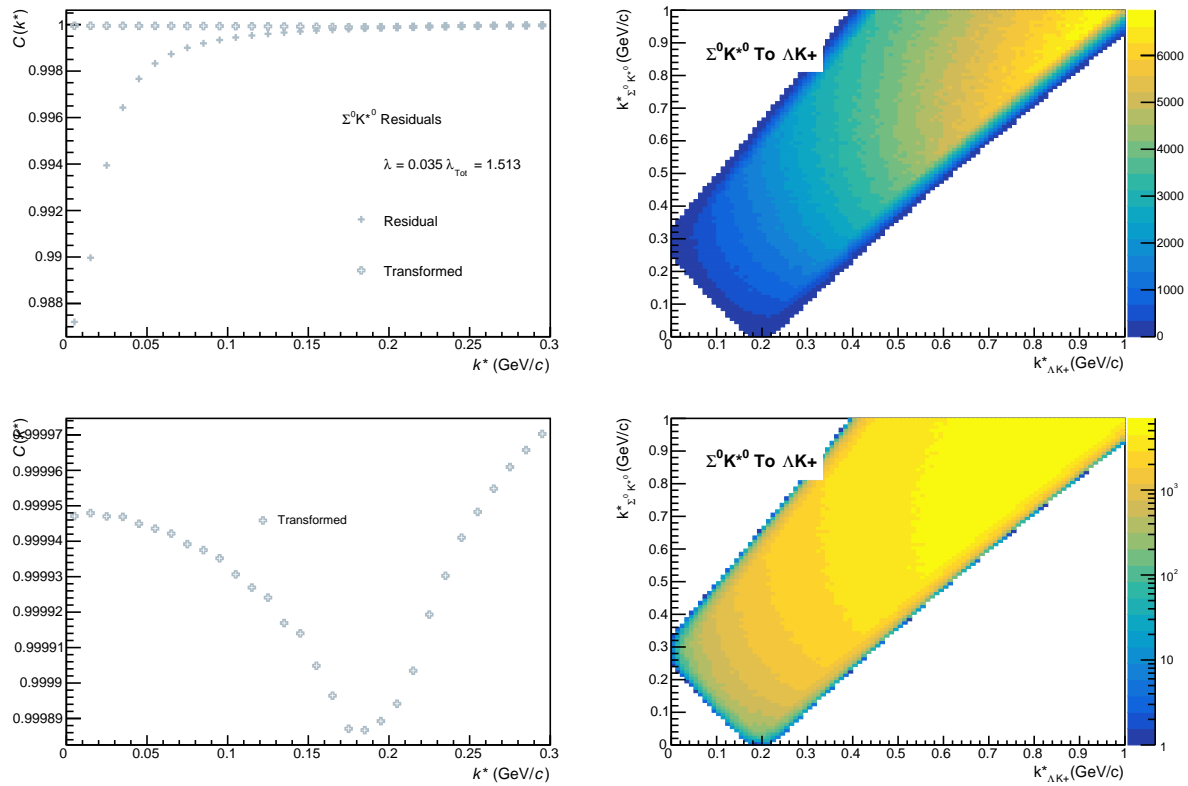


Fig. C.8: Residuals: $\Sigma^0 K^{*0}$ to ΛK^+ (0-10% Centrality)

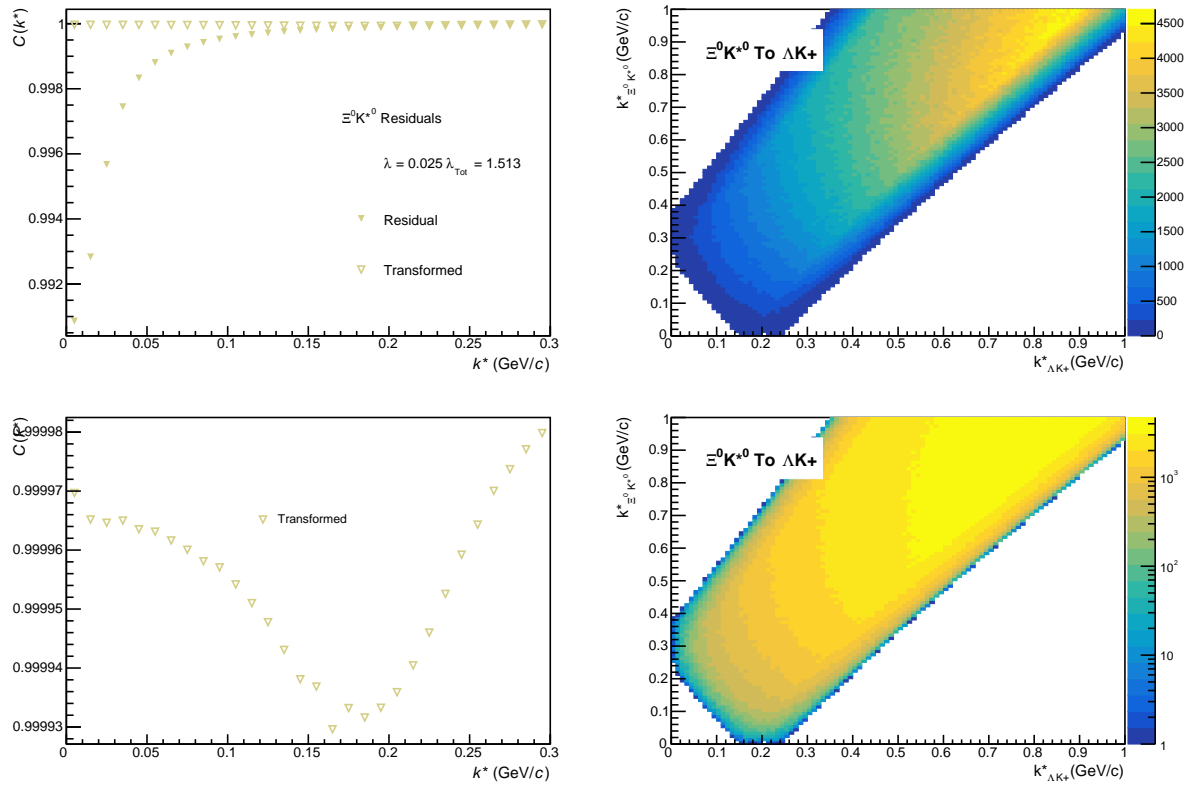


Fig. C.9: Residuals: $\Xi^0 K^{*0}$ to ΛK^+ (0-10% Centrality)

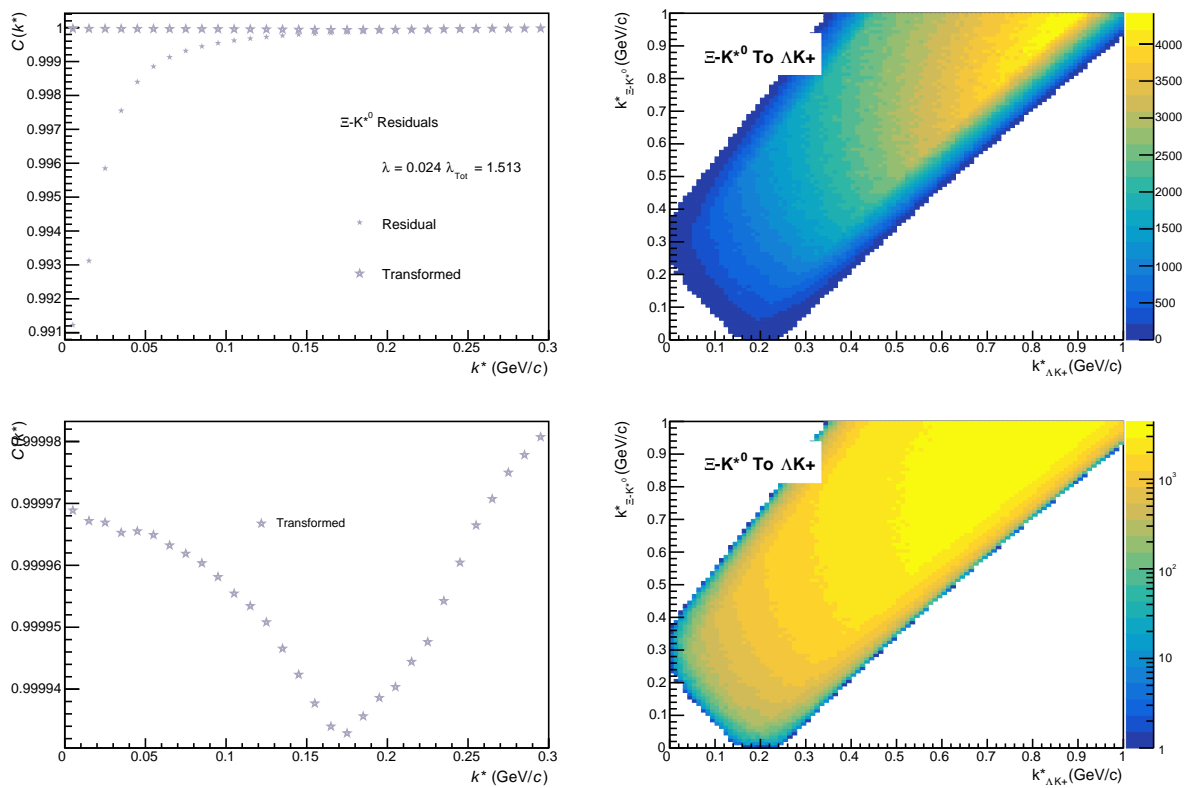
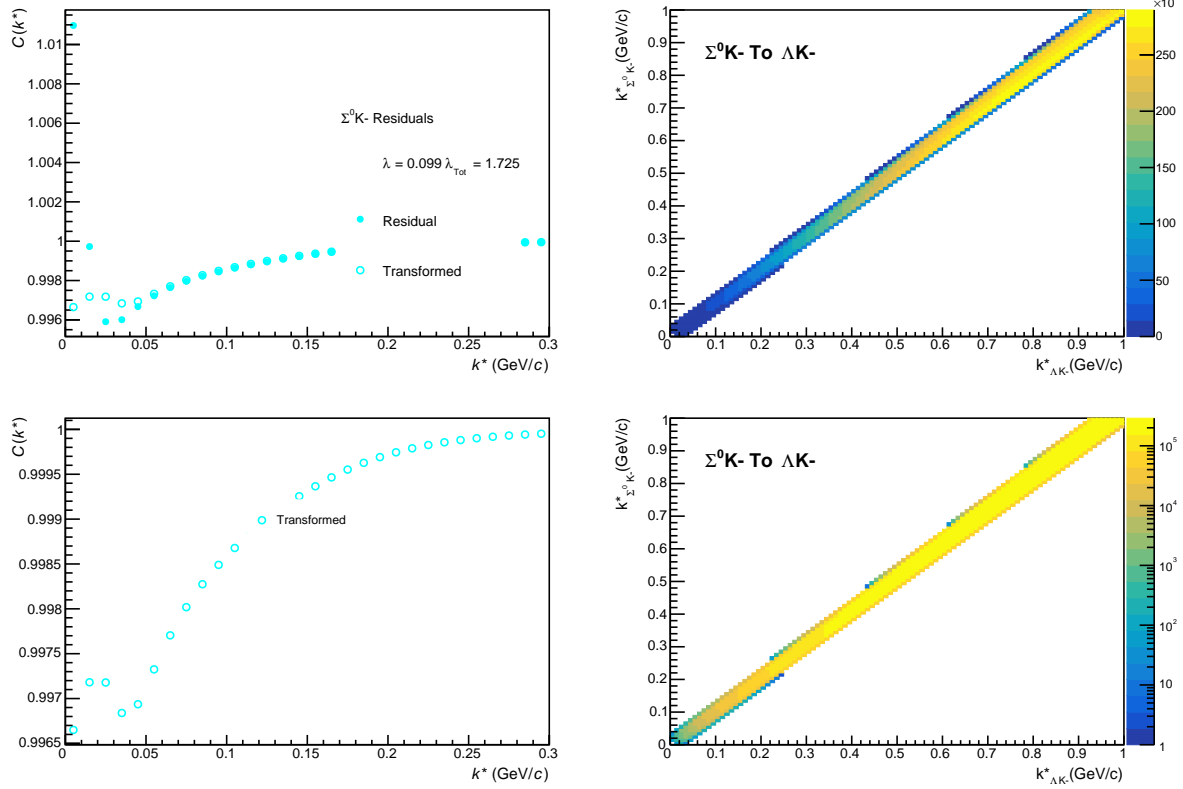
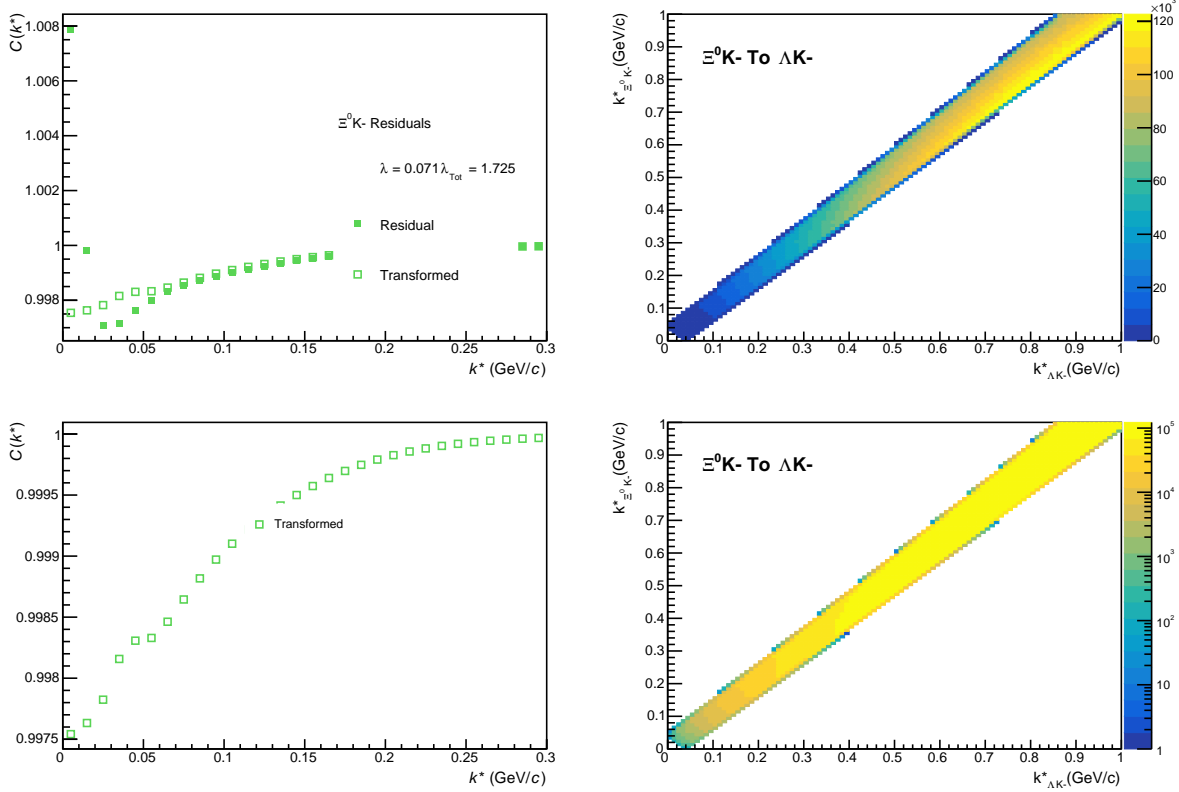
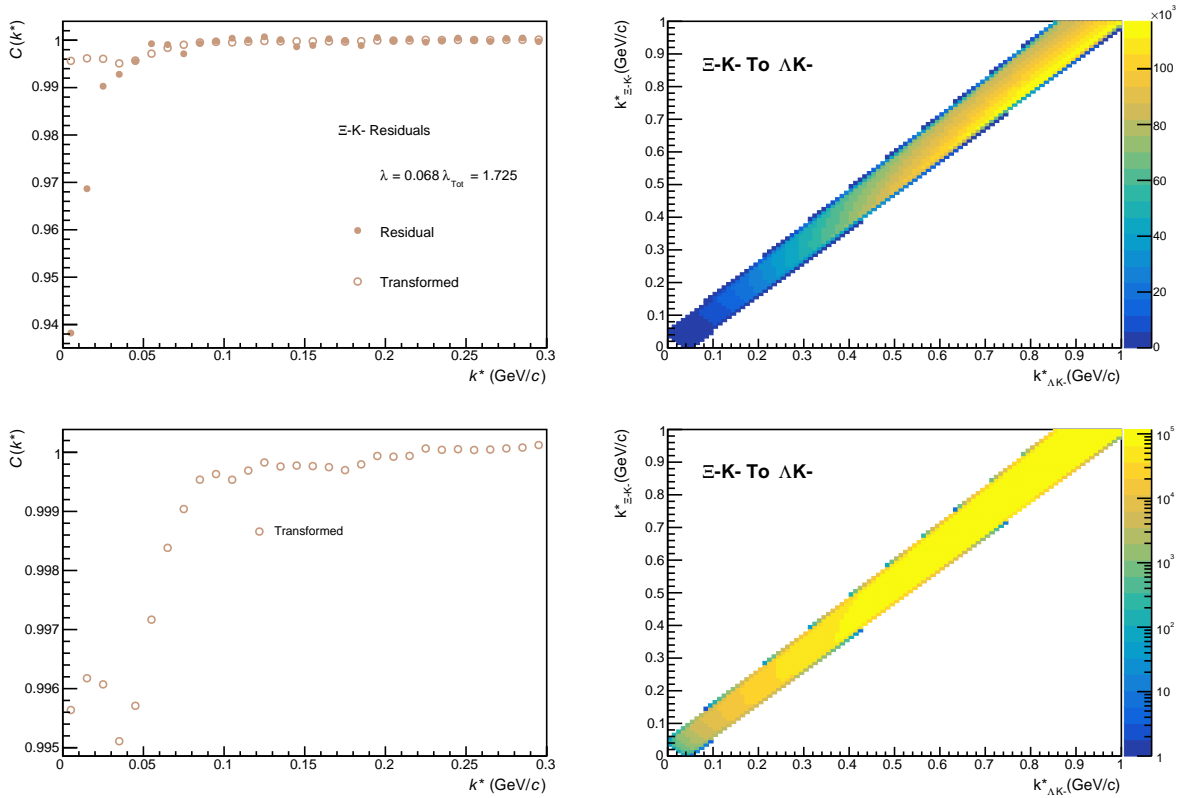


Fig. C.10: Residuals: $\Xi^- K^{*0}$ to ΛK^+ (0-10% Centrality)

1236 **C.1.2 ΛK^- Residuals****Fig. C.11:** Residuals: $\Sigma^0 K^-$ to ΛK^- (0-10% Centrality)

**Fig. C.12:** Residuals: $\Xi^0 K^-$ to ΛK^- (0-10% Centrality)**Fig. C.13:** Residuals: $\Xi^- K^-$ to ΛK^- (0-10% Centrality)

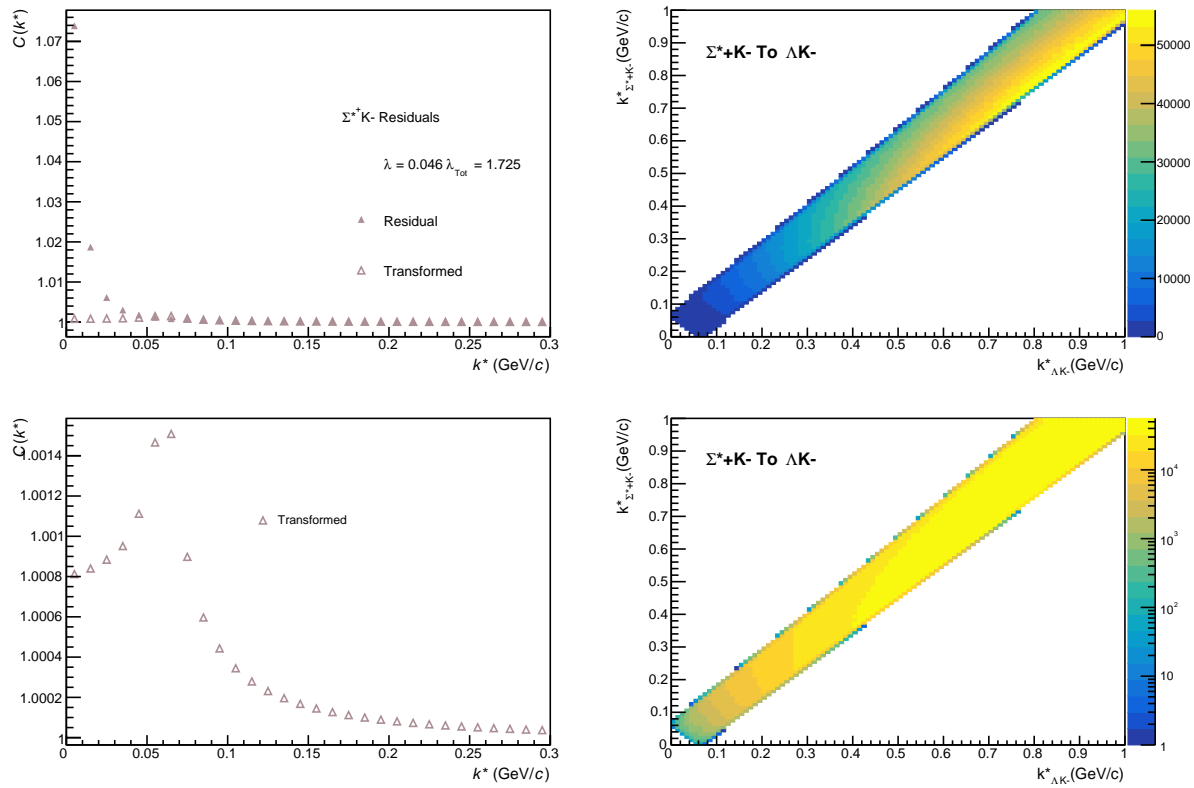


Fig. C.14: Residuals: $\Sigma^+ K^-$ to ΛK^- (0-10% Centrality)

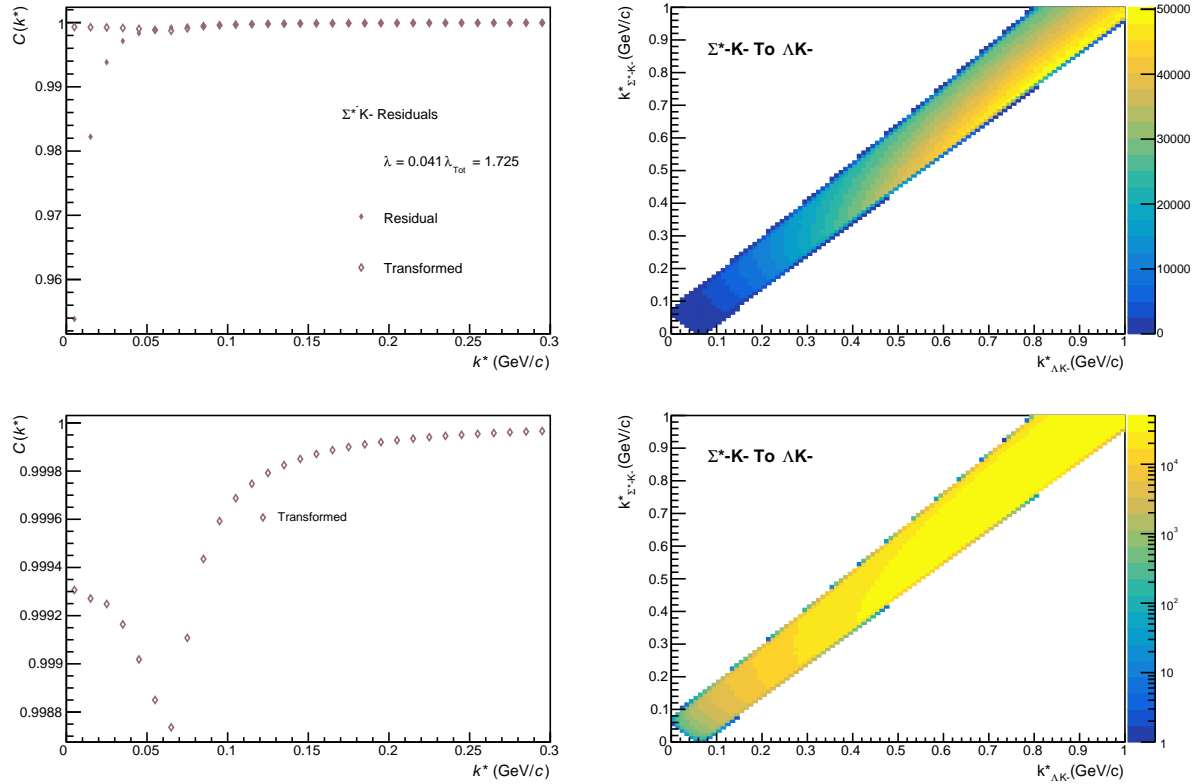
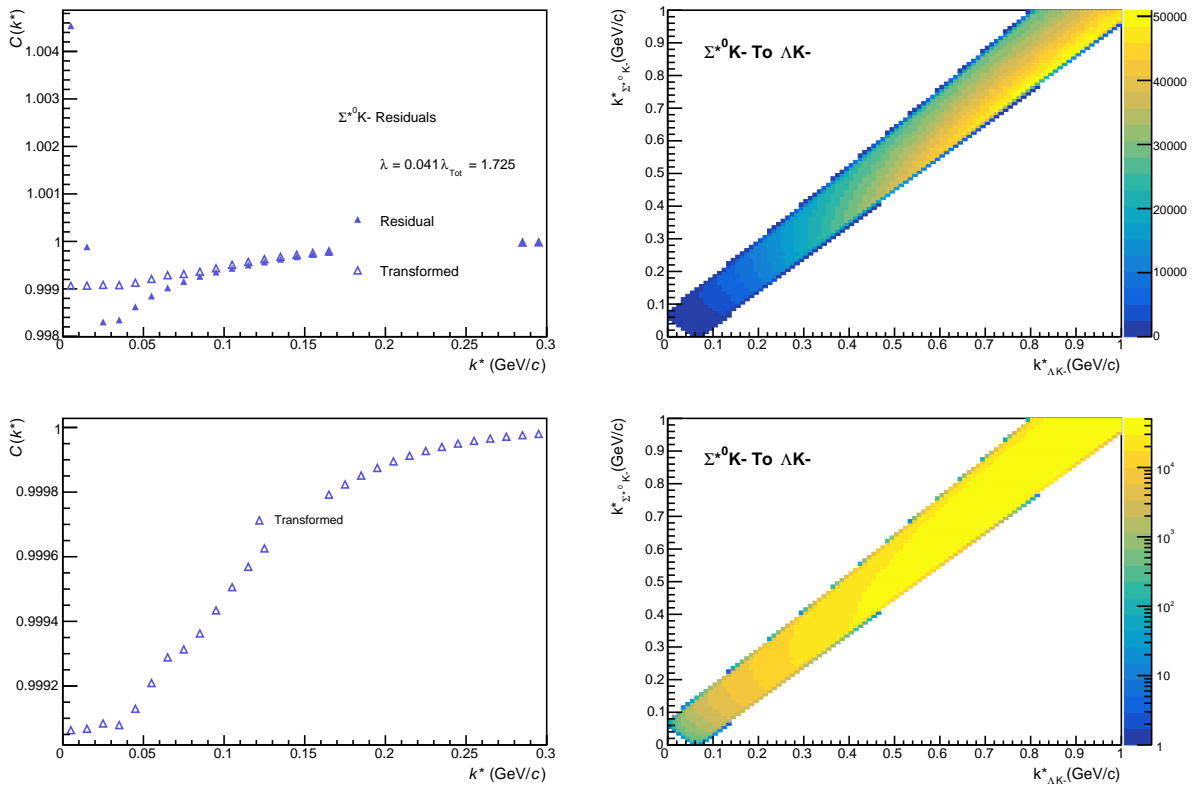
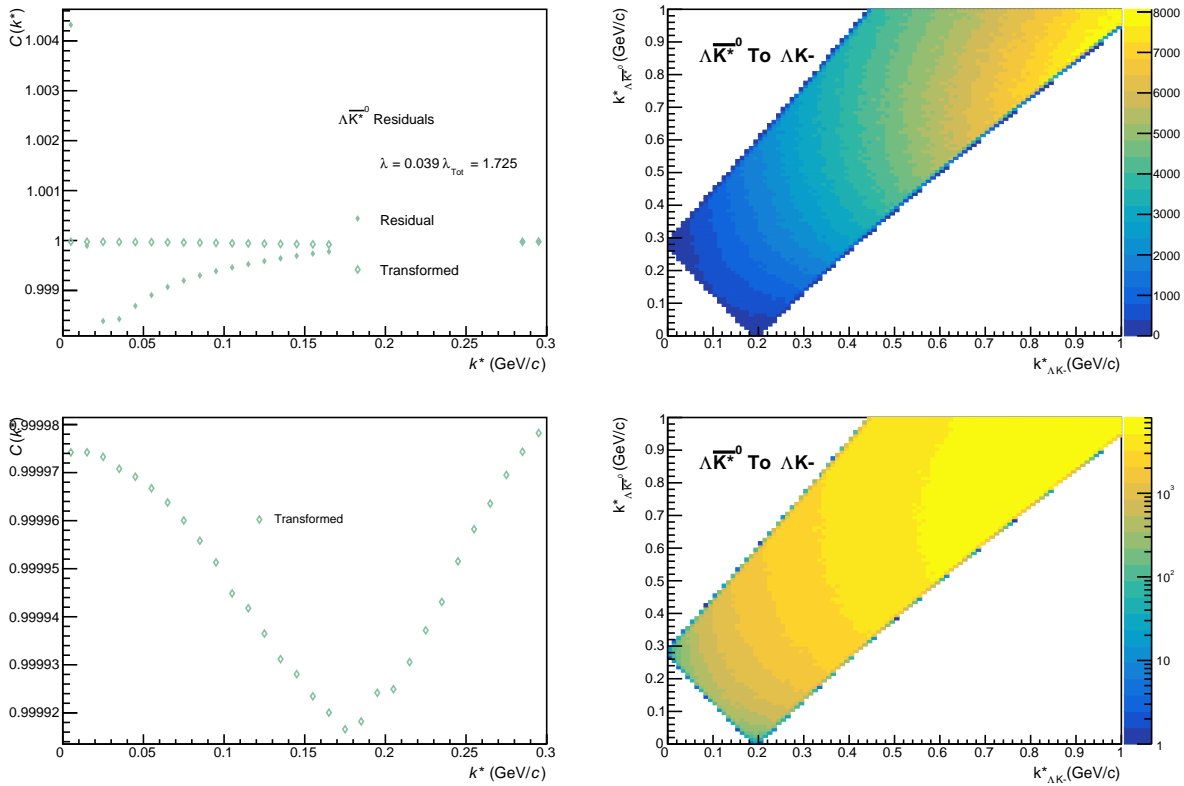


Fig. C.15: Residuals: $\Sigma^+ K^-$ to ΛK^- (0-10% Centrality)


Fig. C.16: Residuals: $\Sigma^{*0} K^-$ to ΛK^- (0-10% Centrality)

Fig. C.17: Residuals: $\Lambda \bar{K}^{*0}$ to ΛK^- (0-10% Centrality)

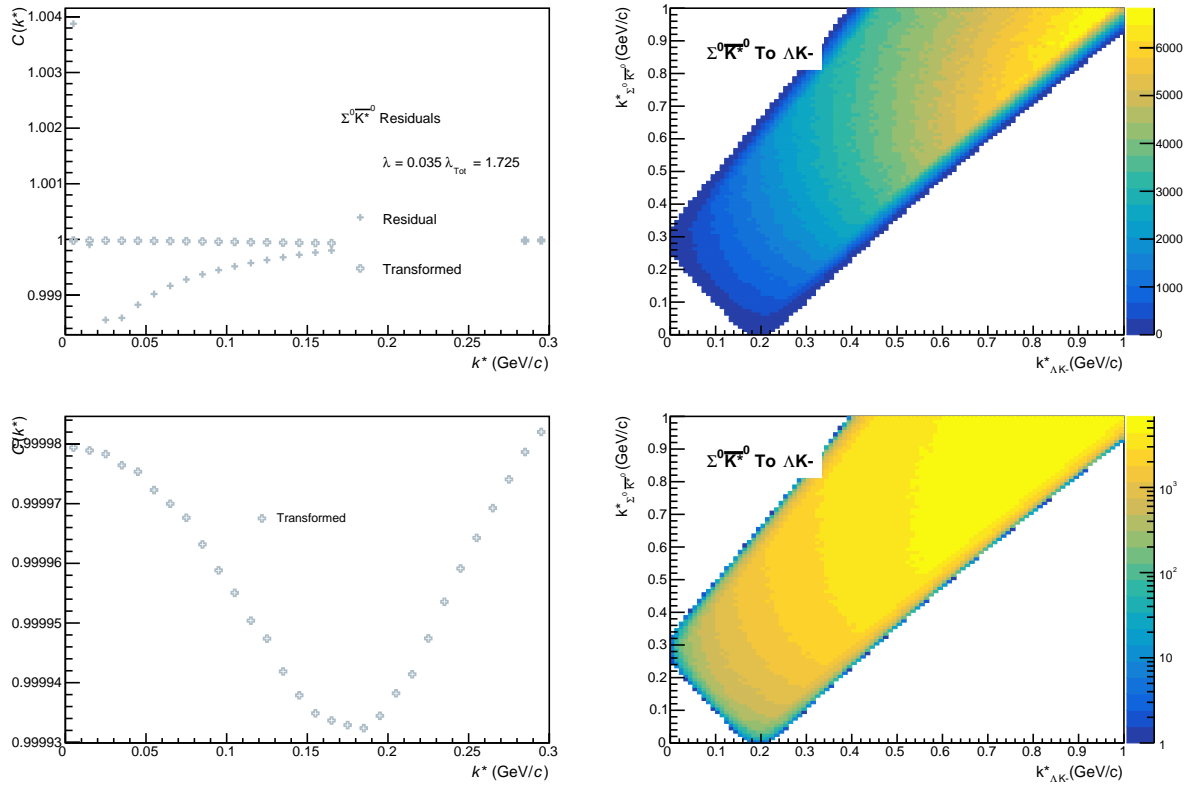


Fig. C.18: Residuals: $\Sigma^0 \bar{K}^0$ to ΛK^- (0-10% Centrality)

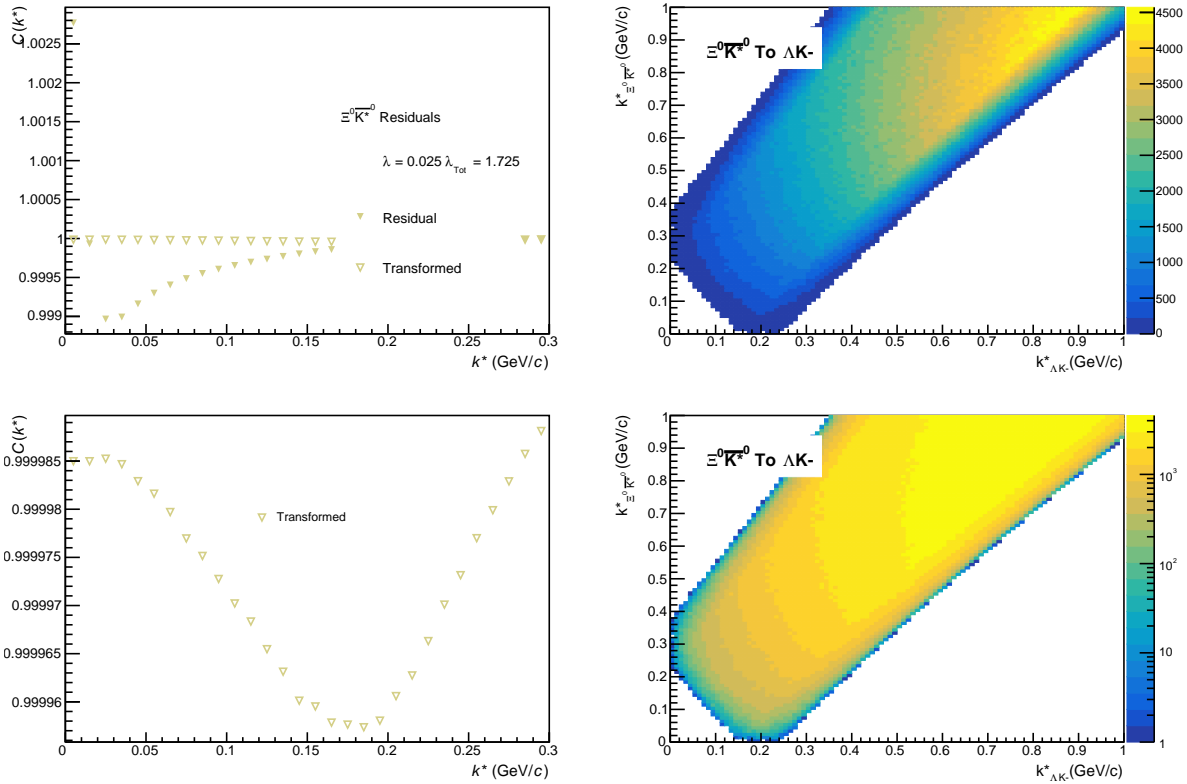


Fig. C.19: Residuals: $\Xi^0 \bar{K}^0$ to ΛK^- (0-10% Centrality)

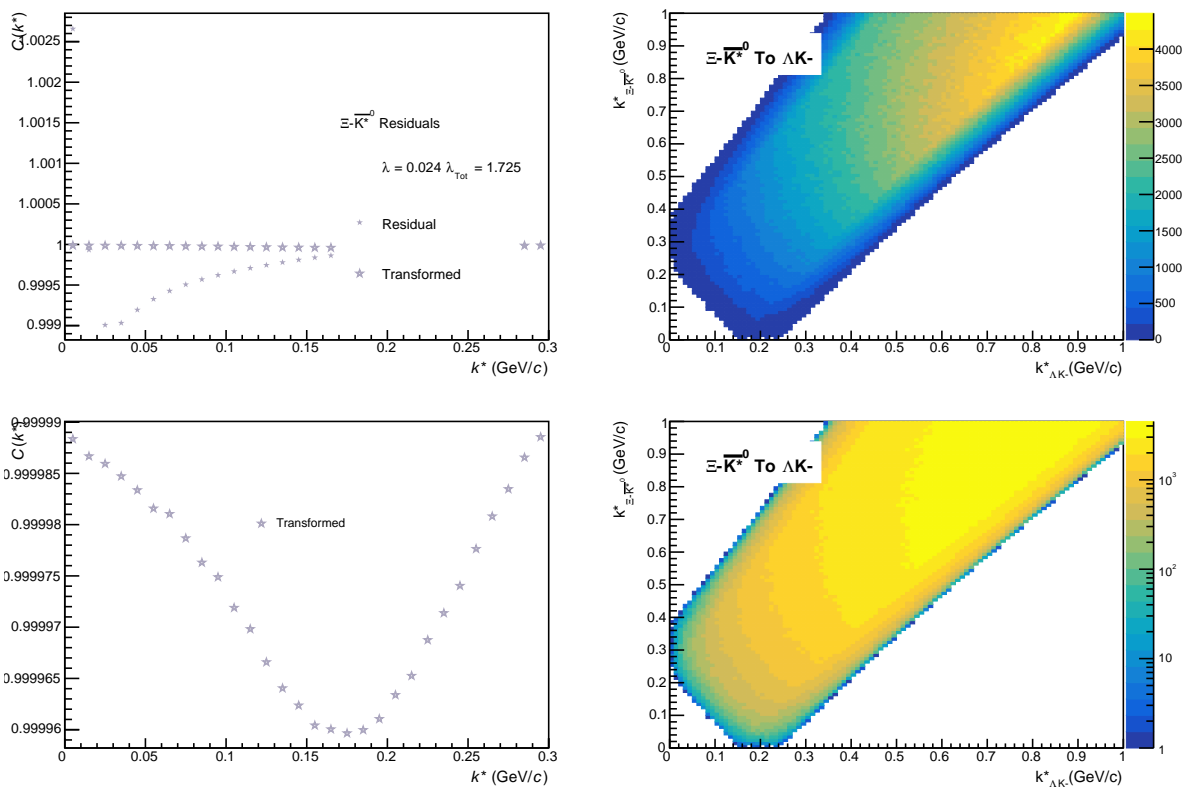


Fig. C.20: Residuals: $\Xi^- \bar{K}^{*0}$ to ΛK^- (0-10% Centrality)

1237 **C.1.3 ΛK_S^0 Residuals**

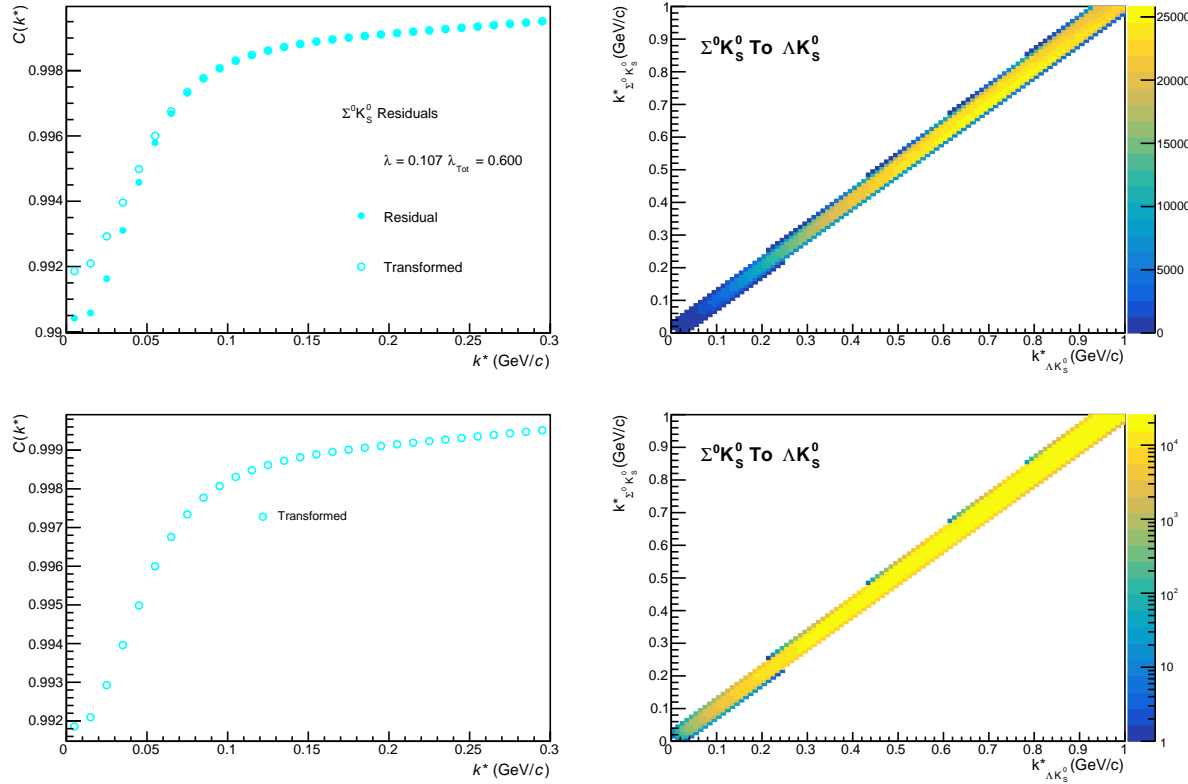


Fig. C.21: Residuals: $\Sigma^0 K_s^0$ to ΛK_s^0 (0-10% Centrality)

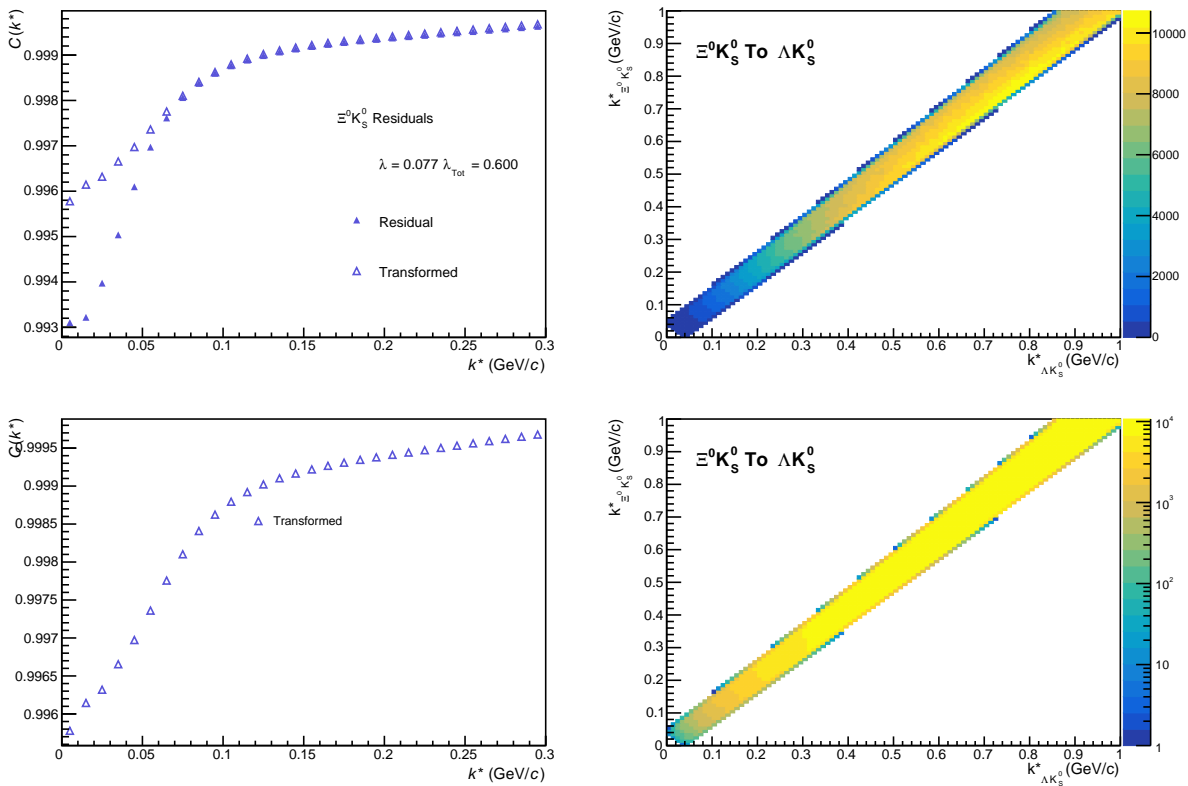


Fig. C.22: Residuals: $\Xi^0 K_S^0$ to ΛK_S^0 (0-10% Centrality)

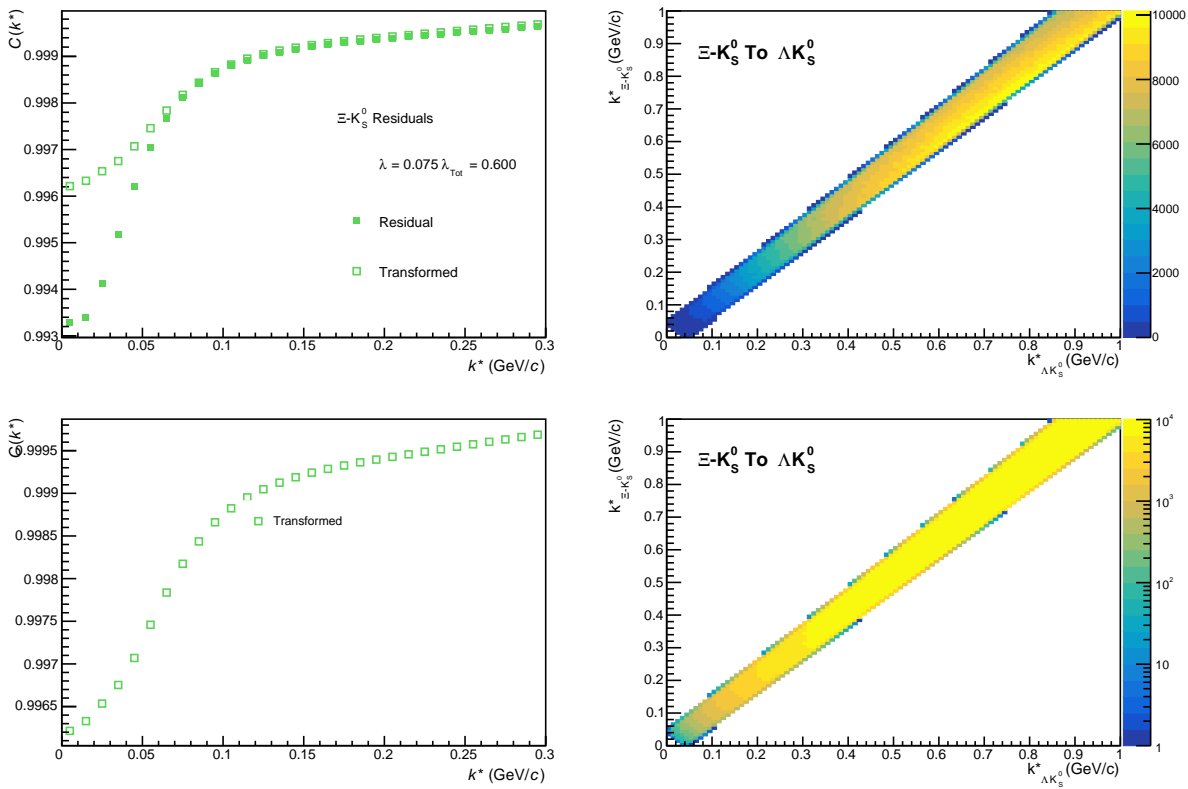


Fig. C.23: Residuals: $\Xi^- K_S^0$ to ΛK_S^0 (0-10% Centrality)

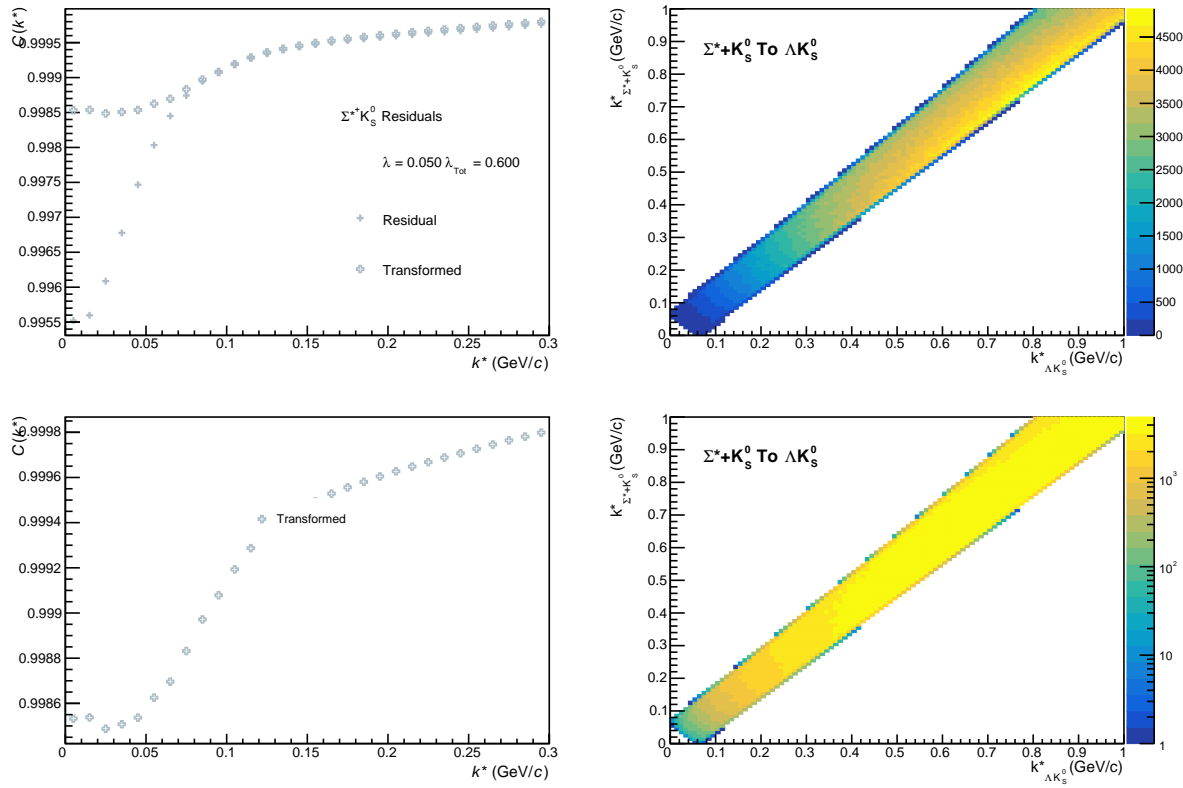


Fig. C.24: Residuals: $\Sigma^+ K_s^0$ to ΛK_s^0 (0-10% Centrality)

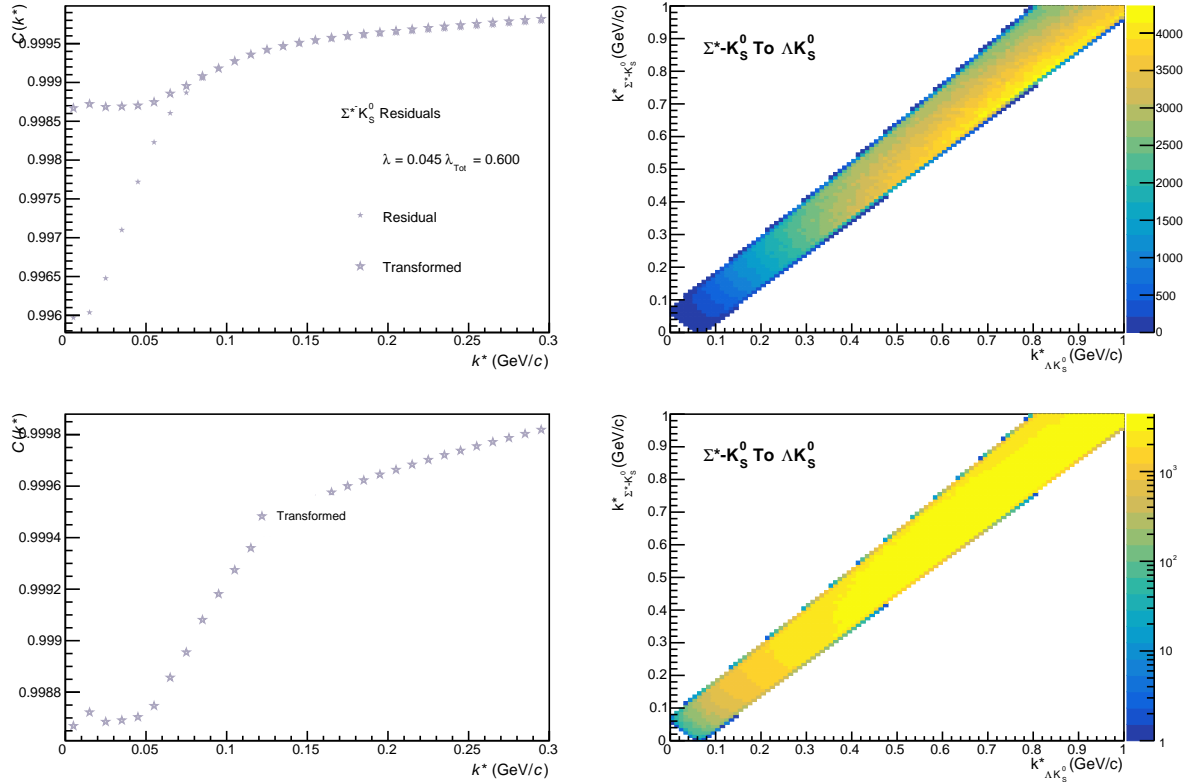
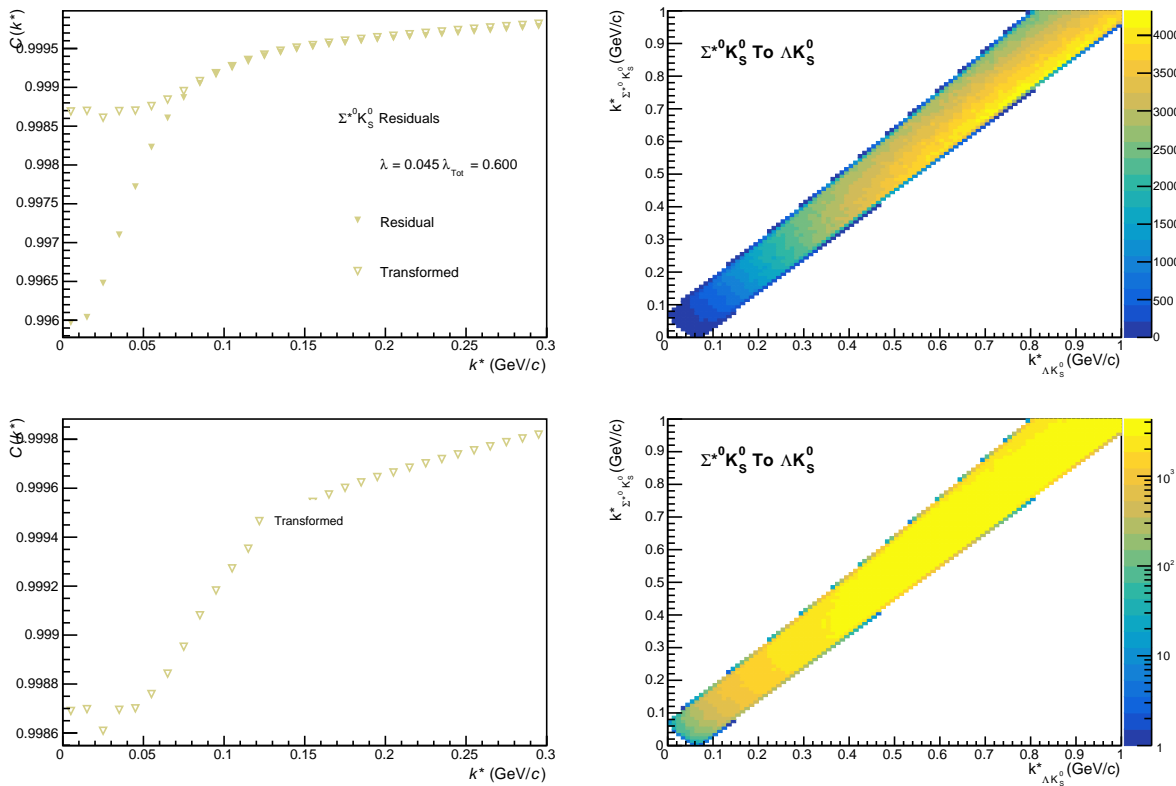
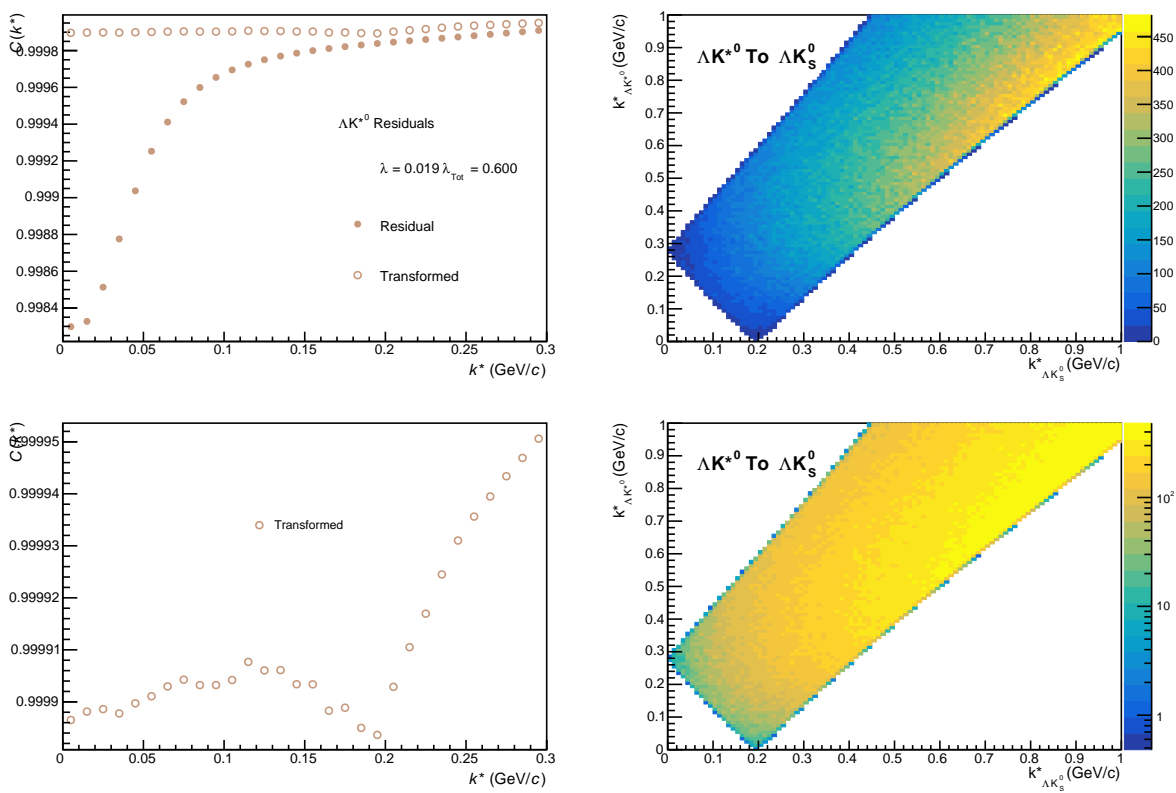


Fig. C.25: Residuals: $\Sigma^- K_s^0$ to ΛK_s^0 (0-10% Centrality)


Fig. C.26: Residuals: $\Sigma^{*0} K_S^0$ to ΛK_S^0 (0-10% Centrality)

Fig. C.27: Residuals: ΛK^{*0} to ΛK_S^0 (0-10% Centrality)

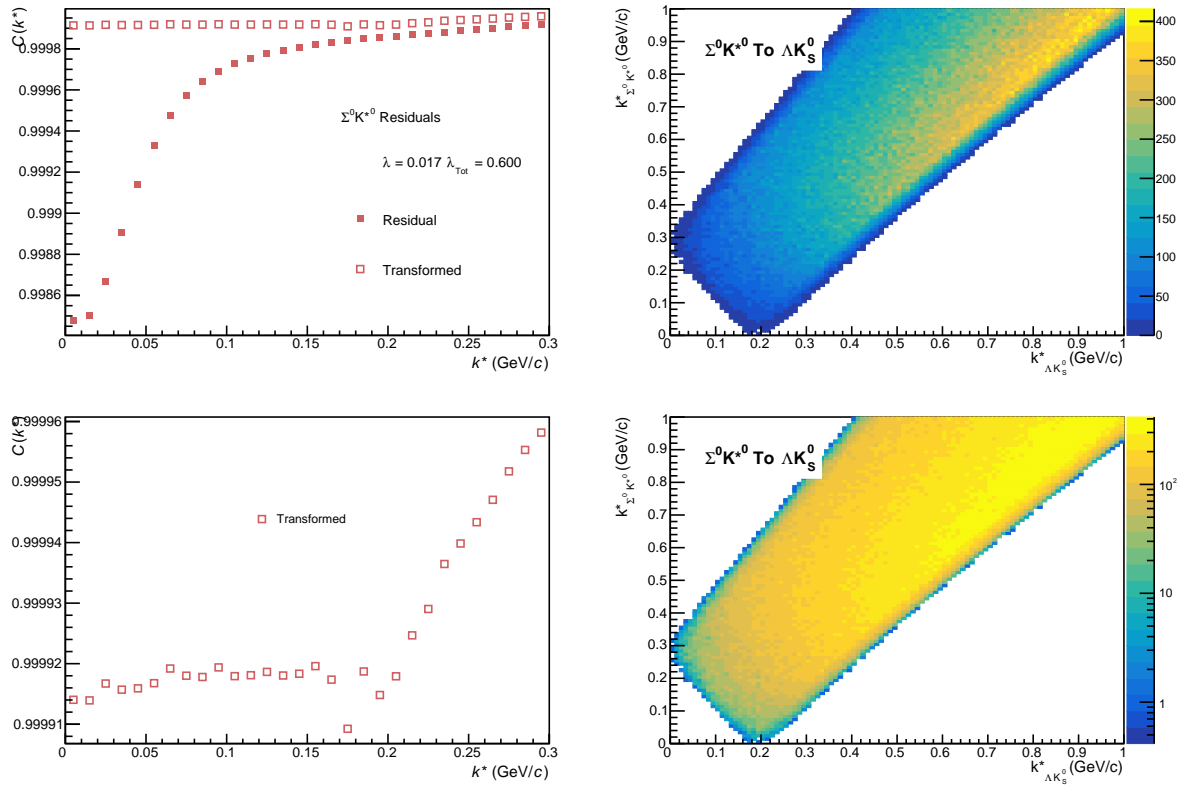


Fig. C.28: Residuals: $\Sigma^0 K^{*0}$ to ΛK_S^0 (0-10% Centrality)

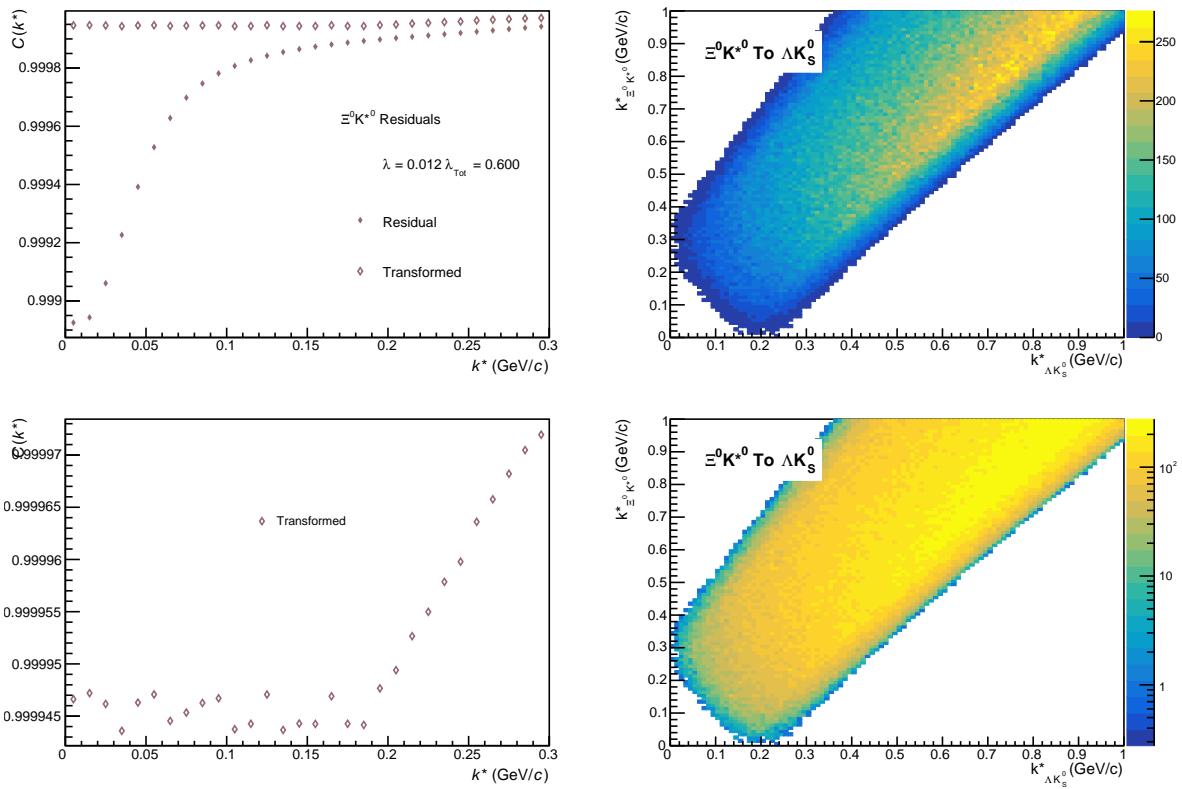


Fig. C.29: Residuals: $\Xi^0 K^{*0}$ to ΛK_S^0 (0-10% Centrality)

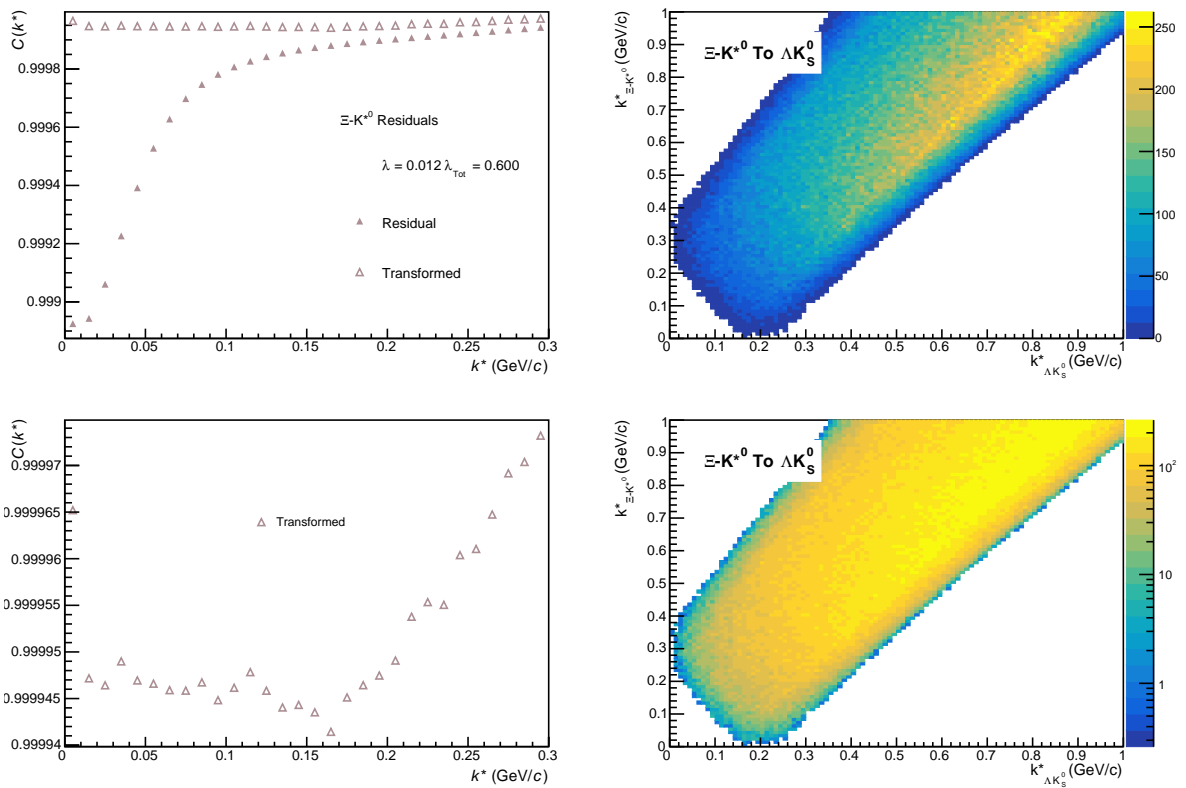


Fig. C.30: Residuals: $\Xi\text{-}K^{*0}$ to $\Lambda\text{-}K_s^0$ (0-10% Centrality)

1238 **D Useful Gaussian Integrals**

1239 **D.1 Simple univariate Gaussian integral**

$$\begin{aligned}
 I &= \int_{-\infty}^{\infty} e^{-x^2/2\sigma^2} dx \\
 \rightarrow I^2 &= \int_{-\infty}^{\infty} e^{-x^2/2\sigma^2} dx \int_{-\infty}^{\infty} e^{-y^2/2\sigma^2} dy = \int_{-\infty}^{\infty} \int_{-\infty}^{\infty} e^{-(x^2+y^2)/2\sigma^2} dxdy \\
 &= \int_0^{\infty} \int_0^{2\pi} e^{-r^2/2\sigma^2} r dr d\theta = -2\pi\sigma^2 \int_0^{\infty} e^{-r^2/2\sigma^2} \frac{-r}{\sigma^2} dr = 2\pi\sigma^2 \\
 \Rightarrow I &= \sigma\sqrt{2\pi}
 \end{aligned} \tag{D.1}$$

1240 This also implies

$$\int_{-\infty}^{\infty} e^{-(x-\mu)^2/2\sigma^2} dx = \sigma\sqrt{2\pi} \tag{D.2}$$

1241 This can be shown by making the substitution $x \rightarrow x - \mu$; but, intuitively this makes sense, as the area
1242 under a Gaussian curve does not depend on where the curve is located.

1243 **D.2 Product of two univariate Gaussian integrals**

$$\begin{aligned}
 f(x) &= \frac{1}{\sigma_f\sqrt{2\pi}} \exp\left[-\frac{(x-\mu_f)^2}{2\sigma_f^2}\right] \\
 g(x) &= \frac{1}{\sigma_g\sqrt{2\pi}} \exp\left[-\frac{(x-\mu_g)^2}{2\sigma_g^2}\right] \\
 \Rightarrow f(x)g(x) &= \frac{1}{2\pi\sigma_f\sigma_g} \exp\left[-\frac{(x-\mu_f)^2}{2\sigma_f^2} - \frac{(x-\mu_g)^2}{2\sigma_g^2}\right] \\
 &\equiv \frac{1}{2\pi\sigma_f\sigma_g} \exp[-\beta]
 \end{aligned} \tag{D.3}$$

$$\begin{aligned}
 \beta &= \frac{(x-\mu_f)^2}{2\sigma_f^2} + \frac{(x-\mu_g)^2}{2\sigma_g^2} \\
 &= \frac{2\sigma_g^2[x^2 - 2\mu_fx + \mu_f^2] + 2\sigma_f^2[x^2 - 2\mu_gx + \mu_g^2]}{4\sigma_f^2\sigma_g^2} \\
 &= \frac{(\sigma_f^2 + \sigma_g^2)x^2 - 2(\mu_f\sigma_f^2 + \mu_g\sigma_g^2)x + \mu_f^2\sigma_g^2 + \mu_g^2\sigma_f^2}{2\sigma_f^2\sigma_g^2} \\
 &= \frac{x^2 - 2\frac{\mu_f\sigma_g^2 + \mu_g\sigma_f^2}{\sigma_f^2 + \sigma_g^2}x + \frac{\mu_f^2\sigma_g^2 + \mu_g^2\sigma_f^2}{\sigma_f^2 + \sigma_g^2}}{2\frac{\sigma_f^2\sigma_g^2}{\sigma_f^2 + \sigma_g^2}}
 \end{aligned} \tag{D.4}$$

$$\begin{aligned}
 \text{Define : } \alpha &\equiv \frac{\mu_f\sigma_g^2 + \mu_g\sigma_f^2}{\sigma_f^2 + \sigma_g^2} \\
 \Rightarrow \beta &= \frac{(x^2 - 2\alpha x + \alpha^2) - \alpha^2 + \frac{\mu_f^2\sigma_g^2 + \mu_g^2\sigma_f^2}{\sigma_f^2 + \sigma_g^2}}{2\frac{\sigma_f^2\sigma_g^2}{\sigma_f^2 + \sigma_g^2}}
 \end{aligned}$$

$$\begin{aligned}
\frac{\mu_f^2 \sigma_g^2 + \mu_g^2 \sigma_f^2}{\sigma_f^2 + \sigma_g^2} - \alpha^2 &= \frac{\mu_f^2 \sigma_g^2 + \mu_g^2 \sigma_f^2}{\sigma_f^2 + \sigma_g^2} - \left(\frac{\mu_f \sigma_g + \mu_g \sigma_f}{\sigma_f^2 + \sigma_g^2} \right)^2 \\
&= \frac{1}{(\sigma_f^2 + \sigma_g^2)^2} [(\mu_f^2 \sigma_g^2 + \mu_g^2 \sigma_f^2)(\sigma_f^2 + \sigma_g^2) - (\mu_f \sigma_g + \mu_g \sigma_f)^2] \\
&= \frac{1}{(\sigma_f^2 + \sigma_g^2)^2} [\mu_f^2 \sigma_f^2 \sigma_g^2 + \mu_g^2 \sigma_f^2 \sigma_g^2 + \mu_f^2 \sigma_g^4 + \mu_g^2 \sigma_f^4 - \dots \\
&\quad - \mu_f^2 \sigma_g^4 - \mu_g^2 \sigma_f^4 - 2\mu_f \mu_g \sigma_f^2 \sigma_g^2] \\
&= \frac{\sigma_f^2 \sigma_g^2}{(\sigma_f^2 + \sigma_g^2)^2} [\mu_f^2 - 2\mu_f \mu_g + \mu_g^2] \\
&= \frac{\sigma_f^2 \sigma_g^2}{(\sigma_f^2 + \sigma_g^2)^2} (\mu_f - \mu_g)^2
\end{aligned} \tag{D.5}$$

$$\begin{aligned}
\beta &= \frac{(x^2 - 2\alpha x + \alpha^2) - \alpha^2 + \frac{\mu_f^2 \sigma_g^2 + \mu_g^2 \sigma_f^2}{\sigma_f^2 + \sigma_g^2}}{2 \frac{\sigma_f^2 \sigma_g^2}{\sigma_f^2 + \sigma_g^2}} \\
&= \frac{(x - \alpha)^2 + \frac{\sigma_f^2 \sigma_g^2}{(\sigma_f^2 + \sigma_g^2)^2} (\mu_f - \mu_g)^2}{2 \frac{\sigma_f^2 \sigma_g^2}{\sigma_f^2 + \sigma_g^2}}
\end{aligned} \tag{D.6}$$

Define : $\gamma^2 = \frac{\sigma_f^2 \sigma_g^2}{\sigma_f^2 + \sigma_g^2}$

$$\beta = \frac{(x - \alpha)^2}{2\gamma^2} + \frac{(\mu_f - \mu_g)^2}{2(\sigma_f^2 + \sigma_g^2)}$$

$$\begin{aligned}
f(x)g(x) &= \frac{1}{2\pi\sigma_f\sigma_g} e^{-\beta} = \frac{1}{2\pi\sigma_f\sigma_g} \exp \left[-\frac{(x - \alpha)^2}{2\gamma^2} \right] \exp \left[\frac{(\mu_f - \mu_g)^2}{2(\sigma_f^2 + \sigma_g^2)} \right] \\
&= \frac{1}{\sigma_f \sigma_g} \gamma \sqrt{(\sigma_f^2 + \sigma_g^2)} \times \frac{1}{\gamma \sqrt{2\pi}} \exp \left[-\frac{(x - \alpha)^2}{2\gamma^2} \right] \times \dots \\
&\quad \times \frac{1}{\sqrt{(\sigma_f^2 + \sigma_g^2)} \sqrt{2\pi}} \exp \left[\frac{(\mu_f - \mu_g)^2}{2(\sigma_f^2 + \sigma_g^2)} \right] \\
\Rightarrow f(x)g(x) &= \frac{1}{\gamma \sqrt{2\pi}} \exp \left[-\frac{(x - \alpha)^2}{2\gamma^2} \right] S_{fg} \\
S_{fg} &= \frac{\gamma \sqrt{(\sigma_f^2 + \sigma_g^2)}}{\sigma_f \sigma_g} \frac{1}{\sqrt{(\sigma_f^2 + \sigma_g^2)} \sqrt{2\pi}} \exp \left[-\frac{(\mu_f - \mu_g)^2}{2(\sigma_f^2 + \sigma_g^2)} \right] \\
&= \frac{1}{\sqrt{2\pi(\sigma_f^2 + \sigma_g^2)}} \exp \left[-\frac{(\mu_f - \mu_g)^2}{2(\sigma_f^2 + \sigma_g^2)} \right]
\end{aligned} \tag{D.7}$$

$$\begin{aligned} \int_{-\infty}^{\infty} f(x)g(x)dx &= \frac{S_{fg}}{\gamma\sqrt{2\pi}} \int_{-\infty}^{\infty} \exp\left[-\frac{(x-\alpha)^2}{2\gamma^2}\right] = S_{fg} \\ &= \frac{1}{\sqrt{2\pi(\sigma_f^2 + \sigma_g^2)}} \exp\left[-\frac{(\mu_f - \mu_g)^2}{2(\sigma_f^2 + \sigma_g^2)}\right] \end{aligned} \quad (\text{D.8})$$

¹²⁴⁴ **D.3 Univariate Gaussian with linear term in exponential**

$$I = \int_{-\infty}^{\infty} \exp\left[-\frac{x^2}{2\sigma^2} + Jx\right] \quad (\text{D.9})$$

¹²⁴⁵ Just as above, the idea is to complete the square

$$\begin{aligned} \frac{x^2}{2\sigma^2} - Jx &= \frac{1}{2\sigma^2} [x^2 - 2\sigma^2 Jx + (\sigma^2 J)^2 - (\sigma^2 J)^2] \\ &= \frac{1}{2\sigma^2} (x - \sigma^2 J)^2 - \frac{1}{2\sigma^2} (\sigma^2 J)^2 = \frac{(x - \sigma^2 J)^2}{2\sigma^2} - \frac{(\sigma J)^2}{2} \end{aligned} \quad (\text{D.10})$$

¹²⁴⁶ Therefore, I find:

$$\begin{aligned} I &= \int_{-\infty}^{\infty} \exp\left[-\frac{x^2}{2\sigma^2} + Jx\right] = \int_{-\infty}^{\infty} \exp\left[\frac{(x - \sigma^2 J)^2}{2\sigma^2} - \frac{(\sigma J)^2}{2}\right] \\ &= \sigma\sqrt{2\pi} \exp\left[\frac{(\sigma J)^2}{2}\right] \end{aligned} \quad (\text{D.11})$$

References

- [1] R. Lednicky and V. L. Lyuboshits. Final State Interaction Effect on Pairing Correlations Between Particles with Small Relative Momenta. *Sov. J. Nucl. Phys.*, 35:770, 1982. [Yad. Fiz.35,1316(1981)].
- [2] C. Patrignani et al. Review of Particle Physics. *Chin. Phys.*, C40(10):100001, 2016.
- [3] Michael Annan Lisa, Scott Pratt, Ron Soltz, and Urs Wiedemann. Femtoscopy in relativistic heavy ion collisions. *Ann. Rev. Nucl. Part. Sci.*, 55:357–402, 2005.
- [4] G. I. Kopylov. Like particle correlations as a tool to study the multiple production mechanism. *Phys. Lett.*, B50:472–474, 1974. [,39(1974)].
- [5] R. Lednicky, V. L. Lyuboshits, B. Erazmus, and D. Nouais. How to measure which sort of particles was emitted earlier and which later. *Phys. Lett.*, B373:30–34, 1996.
- [6] S. E. Koonin. Proton Pictures of High-Energy Nuclear Collisions. *Phys. Lett.*, B70:43–47, 1977.
- [7] S. Pratt, T. Csorgo, and J. Zimanyi. Detailed predictions for two pion correlations in ultrarelativistic heavy ion collisions. *Phys. Rev.*, C42:2646–2652, 1990.
- [8] Adam Kisiel. Non-identical particle femtoscopy at $s(\text{NN})^{**}(1/2) = 200\text{-AGeV}$ in hydrodynamics with statistical hadronization. *Phys. Rev.*, C81:064906, 2010.
- [9] Richard Lednicky. Finite-size effects on two-particle production in continuous and discrete spectrum. *Phys. Part. Nucl.*, 40:307–352, 2009.
- [10] Adam Kisiel, Hanna Zbroszczyk, and Maciej Szymaski. Extracting baryon-antibaryon strong interaction potentials from p $\bar{\Lambda}$ femtoscopy correlation functions. *Phys. Rev.*, C89(5):054916, 2014.
- [11] Mikolaj Chojnacki, Adam Kisiel, Wojciech Florkowski, and Wojciech Broniowski. THERMINATOR 2: THERMal heavy IoN generATOR 2. *Comput. Phys. Commun.*, 183:746–773, 2012.
- [12] A Kisiel. Non-identical particle correlation analysis in the presence of non-femtoscopy correlations. *Acta Physica Polonica B*, 48:717, 04 2017.
- [13] Jaroslav Adam et al. One-dimensional pion, kaon, and proton femtoscopy in Pb-Pb collisions at $\sqrt{s_{\text{NN}}} = 2.76 \text{ TeV}$. *Phys. Rev.*, C92(5):054908, 2015.
- [14] Yan-Rui Liu and Shi-Lin Zhu. Meson-baryon scattering lengths in HB chi PT. *Phys. Rev.*, D75:034003, 2007.
- [15] Maxim Mai, Peter C. Bruns, Bastian Kubis, and Ulf-G. Meissner. Aspects of meson-baryon scattering in three and two-flavor chiral perturbation theory. *Phys. Rev.*, D80:094006, 2009.
- [16] Fabrice Retiere and Michael Annan Lisa. Observable implications of geometrical and dynamical aspects of freeze out in heavy ion collisions. *Phys. Rev.*, C70:044907, 2004.